MSc Thesis Mechanical Engineering

Flange Design for Stress Reduction in Radially Arranged Sheet Flexures with One Rotational Degree of Freedom

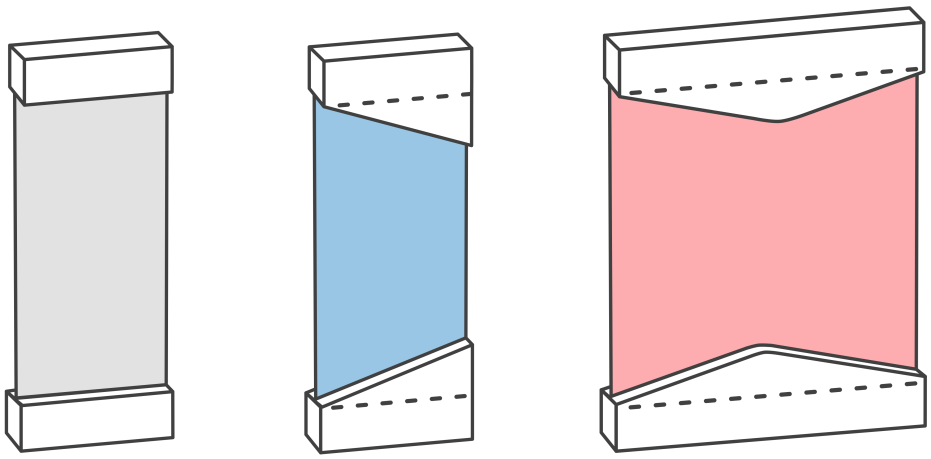

T. Bomer

Chairman: Prof. Dr. Ir. D.M Brouwer EngD
Supervisors: Dr. Ir. M. Nijenhuis
External: Dr. M.I. Abdul Rasheed

March, 2025

Faculty of Engineering Technology,
Chair of Precision Engineering

UNIVERSITY OF TWENTE.

Contents

Flange Design for Stress Reduction in Radially Arranged Sheet Flexures with One Rotational Degree of Freedom

T. Bomer

Faculty of Engineering Technology, University of Twente,
Drienerlolaan 5, 7522 NB, Enschede, The Netherlands

Abstract

Radially arranged sheet flexures enable a single rotational degree of freedom but experience high internal stresses even at small rotations. This paper shows that modifying the flange shapes (top and bottom edges) can effectively reduce the high stresses. An analytical model using nonlinear stiffness was developed to estimate the critical axial stress, highlighting that bending moments are the primary contributors to the reduced stress at initial rotations. ANSYS Workbench was used to model and analyze the stress in the sheet flexures with modified flange shapes. The tapered and bow-tie flange shapes were identified as the most effective shapes for minimizing the maximum stress, with reductions of up to 56% and 67% respectively. A parameter study revealed that the optimal flange shape and corresponding stress reduction are highly dependent on input parameters such as flexure width, thickness, radius and prescribed rotation. The tapered shape has better stress reduction for slender flexures, while the bow-tie shape is more effective for wider configurations. The optimal flange shape is found to be independent of the materials 304SS, Alu 7075-T6, Ti-6Al-4V, ABS, and HDPE. Design guidelines were developed to assist in replacing the sheet flexures with the tapered or bow-tie flexures. They include a shape decision graph for selecting the optimal flexure type based on dimensionless input parameters $\{\frac{W}{L}, \theta, \frac{t}{L}, \frac{R}{L}\}$. These guidelines also incorporate multiple prediction models that enable the estimation of output parameters, without the need for Finite Element Analysis. The prediction models are able to predict maximum stress of the sheet flexure, as well as optimal shape and stress reduction of the tapered and bow-tie flexures with an relative error <20% for 89% of the cases compared to Finite Element Analysis.

Keywords: Flexure mechanisms, Stress reduction, Parameter study

1 Introduction

Flexure mechanisms play an important role in precision engineering applications due to their predictable behavior. These systems operate as flexible mechanisms that transmit force and motion through the deformation of elastic bodies. The flexure mechanisms are carefully designed and arranged to exhibit high compliance in directions where motion is desired, while providing significant stiffness to restrict motion in unintended directions. As a result, their operation is nearly free from hysteresis, operates within a limited range of motion, and is defined exclusively by the stiffness of the elastic components [1].

One type of motion that a system might require is a single rotational degree of freedom. Practical examples of such requirement can be seen in two collaborative projects [2, 3] between the University of Twente and Nova, a company specializing in advanced optical and infrared telescope systems. In these projects, two prisms were required to achieve near-pure rotation around an optical axis of a telescope. It was important that the flexure mechanism did not obstruct the optical path. A method to achieve this motion is through the radial arrangement of sheet flexures, as illustrated in Figure 1.1.

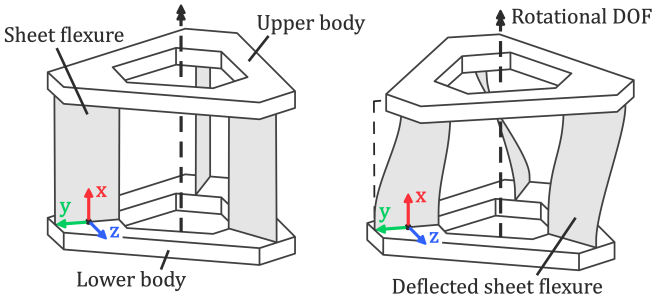

Figure 1.1: Radial arrangement of sheet flexures for one rotational DOF, deflected and undeflected

The sheet flexure (also referred to as leaf spring, flexure strip, or flexure blade) is commonly used in precision engineering applications. It is characterized by a thickness that considerably smaller than its width. A single sheet flexure, such as the one with the attached coordinate system in Figure 1.1, enables rotational x-, y-, and translational z-movement, defined as the degrees of freedom (DOF). While constraining the translational x-, y- and rotational z-movement, defined as the degrees of constraint (DOC). In other words, a single sheet flexure offers high support stiffness in the three DOC directions while being compliant in the remaining three DOF directions.

By radially arranging multiple sheet flexures, the combined system ensures a single rotational DOF. A

system with three sheet flexures provides nine DOC and therefore the combined system has four overconstraints. Other flexure mechanisms, such as cross flexures, can also provide a single rotational degree of freedom. This is typically achieved through bending of the sheet flexures. In the radial arrangement, the sheet flexures experience both bending and torsion.

An advantage of radially arranging multiple sheet flexures, is that it maintains a clear optical path of the rotational DOF. The mechanism is symmetric and the system's rotational DOF is unaffected by the error motions of the sheet flexure. Additionally, the system can be easily expanded to include more than three flexures. A drawback of this system is that even small prescribed rotations can generate high stresses in the sheet flexures. If these stresses exceed the material's elastic limit the flexures will start to deform plastically. This limits the applicable range of motion and thus the potential usability of the design.

The radial arrangement of sheet flexures is briefly discussed in the doctoral thesis by Hale [4]. It highlights that axial stress within sheet flexures can be minimized by modifying the geometry of the flanges (top and bottom edges of the flexure). Specifically, by shaping the flanges in such a way that the sheet flexures experience equal bending stress or equal shortening across their widths.

Figure 1.2a illustrates the shortening effect (also called lenght contraction), where a translation of the upper body in the z-direction results in a simultaneous movement in the x-direction. The extent of shortening depends on the flexure's length L and the magnitude of the z-translation [1].

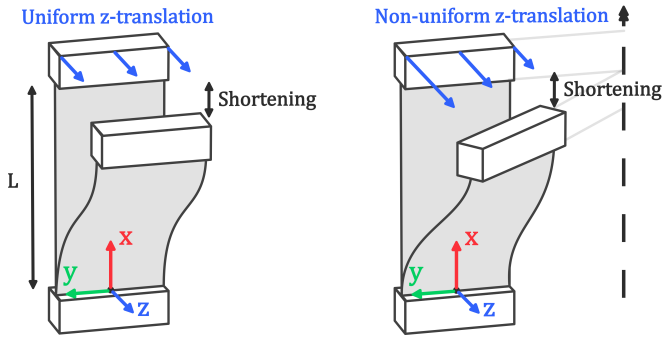

(a) Uniform (b) Non-uniform

Figure 1.2: Shortening effect due to z-translation

A sheet flexure in the radial arrangement does not experience a uniform z-translation across its width, as illustrated in Figure 1.2b. The corner of the sheet flexure at the maximum y-coordinate follows a larger radius compared to the corner at the minimum y-coordinate. This will result in an uneven shortening along the width of the flexure. Because the flexure is constrained by two bodies, this movement is restricted and internal stresses develop within the sheet flexure. As the shortening effect is dependent on the flexure's length, adjusting this length along the width provides a method to achieve equal foreshortening and mitigate these internal stresses [4].

The collaborative projects [2, 3] have observed that modifying the flanges of a sheet flexure can reduce the maximum stress. However, it remains unclear whether this reduction is directly linked to mitigating the shortening effect.

This thesis aims to explore the factors contributing to the high internal stresses and seeks to determine design guidelines for an optimal flange shape that will minimize the stresses within the sheet flexures. The design guidelines are developed to help engineers improve their system's one rotational DOF range of motion and expand the potential application and usability of the design.

First in Chapter 2, an analytical stress model for the one DOF system is developed, addressing the components contributing to the maximum stress. Chapter 3 introduces the modeling of a sheet flexure with tapered flanges and analyzes its impact on maximum stress. In Section 3.2.5 alternative flange shapes are modeled and compared, leading to the selection of two shapes for further research. Chapter 4 includes a parameter study to evaluate how variations in the input parameters influence the optimal flange shape and stress reduction. Chapter 5 provides design guidelines and prediction models to minimize maximum stress in the one DOF radially arranged flexure system. Chapter 6 constains the discussion and in Chapter 7 conclusions on this research are made. At last, in Chapter 8 recommendations for future research are provided.

2 Modeling the 1DOF system with sheet flexures

To understand what contributes to the high stresses in the sheet flexures, this chapter presents the development of an analytical stress model. The approach starts by simplifying the system to a single sheet flexure. A linear stiffness model is developed to support the prediction of stress. As a final step, the model is improved by incorporating nonlinear extensions to the stiffness model.

2.1 Simplifying, BCs and symmetry

A schematic overview of the system, featuring three radially arranged sheet flexures, is illustrated in Figure 2.1a. Each sheet flexure is modeled as a flexible element capable of deformation. All nodes have six degrees of freedom, three translational and three rotational. The lower body is represented by the fixed ground, while the upper body is modeled using rigid elements. The three flexures are all of equal length and are symmetrically positioned on a circle with radial distance R from the center node 0. A rotation θ about the x-axis is applied at node 0 which, due to the shortening effect, is accompanied with a translational motion of the entire rigid body in the negative x-direction. The symmetrical arrangement of the sheet flexures, coupled with their DOC, ensure that the rigid upper body is constrained in all other DOF.

The system can be simplified to a model with a single flexible element and a single rigid element, as shown in Figure 2.1b. This rigid element has a hinge at node 0 which allows for rotation and translation exclusively along the x-axis.

The system can be simplified even further by directly applying the boundary conditions (BCs) at node 2, leaving only the sheet flexure, as illustrated in Figure 2.1c. The motion of this element is governed by the applied rotation θ and the radial distance R. Therefore, the boundary conditions at node 2 are:

$$\begin{aligned} u_{2x} &= \text{free} & \phi_{2x} &= \theta \\ u_{2y} &= R\cos\theta - R & \phi_{2y} &= 0 \\ u_{2z} &= R\sin\theta & \phi_{2z} &= 0 \end{aligned} \tag{1}$$

With node 1 being fixed, all degrees of freedom at this node are constrained to zero.

2.2 Global and local coordinate system

All external constraints and applied loads are expressed in the global coordinate system x, y, z, which is fixed and located at node 1 as shown in Figure 2.2.

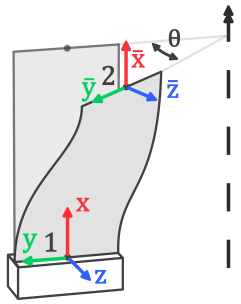

Figure 2.2: Global and local coordinate systems

To calculate stresses within a deformed element, a local 'moving' coordinate system $\bar{x}, \bar{y}, \bar{z}$ is used. The local coordinate system is attached to node 2 such that the $\bar{y}$-axis aligns with the flexures width, the $\bar{z}$-axis is normal to the top edge, and the $\bar{x}$-axis aligns with the global x-axis. The local coordinate system is related to the global coordinate system by a rotation matrix. For example, externally applied moments at node 2 can be transformed into the local coordinate system through:

$$\begin{bmatrix} M_{2\bar{x}} \\ M_{2\bar{y}} \\ M_{2\bar{z}} \end{bmatrix} = \begin{bmatrix} 1 & 0 & 0 \\ 0 & \cos\theta & -\sin\theta \\ 0 & \sin\theta & \cos\theta \end{bmatrix} \begin{bmatrix} M_{2x} \\ M_{2y} \\ M_{2z} \end{bmatrix} \tag{2}$$

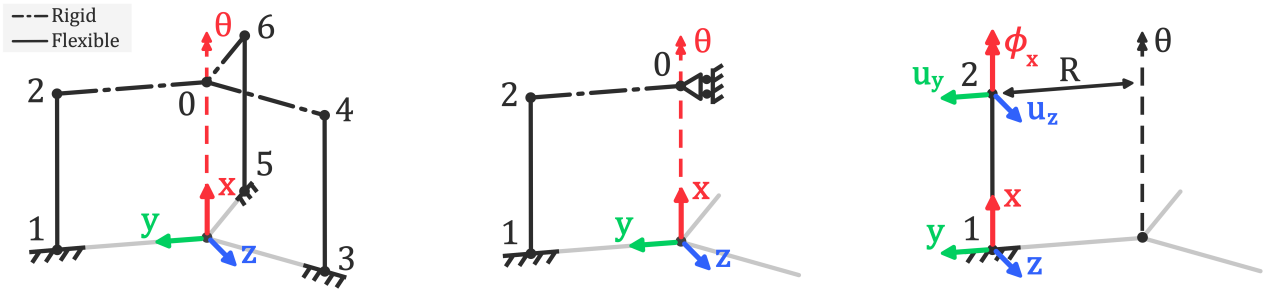

(a) Full radial arrangement (b) Intermediate using symmetry (c) Motion directly applied

Figure 2.1: Schematic overview of the steps taken to simplify the system, the flexible element is positioned at the centerline of the sheet flexure

2.3 Linear stiffness model

To calculate the stresses within the sheet flexure, it is necessary to establish the relationship between the applied displacements $\{u\}$ and reaction forces $\{F\}$. This relationship is expressed through the global stiffness matrix [K]:

$$\{F\} = [K]\{u\} \tag{3}$$

The stiffness matrix $[K]$ is derived using Euler-Bernoulli beam theory which governs the linear-elastic behavior of beams [5]. This theory assumes that the beam's cross-sections remain rigid and thus do not undergo deformation when loads are applied. During deformation, each cross-section is considered to remain planar and perpendicular to the beam's neutral axis. These assumptions are generally valid for slender beams, where the length L is much greater than the thickness t, and the displacements and rotations are small. Bernoulli beam theory is well-suited for beams where bending deformations dominate over shear deformations. To ensure that the effects of shear deformation can be neglected, the sheet flexure is modeled such that the length L is much greater than the width W. The resulting stiffness matrix $[K]$ is a 12×12 matrix, corresponding to the six DOF at each node, as outlined in [6]. The full matrix, along with the substitution of the boundary conditions, can be found in Appendix A. After applying the boundary conditions, the resulting system of equations are:

$$\begin{aligned} F_{1x} &= -\frac{EA}{L}u_{2x} & M_{1x} &= -\frac{GJ}{L}\phi_{2x} \\ F_{1y} &= -\frac{12EI_z}{L^3}u_{2y} & M_{1y} &= \frac{6EI_y}{L^2}u_{2z} \\ F_{1z} &= -\frac{12EI_y}{L^3}u_{2z} & M_{1z} &= -\frac{6EI_z}{L^2}u_{2y} \end{aligned} \tag{4}$$

$$\begin{aligned} F_{2x} &= \frac{EA}{L}u_{2x} & M_{2x} &= \frac{GJ}{L}\phi_{2x} \\ F_{2y} &= \frac{12EI_z}{L^3}u_{2y} & M_{2y} &= \frac{6EI_y}{L^2}u_{2z} \\ F_{2z} &= \frac{12EI_y}{L^3}u_{2z} & M_{2z} &= -\frac{6EI_z}{L^2}u_{2y} \end{aligned} \tag{5}$$

where F_{ix}, F_{iy}, F_{iz} and M_{ix}, M_{iy}, M_{iz} are the reaction forces and moments at nodes $i = 1, 2$. The material and geometric parameters of the sheet flexure include E, which is the Young's modulus of elasticity, A the cross-sectional area, L the length of the beam, J the torsional constant, and I_y and I_z are the second moments of area about the y- and z- axis respectively.

$$\begin{aligned} A &= Wt & J &\approx \frac{Wt^3}{16}\left(\frac{16}{3} - 3.36\frac{t}{W}\left(1 - \frac{t^4}{12W^4}\right)\right) \\ I_y &= \frac{1}{12}Wt^3 & I_z &= \frac{1}{12}tW^3 \end{aligned} \tag{6}$$

The remaining properties of the sheet flexure with a rectangular cross-section [5] are given in equation 6. A visual representation of all the parameters, along with the sign convention for the reaction forces and moments, is provided in Figure 2.3.

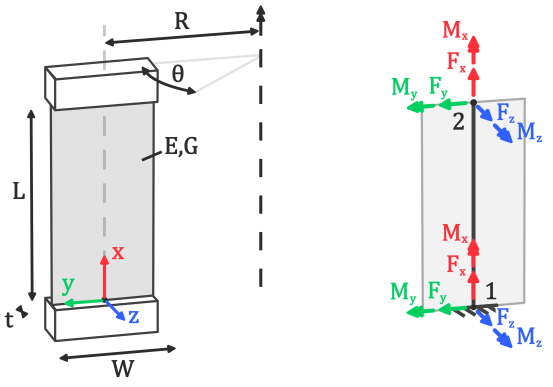

(a) Input parameters (b) Forces, moments

Figure 2.3: Overview of system parameters

2.4 Analytical stress model

Hale [4] states that the axial stress in the sheet flexure can be reduced by adjusting the flange geometry, to ensure uniform shortening across the width. This section will investigate the key factors contributing to the axial stress in the sheet flexure. The analytical stress model uses the linear stiffness model developed in the previous section as a starting point.

The stress tensor defines the state of stress at a specific point in a material under deformation and is formulated as [7]:

$$[\sigma] = \begin{bmatrix} \sigma_{\bar{x}\bar{x}} & \sigma_{\bar{x}\bar{y}} & \sigma_{\bar{x}\bar{z}} \\ \sigma_{\bar{y}\bar{x}} & \sigma_{\bar{y}\bar{y}} & \sigma_{\bar{y}\bar{z}} \\ \sigma_{\bar{z}\bar{x}} & \sigma_{\bar{z}\bar{y}} & \sigma_{\bar{z}\bar{z}} \end{bmatrix} \tag{7}$$

where $\sigma_{\bar{x}\bar{x}}, \sigma_{\bar{y}\bar{y}}, \sigma_{\bar{z}\bar{z}}$ are the normal stresses in the local coordinate system, and the off-diagonal terms $\sigma_{\bar{x}\bar{y}}, \sigma_{\bar{x}\bar{z}}, \sigma_{\bar{y}\bar{z}}$ are the shear stresses expressed in the local coordinate system. The stress tensor is symmetric, reducing the tensors to the six independent components mentioned before. When evaluating the stress state, criteria such as the von Mises stress or other failure theories are often used to determine whether a component exceeds its allowable stress limit. While the full stress tensor provides a comprehensive representation of this stress state, this study focuses on the $\sigma_{\bar{x}\bar{x}}$. This component covers the axial stress referenced by Hale and in Chapter 3.2.1 it is shown that the $\sigma_{\bar{x}\bar{x}}$ is the primary contributor to the maximum stress in the sheet flexure.

The normal stress in the sheet flexure is expressed as a sum of contributing components:

$$\sigma_{\bar{x}\bar{x}} = \sigma_{\bar{x}\bar{x},F_{2x}} + \sigma_{\bar{x}\bar{x},M_{2y}} + \sigma_{\bar{x}\bar{x},M_{2z}} + \sigma_{\bar{x}\bar{x},\varepsilon_{xx}} + \sigma_{\bar{x}\bar{x},\text{cw}} \tag{8}$$

Each component represents a distinct effect on the total axial stress distribution. A detailed explanation of these components is provided in the next section, accompanied by a visual interpretation of these components in Figure 2.4.

Contribution of an axial force

Normal stresses arising from an axial force, such as the weight of the upper body are represented by [5]:

$$\sigma_{\bar{x}\bar{x},F_{2x}} = \frac{F_{2\bar{x}}}{Wt} \tag{9}$$

where $F_{2\bar{x}}$ is the axial force, W the width and t the thickness of the sheet flexure.

Contribution of bending moments

Normal stresses arising from the bending moments, which result from the imposed motion and boundary conditions, are calculated with the flexural formula [5]:

$$\sigma_{\bar{x}\bar{x},M_{2y}} = \frac{M_{2\bar{y}}\bar{z}}{I_y} \qquad \sigma_{\bar{x}\bar{x},M_{2z}} = \frac{M_{2\bar{z}}\bar{y}}{I_z} \tag{10}$$

where $M_{2\bar{y}}$ and $M_{2\bar{z}}$ are the bending moments in the local coordinate system, $\bar{z}$ and $\bar{y}$ are the distance from the neutral axis. The approximated stresses vary linearly with the distances $\bar{z}$ and $\bar{y}$, reaching their maximum at the point farthest from the neutral axis. This corresponds to the outer corner of the flexure, indicated as point A in Figure 2.4b and 2.4c.

Contribution of shortening

The normal stresses caused by the shortening effect is approximated using Hooke's law [7] :

$$\sigma_{\bar{x}\bar{x},\varepsilon_{xx}} = E\varepsilon_{xx} \tag{11}$$

where ε_{xx} represents the strain difference between the overall shortening of the upper body and localized shortening of the flexure along its width. The strain difference is approximated as:

$$\varepsilon_{xx} \approx u_{x,\text{local}} - u_{x,\text{body}} \tag{12}$$

where the shortening effect is approximated by [1]:

$$u_{x,\text{body}} \approx -\frac{3{u_{z,\text{body}}}^2}{5L} \qquad u_{x,\text{local}} = -\frac{3{u_{z,\text{local}}}^2}{5L} \tag{13}$$

where $u_{x,\text{body}}$ represents the shortening of the upper body, while $u_{x,\text{local}}$ denotes the localized shortening at point A in Figure 2.4d. Based on simulations the shortening of the upper body can be approximated by defining $u_{z,\text{body}}$ at the centerline of the sheet flexure. The translation $u_{z,\text{body}}$ is larger as point A moves along a greater radius. Therefore the corresponding translations are given by:

$$u_{z,\text{body}} = R\sin\theta \qquad u_{z,\text{local}} = (R + \frac{W}{2})\sin\theta \tag{14}$$

Contribution of constrained warping

When torsion is applied to a circular beam, the cross-section will start to rotate along the length of the beam. For the rectangular cross-section of the sheet flexure this will cause warping. In other words, the corners of the rectangle will move out of the cross-sectional plane. If the sheet flexure is constrained by a body on both sides, the warping is restrained and will cause axial stresses in the $\sigma_{\bar{x}\bar{x}}$ direction. This is illustrated in Figure 2.4e. However, it has been found that this is only significant for short and wide sheet flexures [8]. It is chosen that the analytical model represents a slender sheet flexure with a small W/L ratio, to ensure that this effect can be neglected.

2.5 Nonlinear stiffness model

The linear model of the sheet flexure, developed using the framework of Euler-Bernoulli beam theory in Chapter 2.3, assumes small displacements and rotations, where the stiffness is treated as constant and

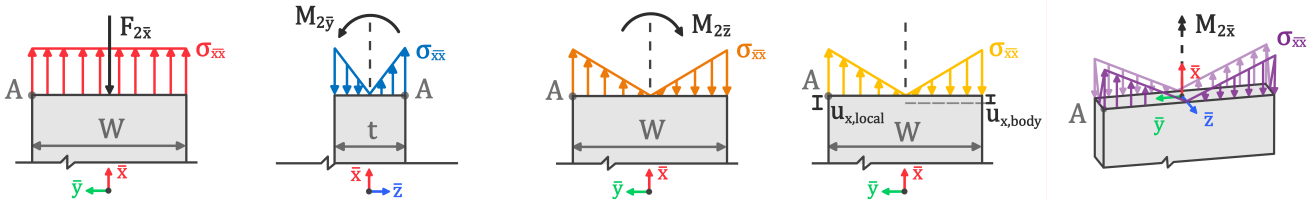

(a) Axial force F_{2x} (b) Bending moment M_{2y} (c) Bending moment M_{2z} (d) Shortening (e) Constrained warping

Figure 2.4: Contributions to the axial stresses developed in the sheet flexure

independent of deformation. However, in practice, deformations are often large, making nonlinear effects from geometrical changes significant [9]. To address these limitations, the work by Nijenhuis [9], [10] develop a nonlinear stiffness model for spatially deforming sheet flexures under general 3D load conditions at moderate deformations. The [9] model accurately predicts stiffness by incorporating bending, elongation, and torsion deformations, while the [10] model extends this approach by also considering shear and warping deformations.

To gain a better understanding of the behavior of axial stress over larger deformations, the nonlinear models are utilized to determine the corresponding moments M_{2y} and M_{2z}. While the general nonlinear models includes many additional terms, not all of them contribute significantly under the given boundary conditions and for a small W/L ratio. To simplify the equations, only the most relevant additional terms are presented in equation 15 and equation 16. The complete equations and detailed derivation of these moments is provided in Appendix B.

$$M_{2y} = \frac{6EI_y u_{2z}}{L^2} - M_{2z}\phi_{2x} \tag{15}$$

$$M_{2z} = -\frac{3\,\mathrm{E}\,I_z\,u_{2y}}{\frac{L^2}{2} + \frac{\mathrm{E}\,I_z\,{u_{2z}}^2}{10\,G\,J}} - \frac{2\,\mathrm{E}\,I_z\,\phi_{2x}\,u_{2z}}{\frac{L^2}{2} + \frac{\mathrm{E}\,I_z\,{u_{2z}}^2}{10\,G\,J}} \tag{16}$$

Comparing equation 15 with the corresponding linear expression in equation 5, it can be observed that an additional term emerges in the nonlinear model. The term $-M_{2z}\phi_{2x}$ captures the load-stiffening behavior due to the applied rotation ϕ_{2x} and the moment M_{2z}. Comparing equation 16 with the corresponding linear expression in equation 5, it is observed that the term previously dependent only on u_{2y} now also includes a dependence on u_{2z}^2. Additionally, a new term appears that depends on $\phi_{2x}u_{2z}$. These quadratic nonlinear terms are kinematic effects that play a role for larger rotations.

2.6 Assumptions

The axial stress $\sigma_{\bar{x}\bar{x}}$ is evaluated at point A across a prescribed rotation θ. The material is set to AISI Type 304 Stainless Steel. To simplify the analysis, it is assumed that there is no axial force acting on the flexure. Additionally, a sheet flexure with an small W/L ratio is selected to ensure bending deformations dominate over shear deformations, and constrained warping is minimized. The input parameters used for the stress calculation are provided in Table 1.

Table 1: Input parameters axial stress calculation

Parameter	Value	Unit	Parameter	Value	Unit
L	100	mm	θ	$[0-5]$	deg
W	10	mm	E	193	GPa
t	0.5	mm	G	74	GPa
R	75	mm			

2.7 Results

The analytical results for the axial stress $\sigma_{\bar{x}\bar{x}}$ are obtained by substituting the input parameters into the contributions of equation 8. The results are generated using both the linear and nonlinear stiffness models and are shown in Figure 2.5. The analytical results are compared with numerical solutions obtained using the Finite Element Method (FEM) software ANSYS. The same input parameters and boundary conditions are applied to simulate the sheet flexure and obtain the $\sigma_{\bar{x}\bar{x}}$ component of the stress tensor. Details on the ANSYS modeling and simulation procedure are provided in Chapter 3.1.1.

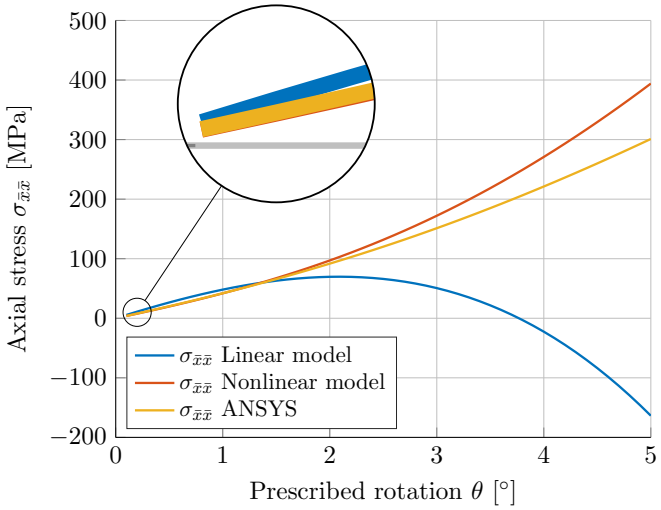

Figure 2.5: Axial stress evaluated in point A

As shown in Figure 2.5 the axial stress increases as the prescribed rotation is applied. The stress response of the linear model is far from linear. This is caused by the nonlinear translations of equation 1 and equation 14. After just 1° of rotation, the linear model starts to deviate significantly from the ANSYS results. This is expected since the Euler-Bernoulli theory is only valid for small motions. In contrast, the nonlinear model closely matches the ANSYS results, even for larger rotations. This indicates that the axial stress contributions of the analytical model effectively capture the stress development in point A for a sheet flexure with a small W/L ratio.

Furthermore, it predicts that this stainless steel sheet flexure with a yield strength of 215 MPa, would yield after 4° of rotation.

The axial stress is composed out of equation 11, 15 and 16. The relative contributions of these equations to the analytical axial stress $\sigma_{\bar{x}\bar{x}}$, are depicted in Figure 2.6. The figure shows that the axial stress resulting from the bending moment M_{2y} is the dominant component across the entire range of motion. The influence of the other bending moment M_{2z} only plays a role after initial rotation. The contribution of shortening to the axial stress is minimal relative to the axial stresses due to the bending moments. The error shows the remaining difference between the analytically calculated axial stress and the stress obtained from the ANSYS simulations. At 0.5° of rotation the bending moment M_{2y} accounts for 94.9% of the calculated axial stress. The linear term of equation 15 is responsible for 99.5% of this stress. At 5° the bending moment accounts for 84.6% of the axial stress, with only 70.8% attributed to the linear term. As the flexure undergoes greater deformation, the load-stiffening term becomes more important. In contrast to M_{2y}, the two terms of M_{2z} in equation 16 have a constant contributions of 42.8% and 57.2% over the whole range of motion. Appendix B provides figures that illustrate how these contributions develop over the applied rotation, along with plots of the M_{2y} and M_{2z} moments.

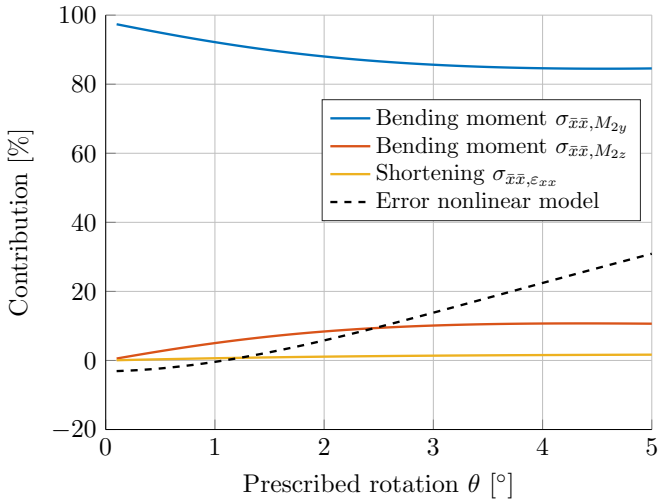

Figure 2.6: Contributions to the $\sigma_{\bar{x}\bar{x}}$ in point A

Appendix C evaluates the analytical model on a wider flexure with $W = 50$ mm. The results show that the derived M_{2y} and M_{2z} require additional terms, as they were formulated for a slender flexure. Additionally, a large difference with the ANSYS results, suggests that additional contributions to the analytical stress model are needed for wider flexures. Lastly, even for the wider flexure, axial stress due to shortening remains a minor contribution compared to the axial stress caused by the bending moments.

3 Modeling the 1DOF system with altered flanges

This chapter will investigate the impact that altered flanges have on the stress distribution within the flexures. A tapered flexure is introduced and other flange shapes are discussed at the end of the chapter. The chapter starts by outlining the modeling methodology applied in the software ANSYS workbench. It discusses methods to address stress singularities and to ensure converging solutions. The chapter then provides results on the stress gradient, stress tensor components, boundary conditions and scaling behaviour of a tapered flexure. In the final section, a comparison of different flange shapes is provided, and the two most effective flange shapes are selected for further study

3.1 Method

The system to be analyzed consists of three identical radially arranged flexures that have altered flanges. It can be simplified to a single flexure using the same approach as Chapter 2.1. The geometry of a flexure with altered flanges is constrained within the length L, width W and thickness t of the sheet flexure. For this design W and t remain unchanged while the flanges (top and bottom edges) are altered in shape. To further simplify the system the flanges are set to be symmetric. There are many flange shapes that are possible within the described design space, a slanted linear line is chosen as a starting point for the modeling process. This design is fully defined by the distance η and will be referred to as a tapered flexure, it is illustrated in Figure 3.1.

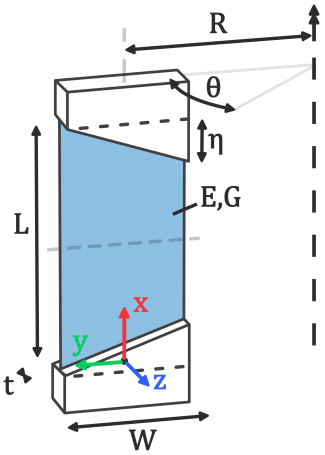

Figure 3.1: Tapered flexure with design parameters

If $\eta = 0$ mm the geometry of the tapered flexure is identical to that of the sheet flexure. Other flange shapes will be explored in Chapter 3.2.5.

The effect that altered flanges have on the internal stresses of the flexure cannot be analyzed using the analytical model developed in Chapter 2.4. That model relies on the assumption of a constant cross-section in the yz-plane along the x-axis. By altering the flanges this cross-section varies along the x-axis of the flexure. Therefore the sheet flexures with altered flanges will be modelled using ANSYS Workbench. This software is the integration and workflow platform that connects various ANSYS products. It is used because it allows 3D modelling, simulation and parametrization all within the same environment.

3.1.1 ANSYS Workbench workflow

A workflow is created in order to parametrically model and simulate a sheet flexure with altered flanges. Several modules within ANSYS workbench are utilized: ANSYS SpaceClaim is used for CAD modeling, ANSYS Mechanical is used for the Finite Element Analysis (FEA) and the ANSYS Design of Experiments (DOE) table is used to aid the parametrization and enable batch-solving of multiple configurations. Detailed explanations of these methods are provided in the subsequent sections.

ANSYS Design Of Experiments

First the simulation input parameters are provided in the DOE table. In this table each row represents a unique configuration, also called design, to be modeled and simulated. The input parameters L, W, t, η define the geometry of the flexure, R and θ describe its motion, and E and G represent the chosen material. After solving for each configuration, the table will output various parameters such as stresses, displacements and reaction forces. Specific configurations can be selected for a more detailed examination of the results. Table 2 lists the default input parameters for this chapter's results. The default stepsize of η is 2 mm. If different values are used, this will be noted accordingly.

Table 2: Default parameters for results chapter

Parameter	Value	Unit	Parameter	Value	Unit
L	100	mm	R	75	mm
W	50	mm	θ	5	deg
t	0.5	mm	E	193	GPa
η	$[0-22]$	mm	G	74	GPa

ANSYS SpaceClaim

This module is used to create the 3D model that is required for the Finite Element Analysis. ANSYS SpaceClaim features a geometry scripting environment that is based on the Python language. This enables the automation of the entire CAD modeling process. A script is written to automate the modeling of the tapered sheet flexure. It uses the geometric configuration from the DOE table as input and generates the complete 3D geometry. The script also creates named selections for specific edges and surfaces. These are utilized for applying boundary conditions, defining result surfaces and assist the mesh creation in ANSYS mechanical. The code that is used for generating the tapered geometry is given in Appendix D.

ANSYS Mechanical

This module serves as the FEA tool that is used to simulate the flexure. After importing the geometry from the SpaceClaim module, ANSYS Mechanical applies the material properties. In the next step, the boundary conditions are applied to the top and bottom edges by using the named selections. The bottom edges of the flexure are fixed while the top edges displace according to equation 1. The element and mesh settings are configured with the help of [11, 12] such that the quality criterion in the mesh quality worksheet do not exceed their warning limits. The solver within ANSYS mechanical is configured to use a large deflection algorithm. This will take into account stiffness changes caused by large deformations and rotations [13]. The solver is then set to output results such as the maximum von Mises stress, displacements and reaction forces.

3.1.2 Convergence and stress singularities

A converging, mesh-independent solution is essential to ensure the numerical accuracy and reliability of the FEA results. In other words, the obtained stress or deformation should converge to a repeatable solution as the element size decreases. In the initial simulations, stress results for both shell and solid elements failed to converge due to stress singularities. These are not physical stresses but are numerical artifacts of the FEA model. To understand how to handle these singularities, it is important to provide some background on its origin.

The structural FEA starts by solving for the displacements at each node of the mesh. From this in a post-processing step the strains are derived using the strain-displacement relations, and stresses are subsequently derived using the constitutive equations. These stresses and strains are obtained at the Gaussian integration points within each element. Stress values at the nodes are then extrapolated us-

ing shape functions, which describe how stresses may vary across the element [14]. Stress singularities can arise from sharp discontinuities in geometry (such as sharp corners) or abrupt changes in loading (like point loads). In these situations, the shape functions cannot effectively capture the abrupt changes. As the mesh is refined and elements become smaller and smaller, the derived stress tends to approach infinity at these locations [14].

By default ANSYS Mechanical displays the averaged stress values at the nodes. If a node is shared by multiple elements, the stress value from each element at that node is taken and averaged. The nodal difference provides the maximum difference between the unaveraged stress values of a shared a node. The stress singularities are clearly visible by plotting the nodal differences of the shell or solid elements. As the singularities only occur in specific elements of the mesh, they result in high nodal differences due to the unaffected surrounding elements.

The stress singularity observed in the FEA exhibits predictable behavior. It consistently occurs in the top and bottom corners of the flexure. Specifically always in the first row of elements adjacent to the top or bottom edge. The behavior is independent of η, appearing in both the standard sheet flexure and the flexures with altered flanges. The stress singularity in the top left corner of a flexure with $\eta = 0$ mm is given as an example in Figure 3.2a. From the nodal differences it is observed that it only significantly impacts the first two row of elements. Stress singularities are typically addressed by adding fillets or relaxing boundary conditions [14] but these measures were ineffective.

Given the predictable location and behavior of the stress singularity, it can be systematically excluded by redefining the result surface with an offset. Instead of evaluating stress across the entire flexure surface, the first two rows of elements near the top and bottom edges are excluded, as illustrated in Figure 3.2b. As the element size decreases the portion of the flexure that is not considered in the analysis becomes negligible. This approach consistently yields a converging solution with low nodal differences. An example of a converged solution is given in Figure 3.3.

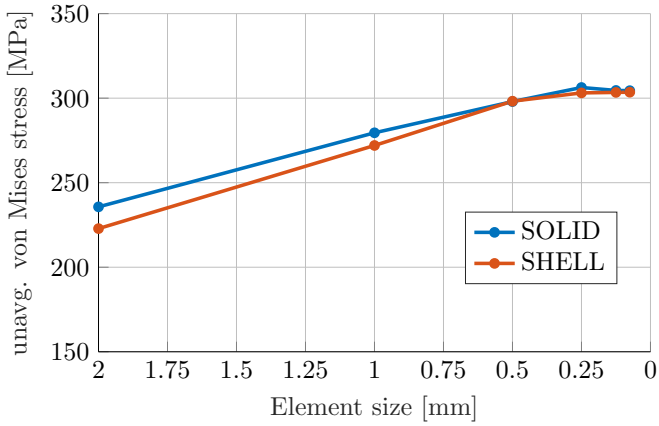

Figure 3.3: Converging solution of result surface with a 2-element offset, $W = 10$ mm and $\eta = 0$ mm

The figure demonstrates that both the shell and solid elements converge to the same value as the element size decreases. The solid elements requires up to three times more computational time compared to shell elements. As both elements achieve similar maximum von Mises stress values after an element size of 0.5 mm, it is chosen to continue with shell elements smaller or equal to 0.25 mm.

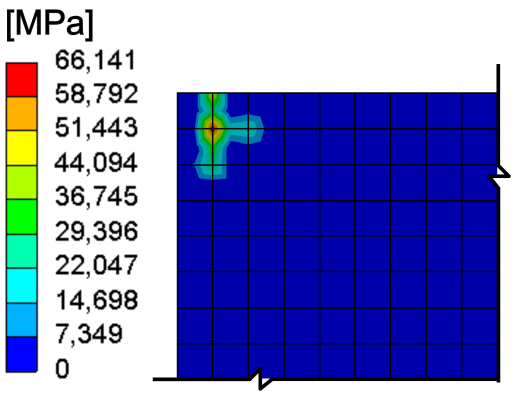

(a) Nodal differences

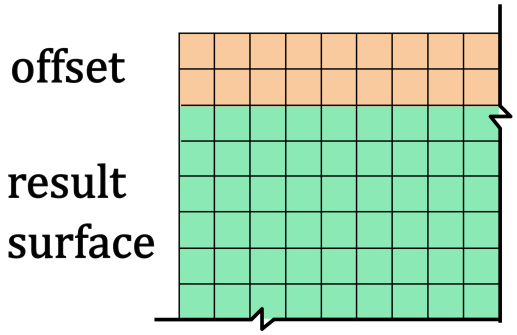

(b) New result surface

Figure 3.2: Stress singularity in top left corner visible due to nodal differences and offset method

3.2 Results

3.2.1 Maximum von Mises stress

The von Mises stress $\sigma_{\text{eq,avg}}$ distribution of a stainless steel sheet flexure with $L = 100$ mm, $W = 50$ mm, $t = 0.5$ mm, $R = 75$ mm, $\theta = 5°$ is illustrated in Figure 3.4a. The maximum von Mises stress $\sigma_{\text{eq,max}}$ on the front surface of the sheet flexure is located at the top left corner. This corresponds to the location where $(x, y) = (L, y_{\max})$. On the back surface of the sheet flexure the stress distribution is identical but mirrored about the y-axis at $x = \frac{L}{2}$. This means that there is a similar maximum stress point on the back surface located in the bottom corner where $(0, y_{\max})$.

The introduction of tapered flanges, represented by an nonzero η, leads to a reduction in the $\sigma_{\text{eq,max}}$. As shown by Figure 3.4b, increasing η to 14 mm reduces the $\sigma_{\text{eq,max}}$ by almost 200 MPa. The maximum stress remains at the same location of that with $\eta = 0$ mm, but it appears to be less concentrated and more distributed over the corner. Additionally, a new stress concentration is observed at the top right corner (front surface) and bottom right corner (back surface) of the tapered flexure. As η increases from 0 mm the magnitude of this new concentration grows. At $\eta = 14$ mm it is almost identical to the magnitude of the previously observed stress concentration.

By increasing η to 22 mm the stress concentration in the top left corner is reduced even further. This is illustrated in Figure 3.4c. However, the $\sigma_{\text{eq,max}}$ does not see a comparable improvement, as the stress in the top right corner and the newly formed concentration along the right edge are now defining the maximum stress value $\sigma_{\text{eq,max}}$. Thus a tapered flexure with $\eta = 14$ mm would be preferred in this case.

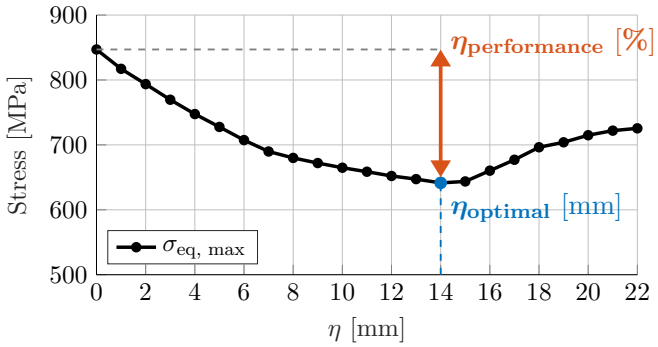

Figure 3.5: The max. von Mises stress and definition of η_{optimal} and $\eta_{\text{performance}}$

The maximum von Mises stress is evaluated for various values of η and illustrated in Figure 3.5. The $\sigma_{\text{eq,max}}$ is not tied to a specific location but represents the highest stress observed on the result surface. As η takes on larger values, the $\sigma_{\text{eq,max}}$ is reduced due to the reduction of stress in the top left corner. After $\eta = 14$ mm other stress concentrations start to dominate leading to a rise in $\sigma_{\text{eq,max}}$. Similar behavior is observed for flexures with different input parameters. In order to compare and find the best flange shape in the upcoming sections, two new variables η_{optimal} and $\eta_{\text{performance}}$ are defined. They are also visually illustrated in Figure 3.5.

$$\eta_{\text{optimal}}(C) = \arg\min_{\eta} \sigma_{\max}(\eta, C) \tag{17}$$

The optimal value of η for a unique configuration C, denoted as η_{optimal}, is defined as the value of η that minimizes the maximum von Mises stress.

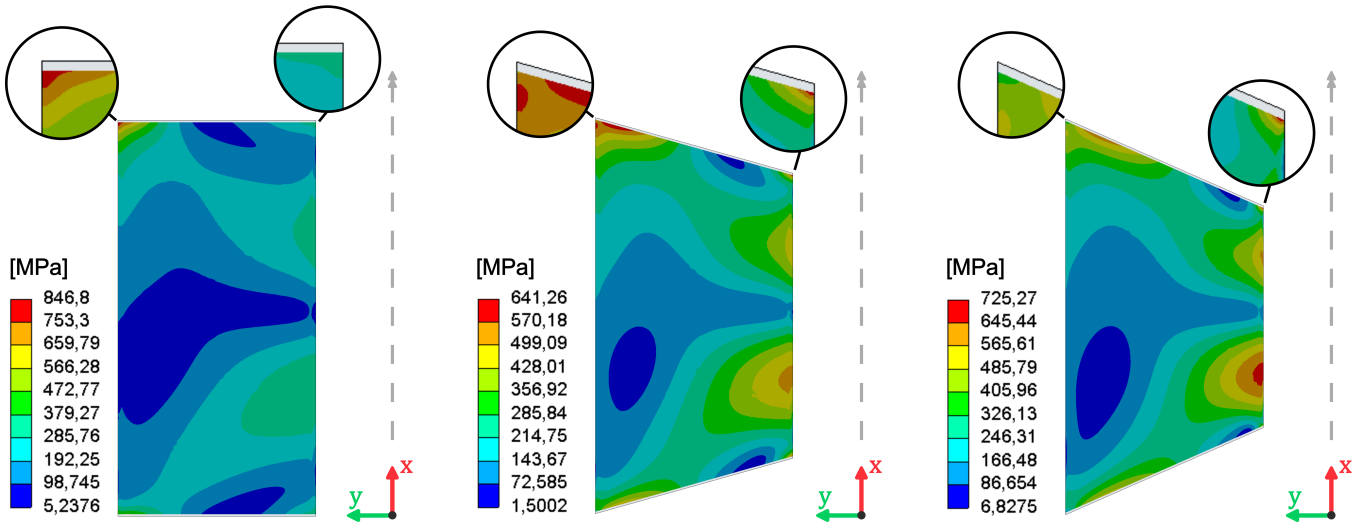

(a) $\eta = 0$ mm | Sheet flexure (b) $\eta = 14$ mm | Tapered flexure (c) $\eta = 22$ mm | Tapered flexure

Figure 3.4: Comparison of the von Mises stress $\sigma_{\text{eq,avg}}$ on the front surface of the flexures for different η

Furthermore, the performance metric, $\eta_{\text{performance}}$, quantifies the improvement in stress by comparing the stress at $\eta = 0$ mm, denoted as η_{sheet}, to the stress at η_{optimal}. It is defined such that a decrease in stress is represented by a negative value, while an increase in stress is represented by a positive value:

$$\eta_{\text{performance}}(C) = \frac{\sigma_{\max}(\eta_{\text{optimal}}) - \sigma_{\max}(\eta_{\text{sheet}})}{\sigma_{\max}(\eta_{\text{sheet}})} \times 100 \tag{18}$$

3.2.2 Stress tensor components

The von Mises stress is a failure criterion that simplifies a three-dimensional stress state into a single scalar value. It is calculated at each mesh node using the stress tensor components at that specific node [7]:

$$\sigma_{\text{eq}} = \sqrt{\frac{1}{2}\begin{bmatrix}(\sigma_{\bar{x}\bar{x}} - \sigma_{\bar{y}\bar{y}})^2 + (\sigma_{\bar{y}\bar{y}} - \sigma_{\bar{z}\bar{z}})^2 \\ + (\sigma_{\bar{z}\bar{z}} - \sigma_{\bar{x}\bar{x}})^2 + 6(\sigma_{\bar{x}\bar{y}}^2 + \sigma_{\bar{y}\bar{z}}^2 + \sigma_{\bar{z}\bar{x}}^2)\end{bmatrix}} \tag{19}$$

Figure 3.6 shows the maximum values of the stress tensor components across the entire surface of the flexure. It illustrates that the normal stress $\sigma_{\bar{x}\bar{x}}$ in the length direction is the only component that decreases with an increase in η. This is also the component that is analytically calculated for a sheet flexure in Chapter 2.4. In contrast, the normal stress $\sigma_{\bar{y}\bar{y}}$ in the width direction and the shear stress $\sigma_{\bar{x}\bar{y}}$ in the $xy-$plane both tend to increase. The normal stress $\sigma_{\bar{z}\bar{z}}$ in the thickness direction and the shear stresses $\sigma_{\bar{y}\bar{z}}$ and $\sigma_{\bar{z}\bar{x}}$ in the $xz-, yz-$planes are zero because a very thin sheet is modeled using shell elements.

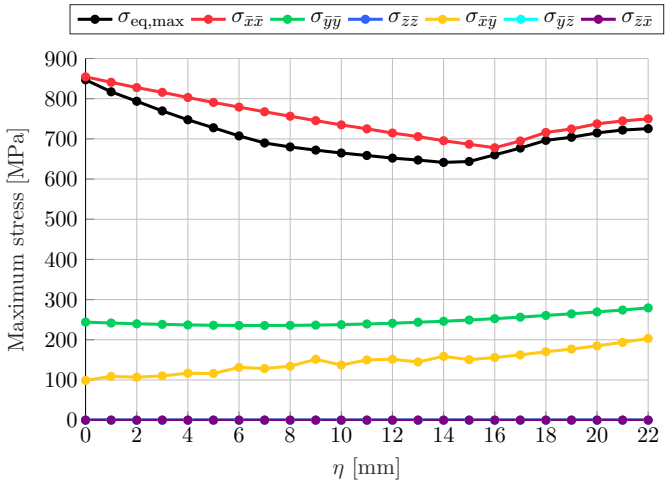

Figure 3.6: max. von Mises stress and max. stress tensor components evaluated for increasing η

It is important to note that the maximum value of each stress component may occur at different locations on the mesh and does not necessarily coincide with the location of the maximum von Mises stress. Appendix E provides the distributions of the stress tensor components for various values of η. These distributions show how each stress component varies across the entire surface of the flexure, rather than only highlighting the maximum values.

3.2.3 Other boundary conditions

To determine whether altered flanges are beneficial for stress reduction in flexure mechanisms that have different boundary conditions, various constraint combinations are evaluated. Instead of prescribing all three boundary conditions u_{2y}, u_{2z} and ϕ_{2x} to a flexure of $W = 10$ mm simultaneously, it is tested to see if a tapering reduces stress under different combinations of these prescribed movements, with the remaining boundary conditions set to zero.

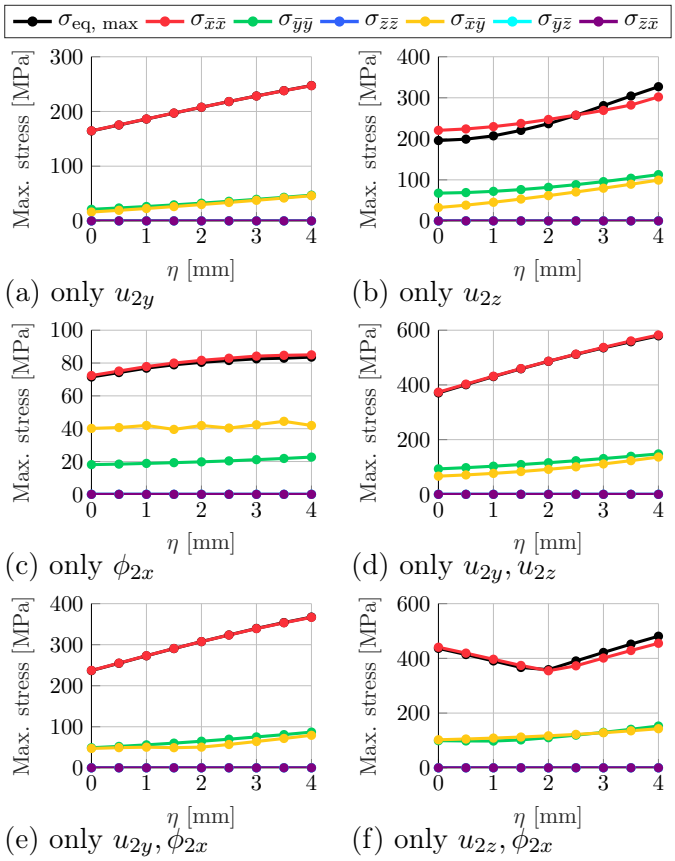

Figure 3.7: Impact of η on the stress tensor for other combinations of the boundary conditions

Figures 3.7a and 3.7b show that when only one of the displacements is applied, increasing η does not lead to a reduction in the maximum von Mises stress or its components. Therefore, adding a tapering has no stress reduction benefit for these boundary conditions. The same applies for just twisting the flexure by prescribing ϕ_{2x} as shown in Figure 3.7c. Only the combination of u_{2z} and ϕ_{2x} in Figure 3.7f, has a similar reduction in stress to what was seen for prescribing u_{2y}, u_{2z} and ϕ_{2x}.

3.2.4 Scaling of input parameters

It is useful to determine whether the input parameters exhibit a scaling relationship. If such a relationship exists, simulations could be performed for a specific range of parameters and extended using the identified scaling rule. To identify a scaling rule, the $\sigma_{\text{eq,max}}$ was evaluated for 520 unique reference configurations, referred to as ANSYS scale 1. The input parameters are scaled, and the resulting $\sigma_{\text{eq,max}}$ is compared to that of the reference configurations. The parameters range is listed in Table 3.

Table 3: Parameters of reference scale 1

Param.	Range	Unit	Param.	Range	Unit
L	100	mm	R	100	mm
W	$[10-100]$	mm	θ	$[0.5-5]$	deg
t	0.2	mm	E	193	GPa
η	$[0-22]$	mm	G	74	GPa

To illustrate how the $\sigma_{\text{eq,max}}$ can be visualized across various configurations, an example is provided for a tapered flexure with $W = 20$ mm in Figure 3.8. Each dot represents the $\sigma_{\text{eq,max}}$ result for one unique configuration i.e. one flexure. The figure displays a total of 80 configurations that all have the same values for L, W, t, R, E and G while evaluated over η and θ. A reduction in $\sigma_{\text{eq,max}}$ for specific values of η is observed across various θ values. This is the same behavior as discussed in Chapter 3.2.1.

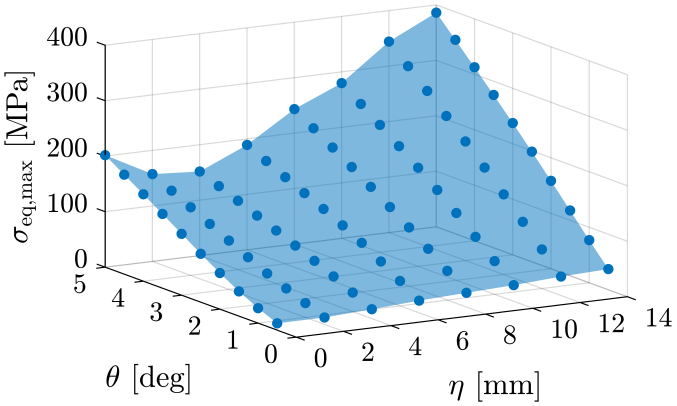

Figure 3.8: max. von Mises stress for 80 configs of ANSYS scale 1 where $W = 20$ mm

It is found that by applying a scaling factor k to only the geometric input parameters with unit [mm]:

$$C_k = \{kL, kW, kt, k\eta, kR, \theta, E, G\}. \tag{20}$$

The maximum stress of the scaled configuration $\sigma_{\text{eq,max}}(C_k)$ is approximately equal to the maximum stress of the reference configuration $\sigma_{\text{eq,max}}(C_1)$.

$$\sigma_{\text{eq,max}}(C_k) \approx \sigma_{\text{eq,max}}(C_1) \tag{21}$$

This scaling relationship is illustrated in Figure 3.9 which shows the $\sigma_{\text{eq,max}}$ for $k = 1, 2, 3$. In this figure, ANSYS Scale 2 can be obtained from ANSYS Scale 1 by simply multiplying η by a factor of 2.

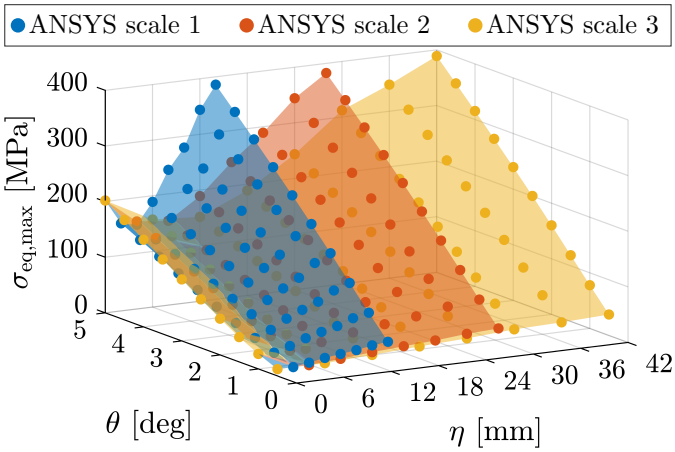

Figure 3.9: max. von Mises stress when scaling all geometric parameters by $k = 1, 2, 3$

This is also illustrated in Figure 3.10, where the $\sigma_{\text{eq,max}}$ of ANSYS scale 2 and 3 are obtained from ANSYS scale 1 by applying the scaling relationship.

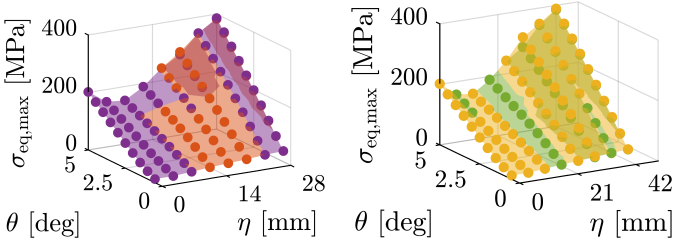

(a) Obtained scale 2 (b) Obtained scale 3

Figure 3.10: Applying the scaling relationship

The scaling relationship is tested for all 520 configurations by finding the difference between the manually scaled results and ANSYS simulated scaled results of each configuration. Figure 3.11 shows that the difference for almost all configurations is very small, approximately 0 MPa with the maximum outliers being 9.3 MPa and 32 MPa for scale 2 and 3 respectively.

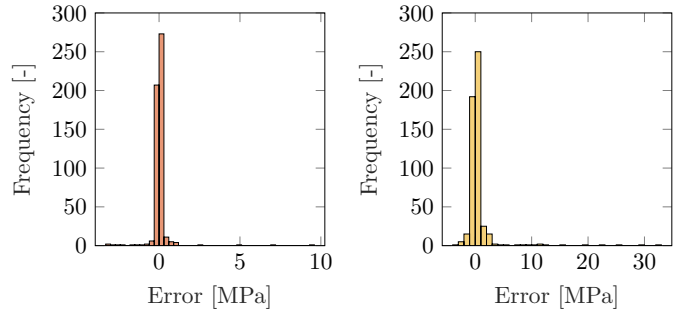

(a) Scale 2 (b) Scale 3

Figure 3.11: Difference in $\sigma_{\text{eq,max}}$ of ANSYS scaling results and applying the scaling relationship

3.2.5 Alternative flange shapes

The tapered flexure is one of many flange shapes that is possible within the design space described in Chapter 3.1. A comparison of these alternatives is desired to see if these shapes achieve similar or even better reductions in the maximum von Mises stress. In order to simplify the modeling, simulation and comparison it is desired that the new shapes are fully defined by as few variables as possible. The resulting shapes are illustrated in Figure 3.12 and are modeled using the SpaceClaim scripting environment as explained in Chapter 3.1.1.

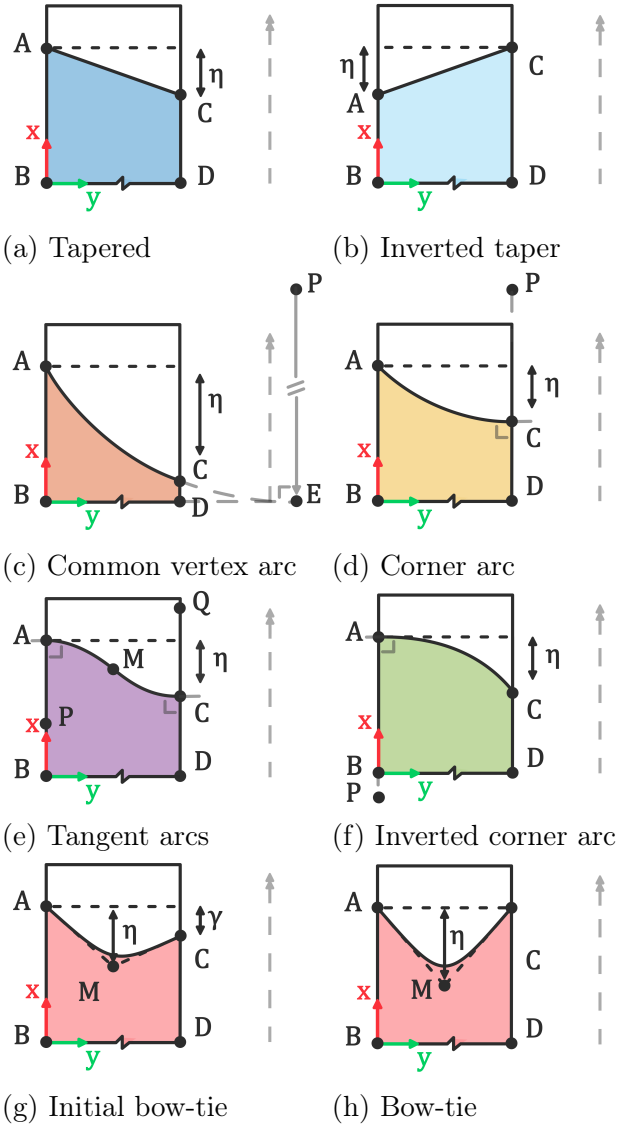

Figure 3.12: Overview of evaluated flange shapes

All of the shapes are derived within the geometry of the (rectangular) sheet flexure. The shapes drawn in Figure 3.12 are mirrored along the $y-$axis. The points A, B and D always have the coordinates $(\frac{L}{2}, 0)$, $(0, 0)$ and $(0, W)$ respectively. All shapes except Figure 3.12g are fully defined by only η and applying specific geometric constraints to the points. The arc of Figure 3.12c is fully defined by the position of the three intersection points A, C and E and has it center at point P. The arc of Figure 3.12d is defined by the perpendicular property of point C and the constraint that point P lies on the same $y-$coordinate as point C and D. The arc or Figure 3.12f is similar but has its perpendicular property at point A instead of point C. The flange shape of Figure 3.12e has point M located at a $y-$coordinate of $\frac{W}{2}$ and the center points P and Q are on the same $y-$coordinate as point C and D respectively. The bow-tie flexure of Figure 3.12h also has point M located at a $y-$coordinate of $\frac{W}{2}$. There is a radius at point M which cannot be to small, as it will become a stress concentration and influence the results. Through simulations of various widths it was determined that if $R_{\mathrm{M}} = \frac{W}{5}$ this would not influence the results.

For each flange shape the $\sigma_{\mathrm{eq,max}}$ is evaluated over a range of η. Following the approach outlined in Chapter 3.2.1, the η_{optimal} is determined and the $\eta_{\mathrm{performance}}$ is calculated. The stepsize of η is set to 2 mm and all other parameters are specified in Table 4. The reduction in the maximum von Mises Stress at $\theta = 5°$ for the evaluated flange shapes is given in Figure 3.13.

Table 4: Parameters of evaluated flange shapes

Param.	Range	Unit	Param.	Range	Unit
L	100	mm	R	75	mm
W	$[10-100]$	mm	θ	$[1,5]$	deg
t	0.5	mm	E	193	GPa
η	$[0-22]$	mm	G	74	GPa

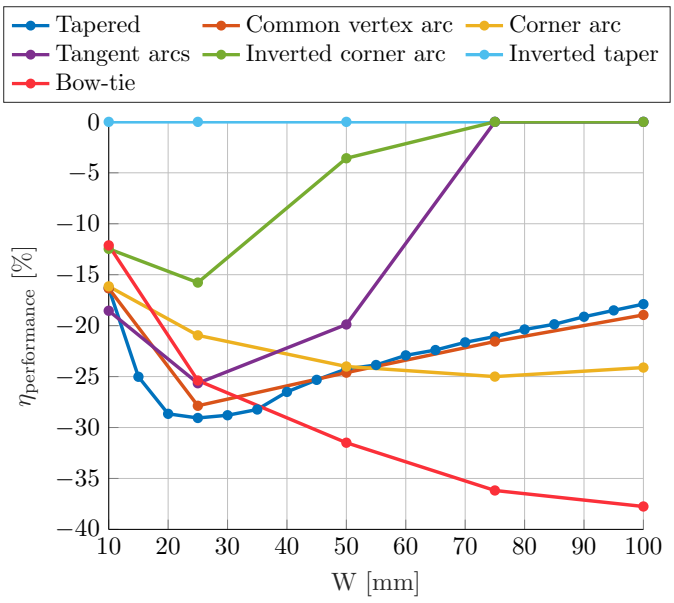

Figure 3.13: $\eta_{\mathrm{performance}}$ at $\theta = 5°$ for various flexure widths, lower values indicate more stress reduction

The flange shapes that have the greatest decrease in $\sigma_{\text{eq,max}}$ compared to a standard sheet flexure are the tapered flexure and bow-tie flexure. The magnitude of the stress reduction is strongly dependent on the width of the flexure. The tapered flexure provides the most significant stress reduction when $W < 35$ mm, while the bow-tie flexure delivers the most stress reduction for $W > 35$ mm. The common vertex arc achieves a stress reduction comparable to that of the tapered flexure, with a resulting flange shape η_{optimal} closely resembling the tapered flexure. The tangent arcs and inverted corner arc do not perform as well as the other shapes. Both share the characteristic that their flange shape is parallel to the y-axis at point A. Therefore, this geometric feature is not considered benificial for stress reduction when modifying the flange shapes. The inverted tapering results in an increase in stress rather than a reduction and is set to 0 in the graph for visibility. This outcome indicates that the orientation of the flange shape with respect to the DoF of the whole system is important.

The initial bow-tie flexure, shown in Figure 3.12g, depends on two variables η and γ. It was found that setting $\gamma = 0$ mm results in the most stress reduction for larger widths. The initial bow-tie with $\gamma > 0$ mm resulted in a performance falling between that of the corner arc and bow-tie flexure. It was also observed that with $W < 50$ mm the η_{optimal} and γ_{optimal} converge toward a shape similar to that of the tapered flexure.

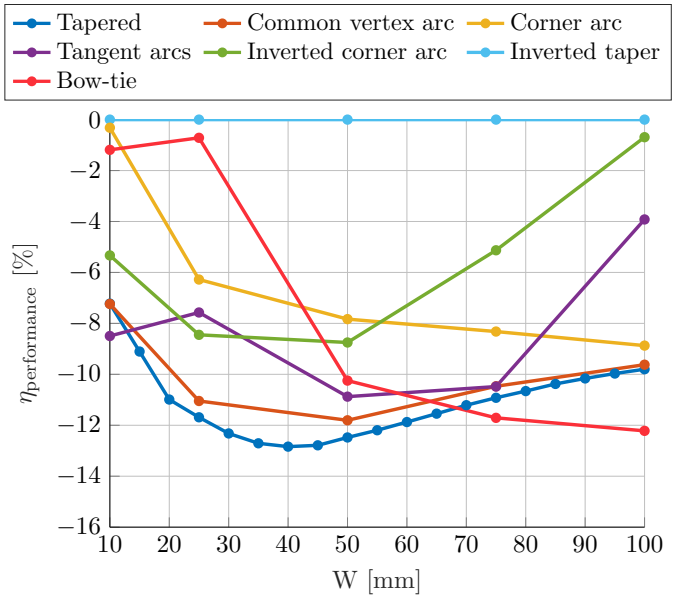

Figure 3.14: $\eta_{\text{performance}}$ at $\theta = 1°$ for various flexure widths, lower values indicate more stress reduction

Figure 3.14 illustrates the reduction in $\sigma_{\text{eq,max}}$ for a smaller prescribed rotation of $\theta = 1°$. Even the slender flexures with $W = 10$ mm exhibit a stress reduction. The amount of stress reduction clearly depends on the magnitude of θ, greater prescribed rotations result in more significant stress reductions. Among the tested flange shapes, the tapered flexure and bow-tie flexure still provide the most significant reductions in $\sigma_{\text{eq,max}}$. However, the tapered flexure is now the better option for $W < 65$ mm, while achieving similar stress reductions to that of the bow-tie flexure for larger widths.

Figure 3.15 illustrates the η_{optimal} values corresponding to the $\eta_{\text{performance}}$ shown in Figures 3.13 and 3.14. The magnitude of η_{optimal} is strongly dependent on the width and prescribed rotation. As W increases, η_{optimal} also increases. A similar trend is observed with θ, although its impact depends on the flange shape and is of a smaller magnitude. This trend does not hold for the inverted taper, tangent arcs, and inverted corner arc shapes, where $\eta_{\text{optimal}} = 0$ mm when no stress reduction is achieved.

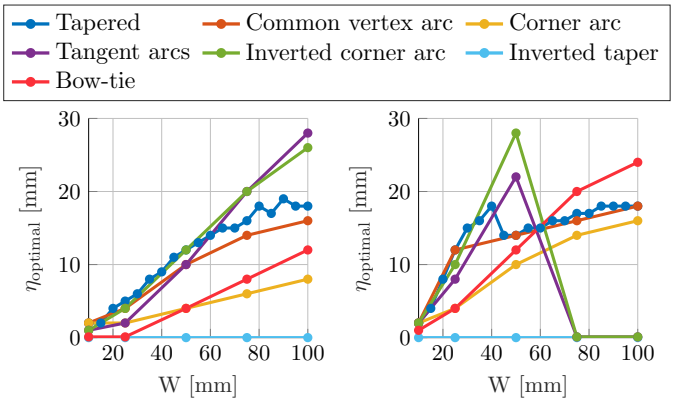

(a) $\theta = 1°$ (b) $\theta = 5°$

Figure 3.15: η_{optimal} related to the $\eta_{\text{performance}}$ values that were evaluated for various W and θ

The tapered and bow-tie flexure are the most effective flange shapes in reducing the maximum von Mises Stress. The $\sigma_{\text{eq,avg}}$ reduction in the tapered flexure is due to a decrease in $\sigma_{\bar{x}\bar{x}}$, as shown in Chapter 3.2.2. In the bow-tie flexure, the reduction in $\sigma_{\text{eq,avg}}$ is primarily driven by a decrease in $\sigma_{\bar{x}\bar{x}}$. The $\sigma_{\bar{y}\bar{y}}$ component also decreases slightly, but its magnitude is ten times smaller. Appendix E provides the stress distributions of the tapered and bow-tie flexure for various values of η. These distributions show how each stress component varies across the entire surface of the flexure.

4 Parameter study

In Chapter 3.2.5, the tapered and bow-tie flexure were found to be the most effective flange shapes in reducing the maximum von Mises Stress. The optimal shape η_{optimal} and the related stress reduction $\eta_{\text{performance}}$ were shown to be highly dependent on W and θ. Since these are not the only input parameters, this chapter focuses on identifying the most important input parameters and understand how they affect η_{optimal} and $\eta_{\text{performance}}$ for the tapered and bow-tie flexures.

4.1 Method

The ANSYS Workbench workflow outlined in Chapter 3.1.1 is used to simulate a wide range of configurations for the tapered and bow-tie flexures. The resulting data is analyzed to investigate how variations in the input parameters influence changes in the output parameters. To quantify these relationships, the Pearson correlation coefficient is used.

The Pearson correlation coefficient measures the strength and direction of the linear relationship between a set of input values X and a set of output values Y [15]. It ranges from -1 to 1 and is calculated using the *corr* function within MATLAB [16]. Figure 4.1 illustrates how different correlation values reflect the relation between the values of X and Y.

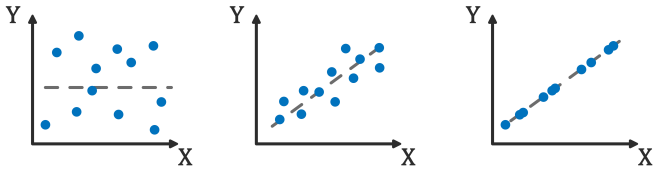

(a) cor(X,Y)=0 (b) cor(X,Y)=0.8 (c) cor(X,Y)=1

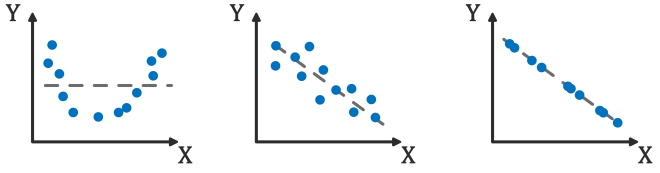

(d) cor(X,Y)=0 (e) cor(X,Y)=-0.8 (f) cor(X,Y)=-1

Figure 4.1: Example of different correlation values

If an positive increase in X leads to an proportional increase in Y it has a strong correlation of 1. Similarly if an positive increase in X leads to a proportional decrease in Y it has a strong correlation of -1. If there is no relationship at all this could be represented by a correlation of 0. It should be noted that the Pearson correlation coefficient only reflects the strength and direction of a linear relationship. It does not reflect the slope or a nonlinear relationships as shown in Figure 4.1d. Other correlation coefficients, such as the Spearman correlation, can capture monotonic nonlinear relationships. But similar coefficient values were observed, so only the Pearson correlation coefficient values are presented in this chapter.

Three input data sets are defined and all input parameters are illustrated in Figure 4.2. Since η_{optimal} is initially unknown, a wide range of η values is simulated for each configuration using a stepsize of $\eta = 2$ mm. The optimal configuration is identified and the corresponding η_{optimal} and $\eta_{\text{performance}}$ are used for the correlation analysis.

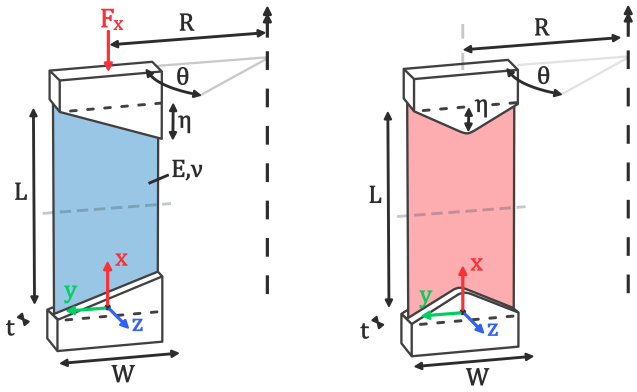

(a) Tapered flexure (b) Bow-tie Flexure

Figure 4.2: Input parameters of parameter study

Input set 1 investigates how variations in geometry and boundary condition values influence the output for both the tapered and the bow-tie flexure. The range of input parameters is provided in Table 5. The initial set contains 12430 unique configurations for each flexure type, which is reduced to 990 unique configurations after determining η_{optimal}.

Table 5: Input range of set 1

Par.	Range	Unit	Par.	Range	Unit
L	100	mm	R	$[120, 160, 200]$	mm
W	$[10-150]$	mm	θ	$[0.5-5]$	deg
t	$[0.2, 0.5, 0.8]$	mm	E	193	GPa
η	$[0-30]$	mm	G	74	GPa

Input set 2 investigates how the use of different materials influence the output for the tapered flexure. The materials of Table 6 are tested for an $R = 120$ mm, $t = 0.5$ mm, $W = [10-150]$ mm and $\theta = [0.5-5]$ degrees. The initial set contains 3580 configurations, which is reduced to 350 unique configurations.

Input set 3 investigates whether the weight of an upper body influences the output of the tapered flexure. This is done by applying an additional F_x force alongside the previously prescribed boundary con-

ditions. An F_x of $[0, 1, 10, 50]$ N is applied for an stainless steel flexure of $R = 120$ mm, $t = 0.5$ mm, $W = [10 - 150]$ mm and $\theta = [0.5 - 5]$ °. The initial set contains 3040 configurations, which is reduced to 280 unique configurations.

Table 6: Materials used in set 2

Material	E [GPa]	ν [-]	ρ [kg/m^3]
304SS	193	0.31	7750
Alu 7075-T6	71.7	0.33	2810
Ti-6Al-4V	114	0.342	4430
ABS	1.63	0.4089	1030
HDPE	1.08	0.4183	958.5

All input sets in this chapter use a reference length of $L = 100$ mm due to the scaling relationship identified in Chapter 3.2.4. It showed that scaling all geometric input parameters by the same factor, results in similar values for $\sigma_{\text{eq,max}}$ and therefore also η_{optimal} and $\eta_{\text{performance}}$. This allows L to be used as a reference length throughout the analysis and reducing the need for an additional input parameter. For example, to study a case with $L = 200$ mm, all geometric parameters can simply be multiplied by 2. While the geometric parameters could be expressed as dimensionless ratios, by dividing them by L, this approach is not used in this chapter to maintain clarity and ease of interpretation.

Lastly, Appendix F provides a parameter study aimed at quantifying the influence of the input parameters on the maximum von Mises stress of the sheet flexure. It follows a similar approach to the parameter study in this chapter.

4.2 Results

4.2.1 Tapered flexure

The correlation coefficients for the tapered flexure are summarized in Table 7.

Table 7: Correlation coefficients tapered flexure

	W	θ	t	R	E	ν	F_x
η_{optimal}	0.83	0.25	-0.15	-0.06	0.06	-0.06	-0.06
$\eta_{\text{performance}}$	-0.06*	-0.59	0.50	-0.20	-0.35	0.38	0.13

*Not representative due to non-monotonic relationship

The width of the tapered flexure shows the strongest positive correlation (0.83) with η_{optimal}. This indicates that increasing the W of the flexure will lead to an increase in η_{optimal}. As it is the largest absolute correlation value, a change in W has the greatest impact on η_{optimal} compared to the other input parameters. This observations is also evident in Figure 4.3. The figure shows that increasing W results in an significant change in η_{optimal} compared to increasing the thickness. Increasing t causes a small decrease in η_{optimal}, being a bit more prominent for wider flexures. This behavior corresponds to the small negative correlation (-0.15) that is observed for t. It is important to note that a 3D figure plots one output variable against two input variables, and requires the other input variables to be fixed. Unlike the figure, the correlation coefficients capture the relationships of that input parameter across all simulated configurations.

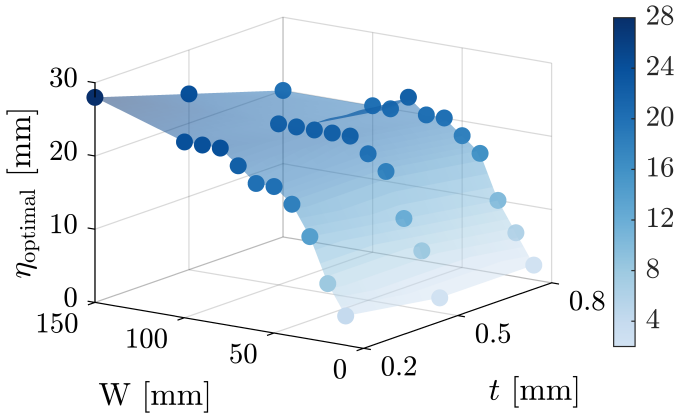

Figure 4.3: Tapered η_{optimal} evaluated for various W and t where $R = 120$ mm and $\theta = 5°$

The prescribed rotation exhibits the second largest correlation (0.25) with η_{optimal}. Increasing θ leads to a higher η_{optimal}, as illustrated in Figure 4.4. The impact of θ is smaller than W, but greater than t. The radius on which the flexure is located has a negligible correlation (-0.06) with η_{optimal}. This is also visible in Figure 4.4 where η_{optimal} remains very constant as R increases.

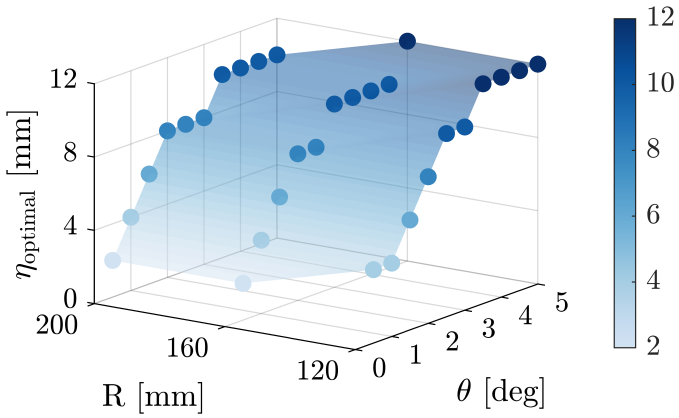

Figure 4.4: Tapered η_{optimal} evaluated for various R and θ where $W = 30$ mm and $t = 0.5$ mm

The width of the tapered flexure appears to have an negligible effect (-0.06) on $\eta_{\text{performance}}$. Figure 4.5 shows that this is not true, and is rather the correlation method that fails to capture the nonlinear non-monotonic behavior.

For slender tapered flexures, as W increases, the stress reduction improves. Once the flexure becomes wide enough, the performance of the tapered flexure begins to decline. Visible by the rise in $\eta_{\text{performance}}$. Examining the responses of $\eta_{\text{performance}}$ for different R and θ, reveals that this trend is consistent for all configurations of the tapered flexure.

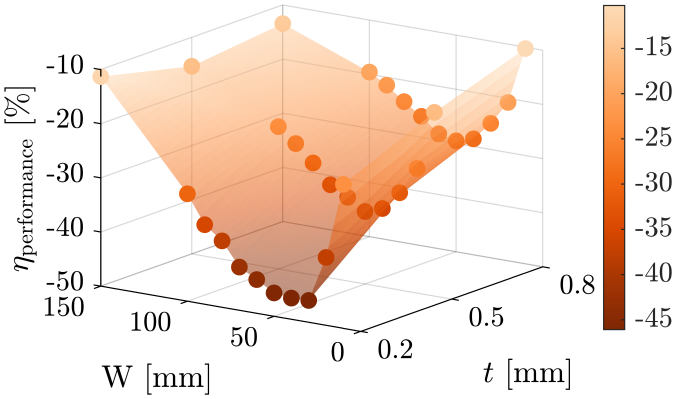

Figure 4.5: Tapered $\eta_{\text{performance}}$ evaluated for various W and t where $R = 120$ mm and $\theta = 5°$

The thickness of the flexure has a positive correlation (0.50) with $\eta_{\text{performance}}$. An increase in t will also result in an increase in $\eta_{\text{performance}}$, as visible in Figure 4.5. This indicates that a thicker flexure obtains less stress reduction by using the optimal tapered flexure.

The prescribed rotation has a negative correlation (-0.59) with $\eta_{\text{performance}}$. The optimal shape is able to achieve more stress reduction for larger values of θ, as is visible in Figure 4.6. The radius has the smallest impact on $\eta_{\text{performance}}$ with a negative correlation (-0.20). As R increases one can observe a slight improvement in the stress reduction for larger rotations.

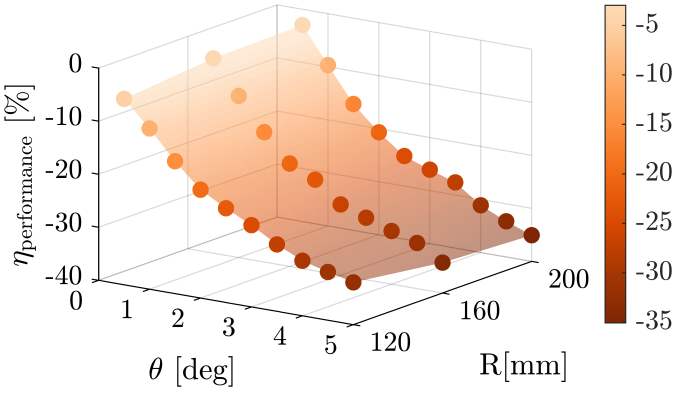

Figure 4.6: Tapered $\eta_{\text{performance}}$ evaluated for various R and θ where $W = 30$ mm and $t = 0.5$ mm

Both material parameters E and ν have a negligible correlation of (0.06) and (-0.06) with η_{optimal}. In Figure 4.7 it is observed that η_{optimal} remains constant for the materials simulated. This suggests that the optimal flange shape is independent of the material.

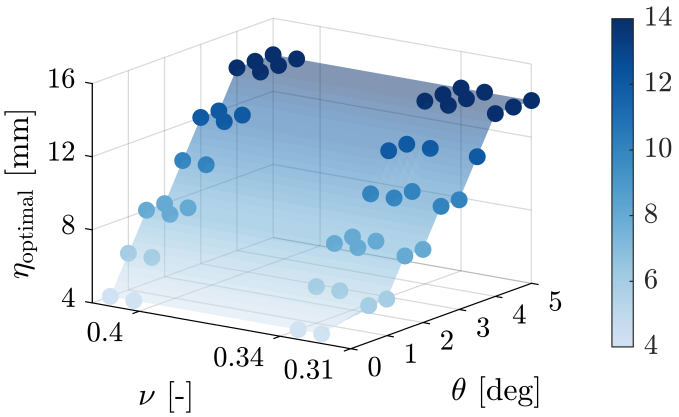

Figure 4.7: Tapered η_{optimal} evaluated for various ν and θ where $W = 30$ mm, $t = 0.5$ mm and $R = 120$ mm

This cannot be said for the correlation that E (-0.35) and ν (0.38) have with $\eta_{\text{performance}}$. An increase in the material's Poisson ratio leads to a higher value of $\eta_{\text{performance}}$, as seen in Figure 4.8. This implies that the optimal flange shape is less effective for materials with a higher Poisson ratio such as the plastics that have been simulated. However for the metals with a Poisson ratio of 0.31-0.34, the maximum difference is around 2%. Suggesting that the simulations of the 304SS material provide a good approximation for the $\eta_{\text{performance}}$ of Alu 7075-T6 and Ti-6Al-4V.

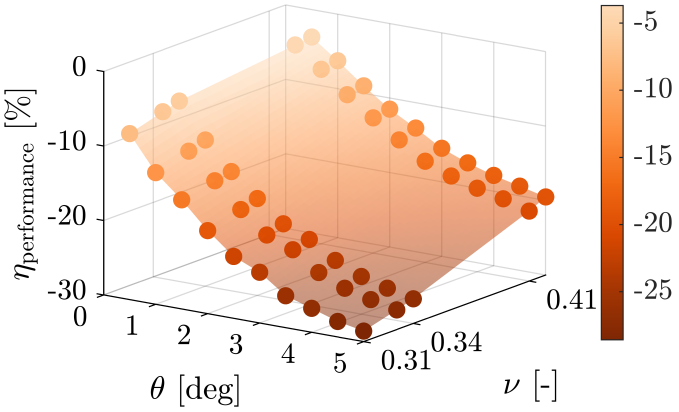

Figure 4.8: Tapered $\eta_{\text{performance}}$ evaluated for various ν and θ where $W = 30$ mm and $t = 0.5$ mm

The η_{optimal} exhibits a negligible correlation (-0.06) with F_x. This indicates that for applied forces smaller than 50 N, the η_{optimal} of the simulated flexures did not change. The $\eta_{\text{performance}}$ has a small negative correlation (0.13) with F_x. As one applies more force the optimal flange shape becomes less effective. However, as illustrated in Figure 4.9, this effect is minimal.

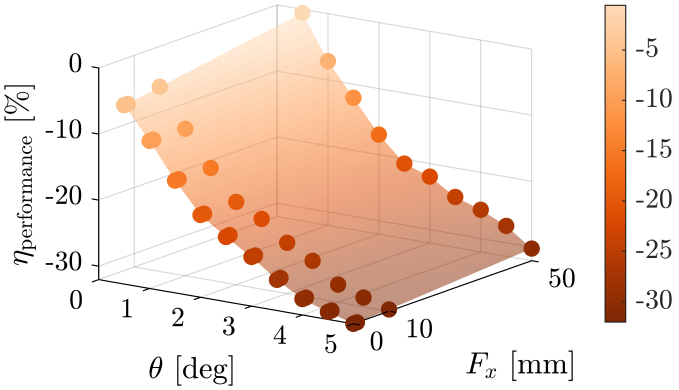

Figure 4.9: Tapered $\eta_{\text{performance}}$ evaluated for various F_x and θ where $W = 30$ mm, $t = 0.5$ mm and $R = 120$ mm

4.2.2 Bow-tie flexure

The correlation coefficients of the bow-tie flexure are summarized in Table 8.

Table 8: Correlation coefficients bow-tie flexure

	W	θ	t	R
η_{optimal}	0.88	0.27	-0.20	-0.16
$\eta_{\text{performance}}$	-0.55	0.53	0.50	-0.02

The correlation coefficients for η_{optimal} are comparable to those of the tapered flexure. The key difference is that Radius has a negative correlation (-0.20) with η_{optimal} for the bow-tie, while the tapered flexure had a negligible correlation of (-0.06). Figure 4.10 shows that η_{optimal} has a small decrease for larger values of R.

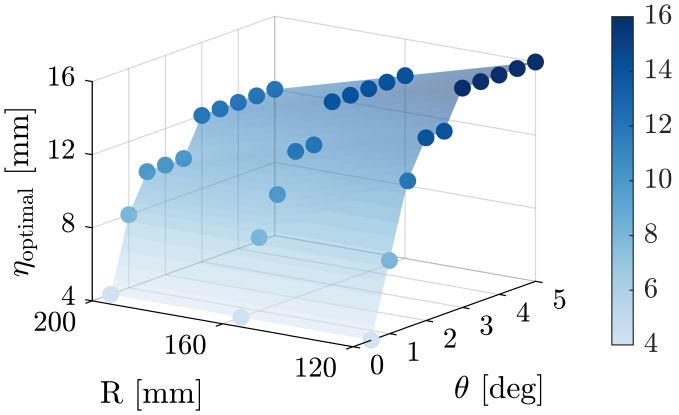

Figure 4.10: Bow-tie η_{optimal} evaluated for various R and θ where $W = 80$ mm and $t = 0.5$ mm

The correlation coefficients for $\eta_{\text{performance}}$ are also comparable to those of the tapered flexure. The key difference for the bow-tie are the correlation with W and R. The width has now a monotonic relationship as shown in Figure 4.11. The W has a negative correlation (-0.55) with $\eta_{\text{performance}}$. This indicates that wider flexures will see a higher stress reduction than slender flexures if one uses the bow-tie shape.

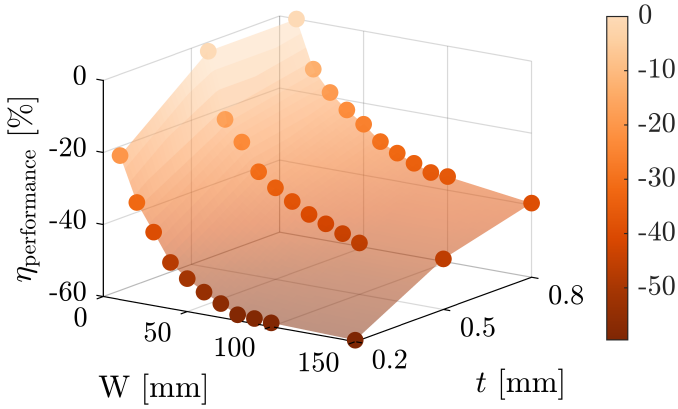

Figure 4.11: Bow-tie $\eta_{\text{performance}}$ evaluated for various W and t where $R = 120$ mm and $\theta = 5°$

The last difference compared to the tapered flexure in correlation values, is that the radius now has a negligible correlation of (-0.02) with the $\eta_{\text{performance}}$. While for the tapered flexure this was a small negative correlation of (-0.20). The bow-tie correlation indicates that the amount of stress reduction of the bow-tie is unaffected by R as visible in Figure 4.12.

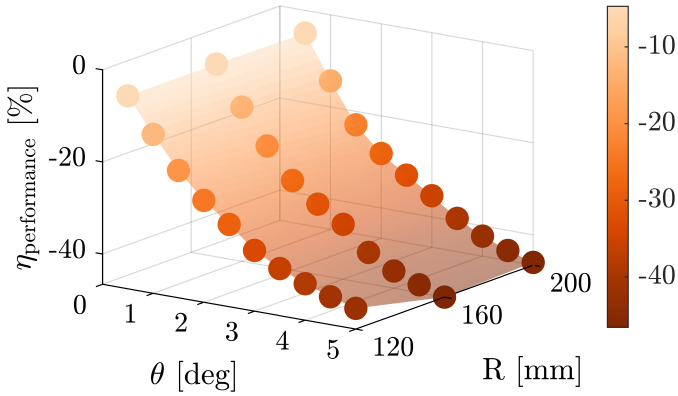

Figure 4.12: Bow-tie $\eta_{\text{performance}}$ evaluated for various R and θ where $W = 80$ mm and $t = 0.5$ mm

5 Design guidelines for the tapered and bow-tie flexure

This chapter provides design guidelines for engineers aiming to reduce the maximum von Mises stress in sheet flexures by implementing a tapered or bow-tie flange shape. The chapter starts with outlining the step-by-step workflow and methodology of the design guidelines. This is followed by explanation of the shape decision graph, which assist in determining whether a tapered or bow-tie flexure is more suitable. Subsequently, prediction models are introduced to estimate the optimal flange shape and corresponding stress reduction without the need for FEA. Finally the accuracy of these models is assessed through a comparison with the FEA data.

5.1 Method

The design guidelines aim to provide a systematic approach for replacing the sheet flexure of the one DOF system, with a flexure that has a lower maximum von Mises stress. These guidelines specifically address the tapered flexure and the bow-tie flexure, as these were identified as the most effective flange shapes in Chapter 3.2.5. The guidelines consist of several key steps:

1. **Shape decision:** determine whether the tapered or bow-tie flexure is the most suitable for a given input $\{L, W, \theta, t, R\}$ using the shape decision graph
2. **Determine optimal shape:** calculate the η_{optimal} for a given input $\{L, W, \theta, t, R\}$ using the η_{optimal} prediction models
3. **Determine baseline stress:** calculate the maximum stress of the standard sheet flexure with $\{L, W, \theta, t, R, E, \nu\}$ by using:
   (a) $\sigma_{\text{eq,max}}$ prediction model for material $E = 193$[GPA] and $\nu = 0.31$[-]
   (b) $\sigma_{\bar{x}\bar{x}}$ analytical model for slender flexures
   (c) custom FEA simulations
4. **Determine stress reduction:** calculate the $\eta_{\text{performance}}$ for a given input $\{L, W, \theta, t, R\}$ using the $\eta_{\text{performance}}$ prediction models

Table 9 outlines the range of input parameters covered by the design guidelines. These parameters define the scope of configurations to which the guidelines can be applied. They are not restricted to only the stainless steel material, as Chapter 4 found that η_{optimal} is independent of the material. Additionally, $\eta_{\text{performance}}$ remains similar for Poisson's ratios between 0.31 and 0.34. Therefore one would only need the $\{L, W, \theta, t, R\}$ input parameters to create the decision graph and prediction models.

Table 9: Applicable input range design guidelines

Par.	Value	Unit	Par.	Value	Unit
W/L	$[0.1 - 1.5]$	-	θ	$[0.5 - 5]$	deg
t/L	$[0.001 - 0.008]$	-	E	193	GPa
R/L	$[1.2 - 2]$	-	ν	0.31	-

To further generalize the applicability of the results, the scaling relationship identified in Chapter 3.2.4 is applied. In this chapter, it was demonstrated that scaling all geometric input parameters by the same factor yields stress results that are equivalent to those obtained from directly simulating the corresponding scaled geometries. Since both η_{optimal} and $\eta_{\text{performance}}$ are derived from $\sigma_{\text{eq,max}}$, they remain unchanged under this scaling relationship. This finding allows for the geometric parameters to be expressed as dimensionless ratios by dividing them by the length L. The $\frac{W}{L}$ ratio is given as an example in Figure 5.1. A ratio of 0.2 represents a slender flexure, and as the ratio increases to 1 the flexure becomes square.

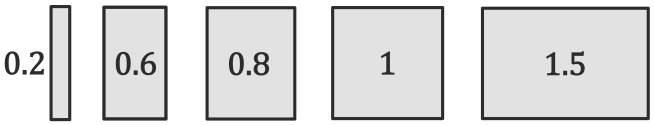

Figure 5.1: Example of $\frac{W}{L}$ ratio

The data that was used for the development of the design guidelines were obtained using the the ANSYS workflow as discussed in Chapter 3.1.1. The dataset contains 18320 unique configurations for each flexure type, which is reduced to 1440 unique configurations after determining η_{optimal}. The simulation output data is provided in Appendix G and serves as a convenient reference, summarizing the simulation results for step 2, 3 and 4 of the design guidelines. If it is possible to predict the maximum von Mises stress for the tapered and bow-tie flexure directly from the input data, it would eliminate the need for the discrete steps 2, 3 and 4 of the design guidelines. However, the additional η input parameter made it difficult to fit a reliable model for direct stress prediction. By first determining the η_{optimal} for each $\{L, W, \theta, t, R, E, \nu\}$ configuration, it is possible to use the remaining dataset to effectively train models to predict η_{optimal} and the corresponding $\eta_{\text{performance}}$. This approach, however, requires an additional step to determine the baseline stress of the standard sheet flexure. The baseline

stress is essential to translate the percentage stress reduction $\eta_{\text{performance}}$ into an absolute stress reduction values in MPa.

5.2 Shape decision graph

To recommend the tapered or bow-tie flexure, it is essential to identify which design offers the best stress reduction for the specified input parameters. In other words, which flexure has the best $\eta_{\text{performance}}$. A comparison of the stress reduction between the tapered flexure and bow-tie flexure is given in Figure 5.2. The flexure with the lower $\eta_{\text{performance}}$ achieves greater stress reduction, making it the preferred choice. For all configurations, the tapered flexure provides better stress reduction at lower $\frac{W}{L}$ ratios. Additionally it is visible how $\eta_{\text{performance}}$ is also dependent on θ.

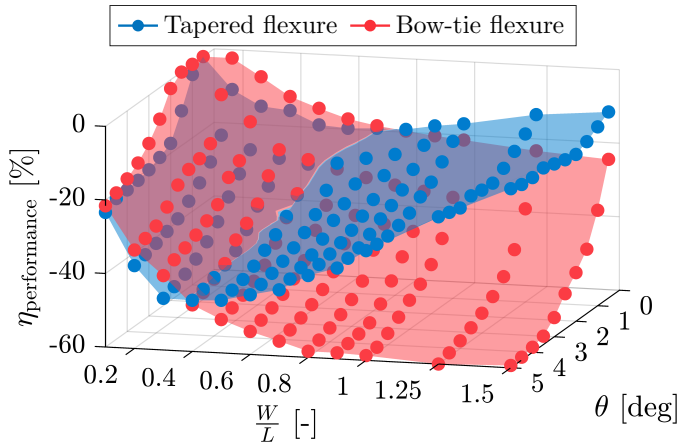

Figure 5.2: $\eta_{\text{performance}}$ evaluated for various $\frac{W}{L}$ and θ where $\frac{R}{L} = 1.2$ [−], $\frac{t}{L} = 0.002$ [−]

The additional dependence of $\frac{t}{L}$ and $\frac{R}{L}$ is illustrated in Figure 5.3. The increase in both the radius and thickness changes the recommended flexure type for some of the configurations.

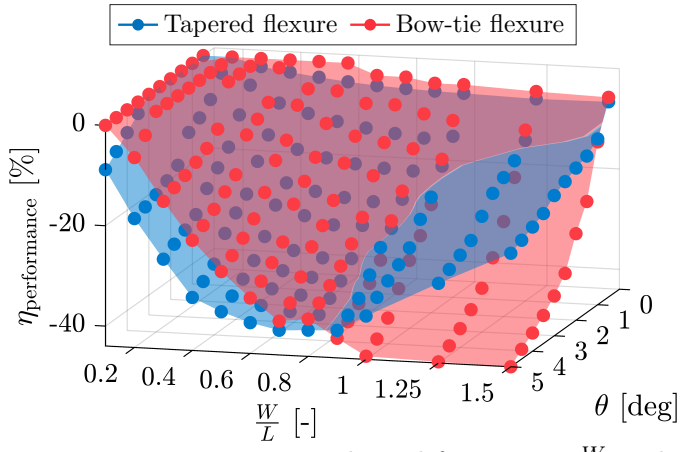

Figure 5.3: $\eta_{\text{performance}}$ evaluated for various $\frac{W}{L}$ and θ where $\frac{R}{L} = 2$ [−] and $\frac{t}{L} = 0.008$ [−]

The shape decision graph in Figure 5.4 helps identify whether the tapered or bow-tie flexure provides better stress reduction for a given configuration. It visualizes the width where the stress reduction of the two flexures are equal. For each specific combination of $\{\theta, \frac{t}{L}, \frac{R}{L}\}$ the $\frac{W_{\text{intersect}}}{L}$ is identified. This can be seen as the intersection line of the blue and red surfaces in Figure 5.2 and 5.3. The shape decision graph is based on the finding that the tapered flexure always outperforms the bow-tie flexure at lower $\frac{W}{L}$ ratios. Therefore, below $\frac{W_{\text{intersect}}}{L}$ the tapered flexure has better stress reduction while above $\frac{W_{\text{intersect}}}{L}$ the bow-tie flexure has better stress reduction. In the shape decision graph an increase in thickness is visualized by the different colors, while an increase in radius is represented by the different line styles. To use the graph locate the line corresponding (close) to your configuration and check whether your point lies above or below.

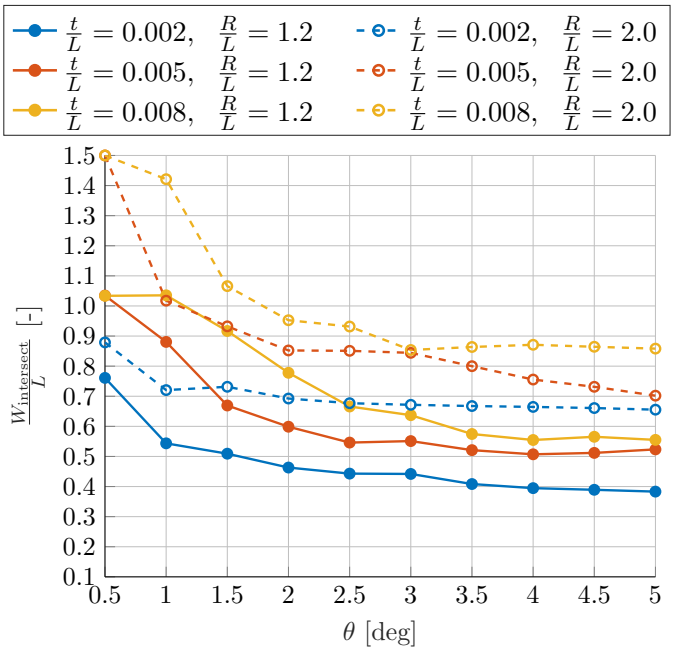

Figure 5.4: Shape decision graph where below line = tapered flexure and above line = bow-tie flexure

For example, consider a sheet flexure with the input parameters $\{\frac{W}{L}, \theta, \frac{t}{L}, \frac{R}{L}\} = \{0.8, 3, 0.002, 2.0\}$. This configuration corresponds to the dashed blue line in Figure 5.4. Locating the point $(\frac{W}{L}, \theta) = (0.8, 3)$ shows that it lies above the blue dashed line, indicating that the bow-tie flexure is recommended for this configuration. If the width were reduced to $\frac{W}{L} = 0.4$, the point now lies below the blue dashed line, indicating that the tapered flexure is recommended. Considering the original example again, if one would change the thickness to $\frac{t}{L} = 0.008$, the orange dashed line now corresponds to that configuration. The resulting point $(\frac{W}{L}, \theta) = (0.8, 3)$, lies below this line making the tapered flexure the recommended choice.

5.3 Prediction models

The prediction models were developed to estimate $\frac{\eta_{\text{optimal}}}{L}$ and $\eta_{\text{performance}}$ without the need for Finite Element Analysis. This is achieved by training regression models using the dataset obtained from the ANSYS simulations. Since $\frac{\eta_{\text{optimal}}}{L}$ is independent of the material and $\eta_{\text{performance}}$ is consistent for the materials 304SS, Alu 7075-T6 and Ti-6Al-4V, only the inputs $\{\frac{W}{L}, \theta, \frac{t}{L}, \frac{R}{L}\}$ are required to directly predict $\frac{\eta_{\text{optimal}}}{L}$ and $\eta_{\text{performance}}$ for these materials.

The MATLAB function *fitlm* [17] provides a framework for constructing different types of regression models. The polynomial regression model *poly-ijk* was chosen because it allows varying polynomial degrees for each input variable. For example, with the input $\{x_1, x_2, x_3, x_4\}$ and output y, the model poly2211 includes term up to degree 2 for x_1 and x_2, and degree 1 for x_3 and x_4. Additionally the model also incorporates interaction terms, where the degree of each interaction does not exceed the maximum specified degree of the individual variables. The poly2211 model therefore also includes terms like x_1x_2, x_1x_3 and x_3x_4 and takes the general form:

$$\begin{aligned} y = {} & c_0 + c_1x_1 + c_2x_2 + c_3x_3 + c_4x_4 + c_5x_1^2 \\ & + c_6x_2^2 + c_7x_1x_2 + c_8x_1x_3 + c_9x_2x_3 \\ & + c_{10}x_1x_4 + c_{11}x_2x_4 + c_{12}x_3x_4 \end{aligned} \tag{22}$$

where the coefficients $c_0, c_1, c_2, \ldots, c_{12}$ are determined through the regression process that minimizes the error between the predicted output values and actual output values of the dataset.

Metrics such as the Root Mean Squared Error (RMSE) and the R-squared value, have been used to evaluate the prediction models. The RMSE measures the average magnitude of the prediction errors, providing an indication of how close the predicted values are to the actual values [17]. The R-squared value quantifies the proportion of variance in the output that is explained by the model, serving as a measure of its overall fit [17]. Appendix H provides the RMSE and R-squared values for different polynomial models.

An overview of the chosen prediction models is given in Table 10. All models required a high polynomial degrees to accurately capture the input-output relationship. Lower polynomial degrees resulted in less accurate fits. The $\frac{W}{L}$ and θ required the highest polynomial degrees in the models. This aligns with the observation in Chapter 4.2, where W and θ were found to have the strongest correlation with $\frac{\eta_{\text{optimal}}}{L}$ and $\eta_{\text{performance}}$. The code for the prediction models is provided in Appendix I. The remainder of this chapter will include prediction examples and error heat maps for each of the prediction models.

Table 10: Overview prediction models

Flexure type	Input	Output	Model	Appendix
Tapered	$\frac{W}{L}, \theta, \frac{t}{L}, \frac{R}{L}$	$\frac{\eta_{\text{optimal}}}{L}$	poly4322	I
Bow-tie	$\frac{W}{L}, \theta, \frac{t}{L}, \frac{R}{L}$	$\frac{\eta_{\text{optimal}}}{L}$	poly4322	I
Sheet	$\frac{W}{L}, \theta, \frac{t}{L}, \frac{R}{L}$	$\sigma_{\max}$	poly4322	I
Tapered	$\frac{W}{L}, \theta, \frac{t}{L}, \frac{R}{L}$	$\eta_{\text{performance}}$	poly4322	I
Bow-tie	$\frac{W}{L}, \theta, \frac{t}{L}, \frac{R}{L}$	$\eta_{\text{performance}}$	poly4322	I

5.3.1 Tapered flexure η_{optimal}

A comparison between the ANSYS FEA output and the poly4322 prediction model for the $\frac{\eta_{\text{optimal}}}{L}$ of the tapered flexure is given in Figure 5.5. In this graph the solid and open dots represent the simulation output data. While the solid and dashed lines represent the poly4322 prediction. Various configurations are shown in the graph. An increase in width is visualized by the different colors, while an increase in radius and thickness is represented by the different line styles. The solid dots and solid lines exhibit similar behavior, as do the open dots and dashed lines. This indicates that the poly4322 model effectively predicts $\frac{\eta_{\text{optimal}}}{L}$ of the tapered flexure for different kinds of input configurations. It is evident that some of the

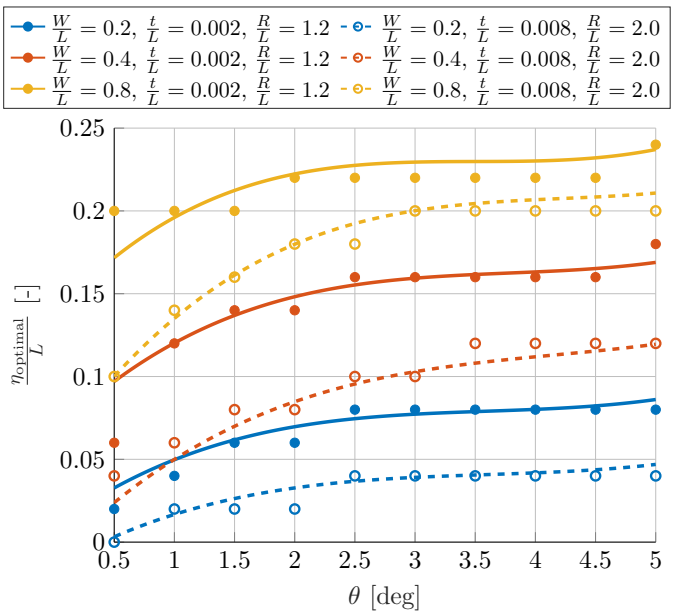

Figure 5.5: Comparison of simulated $\frac{\eta_{\text{optimal}}}{L}$ (dots) and poly4322 prediction model (lines)

simulated dots may be affected by the resolution of the η. This can be clearly seen with the open blue dots and dashed blue lines at $\theta = 2°$. Here, the simulated $\frac{\eta_{\text{optimal}}}{L}$ should likely be higher and appears to be limited by the step size of η. The poly4322 model seems to smooth out this behavior.

The difference between the FEA output (dots) and the prediction model output (lines) for a given configuration represents the prediction model's error. The magnitude of this error is dependend on the input configuration. To evaluate this error, the heat map in Figure 5.6 presents the maximum relative error between the poly4322 model and the ANSYS output across different $\frac{W}{L}$ and θ configurations. All configurations that share the same $\frac{W}{L}$ and θ values are grouped within a single cell, the maximum absolute error among these configurations is then used to generate the heat map. The error is expressed as a relative value because the $\frac{\eta_{\text{optimal}}}{L}$ tends to fall within smaller ranges for smaller input parameters, making relative comparisons more meaningful across configurations. If the simulation output $\frac{\eta_{\text{opt}}}{L} = 0$, the relative error cannot be calculated due to division by zero and a NaN value is inserted. A larger version of the heat map, including both the minimum and maximum relative errors, is provided in Appendix J.

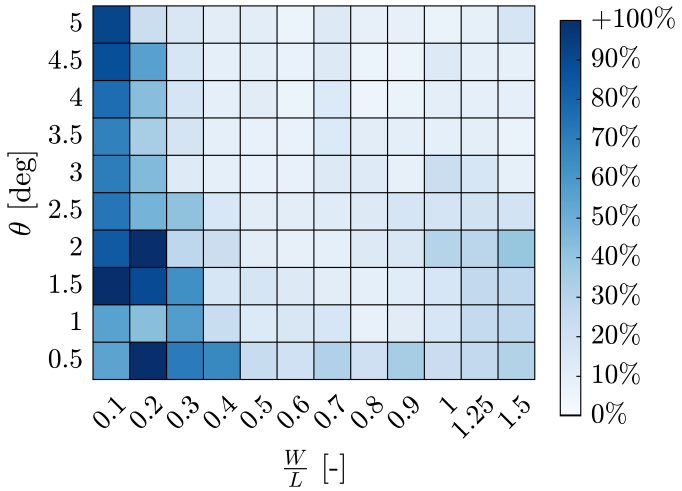

Figure 5.6: Maximum relative |error| [%] for predicted η_{optimal} tapered flexure

The poly4322 model for $\frac{\eta_{\text{optimal}}}{L}$ of the tapered flexure has a relative |error| smaller than 20% for 90% of the predictions. This is especially true for configurations that have larger $\frac{W}{L}$ and θ. The heat map shows a large area with low error percentages, which suggests that the prediction model can adapt well to different $\frac{W}{L}$ and θ configurations. Since each cell represents the maximum error among all underlying configurations with different $\frac{R}{L}$ and $\frac{t}{L}$ values, this also confirms that the model performs well across a wide range of geometric parameters. The largest errors occur in the row where $\theta = 0.5°$ and the column where $\frac{W}{L} = 0.1, 0.2$. This can also be seen in Figure 5.5 where the model has difficulties fitting for some configurations at $\theta = 0.5°$.

5.3.2 Bow-tie flexure η_{optimal}

A comparison between the ANSYS FEA output and the poly4322 prediction model for the $\frac{\eta_{\text{optimal}}}{L}$ of the bow-tie flexure is given in Figure 5.7. The solid dots and solid lines exhibit similar behavior, as do the open dots and dashed lines. This indicates that the poly4322 model effectively predicts $\frac{\eta_{\text{optimal}}}{L}$ of the bow-tie flexure for different kinds of input configurations.

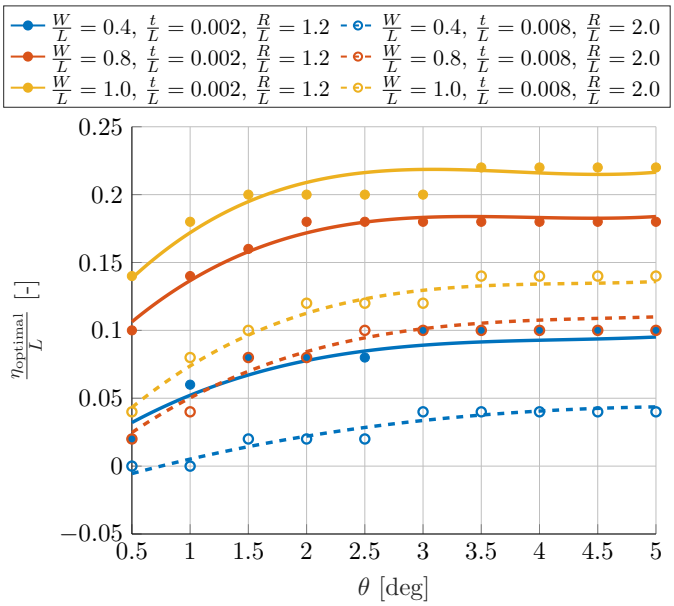

Figure 5.7: Comparison of simulated $\frac{\eta_{\text{optimal}}}{L}$ (dots) and poly4322 prediction model (lines)

The maximum relative error between the poly4322 model and the ANSYS output is illustrated in Figure 5.8. A larger version of the heat map, including both the minimum and maximum relative errors, is provided in Appendix J.

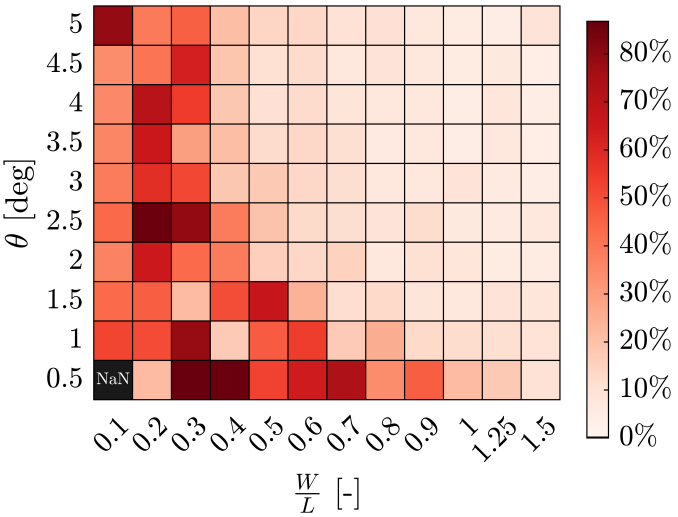

Figure 5.8: Maximum relative |error| [%] for predicted η_{optimal} bow-tie flexure

The poly4322 model for $\frac{\eta_{\text{optimal}}}{L}$ of the bow-tie flexure has a relative |error| smaller than 20% for 89% of the predictions. The heat map shows a large area with low error percentages, suggesting that the prediction model adapts well across different configurations. This prediction model also has smaller errors for the larger input values. The largest errors occur in the rows where $\theta = 0.5°$ and the column where $\frac{W}{L} = 0.1$. Notably, the model has a relative |error| of less than 10% for 98% for the configurations that have a bow-tie recommendation. This indicates that the model performs significantly better for the configurations it is recommended for.

5.3.3 Sheet flexure σ_{max}

A comparison between the ANSYS FEA output and the poly4322 prediction model for the $\sigma_{\text{eq,max}}$ of the sheet flexure is given in Figure 5.9. The solid dots and solid lines exhibit almost identical behavior, as do the open dots and dashed lines. This indicates that the poly4322 model effectively predicts $\sigma_{\text{eq,max}}$ of the sheet flexure for different kinds of input configurations. The figure also shows that as the flexure widens (indicated by the color change), the stresses increase. Additionally, thicker flexures positioned at a larger radius (indicated by line style change) also experience significantly higher stresses.

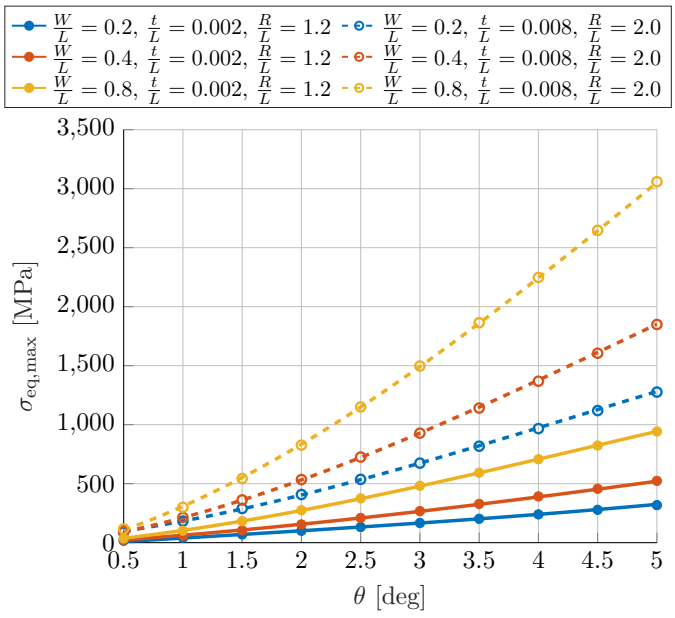

Figure 5.9: Comparison of simulated $\sigma_{\text{eq,max}}$ (dots) and poly4322 prediction model (lines)

The maximum relative error between the poly4322 model and the ANSYS output is illustrated in Figure 5.10. A larger version of the heat map, including both the minimum and maximum relative errors, is provided in Appendix J.

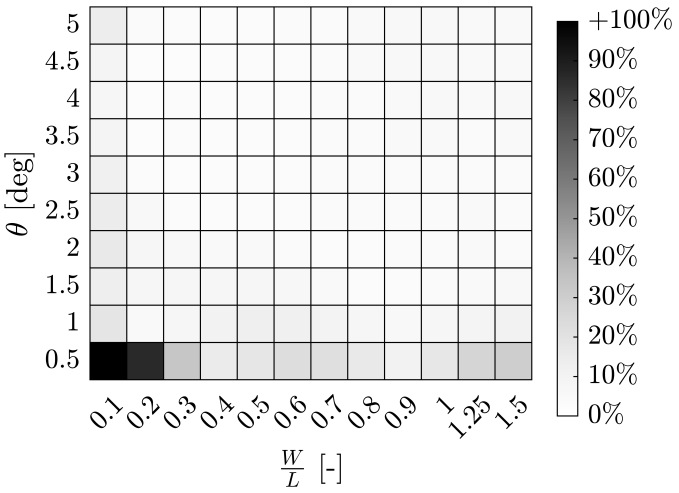

Figure 5.10: Maximum relative |error| [%] for predicted $\sigma_{\text{eq,max}}$ sheet flexure

The poly4322 model for $\sigma_{\text{eq,max}}$ of the sheet flexure has a relative |error| smaller than 10% for 95% of the predictions. The heat map shows a large area with low error percentages, suggesting that the prediction model adapts well across different configurations. The largest errors occur in the rows where $\theta = 0.5°$ and the column where $\frac{W}{L} = 0.1$.

5.3.4 Tapered flexure $\eta_{\text{performance}}$

A comparison between the ANSYS FEA output and the poly4322 prediction model for the $\eta_{\text{performance}}$ of the tapered flexure is given in Figure 5.11. The solid dots and solid lines also exhibit similar behavior, as do the open dots and dashed lines. This indicates that the poly4322 model effectively predicts $\eta_{\text{performance}}$ of the tapered flexure for different kinds of input configurations.

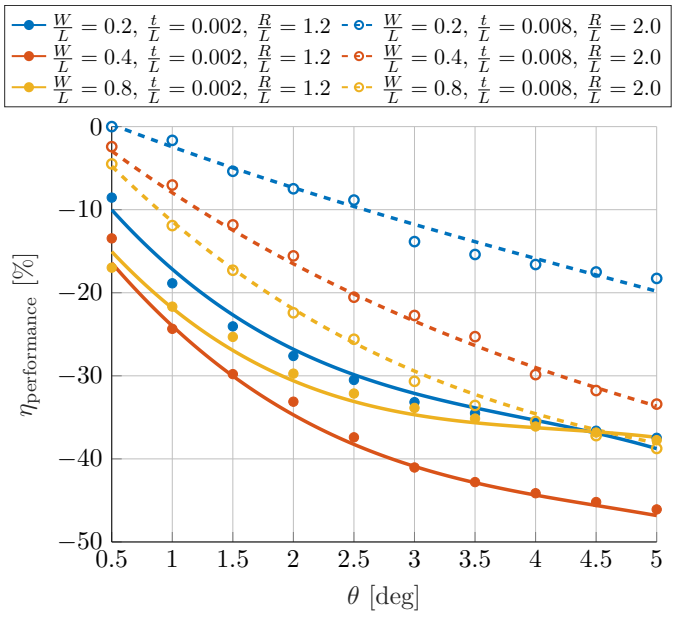

Figure 5.11: Comparison of simulated η_{perf} (dots) and poly4322 prediction model (lines)

The maximum relative error between the poly4322 model and the ANSYS output is illustrated in Figure 5.12. A larger version of the heat map, including both the minimum and maximum relative errors, is provided in Appendix J.

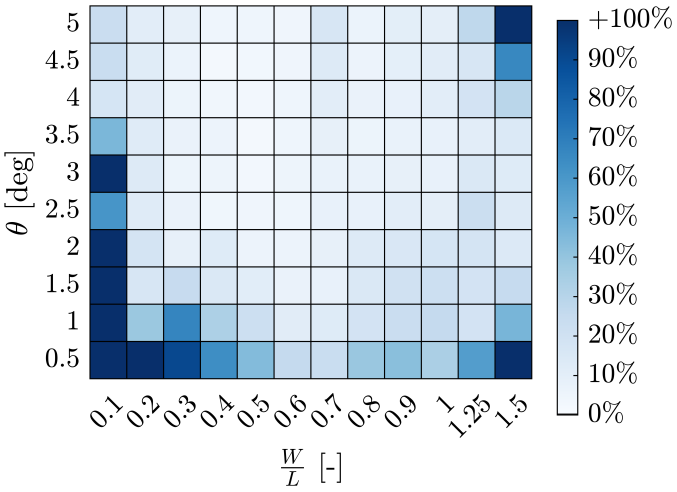

Figure 5.12: Maximum relative |error| [%] for predicted $\eta_{\text{performance}}$ tapered flexure

The poly4322 model for $\eta_{\text{performance}}$ of the tapered flexure has a relative |error| smaller than 20% for 94% of the predictions. All relative |errors| that are larger than 20% occur in the column where $\frac{W}{L} = 0.1, 1.5$ or where the row is equal to $\theta = 0.5°$. This heat map also shows a large area with low error percentages, suggesting that the prediction model adapts well across different configurations.

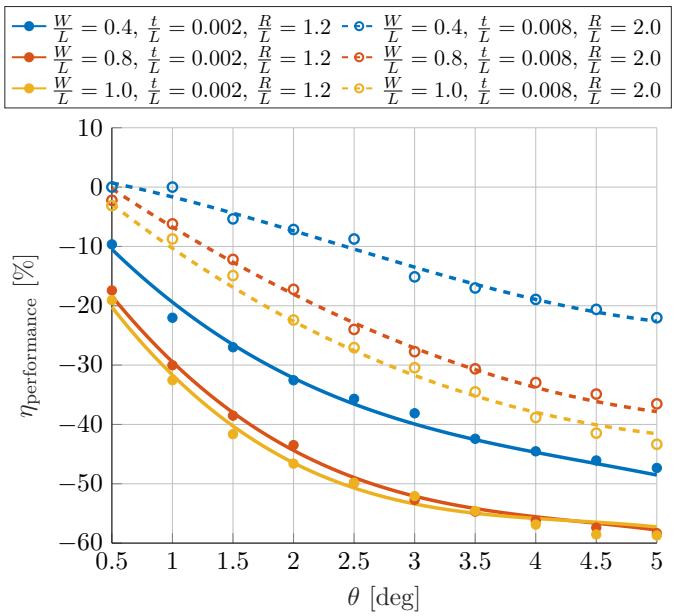

Figure 5.13: Comparison of simulated $\eta_{\text{performance}}$ (dots) and poly4322 prediction model (lines)

5.3.5 Bow-tie flexure $\eta_{\text{performance}}$

A comparison between the ANSYS FEA output and the poly4322 prediction model for the $\eta_{\text{performance}}$ of the bow-tie flexure is given in Figure 5.13. The solid dots and solid lines also exhibit similar behavior, as do the open dots and dashed lines. This indicates that the poly4322 model effectively predicts $\eta_{\text{performance}}$ of the bow-tie flexure for different kinds of input configurations.

The maximum relative error between the poly4322 model and the ANSYS output is illustrated in Figure 5.14. A larger version of the heat map, including both the minimum and maximum relative errors, is provided in Appendix J.

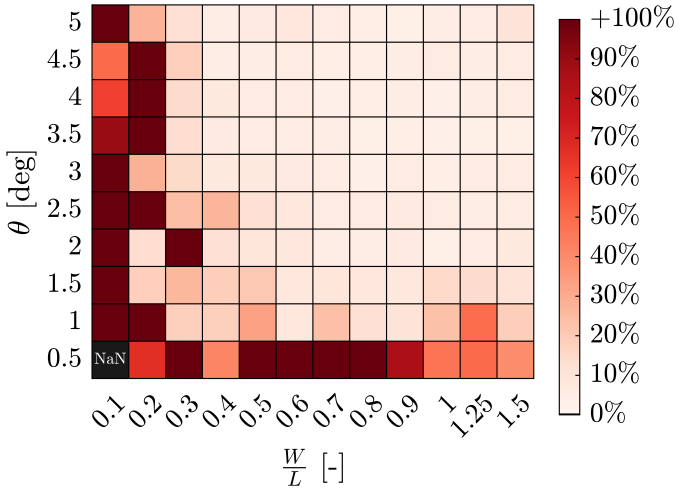

Figure 5.14: Maximum relative |error| [%] for predicted η_{optimal} bow-tie flexure

The poly4322 model for $\eta_{\text{performance}}$ of the bow-tie flexure has a relative |error| smaller than 20% for 92% of the predictions. Again the lower values of $\frac{W}{L}$ and θ contain the largest errors. Notably, the model has a relative |error| of less than 10% for 96% of the predictions that have a bow-tie recommendation. Indicating that this model also performs significantly better for the configurations it is recommended for.

6 Discussion

To circumvent the impact of stress singularities on the FEA results, an offset of 0.5 mm was applied to exclude the first two rows of elements near the top and bottom flanges. This offset influences the stress values as it removes a small region at the critical stress location. Reducing this offset would result in higher stress values, narrowing the gap between the nonlinear model and the ANSYS predictions in Figure 2.5. Selecting the mesh size was a balance between the accuracy of the results and the computation time required for all of the simulations. All flexures are analyzed with the same offset ensuring a fair comparison, however the actual stress value could be slightly higher than the results suggest.

Hale [4] briefly discusses the radial arrangement of sheet flexures and suggests modifying the geometry of the flange shapes to achieve equal shortening or bending stress across the width of the flexure. Hale provides the conditions that can be used to calculate the resulting flange shapes. Maintaining equal shortening results in a paraboloid shape that shares a common vertex at the rotational axis of the radially arranged flexure system. This shape resembles the common vertex arc shown in Figure 3.12c, assuming point E is fixed at the rotational DOF of the system. Maintaining equal bending stress results in a tapered like flange shape. The derived shapes only depend on the radius at which the flexure is located, width and length of the flexure. However, as demonstrated in Chapter 4.2, the optimal flange shape is also highly dependent on the prescribed rotation and thickness. Therefore, the proposed equations cannot be used to calculate the optimal flange shape.

The solver within ANSYS mechanical is configured to use a large deflection algorithm. This option accounts for stiffness changes due to large deformations and rotations by updating the stiffness matrix as the structure deforms. To better understand the influence of nonlinear effects, additional simulations were performed with the large deflection option turned off. This showed that increasing η reduces stress even for the linear simulation. For slender flexures, the stress reduction is similar between the two options, but as the flexure becomes wider the difference the option on or off increases. This seems to suggest that the altered flange shape has an impact on the linear components contributing to the stress. This is supported by Chapter 2.7, where the critical stress in a slender flexure at initial rotation is primarily determined by the linear terms. Furthermore, Chapter 3.2.5 indicates that the modified flanges influence the stress distribution at initial rotation even for the smaller widths.

The $\frac{\eta_{\text{optimal}}}{L}$ that is obtained through the simulations does not have to be the true optimum. This true optimum might be slightly higher or lower, as it is restricted by the resolution used of $\frac{\eta_{\text{optimal}}}{L} = 0.02$. This limitation is more pronounced for flexures with a $\frac{W}{L} < 0.3$, as these configurations tend to have smaller values for $\frac{\eta_{\text{optimal}}}{L}$. The prediction models have shown to smooth out this behavior, but they still exhibit large error values for the smaller $\frac{W}{L}$ ratios. Future simulations could adjust this resolution based on the $\frac{W}{L}$ ratio to determine an more accurate optimum.

The design guidelines provide tools for finding $\frac{\eta_{\text{optimal}}}{L}$ and $\eta_{\text{performance}}$ but do not guarantee that these designs can withstand the applied loads. It is still necessary to compare the predicted stresses with the material limits.

This research focused on the stress reduction by modifying the flange shapes of the sheet flexure. Appendix K examines whether altering the inner vertical edge of the tapered flexure can reduce the stress even further. To ensure a fair comparison between the inner edge flexure, sheet flexure and tapered flexure, the support stiffness in global $x-$direction was included as a performance metric. The results in Appendix K indicate that modifying the inner vertical edge is not effective for stress reduction, as it also significantly reduces the support stiffness. However, both the tapered and bow-tie flexures exhibit higher support stiffness in the global $x-$direction, compared to the sheet flexure. For both designs, increasing η leads to a increase in support stiffness. This suggests that η does not only reduce stress, but also improves the support stiffness in $x-$direction. Further study is needed to develop a better understanding of how η influences the overall stiffness behavior of the tapered and bow-tie flexure.

7 Conclusions

This research has demonstrated that modifying the flange shapes of sheet flexures, which are arranged radially with one degree of freedom, can effectively reduce maximum internal stresses. Using the analytical model it examined the factors contributing to the high stresses in the sheet flexure. It evaluated how various input parameters influence the optimal flange shape and corresponding stress reduction. Addition-

ally, the study provided design guidelines to assist in identifying the optimal flange shape to minimize the internal stresses.

An analytical stress model was developed to estimate the critical axial stress component $\sigma_{\bar{x}\bar{x}}$ in the sheet flexures. The radial arrangement of three sheet flexures was simplified to a model with a single flexure subjected to u_{2y}, u_{2z} and ϕ_{2x} at one flange and the other flange fixed.

The developed model accounts for the axial stress induced by both bending moments and the shortening effect. To simplify the analysis, it is applied to a slender sheet flexure, where shear deformation and constrained warping effects can be neglected. Additionally, it is assumed that no axial forces are applied to the sheet flexure.

Using a linear stiffness model for the moments, resulted in deviations from the numerical axial stress results after only 1° of rotation. To address this limitation, a nonlinear stiffness model was incorporated which introduces additional load-stiffening and kinematic terms. This model showed a good agreement with the numerical axial stress results, even for larger rotations. An evaluation of the components contributing to the axial stress reveals that the effect of shortening is negligible compared to the influence of the bending moments.

The analytical model does not hold for flexures with altered flange shapes. This is because the theories used, rely on the assumption of a uniform cross-section along the length of the flexure. As a result, ANSYS Workbench was used to model and analyze the stress distributions in the sheet flexures with altered flange shapes. A workflow was developed using python scripts in ANSYS workbench, to enable parametrization and automation of the whole CAD and FEA process.

The tapered flexure was chosen as the initial flange shape to be analyzed. This flexure features symmetrically slanted top and bottom flanges defined by the distance η. The geometry of the tapered flexure is identical to that of the sheet flexure for $\eta = 0$ mm. The maximum von Mises stress in the sheet flexure occurs at the top and bottom corners furthest from the system's single degree of freedom. This behavior is consistent across various flexure dimensions. Increasing η reduced the stress in those corners resulting in a gradual reduction of the maximum von Mises stress. This reduction continues up to a certain point, after which a new stress concentration becomes dominant and increasing η will no longer improve the stress distribution. To quantify this η_{optimal} is defined as the value of η that minimizes the maximum von Mises stress compared to that of the sheet flexure. The percentage of stress reduction at η_{optimal} is expressed as $\eta_{\text{performance}}$.

The study evaluates six alternative flange shapes that are all defined by the distance η and geometric constraints. The shapes were tested across various flexure widths and prescribed rotations to determine their effectiveness in reducing the maximum von Mises stress. The inverted taper resulted in an increase in stress rather than a reduction, indicating that the orientation of the flange shape with respect to the rotational DOF is important. The tangent arc and inverted corner arc flange shapes did not perform as well as the other shapes. Both share the characteristic that their flange shape is parallel to the top edge of the sheet flexure. The tapered flexure and bow-tie flexure provide the most significant stress reductions among the evaluated shapes. Generally, the tapered shape performs better for slender flexures, while the bow-tie shape is more effective for wider flexures. The amount of stress reduction is heavily dependent on the input parameters. Depending on the configuration, the tapered flexure was able to achieve up to 56% stress reduction, while the bow-tie achieved up to 67% stress reduction.

In the tapered flexure, $\sigma_{\bar{x}\bar{x}}$ is the only stress tensor component affected by η. It shows a reduction similar to that of the maximum von Mises stress. The other stress tensor components generally increase. In the bow-tie flexure, $\sigma_{\bar{x}\bar{x}}$ also decreases and is the main contributor to the reduction in $\sigma_{\text{eq,avg}}$. The $\sigma_{\bar{y}\bar{y}}$ component also decreases slightly, but its magnitude is ten times smaller compared to that of $\sigma_{\bar{x}\bar{x}}$.

The stress reduction only occurred under the boundary conditions $u_{2y}, u_{2z}, \phi_{2x}$ or u_{2z}, ϕ_{2x} other combinations showed no improvement by η.

A correlation analysis was conducted to quantify the influence of the input parameters $W, \theta, t, R, E, \nu, F_x$ on the optimal shape η_{optimal}. The results show that the W has the largest impact on η_{optimal} for both the tapered and bow-tie flexure, with η_{optimal} increasing as the flexure becomes wider. The θ is the next most significant factor, with higher θ values resulting in a larger η_{optimal}. The R and t also affect the optimal flexure shape but their influence is less significant compared to that of W and θ. The analysis showed that the optimal shape is material independent, as η_{optimal} remains consistent across the materials 304SS, Alu 7075-T6, Ti-6Al-4V,

ABS, and HDPE. Additionally, an axial force up to 50 N did not alter the optimal shape for the evaluated 304SS configurations.

A similar correlation analysis was conducted to quantify the influence of the input parameters on the stress reduction $\eta_{\text{performance}}$. The stress reduction of the tapered flexure has a nonmonotic relationship with W. As the flexure becomes wider the stress reduction increases but at a certain point it starts to decline. In contrast, the bow-tie flexure shows a consistent increase in stress reduction as the flexure becomes wider. The θ and t are the next most significant parameters. Larger values of θ and smaller values of t will result in more stress reduction. Material properties influence the stress reduction, with plastics showing less stress reduction than metals. The simulated metals 304SS, Alu 7075-T6 and Ti-6Al-4V all demonstrated similar stress reduction, indicating that only one of these materials is required for a good approximation.

In order to reduce the maximum von Mises stress, design guidelines have been developed to assist in replacing the conventional sheet flexures with the tapered flexure or bow-tie flexure. These guidelines incorporate a scaling relationship, which generalizes their applicability by expressing geometric input parameters as dimensionless ratios. The guidelines consist of a shape decision graph enabling the selection of the optimal flexure type: tapered or bow-tie, for a set of input parameters $\{\frac{W}{L}, \theta, \frac{t}{L}, \frac{R}{L}\}$. The guidelines conclude with multiple prediction models that enable the estimation of output parameters, without the need for Finite Element Analysis. The prediction models are able to predict $\sigma_{\max}$ of the sheet flexure, as well as η_{optimal} and $\eta_{\text{performance}}$ of the tapered and bow-tie flexures using the input parameters $\{\frac{W}{L}, \theta, \frac{t}{L}, \frac{R}{L}\}$. All prediction models have an relative error $<$20% for 89% of the cases compared to Finite Element Analysis. The maximum relative errors between the prediction model and the simulation output have been documented in accompanied heat maps.

8 Future directions

The current analytical model suggests that stress reduction at initial rotation arises primarily from the linear components. While FEA simulations demonstrate how variations in the input parameters influence the optimal flange shape and stress reduction. They do not explain the underlying mechanisms contributing to the reduced stresses. Future research could focus on the development of an analytical model that is able to account for the altered geometry of the flexures with altered flange shapes.

The various flange shapes in this study are all fully determined by the distance η and specific geometric constraints. Future research could focus on the development of a more flexible parametric flange shape. By optimizing such shape it would be possible to identify the true optimal flange shape that minimizes stress.

A dedicated test setup could be designed to evaluate the stress limits of different flexure types. Future research could focus on the experimental validation of the tapered and bow-tie flexures. For instance, a sheet flexure that would typically deform under certain loads could be tested alongside the optimal tapered or bow-tie flexures to assess whether the proposed shapes maintain their structural integrity.

References

[1] H. Soemers, *Design principles for precision mechanisms*. Netherlands: University of Twente, 2010.

[2] E. Klomp, "Design of a flexible hollow hinge for a cryogenic environment," Master's Thesis, University of Twente, September 30 2021.

[3] W. Kamphof, "Design of a flexible hinge for an atmospheric dispersion corrector," Master's Thesis, University of Twente, October 27 2023.

[4] L. Hale, *Principles And Techniques For Designing Precision Machines*. Ph.D. Thesis, University of California, 1999.

[5] B. Goodno and J. Gere, *Mechanics of materials, enhanced, SI edition*. KY, USA: Cengage Learning, 9 ed., Jan. 2020.

[6] D. Logan, *A first course in the finite element method, enhanced edition, SI version*. KY, USA: Cengage Learning, 6 ed., Jan. 2022.

[7] M. Ellenbroek, *Linear Solid Mechanics - Theory*. December 17, 2019: Faculty of Engineering Technology (ET), 2019. Lecture notes.

[8] S. Sen, *Beam Constraint Model: Generalized Nonlinear Closed-form Modeling of Beam Flexures for Flexure Mechanism Design*. Ph.D. Thesis, University of Michigan, 01 2013.

[9] M. Nijenhuis, J. P. Meijaard, and D. M. Brouwer, "A spatial parametric model for the nonlinear stiffness characteristics of flexure strips," vol. Volume 5A: 42nd Mechanisms and Robotics Conference, p. V05AT07A014, 08 2018.

[10] M. Nijenhuis, J. Meijaard, and D. Brouwer, "A spatial closed-form nonlinear stiffness model for sheet flexures based on a mixed variational principle including third-order effects," *Precision engineering*, vol. 66, pp. 429–444, Nov. 2020. Elsevier deal.

[11] ANSYS, *ANSYS Meshing User's Guide*, July 2023. release 2023 R2.

[12] ANSYS, *Element Reference*, July 2023. release 2023 R2.

[13] ANSYS, *Mechanical User's Guide*, July 2023. release 2023 R2.

[14] O. C. Zienkiewicz, R. L. Taylor, and J. Z. Zhu, *The Finite Element Method: Its Basis and Fundamentals, Seventh Edition*. Butterworth-Heinemann, 7 ed., May 2013.

[15] P. Schober, C. Boer, and L. A. Schwarte, "Correlation coefficients: Appropriate use and interpretation," *Anesthesia & Analgesia*, vol. 126, pp. 1763–1768, May 2018.

[16] The MathWorks, Inc., *Linear or rank correlation*, 2025. https://mathworks.com/help/stats/corr.html.

[17] The MathWorks, Inc., *Fit Linear Regression Model*, 2025. https://mathworks.com/help/stats/fitlm.html.

Appendix A - Linear stiffness model

Appendix A provides the complete linear stiffness matrix $[K]$ and derives the resulting system of equations by incorporating the boundary conditions.

The relationship between the applied displacements $\{u\}$ and reaction forces $\{F\}$ in a three-dimensional beam element is governed by the global stiffness matrix [K]:

$$\{F\} = [K]\{u\}, \qquad \{u\} = [K]^{-1}\{F\} \tag{23}$$

The stiffness matrix is derived using Euler-Bernoulli beam theory which governs the linear-elastic behavior of beams [5]. The resulting stiffness matrix is a 12×12 matrix, corresponding to the six DOF at each node of the three-dimensional beam element [6]:

$$\begin{Bmatrix} F_{1x} \\ F_{1y} \\ F_{1z} \\ M_{1x} \\ M_{1y} \\ M_{1z} \\ \hdashline F_{2x} \\ F_{2y} \\ F_{2z} \\ M_{2x} \\ M_{2y} \\ M_{2z} \end{Bmatrix} = \left[\begin{array}{cccccc:cccccc} u_{1x} & u_{1y} & u_{1z} & \phi_{1x} & \phi_{1y} & \phi_{1z} & u_{2x} & u_{2y} & u_{2z} & \phi_{2x} & \phi_{2y} & \phi_{2z} \\ \hline \frac{EA}{L} & 0 & 0 & 0 & 0 & 0 & -\frac{EA}{L} & 0 & 0 & 0 & 0 & 0 \\ 0 & \frac{12EI_z}{L^3} & 0 & 0 & 0 & \frac{6EI_z}{L^2} & 0 & -\frac{12EI_z}{L^3} & 0 & 0 & 0 & \frac{6EI_z}{L^2} \\ 0 & 0 & \frac{12EI_y}{L^3} & 0 & -\frac{6EI_y}{L^2} & 0 & 0 & 0 & -\frac{12EI_y}{L^3} & 0 & -\frac{6EI_y}{L^2} & 0 \\ 0 & 0 & 0 & \frac{GJ}{L} & 0 & 0 & 0 & 0 & 0 & -\frac{GJ}{L} & 0 & 0 \\ 0 & 0 & -\frac{6EI_y}{L^2} & 0 & \frac{4EI_y}{L} & 0 & 0 & 0 & \frac{6EI_y}{L^2} & 0 & \frac{2EI_y}{L} & 0 \\ 0 & \frac{6EI_z}{L^2} & 0 & 0 & 0 & \frac{4EI_z}{L} & 0 & -\frac{6EI_z}{L^2} & 0 & 0 & 0 & \frac{2EI_z}{L} \\ \hdashline -\frac{EA}{L} & 0 & 0 & 0 & 0 & 0 & \frac{EA}{L} & 0 & 0 & 0 & 0 & 0 \\ 0 & -\frac{12EI_z}{L^3} & 0 & 0 & 0 & -\frac{6EI_z}{L^2} & 0 & \frac{12EI_z}{L^3} & 0 & 0 & 0 & -\frac{6EI_z}{L^2} \\ 0 & 0 & -\frac{12EI_y}{L^3} & 0 & \frac{6EI_y}{L^2} & 0 & 0 & 0 & \frac{12EI_y}{L^3} & 0 & \frac{6EI_y}{L^2} & 0 \\ 0 & 0 & 0 & -\frac{GJ}{L} & 0 & 0 & 0 & 0 & 0 & \frac{GJ}{L} & 0 & 0 \\ 0 & 0 & -\frac{6EI_y}{L^2} & 0 & \frac{2EI_y}{L} & 0 & 0 & 0 & \frac{6EI_y}{L^2} & 0 & \frac{4EI_y}{L} & 0 \\ 0 & \frac{6EI_z}{L^2} & 0 & 0 & 0 & \frac{2EI_z}{L} & 0 & -\frac{6EI_z}{L^2} & 0 & 0 & 0 & \frac{4EI_z}{L} \end{array}\right] \begin{Bmatrix} u_{1x} \\ u_{1y} \\ u_{1z} \\ \phi_{1x} \\ \phi_{1y} \\ \phi_{1z} \\ \hdashline u_{2x} \\ u_{2y} \\ u_{2z} \\ \phi_{2x} \\ \phi_{2y} \\ \phi_{2z} \end{Bmatrix} \tag{24}$$

The system of three radially arranged sheet flexures is simplified to a single beam element in Chapter 2.1. The motion of this element is governed by the applied rotation θ and radial distance R. Therefore the boundary conditions of the beam element are:

$$\begin{Bmatrix} u_{1x} \\ u_{1y} \\ u_{1z} \\ \phi_{1x} \\ \phi_{1y} \\ \phi_{1z} \\ \hdashline u_{2x} \\ u_{2y} \\ u_{2z} \\ \phi_{2x} \\ \phi_{2y} \\ \phi_{2z} \end{Bmatrix} = \begin{Bmatrix} 0 \\ 0 \\ 0 \\ 0 \\ 0 \\ 0 \\ \hdashline \text{free} \\ R\cos\theta - R \\ R\sin\theta \\ \theta \\ 0 \\ 0 \end{Bmatrix} \tag{25}$$

After substitution of the boundary conditions the resulting system of equations becomes:

$$\begin{aligned} F_{1x} &= \frac{EA}{L}u_{1x} - \frac{EA}{L}u_{2x} \\ &= -\frac{EA}{L}u_{2x} \end{aligned} \tag{26}$$

$$\begin{aligned} F_{2x} &= -\frac{EA}{L}u_{1x} + \frac{EA}{L}u_{2x} \\ &= \frac{EA}{L}u_{2x} \end{aligned} \tag{32}$$

$$\begin{aligned} F_{1y} &= \frac{12EI_z}{L^3}u_{1y} + \frac{6EI_z}{L^2}\phi_{1z} - \frac{12EI_z}{L^3}u_{2y} + \frac{6EI_z}{L^2}\phi_{2z} \\ &= -\frac{12EI_z}{L^3}u_{2y} \\ &= -\frac{12EI_z}{L^3}(R\cos\theta - R) \end{aligned} \tag{27}$$

$$\begin{aligned} F_{2y} &= -\frac{12EI_z}{L^3}u_{1y} - \frac{6EI_z}{L^2}\phi_{1z} + \frac{12EI_z}{L^3}u_{2y} - \frac{6EI_z}{L^2}\phi_{2z} \\ &= \frac{12EI_z}{L^3}u_{2y} \\ &= \frac{12EI_z}{L^3}(R\cos\theta - R) \end{aligned} \tag{33}$$

$$\begin{aligned} F_{1z} &= \frac{12EI_y}{L^3}u_{1z} - \frac{6EI_y}{L^2}\phi_{1y} - \frac{12EI_y}{L^3}u_{2z} - \frac{6EI_y}{L^2}\phi_{2y} \\ &= -\frac{12EI_y}{L^3}u_{2z} \\ &= -\frac{12EI_y}{L^3}R\sin\theta \end{aligned} \tag{28}$$

$$\begin{aligned} F_{2z} &= -\frac{12EI_y}{L^3}u_{1z} + \frac{6EI_y}{L^2}\phi_{1y} + \frac{12EI_y}{L^3}u_{2z} + \frac{6EI_y}{L^2}\phi_{2y} \\ &= \frac{12EI_y}{L^3}Ru_{2z} \\ &= \frac{12EI_y}{L^3}R\sin\theta \end{aligned} \tag{34}$$

$$\begin{aligned} M_{1x} &= \frac{GJ}{L}\phi_{1x} - \frac{GJ}{L}\phi_{2x} \\ &= -\frac{GJ}{L}\phi_{2x} \\ &= -\frac{GJ}{L}\theta \end{aligned} \tag{29}$$

$$\begin{aligned} M_{2x} &= -\frac{GJ}{L}\phi_{1x} + \frac{GJ}{L}\phi_{2x} \\ &= \frac{GJ}{L}\phi_{2x} \\ &= \frac{GJ}{L}\theta \end{aligned} \tag{35}$$

$$\begin{aligned} M_{1y} &= -\frac{6EI_y}{L^2}u_{1z} + \frac{4EI_y}{L}\phi_{1y} + \frac{6EI_y}{L^2}u_{2z} + \frac{2EI_y}{L}\phi_{2y} \\ &= \frac{6EI_y}{L^2}u_{2z} \\ &= \frac{6EI_y}{L^2}R\sin\theta \end{aligned} \tag{30}$$

$$\begin{aligned} M_{2y} &= -\frac{6EI_y}{L^2}u_{1z} + \frac{2EI_y}{L}\phi_{1y} + \frac{6EI_y}{L^2}u_{2z} + \frac{4EI_y}{L}\phi_{2y} \\ &= \frac{6EI_y}{L^2}u_{2z} \\ &= \frac{6EI_y}{L^2}R\sin\theta \end{aligned} \tag{36}$$

$$\begin{aligned} M_{1z} &= \frac{6EI_z}{L^2}u_{1y} + \frac{4EI_z}{L}\phi_{1z} - \frac{6EI_z}{L^2}u_{2y} + \frac{2EI_z}{L}\phi_{2z} \\ &= -\frac{6EI_z}{L^2}u_{2y} \\ &= -\frac{6EI_z}{L^2}(R\cos\theta - R) \end{aligned} \tag{31}$$

$$\begin{aligned} M_{2z} &= \frac{6EI_z}{L^2}u_{1y} + \frac{2EI_z}{L}\phi_{1z} - \frac{6EI_z}{L^2}u_{2y} + \frac{4EI_z}{L}\phi_{2z} \\ &= -\frac{6EI_z}{L^2}u_{2y} \\ &= -\frac{6EI_z}{L^2}(R\cos\theta - R) \end{aligned} \tag{37}$$

Appendix B - Nonlinear stiffness model

Appendix B provides the derivation of the non-linear stiffness model. The linear model of the sheet flexure, developed using the framework of Euler-Bernoulli beam theory in Chapter 2.3, assumes small displacements and rotations, where the stiffness is treated as constant and independent of deformation. However, in practice deformations are often large, making nonlinear effects from geometrical changes significant [9]. To address these limitations, the M_{2y} and M_{2z} are rewritten using the work by Nijenhuis [9], [10]. The analytical results are compared with numerical simulations obtained using ANSYS Workbench. Details on the ANSYS modeling and simulation procedure are provided in Chapter 3.1.1.

Coordinate system transformation

A different coordinate system is used in [9] and [10], this requires the equations to be transformed to the current CS. The old CS is expressed in terms of the current CS using Table 11.

Table 11: Transformation between current and old Coordinate System

current CS	old CS [9], [10]	Reference axis sheet flexure
x	x	along length
y	$-z$	along width
z	y	along thickness

Formulation of M_{2z}

The M_{2z} is obtained using the nonlinear model [9] that provides accurate stiffness predictions by accounting for bending, elongation and torsion deformations. The M_{2z} is not explicitly provided, as the nonlinear model is expressed as a function of three actuation loads and three degrees of freedom. To determine M_{2z} a system of two equations and two unknowns is constructed. In this system M_{2z} and F_{2y} are the unknown variables while the equations corresponding to u_{2y} and ϕ_{2z} are used to solve the system. A different coordinate system is used in [9], the expression for u_{2y} is derived by taking u_{2z} in the old coordinate system and subsequently applying the coordinate transformation. The u_{2z} in the **old** coordinate system is given by [9]:

$$\begin{aligned} u_{2z} =& \frac{L\,\phi_{2x}\,\phi_{2z}}{6} + \frac{F_{2z}\,L^3}{3\,\mathrm{E}\,I_y} - \frac{L^2\,M_{2y}}{2\,\mathrm{E}\,I_y} - \frac{M_{2y}\,{u_{2y}}^2}{10\,G\,J} + \frac{3\,F_{2z}\,L\,{u_{2y}}^2}{35\,G\,J} + \frac{F_{2z}\,L^3\,{\phi_{2x}}^2}{180\,\mathrm{E}\,I_z} + \frac{13\,F_{2z}\,L^3\,{\phi_{2z}}^2}{1260\,G\,J} \\ & - \frac{L^2\,M_{2y}\,{\phi_{2z}}^2}{30\,G\,J} + \frac{L\,M_{2y}\,\phi_{2z}\,u_{2y}}{30\,G\,J} - \frac{F_{2x}\,L^3\,\phi_{2x}\,\phi_{2z}}{360\,\mathrm{E}\,I_z} - \frac{2\,F_{2z}\,L^2\,\phi_{2z}\,u_{2y}}{105\,G\,J} \end{aligned} \tag{38}$$

Applying the coordinate transformation to obtain u_{2y} in the current coordinate system:

$$\begin{aligned} u_{2y} =& \frac{L\,\phi_{2x}\,\phi_{2y}}{6} + \frac{F_{2y}\,L^3}{3\,\mathrm{E}\,I_z} + \frac{L^2\,M_{2z}}{2\,\mathrm{E}\,I_z} + \frac{M_{2z}\,{u_{2z}}^2}{10\,G\,J} + \frac{3\,F_{2y}\,L\,{u_{2z}}^2}{35\,G\,J} + \frac{F_{2y}\,L^3\,{\phi_{2x}}^2}{180\,\mathrm{E}\,I_y} + \frac{13\,F_{2y}\,L^3\,{\phi_{2y}}^2}{1260\,G\,J} \\ & + \frac{L^2\,M_{2z}\,{\phi_{2y}}^2}{30\,G\,J} + \frac{L\,M_{2z}\,\phi_{2y}\,u_{2z}}{30\,G\,J} - \frac{F_{2x}\,L^3\,\phi_{2x}\,\phi_{2y}}{360\,\mathrm{E}\,I_y} + \frac{2\,F_{2y}\,L^2\,\phi_{2y}\,u_{2z}}{105\,G\,J} \end{aligned} \tag{39}$$

Substituting the boundary conditions $\phi_{2y} = 0, \phi_{2z} = 0$:

$$u_{2y} = \frac{F_{2y}\,L^3}{3\,\mathrm{E}\,I_z} + \frac{L^2\,M_{2z}}{2\,\mathrm{E}\,I_z} + \frac{M_{2z}\,{u_{2z}}^2}{10\,G\,J} + \frac{3\,F_{2y}\,L\,{u_{2z}}^2}{35\,G\,J} + \frac{F_{2y}\,L^3\,{\phi_{2x}}^2}{180\,\mathrm{E}\,I_y} \tag{40}$$

The u_{2y} consist out of the standard linear elastic components given by $\frac{F_{2y}\,L^3}{3\,\mathrm{E}\,I_z} + \frac{L^2\,M_{2z}}{2\,\mathrm{E}\,I_z}$. The additional terms are all elasto-kinematic terms that are quadratic in the DOFs and linear in the applied loads. These effects

can be seen as additional displacement due to a load and the flexibility that the sheet flexure has in deflected state.

Since a different coordinate system is used in [9], the expression for ϕ_{2z} is derived by taking ϕ_{2y} in the old coordinate system and subsequently applying the coordinate transformation. The ϕ_{2y} in the **old** coordinate system is given by [9]:

$$\begin{aligned}\phi_{2y} =&\frac{\phi_{2x}\, u_{2y}}{L} - \phi_{2x}\, \phi_{2z} + \frac{L\, M_{2y}}{\mathrm{E}\, I_y} - \frac{F_{2z}\, L^2}{2\,\mathrm{E}\, I_y} - \frac{F_{2z}\, {u_{2y}}^2}{10\, G\, J} + \frac{2\, L\, M_{2y}\, {\phi_{2z}}^2}{15\, G\, J} - \frac{F_{2z}\, L^2\, {\phi_{2z}}^2}{30\, G\, J} + \frac{M_{2y}\, {u_{2y}}^2}{5\, G\, J\, L} \\ &- \frac{M_{2y}\, \phi_{2z}\, u_{2y}}{5\, G\, J} + \frac{F_{2z}\, L\, \phi_{2z}\, u_{2y}}{30\, G\, J}\end{aligned} \tag{41}$$

Applying the coordinate transformation to obtain ϕ_{2z} in the current coordinate system:

$$\begin{aligned}\phi_{2z} =&\phi_{2x}\, \phi_{2y} + \frac{\phi_{2x}\, u_{2z}}{L} + \frac{L\, M_{2z}}{\mathrm{E}\, I_z} + \frac{F_{2y}\, L^2}{2\,\mathrm{E}\, I_z} + \frac{F_{2y}\, {u_{2z}}^2}{10\, G\, J} + \frac{2\, L\, M_{2z}\, {\phi_{2y}}^2}{15\, G\, J} + \frac{F_{2y}\, L^2\, {\phi_{2y}}^2}{30\, G\, J} + \frac{M_{2z}\, {u_{2z}}^2}{5\, G\, J\, L} \\ &+ \frac{M_{2z}\, \phi_{2y}\, u_{2z}}{5\, G\, J} + \frac{F_{2y}\, L\, \phi_{2y}\, u_{2z}}{30\, G\, J}\end{aligned} \tag{42}$$

Substituting the boundary conditions $\phi_{2y} = 0, \phi_{2z} = 0$:

$$0 = \frac{L\, M_{2z}}{\mathrm{E}\, I_z} + \frac{F_{2y}\, L^2}{2\,\mathrm{E}\, I_z} + \frac{\phi_{2x}\, u_{2z}}{L} + \frac{F_{2y}\, {u_{2z}}^2}{10\, G\, J} + \frac{M_{2z}\, {u_{2z}}^2}{5\, G\, J\, L} \tag{43}$$

The ϕ_{2z} consist out of the standard linear elastic components given by $\frac{L\, M_{2z}}{\mathrm{E}\, I_z} + \frac{F_{2y}\, L^2}{2\,\mathrm{E}\, I_z}$. Additionally the $\frac{\phi_{2x}\, u_{2z}}{L}$ is a kinematic term that takes into account shortening. The remaining terms are all elasto-kinematic that are quadratic in the DOFs and linear in the applied loads.

In order to simplify equation 40 and 43, the u_{2y} and ϕ_{2z} component are evaluated using the known boundary conditions u_{2z},ϕ_{2x}, and reaction forces F_{2y}, M_{2z} that obtained from ANSYS numerical simulations. The relative contributions of the components in u_{2y} and ϕ_{2y} are plotted to see if there are any components that can be neglected. For a slender sheet flexure with $L = 100$ mm, $W = 10$ mm, $t = 0.5$ mm, $R = 75$ mm, $E = 193$ GPa, $G = 74$ GPa and a prescribed rotation of $\theta = [0 - 5]°$ the contributing components are illustrated in Figure K.4a and B.1b.

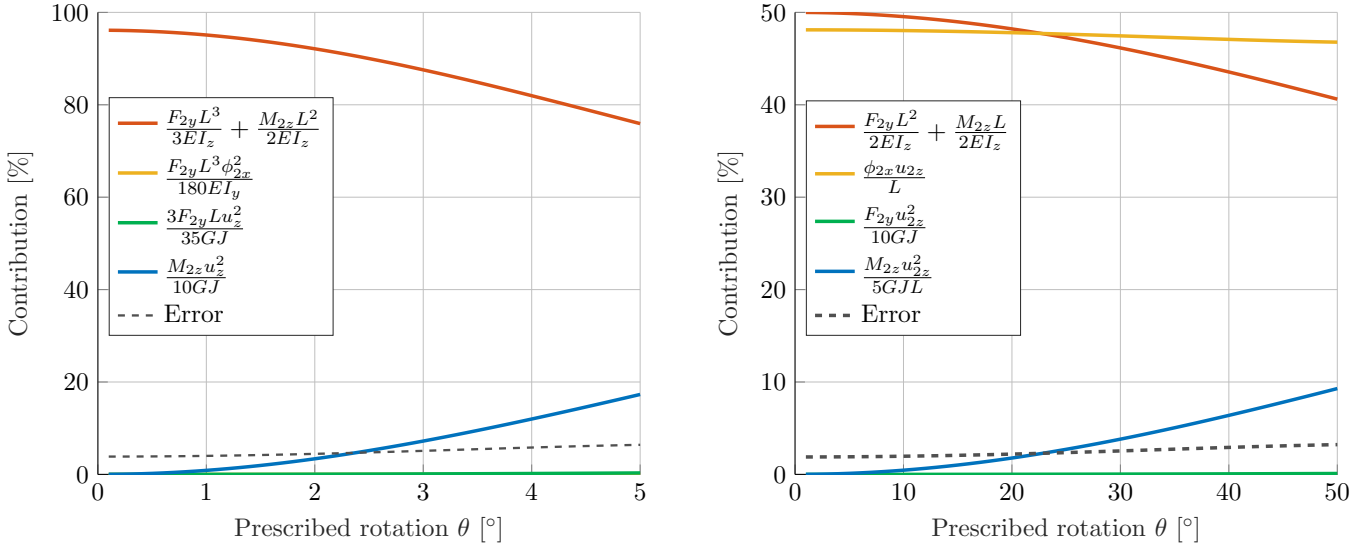

(a) Contributions to the u_{2y} error motion (b) Contributions to the ϕ_{2z} error motion

Figure B.1: Overview of components that contribute to the relevant error motions of M_{2z}

Rewriting the u_{2y} and ϕ_{2z} using only the contributing parts:

$$u_{2y} = \frac{F_{2y}\,L^3}{3\,\mathrm{E}\,I_z} + \frac{L^2\,M_{2z}}{2\,\mathrm{E}\,I_z} + \frac{M_{2z}\,{u_{2z}}^2}{10\,G\,J}, \quad 0 = \frac{\phi_{2x}\,u_{2z}}{L} + \frac{L\,M_{2z}}{\mathrm{E}\,I_z} + \frac{F_{2y}\,L^2}{2\,\mathrm{E}\,I_z} + \frac{M_{2z}\,{u_{2z}}^2}{5\,G\,J\,L} \tag{44}$$

Rewriting F_{2y} to the left hand side in both equations:

$$F_{2y} = \frac{3\,\mathrm{E}\,I_z\,u_{2y}}{L^3} - \frac{3\,M_{2z}}{2\,L} - \frac{3\,\mathrm{E}\,I_z\,M_{2z}\,{u_{2z}}^2}{10\,G\,J\,L^3}, \quad F_{2y} = -\frac{2\,M_{2z}}{L} - \frac{2\,\mathrm{E}\,I_z\,\phi_{2x}\,u_{2z}}{L^3} - \frac{2\,\mathrm{E}\,I_z\,M_{2z}\,{u_{2z}}^2}{5\,G\,J\,L^3} \tag{45}$$

Setting both expressions of F_{2y} equal to each other, allows for solving M_{2z}:

$$M_{2z} = -\frac{3\,\mathrm{E}\,I_z\,u_{2y}}{\frac{L^2}{2} + \frac{\mathrm{E}\,I_z\,{u_{2z}}^2}{10\,G\,J}} - \frac{2\,\mathrm{E}\,I_z\,\phi_{2x}\,u_{2z}}{\frac{L^2}{2} + \frac{\mathrm{E}\,I_z\,{u_{2z}}^2}{10\,G\,J}} \tag{46}$$

Substituting the M_{2z} into one of the F_{2y} equations yields:

$$F_{2y} = \frac{12\,\mathrm{E}\,I_z\,u_{2y}}{L^3} + \frac{6\,\mathrm{E}\,I_z\,\phi_{2x}\,u_{2z}}{L^3} \tag{47}$$

The obtained M_{2z} consist out of the standard linear elastic component (left) that now is also dependent on u_{2z}^2. Additionally, a completely new term (right) appears that depends on $\phi_{2x}u_{2z}$. These quadratic nonlinear terms are kinematic effects that play a role for larger rotations. If one would set the dependence of u_{2z} and ϕ_{2x} to zero one obtains the moment of the linear model $M_{2z} = -\frac{6\,\mathrm{E}\,I_z\,u_{2y}}{L^2}$. The F_{2y} consist out of the linear elastic component $\frac{12\,\mathrm{E}\,I_z\,u_{2y}}{L^3}$ and an additional kinematic term $\frac{6\,\mathrm{E}\,I_z\,\phi_{2x}\,u_{2z}}{L^3}$.

The analytical M_{2z} is compared with a numerical solution obtained in ANSYS mechanical. The M_{2z} of a sheet flexure with $L = 100$ mm, $W = 10$ mm, $t = 0.5$ mm, $R = 75$ mm, $E = 193$ GPa, $G = 74$ GPa is evaluated for $\theta = [0 - 5]°$ and is illustrated in Figure B.2a. The linear model fails to capture the behavior of M_{2z} for larger prescribed rotations. The nonlinear model closely matches the ANSYS results, even for larger rotations. The relative contributions to this nonlinear M_{2z} are depicted in Figure B.2b. The contribution of both the left and right term remain constant at the values of 42.8% and 57.2% respectively. This indicates that even for the smaller rotations the nonlinear model is required to accurately describe the M_{2z} moment.

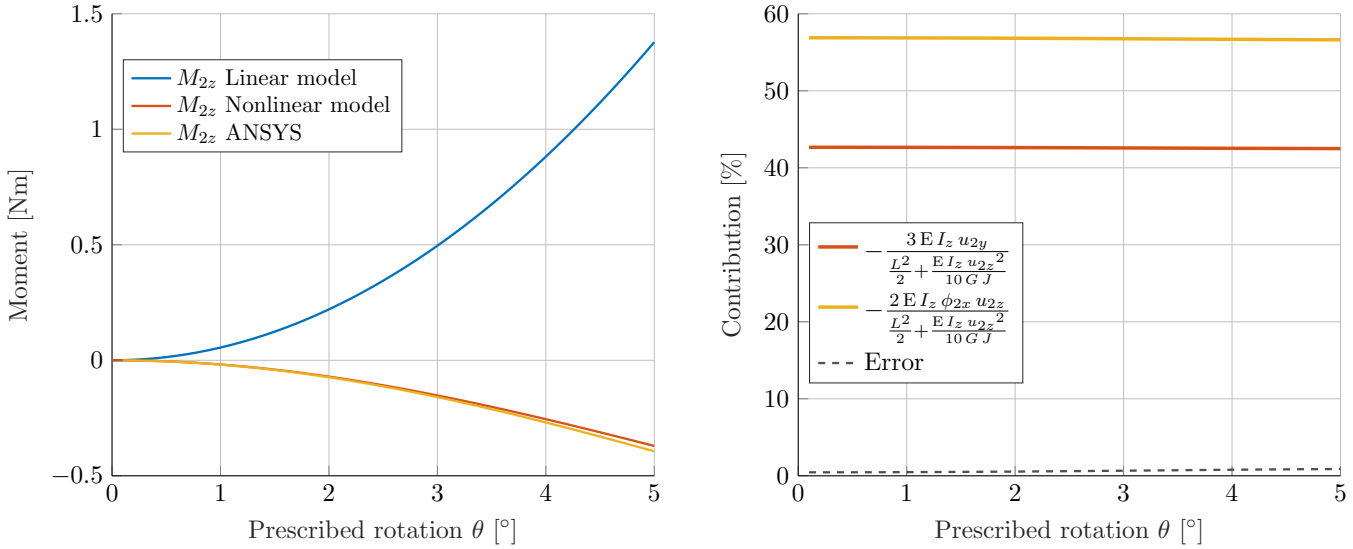

(a) Comparison of analytical and numerical M_{2z} (b) Contributions to the M_{2z}

Figure B.2: Overview of M_{2z} and its contributing components

Formulation of M_{2y}

The M_{2y} is obtained using the nonlinear model [10] that provides accurate stiffness predictions by accounting for bending, shear, elongation, torsion, and warping deformations. Since a different coordinate system is used in [10], the expression for M_{2y} is derived by taking M_{2z} in the old coordinate system and subsequently applying the coordinate transformation. The M_{2z} in the **old** coordinate system is given by [10]:

$$M_z = \frac{2\,F_{2x}\,L\,\phi_{2z}}{15} - \frac{F_{2x}\,u_{2y}}{10} + M_{2y}\,\phi_{2x}\left(\frac{w_4-1}{w_6}+1\right) + \frac{4\,\mathrm{E}\,I_z\,\phi_{2z}}{L} - \frac{6\,\mathrm{E}\,I_z\,u_{2y}}{L^2} - \frac{F_{2z}\,L\,\phi_{2x}\,w_5}{6\,w_6} \tag{48}$$

In this equation the w_i terms represent the warping coefficients that account for the warping deformation. As the analytical model represents a slender sheet flexure with a small W/L ratio where warping effects are neglected, these terms are set to 1:

$$M_{2z} = M_{2y}\,\phi_{2x} - \frac{F_{2x}\,u_{2y}}{10} + \frac{2\,F_{2x}\,L\,\phi_{2z}}{15} - \frac{F_{2z}\,L\,\phi_{2x}}{6} + \frac{4\,\mathrm{E}\,I_z\,\phi_{2z}}{L} - \frac{6\,\mathrm{E}\,I_z\,u_{2y}}{L^2} \tag{49}$$

Applying the coordinate transformation to obtain M_{2y} in the current coordinate system:

$$M_{2y} = \frac{F_{2x}\,u_{2z}}{10} - M_{2z}\,\phi_{2x} + \frac{2\,F_{2x}\,L\,\phi_{2y}}{15} - \frac{F_{2y}\,L\,\phi_{2x}}{6} + \frac{4\,\mathrm{E}\,I_y\,\phi_{2y}}{L} + \frac{6\,\mathrm{E}\,I_y\,u_{2z}}{L^2} \tag{50}$$

Substituting the boundary conditions $\phi_{2y}=0, \phi_{2z}=0$ and $F_{2x}=0$:

$$M_{2y} = \frac{6\,\mathrm{E}\,I_y\,u_{2z}}{L^2} - M_{2z}\,\phi_{2x} - \frac{F_{2y}\,L\,\phi_{2x}}{6} \tag{51}$$

The M_{2y} consist out of a linear component given by $\frac{6\,\mathrm{E}\,I_y\,u_{2z}}{L^2}$. Additionally, the term $-M_{2z}\phi_{2x}$ captures the load-stiffening behavior due to the applied rotation ϕ_{2x} and the moment M_{2z}. Similarly, the term $-\frac{F_{2y}\,L\,\phi_{2x}}{6}$ captures the load-stiffening behavior due to the applied rotation ϕ_{2x} and the force F_{2y}.

The analytical M_{2y} is compared with a numerical solution obtained in ANSYS mechanical. The M_{2y} of a sheet flexure with $L = 100$ mm, $W = 10$ mm, $t = 0.5$ mm, $R = 75$ mm, $E = 193$ GPa, $G = 74$ GPa is evaluated for $\theta = [0-5]^\circ$ and is illustrated in Figure B.3a. The linear model matches the ANSYS results for small rotations. The linear component initially contributes the most as shown in Figure B.3b. The contribution of the $-\frac{F_{2y}\,L\,\phi_{2x}}{6}$ load-stiffening term is negligible. In contrast to the linear model, the nonlinear model remains consistent with the ANSYS results even for larger rotations. This indicates that the additional nonlinear terms become significant at larger rotations.

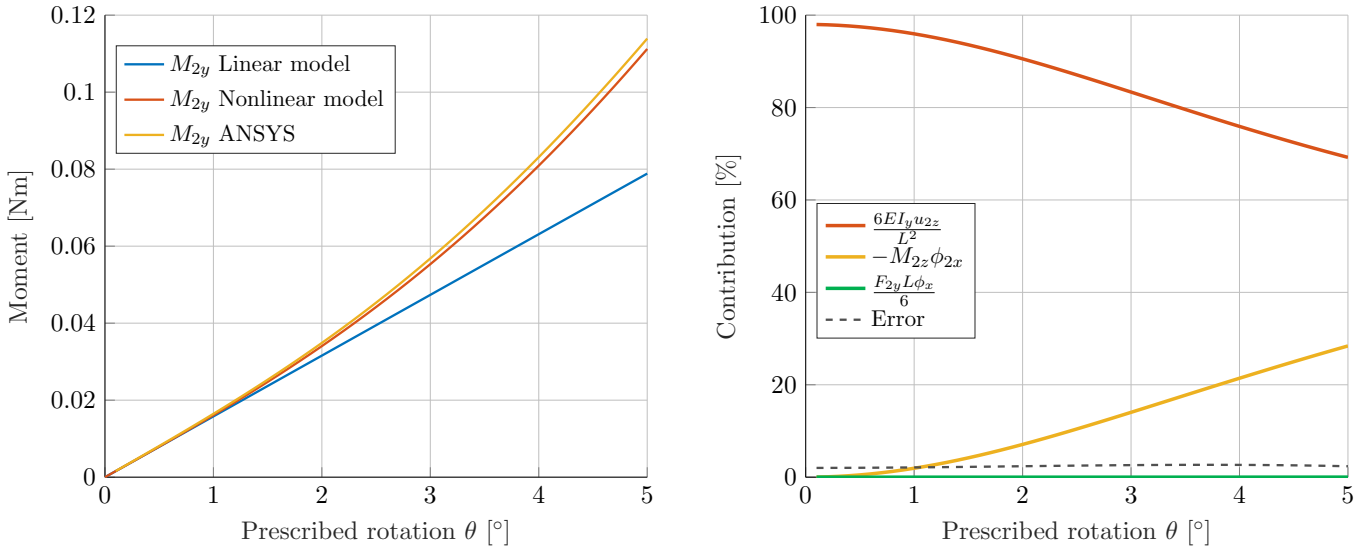

(a) Comparison of analytical and numerical M_{2y} (b) Contributions to the M_{2y}

Figure B.3: Overview of M_{2y} and its contributing components

Appendix C - Evaluating the analytical stress model for wider flexures

Appendix C evaluates the analytical stress model on a wider flexure with $W = 50$ mm. The analytical stress model that is developed in Chapter 2.4, is formulated for sheet flexures with a small W/L ratio. This ensures that bending deformations dominate over shear deformations while constrained warping is minimized. By applying the model to a wider flexure and comparing the analytical predictions with numerical solutions, valuable insights can be obtained regarding the model's performance and its applicability.

The axial stress $\sigma_{\bar{x}\bar{x}}$ is computed for the flexure where $W = 10$ mm and $W = 50$ mm, using the following input parameters: $L = 100$ mm, $t = 0.5$ mm, $R = 75$ mm, $E = 193$ GPa, $G = 74$ GPa and a prescribed rotation of $\theta = [0 - 5]°$. Note that the flexure with $W = 10$ mm is identical to that in Chapter 2.7.

Axial stress results

The analytical and numerical results are presented in Figure C.1. The figures contain an additional axial stress result labeled as "Analytical, ANSYS moments". This model uses the bending moments obtained from the ANSYS simulations. Instead of substituting the input parameters in the nonlinear equations of M_{2y} and M_{2z}, these moments are now obtained through ANSYS and substituted in the analytical stress model to compute the axial stress. As shown in Figure C.1a, the nonlinear model and analytical model with ANSYS moments are very similar. This is because the derived nonlinear moments M_{2y} and M_{2z} accurately capture the behavior of the slender flexure.

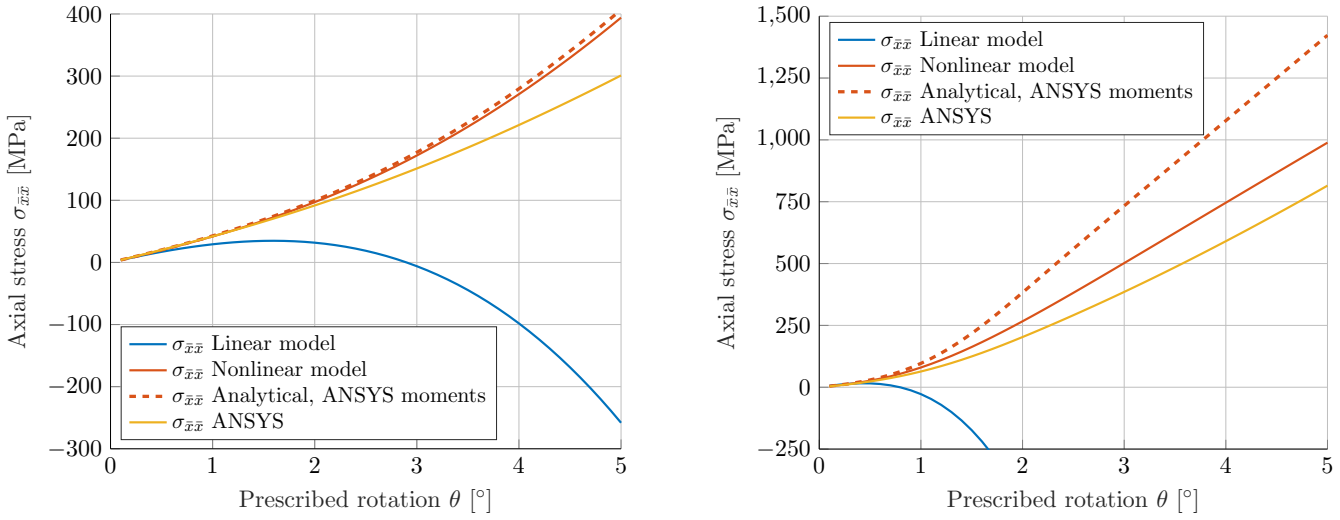

(a) $W = 10$ mm (b) $W = 50$ mm

Figure C.1: Comparison of axial stress evaluated in point A of the sheet flexure

In contrast, for the wider flexure Figure C.1b demonstrates a significant difference between the nonlinear model and analytical model with ANSYS moments. This difference arises from the assumptions of the small W/L ratio, that is used in the derivation of the nonlinear model. If the nonlinear model were reformulated to account for larger W/L ratios, the results would likely align more closely. However, there is still a large deviation between the analytical model with ANSYS moments and the ANSYS numerical stress results. In other words, even if the nonlinear model is reformulated with M_{2y} and M_{2z} suited for larger widths, there is still a large difference between the analytical stress model and the ANSYS simulations. This indicates that there are additional effects that play a role for larger flexure widths that are not included in the analytical stress model.

Contributing components to the axial stress

The relative contributions for the flexure with $W = 10$ mm are given in Figure C.2a. The contributions of the bending moments are calculated using the nonlinear model. The absolute error is defined as the difference between the stress predicted by the nonlinear model and the stress obtained from the ANSYS simulation. The relative error, plotted in Figure C.2a, is calculated by dividing the absolute error by the stress obtained from the ANSYS simulations and expressing it as a percentage.

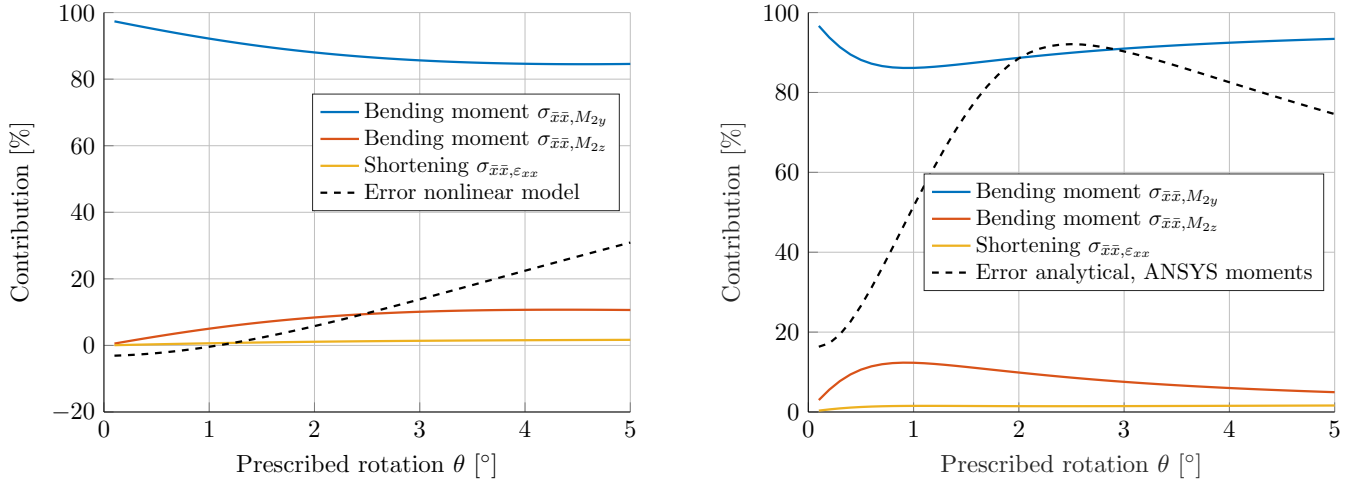

(a) $W = 10$ mm | nonlinear model (b) $W = 50$ mm | analytical, ANSYS moments

Figure C.2: Contributions to the axial stress of analytical stress in point A

The relative contributions for the flexure with $W = 50$ mm are given in Figure C.2b. As the derived nonlinear model is not accurate for wider flexures this figure uses analytical model with bending moments obtained from the ANSYS simulations. Therefore, the absolute error is defined as the difference between the stress predicted by analytical model with ANSYS moments and the stress obtained from the ANSYS simulation. The relative error, plotted in Figure C.2b, is calculated by dividing the absolute error by the stress obtained from the ANSYS simulations and expressing it as a percentage. The absolute error increases as the prescribed rotation grows. However, the increase in stress is larger than the increase in absolute error. As a result the relative error rises initially but eventually decreases. This large relative error indicates that analytical stress model with ANSYS moments is incomplete for larger widths. Furthermore, it can be noted that even for the wider flexure, the contribution of shortening remains relatively small compared to the contribution of the bending moments.

Appendix D - Python code for CAD modeling in ANSYS SpaceClaim

Appendix D provides the Python code for generating the tapered and bow-tie flexure geometry in SpaceClaim. Additionally, it provides a step-by-step guide to run these scripts.

Step by step guide to run the ANSYS SpaceClaim python scripts:

1. Open SpaceClaim in ANSYS workbench and navigate to **File** > **New** > **Script**.
2. In the Script Editor, open the dropdown menu on the **Save** button.
3. Scripts can be saved to Groups in order to store them in the model. Check **Save Script to Group**.
4. Click the **Save** button to create the group and add it to the **Scripts** folder in the Groups Pane.
5. To convert the script variables into parameters that are recognizable by ANSYS Workbench, right-click in the **Groups** tab, select **Add Parameter**, and rename the parameters to **L**, **W**, **t**, **Offset**, **Offset_finemesh**, and **eta**.
6. Run the script to create the model. Upon returning to ANSYS Workbench, the created parameters will be visible and can be edited/updated directly from there.

In order to create different CAD models, one can use the record feature to observe how various modeling steps within SpaceClaim translate to Python code. In ANSYS workbench, each parameter update will recreate the model from scratch. Therefore, ANSYS mechanical must be configured to use named selections defined by the code. Otherwise, the assigned material and geometric selections will be lost with every parameter update. Additionally, it is highly recommended to view the SimuTech tutorial on how to use scripting features for CAD design iterations in ANSYS SpaceClaim: `https://youtu.be/Av_1Jo1IjkI?si=-YgHH96Yi2P2Vcqn`

Tapered flexure

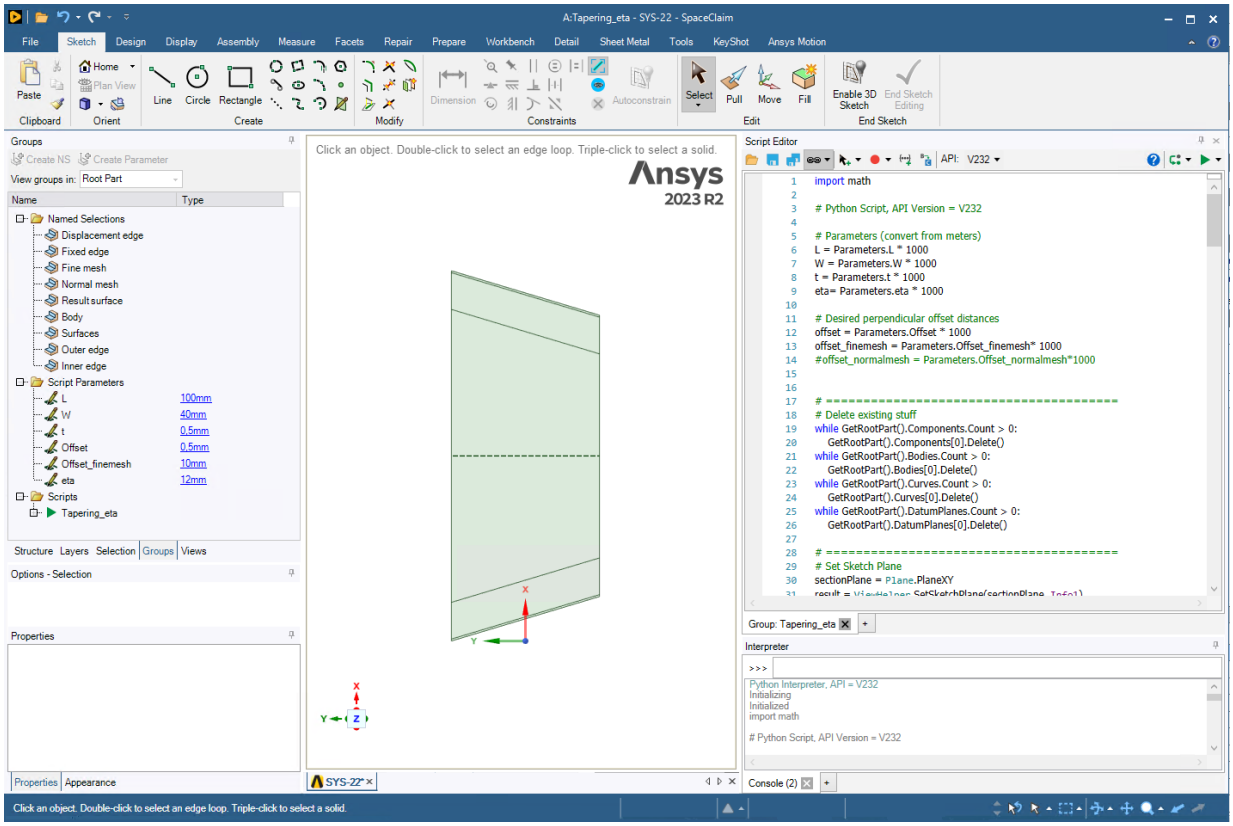

Figure D.1: ANSYS SpaceClaim interface showing the Groups pane with named selections, script parameters, and script (left); the generated tapered flexure CAD model (center); and the Script Editor (right).

```
import math
# Python Script, API Version = V232
# Parameters (convert from meters)
L = Parameters.L * 1000
W = Parameters.W * 1000
t = Parameters.t * 1000
eta= Parameters.eta * 1000

# Desired perpendicular offset distances
offset = Parameters.Offset * 1000
offset_finemesh = Parameters.Offset_finemesh* 1000

# Delete existing stuff
while GetRootPart().Components.Count > 0:
    GetRootPart().Components[0].Delete()
while GetRootPart().Bodies.Count > 0:
    GetRootPart().Bodies[0].Delete()
while GetRootPart().Curves.Count > 0:
    GetRootPart().Curves[0].Delete()
while GetRootPart().DatumPlanes.Count > 0:
    GetRootPart().DatumPlanes[0].Delete()

# Set Sketch Plane
sectionPlane = Plane.PlaneXY
result = ViewHelper.SetSketchPlane(sectionPlane, Info1)
# Naming convention:
#     A          C
#     F          G               #offset
#     H          I               #offset fine mesh
#     B          D               #mirror line

# Step 1: defining known points
A_x = L/2
A_y = 0
B_x = 0
B_y = 0
C_x = L/2 - eta
C_y = W
D_x = 0
D_y = W

# Creating the points (outline) by transforming
PointA = Point2D.Create(MM(A_x + L/2), MM(A_y + W/2))
PointB = Point2D.Create(MM(B_x + L/2 ), MM(B_y + W / 2))
PointC = Point2D.Create(MM(C_x + L/2), MM(W / 2 - C_y))
PointD = Point2D.Create(MM(D_x + L/2 ), MM(W / 2 - D_y))

# Drawing the general outline lines
result = SketchLine.Create(PointA, PointB)
result =SketchLine.Create(PointB, PointD,True) #construction line
result = SketchLine.Create(PointC, PointD)
result = SketchLine.Create(PointA, PointC)

# Calculate the angle of the AC line
delta_x_AC = (L - (L - eta))
delta_y_AC = (W / 2 - (-W / 2))
theta_AC = math.atan2(delta_y_AC, delta_x_AC)  # Angle of the AC line in radians

# Calculate the horizontal distance to keep the offset perpendicular (keeping y constant)
def calc_x_offset(d, theta):
    return d / math.sin(theta)  # Adjust only in x-direction based on angle

# Calculate the x offsets for each distance
x_offset = calc_x_offset(offset, theta_AC)
x_finemesh = calc_x_offset(offset_finemesh, theta_AC)

# Create new points with the x-offset only (y remains the same)
E_x =  L/2- x_offset
E_y = 0
F_x =  L/2 - eta - x_offset
F_y = W
PointE = Point2D.Create(MM(E_x + L/2 ), MM(E_y + W / 2))
PointF = Point2D.Create(MM(F_x + L/2 ), MM(W/2 -F_y))
```

```
# Drawing the finemesh offset (keeping y same, adjusting x)
G_x =  L/2- x_finemesh
G_y = 0
H_x =  L/2 - eta - x_finemesh
H_y = W
PointG = Point2D.Create(MM(G_x + L/2 ), MM(G_y + W / 2))
PointH = Point2D.Create(MM(H_x + L/2 ), MM(W/2 -H_y))
result = SketchLine.Create(PointE, PointF)
result = SketchLine.Create(PointG, PointH)

# Creating mirror (lower side of flexure)
selection = Selection.Create(GetRootPart().DatumPlanes[0].Curves[0])
mirrorPlane = Selection.Create(GetRootPart().DatumPlanes[0].Curves[1])
options = MoveOptions()
options.Copy = True
options.SnapAssociatedVertices = False
result = Move.MirrorEntities(selection, mirrorPlane, options)

selection = Selection.Create(GetRootPart().DatumPlanes[0].Curves[2])
mirrorPlane = Selection.Create(GetRootPart().DatumPlanes[0].Curves[1])
options = MoveOptions()
options.Copy = True
options.SnapAssociatedVertices = False
result = Move.MirrorEntities(selection, mirrorPlane, options)

selection = Selection.Create(GetRootPart().DatumPlanes[0].Curves[3])
mirrorPlane = Selection.Create(GetRootPart().DatumPlanes[0].Curves[1])
options = MoveOptions()
options.Copy = True
options.SnapAssociatedVertices = False
result = Move.MirrorEntities(selection, mirrorPlane, options)

selection = Selection.Create(GetRootPart().DatumPlanes[0].Curves[4])
mirrorPlane = Selection.Create(GetRootPart().DatumPlanes[0].Curves[1])
options = MoveOptions()
options.Copy = True
options.SnapAssociatedVertices = False
result = Move.MirrorEntities(selection, mirrorPlane, options)

selection = Selection.Create(GetRootPart().DatumPlanes[0].Curves[5])
mirrorPlane = Selection.Create(GetRootPart().DatumPlanes[0].Curves[1])
options = MoveOptions()
options.Copy = True
options.SnapAssociatedVertices = False
result = Move.MirrorEntities(selection, mirrorPlane, options)

# Solidify Sketch
mode = InteractionMode.Solid
result = ViewHelper.SetViewMode(mode, Info2)

# Creating named selections
sel =EdgeSelection.Create(GetRootPart().Bodies[0].Edges[15])
sel.CreateAGroup("Displacement edge")

sel =EdgeSelection.Create(GetRootPart().Bodies[0].Edges[5])
sel.CreateAGroup("Fixed edge")

sel = FaceSelection.Create([GetRootPart().Bodies[0].Faces[0],
    GetRootPart().Bodies[0].Faces[1],
    GetRootPart().Bodies[0].Faces[3],
    GetRootPart().Bodies[0].Faces[4]])
sel.CreateAGroup("Fine mesh")

sel = FaceSelection.Create(GetRootPart().Bodies[0].Faces[2])
sel.CreateAGroup("Normal mesh")

sel = FaceSelection.Create([GetRootPart().Bodies[0].Faces[2],
    GetRootPart().Bodies[0].Faces[0],
    GetRootPart().Bodies[0].Faces[3]])
sel.CreateAGroup("Result surface")

sel =BodySelection.Create(GetRootPart().Bodies[0])
```

```
sel.CreateAGroup("Body")

sel = FaceSelection.Create([GetRootPart().Bodies[0].Faces[2],
    GetRootPart().Bodies[0].Faces[0],
    GetRootPart().Bodies[0].Faces[3],
    GetRootPart().Bodies[0].Faces[1],
    GetRootPart().Bodies[0].Faces[4]])
sel.CreateAGroup("Surfaces")

sel =EdgeSelection.Create([GetRootPart().Bodies[0].Edges[4],
    GetRootPart().Bodies[0].Edges[1],
    GetRootPart().Bodies[0].Edges[9],
    GetRootPart().Bodies[0].Edges[8],
    GetRootPart().Bodies[0].Edges[13],
    GetRootPart().Bodies[0].Edges[16]])
sel.CreateAGroup("Outer edge")

sel =EdgeSelection.Create([GetRootPart().Bodies[0].Edges[6],
    GetRootPart().Bodies[0].Edges[3],
    GetRootPart().Bodies[0].Edges[10],
    GetRootPart().Bodies[0].Edges[11],
    GetRootPart().Bodies[0].Edges[14],
    GetRootPart().Bodies[0].Edges[17]])
sel.CreateAGroup("Inner edge")

# Applying thickness to surface
result = Midsurface.Convert(Selection.CreateByGroups(SelectionType.Primary, "Body"), MM(t))
```

Bow-tie Flexure

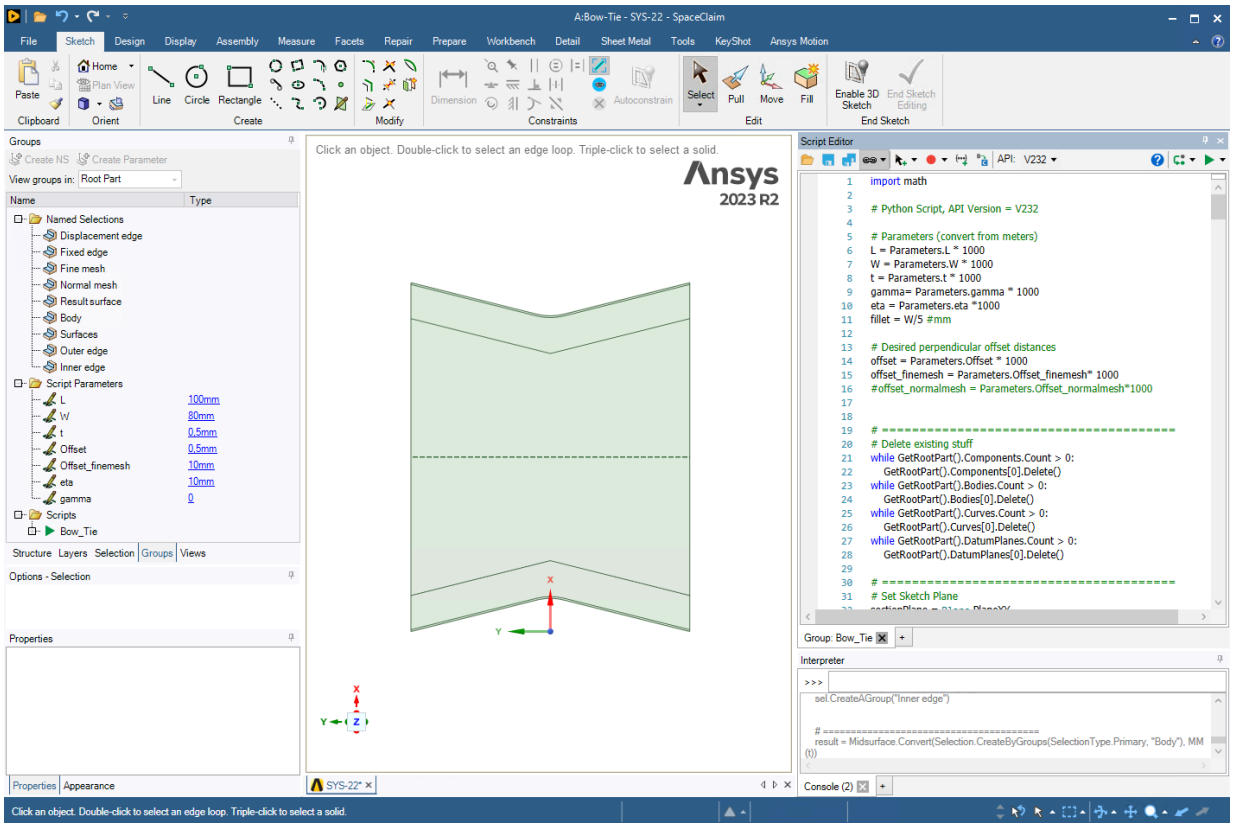

Figure D.2: ANSYS SpaceClaim interface showing the Groups pane with named selections, script parameters, and script (left); the generated bow-tie flexure CAD model (center); and the Script Editor (right).

```
import math
# Python Script, API Version = V232
# Parameters (convert from meters)
L = Parameters.L * 1000
W = Parameters.W * 1000
t = Parameters.t * 1000
gamma= Parameters.gamma * 1000  #set to 0 for bow-tie flexure
eta = Parameters.eta *1000
fillet = W/5 #dynamic fillet

# Desired perpendicular offset distances
offset = Parameters.Offset * 1000
offset_finemesh = Parameters.Offset_finemesh* 1000
#offset_normalmesh = Parameters.Offset_normalmesh*1000

# Delete existing stuff
while GetRootPart().Components.Count > 0:
    GetRootPart().Components[0].Delete()
while GetRootPart().Bodies.Count > 0:
    GetRootPart().Bodies[0].Delete()
while GetRootPart().Curves.Count > 0:
    GetRootPart().Curves[0].Delete()
while GetRootPart().DatumPlanes.Count > 0:
    GetRootPart().DatumPlanes[0].Delete()

# Set Sketch Plane
sectionPlane = Plane.PlaneXY
result = ViewHelper.SetSketchPlane(sectionPlane, Info1)

# Naming convention:
#     A          C
#     F          G                        #offset
#     H          I                        #offset fine mesh
#     B          D                        #mirror line!!

# Step 1: defining known points
A_x = L/2
A_y = 0
B_x = 0
B_y = 0
C_x = L/2 - gamma
C_y = W
M_y = W/2  # y-coordinate of point C
D_x = 0
D_y = W
M_x = L/2 - eta

# unknown points: y_center, Radius using derived equations:
#radius = ((A_x - M_x)**2 + (A_y - M_y)**2)/(2*A_x - 2*M_x)
#y_center = W/2

# Creating the points  (while shifting the CS back to normal)
#PointP = Point2D.Create(MM(M_x + radius+ L/2), MM(M_y-W/2))
PointA = Point2D.Create(MM(L), MM(W/2))
PointB = Point2D.Create(MM(L/2), MM(W/2))    #is now centerline!
PointC = Point2D.Create(MM(L/2 + C_x), MM(-W/2))
PointD = Point2D.Create(MM(L/2), MM(-W/2))
PointM = Point2D.Create(MM(L/2 + M_x), MM(M_y-W/2))
PointN = Point2D.Create(MM(L/2 + M_x+1), MM(M_y-W/2))

# Drawing the general outline lines
result = SketchLine.Create(PointA, PointB)
result = SketchLine.Create(PointC, PointD)
result = SketchLine.Create(PointC, PointM)
result =SketchLine.Create(PointB, PointD,True) #construction line
result = SketchLine.Create(PointA, PointM)

# Creating fine mesh offset, because that one does not have a radius (otherwise we get invalid
    sketch for smaller widths)
curvesToOffset = Selection.Create([GetRootPart().DatumPlanes[0].Curves[4],
    GetRootPart().DatumPlanes[0].Curves[2]])
offsetDistance = MM(-offset_finemesh)
result = SketchOffsetCurve.Create(curvesToOffset, offsetDistance)
```

```
# Rules for handling various configurations of eta and gamma
if eta <= gamma:
    # Trim Sketch Curve
    curveSelPoint = SelectionPoint.Create(GetRootPart().DatumPlanes[0].Curves[5], 0)
    result = TrimSketchCurve.Execute(curveSelPoint)

    # Trim Sketch Corner
    curveOneSelPoint = SelectionPoint.Create(GetRootPart().DatumPlanes[0].Curves[6], 0)
    curveTwoSelPoint = SelectionPoint.Create(GetRootPart().DatumPlanes[0].Curves[1],0)
    options = SketchCornerOptions()
    options.TrimOneSide = True
    result = SketchCorner.Create(curveOneSelPoint, curveTwoSelPoint, options)

    # Create 2D Round FORMAT: looks like it is the 0 is starting point on  lenght of the line , but
    radius will be determined by the Sketch2DRound
    curveSelPoint1 = SelectionPoint.Create(GetRootPart().DatumPlanes[0].Curves[4], 0.000)
    curveSelPoint2 = SelectionPoint.Create(GetRootPart().DatumPlanes[0].Curves[2], 0.000)
    result = Sketch2DRound.Create(curveSelPoint1, curveSelPoint2, MM(fillet))

    # Creating Offset Sketch Curve
    curvesToOffset = Selection.Create([GetRootPart().DatumPlanes[0].Curves[4],
        GetRootPart().DatumPlanes[0].Curves[7],
        GetRootPart().DatumPlanes[0].Curves[2]])
    offsetDistance = MM(-offset)
    result = SketchOffsetCurve.Create(curvesToOffset, offsetDistance)

    # Trim Sketch Curve
    curveSelPoint = SelectionPoint.Create(GetRootPart().DatumPlanes[0].Curves[8], 0)
    result = TrimSketchCurve.Execute(curveSelPoint)

    # Trim Sketch Corner
    curveOneSelPoint = SelectionPoint.Create(GetRootPart().DatumPlanes[0].Curves[10], 0)
    curveTwoSelPoint = SelectionPoint.Create(GetRootPart().DatumPlanes[0].Curves[1], 0)
    options = SketchCornerOptions()
    options.TrimOneSide = True
    result = SketchCorner.Create(curveOneSelPoint, curveTwoSelPoint, options)

    # Trim Sketch Curve
    #curveSelPoint = SelectionPoint.Create(GetRootPart().DatumPlanes[0].Curves[10], 0)
    #result = TrimSketchCurve.Execute(curveSelPoint)

    # Creating mirror (lower side of flexure)
    selection = Selection.Create(GetRootPart().DatumPlanes[0].Curves[0])
    mirrorPlane = Selection.Create(GetRootPart().DatumPlanes[0].Curves[3])
    options = MoveOptions()
    options.Copy = True
    options.SnapAssociatedVertices = False
    result = Move.MirrorEntities(selection, mirrorPlane, options)

    selection = Selection.Create(GetRootPart().DatumPlanes[0].Curves[1])
    mirrorPlane = Selection.Create(GetRootPart().DatumPlanes[0].Curves[3])
    options = MoveOptions()
    options.Copy = True
    options.SnapAssociatedVertices = False
    result = Move.MirrorEntities(selection, mirrorPlane, options)

    selection = Selection.Create(GetRootPart().DatumPlanes[0].Curves[2])
    mirrorPlane = Selection.Create(GetRootPart().DatumPlanes[0].Curves[3])
    options = MoveOptions()
    options.Copy = True
    options.SnapAssociatedVertices = False
    result = Move.MirrorEntities(selection, mirrorPlane, options)

    selection = Selection.Create(GetRootPart().DatumPlanes[0].Curves[4])
    mirrorPlane = Selection.Create(GetRootPart().DatumPlanes[0].Curves[3])
    options = MoveOptions()
    options.Copy = True
    options.SnapAssociatedVertices = False
    result = Move.MirrorEntities(selection, mirrorPlane, options)

    selection = Selection.Create(GetRootPart().DatumPlanes[0].Curves[5])
    mirrorPlane = Selection.Create(GetRootPart().DatumPlanes[0].Curves[3])
```

```
options = MoveOptions()
options.Copy = True
options.SnapAssociatedVertices = False
result = Move.MirrorEntities(selection, mirrorPlane, options)

selection = Selection.Create(GetRootPart().DatumPlanes[0].Curves[6])
mirrorPlane = Selection.Create(GetRootPart().DatumPlanes[0].Curves[3])
options = MoveOptions()
options.Copy = True
options.SnapAssociatedVertices = False
result = Move.MirrorEntities(selection, mirrorPlane, options)

selection = Selection.Create(GetRootPart().DatumPlanes[0].Curves[7])
mirrorPlane = Selection.Create(GetRootPart().DatumPlanes[0].Curves[3])
options = MoveOptions()
options.Copy = True
options.SnapAssociatedVertices = False
result = Move.MirrorEntities(selection, mirrorPlane, options)

selection = Selection.Create(GetRootPart().DatumPlanes[0].Curves[8])
mirrorPlane = Selection.Create(GetRootPart().DatumPlanes[0].Curves[3])
options = MoveOptions()
options.Copy = True
options.SnapAssociatedVertices = False
result = Move.MirrorEntities(selection, mirrorPlane, options)

selection = Selection.Create(GetRootPart().DatumPlanes[0].Curves[9])
mirrorPlane = Selection.Create(GetRootPart().DatumPlanes[0].Curves[3])
options = MoveOptions()
options.Copy = True
options.SnapAssociatedVertices = False
result = Move.MirrorEntities(selection, mirrorPlane, options)

selection = Selection.Create(GetRootPart().DatumPlanes[0].Curves[10])
mirrorPlane = Selection.Create(GetRootPart().DatumPlanes[0].Curves[3])
options = MoveOptions()
options.Copy = True
options.SnapAssociatedVertices = False
result = Move.MirrorEntities(selection, mirrorPlane, options)

selection = Selection.Create(GetRootPart().DatumPlanes[0].Curves[11])
mirrorPlane = Selection.Create(GetRootPart().DatumPlanes[0].Curves[3])
options = MoveOptions()
options.Copy = True
options.SnapAssociatedVertices = False
result = Move.MirrorEntities(selection, mirrorPlane, options)

# Solidify Sketch
mode = InteractionMode.Solid
result = ViewHelper.SetViewMode(mode, Info2)

# Creating named selections
sel =EdgeSelection.Create([GetRootPart().Bodies[0].Edges[27],
    GetRootPart().Bodies[0].Edges[23],
    GetRootPart().Bodies[0].Edges[26]])
#sel = Selection.Create(Edge1)
sel.CreateAGroup("Displacement edge")

sel = EdgeSelection.Create([GetRootPart().Bodies[0].Edges[10],
    GetRootPart().Bodies[0].Edges[9],
    GetRootPart().Bodies[0].Edges[8]])
#sel = Selection.Create(Edge2)
sel.CreateAGroup("Fixed edge")

sel = FaceSelection.Create([GetRootPart().Bodies[0].Faces[0],
    GetRootPart().Bodies[0].Faces[1],
    GetRootPart().Bodies[0].Faces[3],
    GetRootPart().Bodies[0].Faces[4]])
sel.CreateAGroup("Fine mesh")

sel = FaceSelection.Create(GetRootPart().Bodies[0].Faces[2])
sel.CreateAGroup("Normal mesh")
```

```
    sel = FaceSelection.Create([GetRootPart().Bodies[0].Faces[2],
        GetRootPart().Bodies[0].Faces[0],
        GetRootPart().Bodies[0].Faces[3]])
    sel.CreateAGroup("Result surface")

    sel =BodySelection.Create(GetRootPart().Bodies[0])
    sel.CreateAGroup("Body")

    sel = FaceSelection.Create([GetRootPart().Bodies[0].Faces[2],
        GetRootPart().Bodies[0].Faces[0],
        GetRootPart().Bodies[0].Faces[3],
        GetRootPart().Bodies[0].Faces[1],
        GetRootPart().Bodies[0].Faces[4]])
    sel.CreateAGroup("Surfaces")

    sel =EdgeSelection.Create([GetRootPart().Bodies[0].Edges[7],
        GetRootPart().Bodies[0].Edges[1],
        GetRootPart().Bodies[0].Edges[14],
        GetRootPart().Bodies[0].Edges[13],
        GetRootPart().Bodies[0].Edges[19],
        GetRootPart().Bodies[0].Edges[24]])
    sel.CreateAGroup("Outer edge")

    sel =EdgeSelection.Create([GetRootPart().Bodies[0].Edges[25],
        GetRootPart().Bodies[0].Edges[20],
        GetRootPart().Bodies[0].Edges[16],
        GetRootPart().Bodies[0].Edges[15],
        GetRootPart().Bodies[0].Edges[5],
        GetRootPart().Bodies[0].Edges[11]])
    sel.CreateAGroup("Inner edge")

    # Applying thickness to surface
    result = Midsurface.Convert(Selection.CreateByGroups(SelectionType.Primary, "Body"), MM(t))

# Rules for handling various configurations of eta and gamma
if gamma < eta:
    # Trim Sketch Curve
    curveSelPoint = SelectionPoint.Create(GetRootPart().DatumPlanes[0].Curves[5], 0)
    result = TrimSketchCurve.Execute(curveSelPoint)

    # Trim Sketch Curve when eta is smaller than gamma
    curveSelPoint = SelectionPoint.Create(GetRootPart().DatumPlanes[0].Curves[6], 0)
    result = TrimSketchCurve.Execute(curveSelPoint)

    # Create 2D Round FORMAT: looks like it is the 0 is starting point on  lenght of the line , but
    radius will be determined by the Sketch2DRound
    curveSelPoint1 = SelectionPoint.Create(GetRootPart().DatumPlanes[0].Curves[4], 0.000)
    curveSelPoint2 = SelectionPoint.Create(GetRootPart().DatumPlanes[0].Curves[2], 0.000)
    result = Sketch2DRound.Create(curveSelPoint1, curveSelPoint2, MM(fillet))

    # Creating Offset Sketch Curve
    curvesToOffset = Selection.Create([GetRootPart().DatumPlanes[0].Curves[4],
        GetRootPart().DatumPlanes[0].Curves[7],
        GetRootPart().DatumPlanes[0].Curves[2]])
    offsetDistance = MM(-offset)
    result = SketchOffsetCurve.Create(curvesToOffset, offsetDistance)

    # Trim Sketch Curve
    curveSelPoint = SelectionPoint.Create(GetRootPart().DatumPlanes[0].Curves[8], 0)
    result = TrimSketchCurve.Execute(curveSelPoint)

    # Trim Sketch Curve
    curveSelPoint = SelectionPoint.Create(GetRootPart().DatumPlanes[0].Curves[10], 0)
    result = TrimSketchCurve.Execute(curveSelPoint)

    # Creating mirror (lower side of flexure)
    selection = Selection.Create(GetRootPart().DatumPlanes[0].Curves[0])
    mirrorPlane = Selection.Create(GetRootPart().DatumPlanes[0].Curves[3])
    options = MoveOptions()
    options.Copy = True
    options.SnapAssociatedVertices = False
    result = Move.MirrorEntities(selection, mirrorPlane, options)
```

```
selection = Selection.Create(GetRootPart().DatumPlanes[0].Curves[1])
mirrorPlane = Selection.Create(GetRootPart().DatumPlanes[0].Curves[3])
options = MoveOptions()
options.Copy = True
options.SnapAssociatedVertices = False
result = Move.MirrorEntities(selection, mirrorPlane, options)

selection = Selection.Create(GetRootPart().DatumPlanes[0].Curves[2])
mirrorPlane = Selection.Create(GetRootPart().DatumPlanes[0].Curves[3])
options = MoveOptions()
options.Copy = True
options.SnapAssociatedVertices = False
result = Move.MirrorEntities(selection, mirrorPlane, options)

selection = Selection.Create(GetRootPart().DatumPlanes[0].Curves[4])
mirrorPlane = Selection.Create(GetRootPart().DatumPlanes[0].Curves[3])
options = MoveOptions()
options.Copy = True
options.SnapAssociatedVertices = False
result = Move.MirrorEntities(selection, mirrorPlane, options)

selection = Selection.Create(GetRootPart().DatumPlanes[0].Curves[5])
mirrorPlane = Selection.Create(GetRootPart().DatumPlanes[0].Curves[3])
options = MoveOptions()
options.Copy = True
options.SnapAssociatedVertices = False
result = Move.MirrorEntities(selection, mirrorPlane, options)

selection = Selection.Create(GetRootPart().DatumPlanes[0].Curves[6])
mirrorPlane = Selection.Create(GetRootPart().DatumPlanes[0].Curves[3])
options = MoveOptions()
options.Copy = True
options.SnapAssociatedVertices = False
result = Move.MirrorEntities(selection, mirrorPlane, options)

selection = Selection.Create(GetRootPart().DatumPlanes[0].Curves[7])
mirrorPlane = Selection.Create(GetRootPart().DatumPlanes[0].Curves[3])
options = MoveOptions()
options.Copy = True
options.SnapAssociatedVertices = False
result = Move.MirrorEntities(selection, mirrorPlane, options)

selection = Selection.Create(GetRootPart().DatumPlanes[0].Curves[8])
mirrorPlane = Selection.Create(GetRootPart().DatumPlanes[0].Curves[3])
options = MoveOptions()
options.Copy = True
options.SnapAssociatedVertices = False
result = Move.MirrorEntities(selection, mirrorPlane, options)

selection = Selection.Create(GetRootPart().DatumPlanes[0].Curves[9])
mirrorPlane = Selection.Create(GetRootPart().DatumPlanes[0].Curves[3])
options = MoveOptions()
options.Copy = True
options.SnapAssociatedVertices = False
result = Move.MirrorEntities(selection, mirrorPlane, options)

selection = Selection.Create(GetRootPart().DatumPlanes[0].Curves[10])
mirrorPlane = Selection.Create(GetRootPart().DatumPlanes[0].Curves[3])
options = MoveOptions()
options.Copy = True
options.SnapAssociatedVertices = False
result = Move.MirrorEntities(selection, mirrorPlane, options)

selection = Selection.Create(GetRootPart().DatumPlanes[0].Curves[11])
mirrorPlane = Selection.Create(GetRootPart().DatumPlanes[0].Curves[3])
options = MoveOptions()
options.Copy = True
options.SnapAssociatedVertices = False
result = Move.MirrorEntities(selection, mirrorPlane, options)

# Solidify Sketch
mode = InteractionMode.Solid
result = ViewHelper.SetViewMode(mode, Info2)
```

```
# Creating named selections
sel =EdgeSelection.Create([GetRootPart().Bodies[0].Edges[27],
    GetRootPart().Bodies[0].Edges[23],
    GetRootPart().Bodies[0].Edges[26]])
#sel = Selection.Create(Edge1)
sel.CreateAGroup("Displacement edge")

sel = EdgeSelection.Create([GetRootPart().Bodies[0].Edges[10],
    GetRootPart().Bodies[0].Edges[9],
    GetRootPart().Bodies[0].Edges[8]])
#sel = Selection.Create(Edge2)
sel.CreateAGroup("Fixed edge")

sel = FaceSelection.Create([GetRootPart().Bodies[0].Faces[0],
    GetRootPart().Bodies[0].Faces[1],
    GetRootPart().Bodies[0].Faces[3],
    GetRootPart().Bodies[0].Faces[4]])
sel.CreateAGroup("Fine mesh")

sel = FaceSelection.Create(GetRootPart().Bodies[0].Faces[2])
sel.CreateAGroup("Normal mesh")

sel = FaceSelection.Create([GetRootPart().Bodies[0].Faces[2],
    GetRootPart().Bodies[0].Faces[0],
    GetRootPart().Bodies[0].Faces[3]])
sel.CreateAGroup("Result surface")

sel =BodySelection.Create(GetRootPart().Bodies[0])
sel.CreateAGroup("Body")

sel = FaceSelection.Create([GetRootPart().Bodies[0].Faces[2],
    GetRootPart().Bodies[0].Faces[0],
    GetRootPart().Bodies[0].Faces[3],
    GetRootPart().Bodies[0].Faces[1],
    GetRootPart().Bodies[0].Faces[4]])
sel.CreateAGroup("Surfaces")

sel =EdgeSelection.Create([GetRootPart().Bodies[0].Edges[7],
    GetRootPart().Bodies[0].Edges[1],
    GetRootPart().Bodies[0].Edges[14],
    GetRootPart().Bodies[0].Edges[13],
    GetRootPart().Bodies[0].Edges[19],
    GetRootPart().Bodies[0].Edges[24]])
sel.CreateAGroup("Outer edge")

sel =EdgeSelection.Create([GetRootPart().Bodies[0].Edges[25],
    GetRootPart().Bodies[0].Edges[20],
    GetRootPart().Bodies[0].Edges[16],
    GetRootPart().Bodies[0].Edges[15],
    GetRootPart().Bodies[0].Edges[5],
    GetRootPart().Bodies[0].Edges[11]])
sel.CreateAGroup("Inner edge")

# Applying thickness to surface
result = Midsurface.Convert(Selection.CreateByGroups(SelectionType.Primary, "Body"), MM(t))
```

Appendix E - Stress distributions of the tapered and bow-tie flexure

Appendix E provides the stress distributions for the tapered and bow-tie flexures across various values of η. It includes the von Mises stress distribution, $\sigma_{\text{eq,avg}}$, as well as the normal stress $\sigma_{\bar{x}\bar{x}}$ along the length, $\sigma_{\bar{y}\bar{y}}$ along the width, and the shear stress $\sigma_{\bar{x}\bar{y}}$ in the xy-plane. The normal stress $\sigma_{\bar{z}\bar{z}}$ in the thickness direction and the shear stresses $\sigma_{\bar{y}\bar{z}}$ and $\sigma_{\bar{z}\bar{x}}$ in the $xz-, yz-$ planes, are zero because a very thin sheet is modeled using shell elements.

Tapered flexure

The tapered flexure is modeled with $L = 100$ mm, $W = 50$ mm, $t = 0.5$ mm, $R = 75$ mm, $E = 193$ GPa, $G = 74$ GPa and a prescribed rotation of $\theta = 5°$. The rotational degree of freedom, located at a distance R from the centerline of the flexure, is also illustrated but not to scale. Subfigures (a) represent the stress distributions of the sheet flexure. Subfigures (b) represent the tapered flexure with η_{optimal} for the given input configuration, with a corresponding $\eta_{\text{performance}} = 24.2\%$. Subfigures (c) represent a further increase in η. The von Mises stress $\sigma_{\text{eq,avg}}$ reduction that is visible in Figure E.1 is a result of the reduction in the axial stress component $\sigma_{\bar{x}\bar{x}}$ in Figure E.2. The other stress tensor components remain fairly constant or increase due to a non zero η.

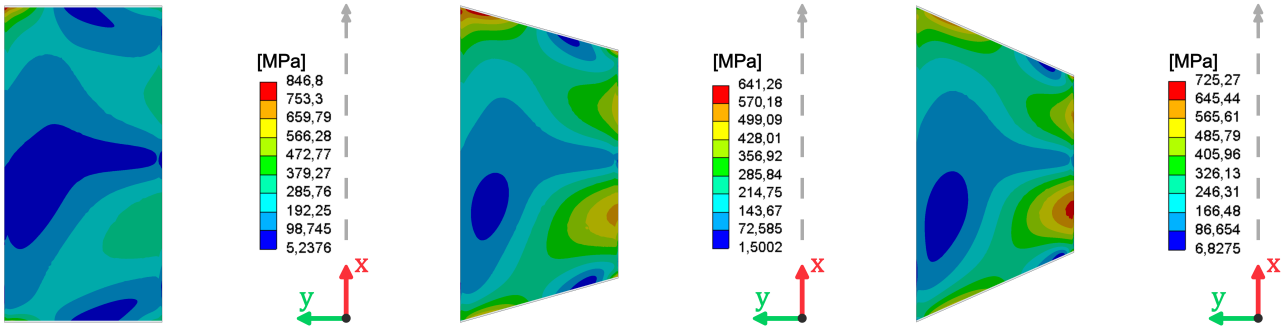

(a) $\eta = 0$ mm | Sheet flexure (b) $\eta = 14$ mm | Tapered flexure (c) $\eta = 22$ mm | Tapered flexure

Figure E.1: Comparison of the von Mises stress $\sigma_{\text{eq,avg}}$ on the front surface of the flexures for different η

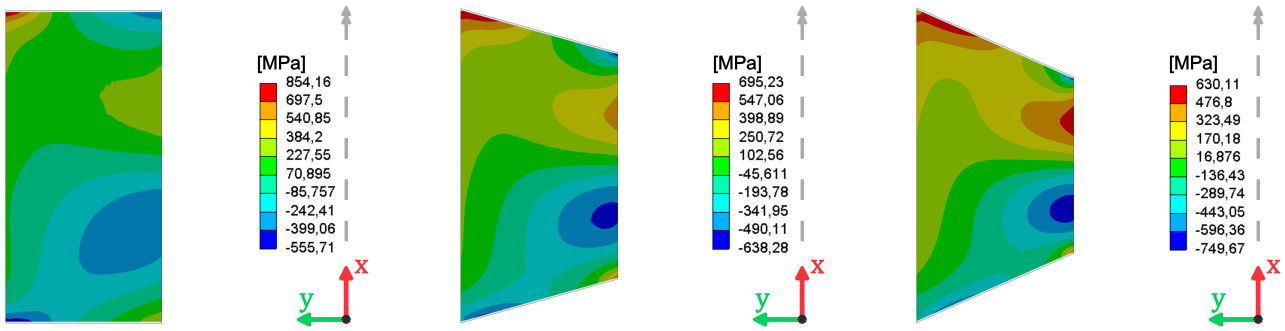

(a) $\eta = 0$ mm | Sheet flexure (b) $\eta = 14$ mm | Tapered flexure (c) $\eta = 22$ mm | Tapered flexure

Figure E.2: Comparison of the $\sigma_{\bar{x}\bar{x}}$ on the front surface of the flexures for different η

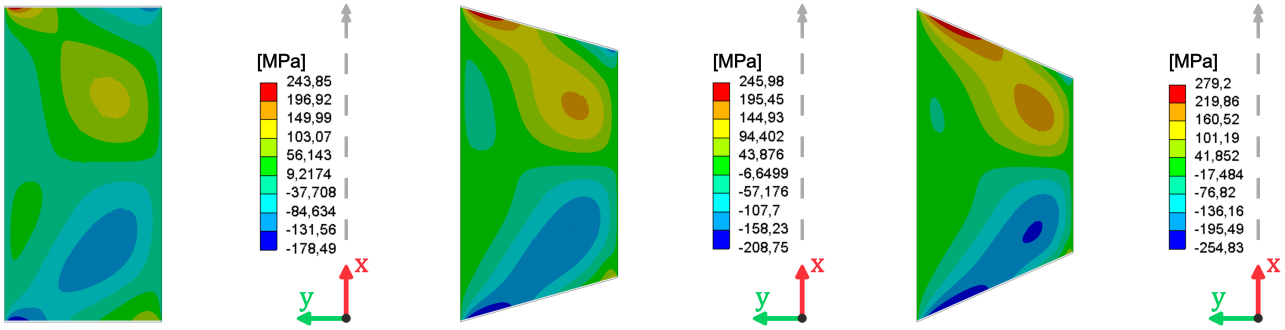

(a) $\eta = 0$ mm | Sheet flexure (b) $\eta = 14$ mm | Tapered flexure (c) $\eta = 22$ mm | Tapered flexure

Figure E.3: Comparison of the $\sigma_{\bar{y}\bar{y}}$ on the front surface of the flexures for different η

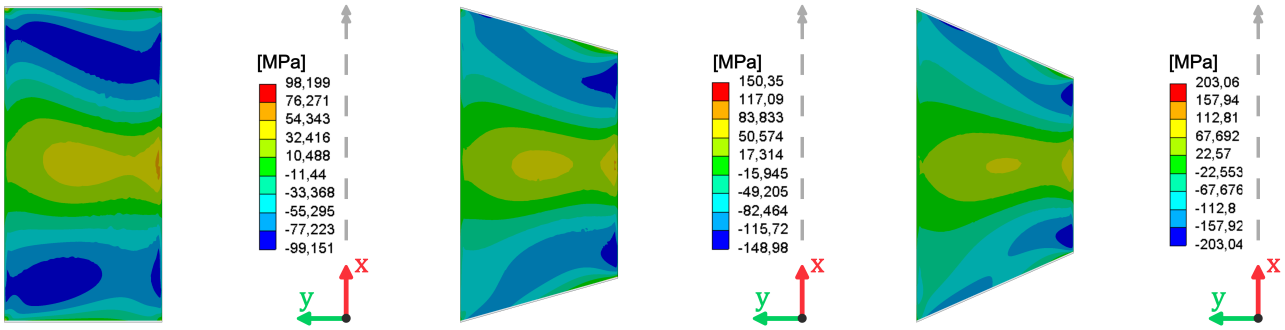

(a) $\eta = 0$ mm | Sheet flexure (b) $\eta = 14$ mm | Tapered flexure (c) $\eta = 22$ mm | Tapered flexure

Figure E.4: Comparison of the $\sigma_{\bar{x}\bar{y}}$ on the front surface of the flexures for different η

Bow-tie flexure

The bow-tie flexure is modeled with $L = 100$ mm, $W = 100$ mm, $t = 0.5$ mm, $R = 120$ mm, $E = 193$ GPa, $G = 74$ GPa and a prescribed rotation of $\theta = 5°$. The rotational degree of freedom, located at a distance R from the centerline of the flexure, is also illustrated but not to scale. Subfigures (a) represent the stress distributions of the sheet flexure. Subfigures (b) represent the bow-tie flexure with η_{optimal} for the given input configuration, with a corresponding $\eta_{\text{performance}} = 46.2\%$. Subfigures (c) represent a further increase in η, it highlights the new critical stress locations. The von Mises stress $\sigma_{\text{eq,avg}}$ reduction that is visible in Figure E.5 is primarily a result of the reduction in the axial stress components $\sigma_{\bar{x}\bar{x}}$ in Figure E.6. The bow-tie flexure also sees a small reduction in $\sigma_{\bar{y}\bar{y}}$ of Figure E.7, but this is 10 times smaller in magnitude. The shear stress component $\sigma_{\bar{x}\bar{y}}$ increases due to a nonzero η.

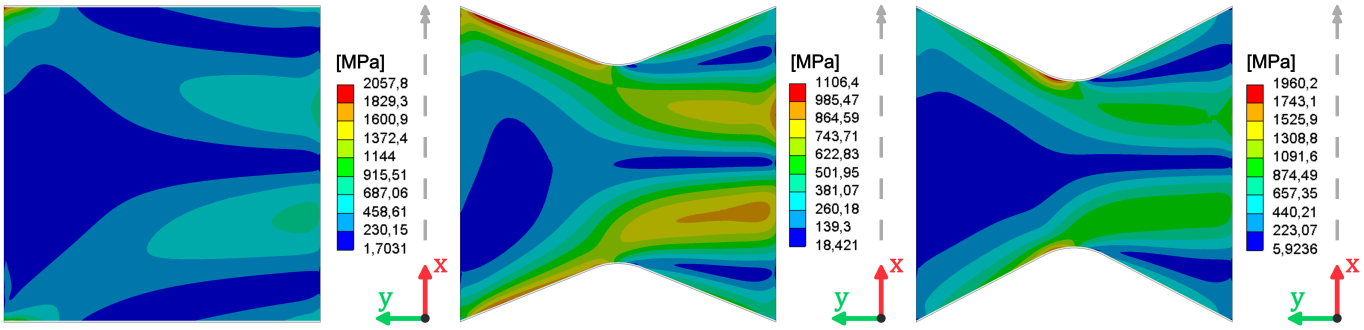

(a) $\eta = 0$ mm | Sheet flexure (b) $\eta = 20$ mm | Bow-tie flexure (c) $\eta = 26$ mm | Bow-tie flexure

Figure E.5: Comparison of the von Mises stress $\sigma_{\text{eq,avg}}$ on the front surface of the flexures for different η

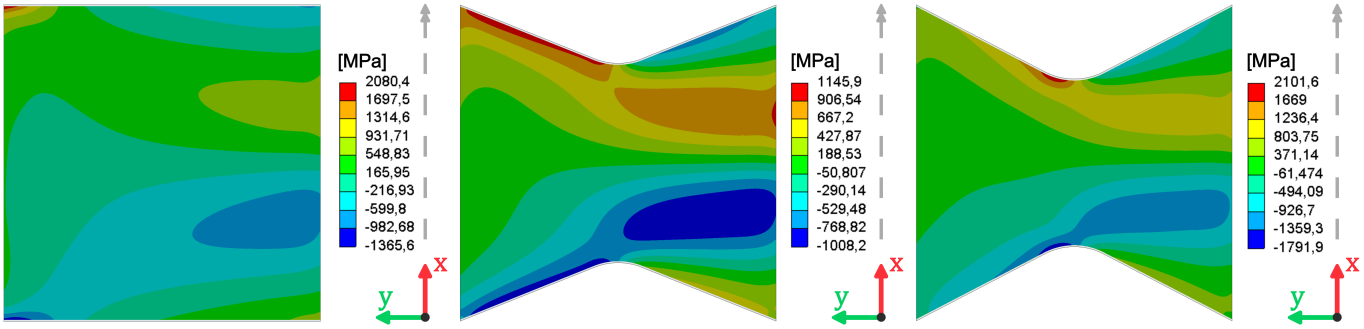

(a) $\eta = 0$ mm | Sheet flexure (b) $\eta = 20$ mm | Bow-tie flexure (c) $\eta = 26$ mm | Bow-tie flexure

Figure E.6: Comparison of the von Mises stress $\sigma_{\bar{x}\bar{x}}$ on the front surface of the flexures for different η

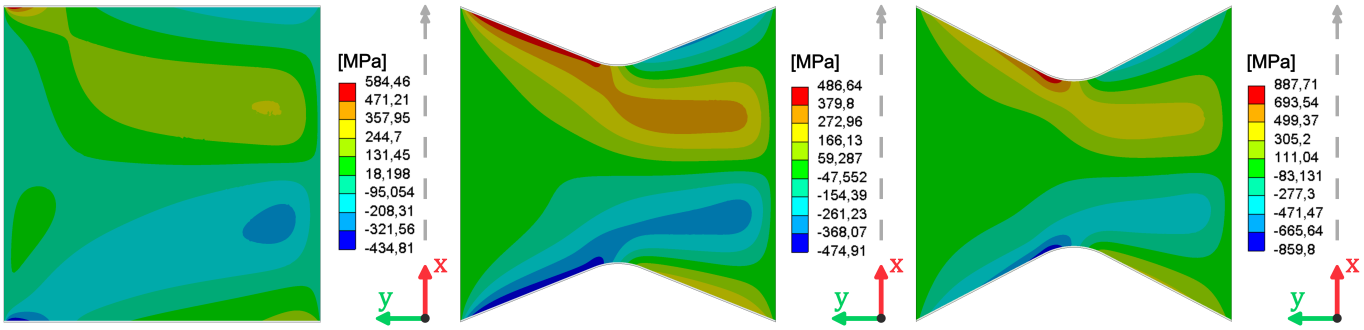

(a) $\eta = 0$ mm | Sheet flexure (b) $\eta = 20$ mm | Bow-tie flexure (c) $\eta = 26$ mm | Bow-tie flexure

Figure E.7: Comparison of the von Mises stress $\sigma_{\bar{y}\bar{y}}$ on the front surface of the flexures for different η

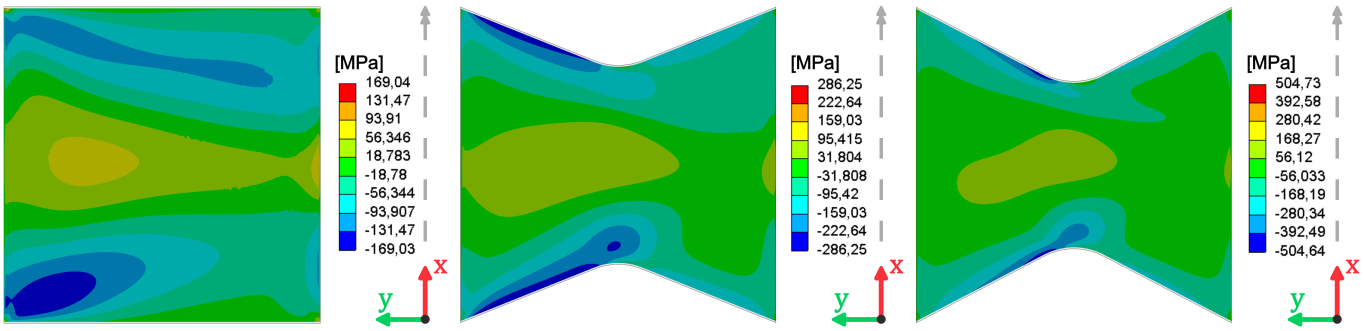

(a) $\eta = 0$ mm | Sheet flexure (b) $\eta = 20$ mm | Bow-tie flexure (c) $\eta = 26$ mm | Bow-tie flexure

Figure E.8: Comparison of the von Mises stress $\sigma_{\bar{x}\bar{y}}$ on the front surface of the flexures for different η

Appendix F - Parameter study of the sheet flexure

Appendix F provides a parameter study aimed at quantifying the influence of the input parameters $W, \theta, t, R, E, \nu, F_x$ on the maximum von Mises stress of the sheet flexure. It follows a similar approach to the parameter study in Chapter 4, but in this case the output is $\sigma_{\text{eq,max}}$ for the sheet flexure ($\eta = 0$mm).

Three input data sets are defined: Input set 1 investigates how variations in geometry and boundary conditions influence the $\sigma_{\text{eq,max}}$ of the sheet flexure. Input set 2 investigates how the use of different materials influences the $\sigma_{\text{eq,max}}$ of the sheet flexure. Input set 3 investigates whether the weight of an upper body influences $\sigma_{\text{eq,max}}$ of the sheet flexure.

Table 12: Input set 1

Par.	Range	Unit
L	100	mm
W	$[10-150]$	mm
t	$[0.1, 0.2, 0.5, 0.8]$	mm
R	$[120, 160, 200]$	mm
θ	$[0.5-5]$	deg
E	193	GPa
G	74	GPa

Table 13: Input set 2

Material	E [GPa]	ν [-]	ρ [kg/m^3]
304SS	193	0.31	7750
Alu 7075-T6	71.7	0.33	2810
Ti-6Al-4V	114	0.342	4430
ABS	1.63	0.4089	1030
HDPE	1.08	0.4183	958.5

Table 14: Input set 3

Par.	Range	Unit
L	100	mm
W	$[10-150]$	mm
t	0.5	mm
R	120	mm
θ	$[0.5-5]$	deg
E	193	GPa
G	74	GPa
F_x	$[0, 1, 10, 50]$	N

The correlation coefficients of the sheet flexure are summarized in Table 15.

Table 15: Correlation coefficients sheet flexure

	W	θ	t	R	E	ν	F_x
$\sigma_{\text{eq,max}}$	0.42	0.60	0.44	0.12	0.55	-0.50*	-0.02

*Not representative due to non-monotonic relationship

All geometric input parameters W, θ, t, R have a positive correlation with $\sigma_{\text{eq,max}}$. This indicates that increasing any of these parameters will result in an increase of the maximum von Mises stress. These observations are also evident in Figure F.1 and F.2. The prescribed rotation θ has the strongest positive correlation (0.60) with $\sigma_{\text{eq,max}}$. While the Radius has the weakest positive correlation (0.12) with $\sigma_{\text{eq,max}}$. This is especially true for the initial prescribed rotation, however as seen in Figure F.2, the radius has more influence at larger values of θ. Overall the maximum stress is more sensitive to changes in the θ, W or t than to changes in R. By increasing the width or thickness, a similar positive correlation of (0.42) and (0.44) is observed.

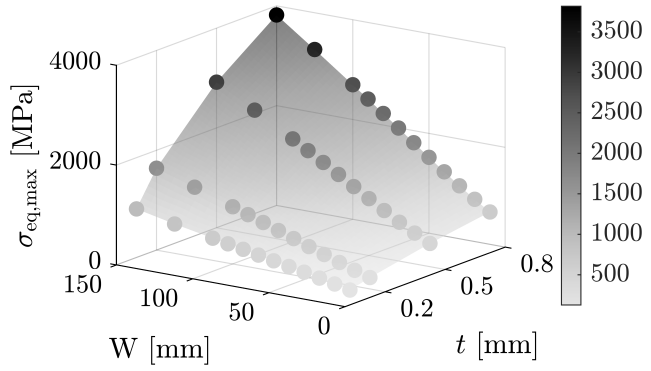

Figure F.1: Sheet flexure $\sigma_{\text{eq,max}}$ evaluated for various W and t where $R = 120$ mm and $\theta = 5°$

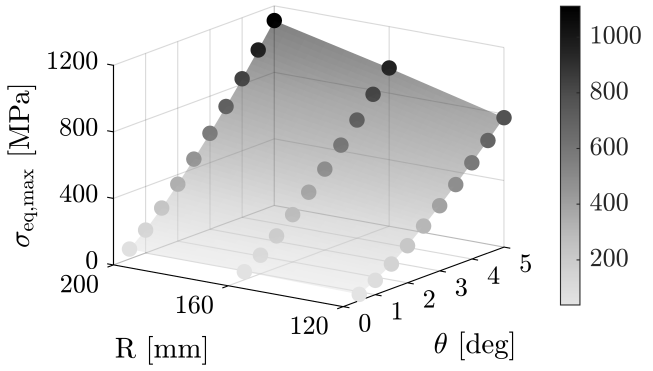

Figure F.2: Sheet flexure $\sigma_{\text{eq,max}}$ evaluated for various R and θ where $W = 30$ mm and $t = 0.5$ mm

The material parameter E has a positive corelation of (0.55) with $\sigma_{\text{eq,max}}$. This indicates that materials with a higher E, such as the metals, will have higher stresses than the plastics with a lower E. This is also visible in Figure F.3. In contrast, the parameter ν has a non-monotic relationship with $\sigma_{\text{eq,max}}$. This is due to the fact that Alu 7075-T6 has a Poisson's ratio that is similar to 304SS and Ti-6Al-4V, but Alu 7075-T6 has a significantly lower E leading to much lower stress values. This behavior is visible in Figure F.4. This suggest that the stress response is primarily influenced by E rather than ν.

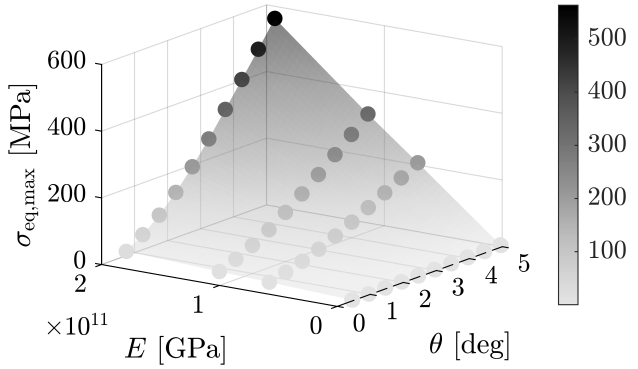

Figure F.3: Sheet flexure $\sigma_{\text{eq,max}}$ evaluated for various E and θ where $W = 30$ mm, $t = 0.5$ mm and $R = 120$ mm

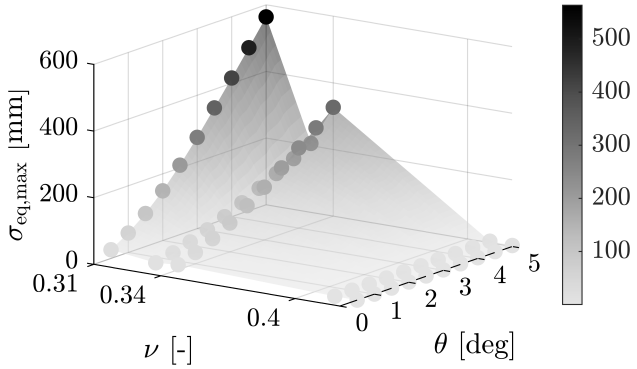

Figure F.4: Sheet flexure $\sigma_{\text{eq,max}}$ evaluated for various ν and θ where $W = 30$ mm, $t = 0.5$ mm and $R = 120$ mm

The $\sigma_{\text{eq,max}}$ exhibits a negligible correlation with the F_x. This indicates that for applied forces smaller than 50 N, the $\sigma_{\text{eq,max}}$ of the sheet flexure does see any significant changes. This is also illustrated in Figure F.5 where the effect of an increasing F_x is minimal on the measured maximum stress.

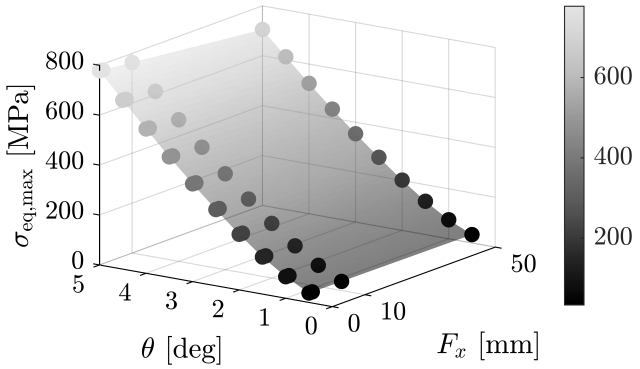

Figure F.5: Sheet flexure $\sigma_{\text{eq,max}}$ evaluated for various F_x and θ where $W = 30$ mm, $t = 0.5$ mm and $= R = 120$ mm

Appendix G - Dataset used for the development of the design guidelines

Appendix G provides the data that was used for the development of the decision graph and the prediction models. The original dataset included 18320 unique configurations of the tapered and bow-tie flexure. After determining η_{optimal} for each configuration, the dataset was reduced to 1,440 configurations. The appendix provides a lookup table for accessing this reduced dataset.

The dataset was generated using ANSYS simulations with the material 304SS where $E = 193$ GPa and $\nu = 0.31$. While $\sigma_{\text{eq,max}}$ depends on the material properties, Chapter 4 showed that $\frac{\eta_{\text{opt}}}{L}$ is independent for the materials 304SS, Alu 7075-T6, Ti-6Al-4V, ABS, and HDPE. It also showed that η_{perf} remains consistent for the metals with a Poisson's ratios between 0.31 and 0.34. The reference length in the simulations was set to $L = 100$ mm, and to generalize the results the scaling relationship of Chapter 3.2.4 is applied. Each row in Table 16 represents a unique input configuration along with the corresponding outputs for the sheet flexure, tapered flexure, and bow-tie flexure. To optimize space, the table spans multiple pages and is split into two large columns. It is organized into four distinct sections, separated by vertical dashed lines. The first section contains the input parameters: $\frac{W}{L}$, θ, $\frac{t}{L}$, and $\frac{R}{L}$. The second section provides the related maximum von Mises stress $\sigma_{\text{eq,max}}$ for the sheet flexure. The third section presents the optimal shape $\frac{\eta_{\text{opt}}}{L}$, stress reduction η_{perf}, and maximum von Mises stress $\sigma_{\text{eq,max}}$ of the tapered flexure for that input configuration. Similarly, the fourth section presents these parameters for the bow-tie flexure.

Table 16: Dataset used for the development of the decision graph and prediction models

$\frac{W}{L}$ [−]	θ [deg]	$\frac{t}{L}$ [−]	$\frac{R}{L}$ [−]	$\sigma_{\text{eq,max}}$ [MPa]	$\frac{\eta_{\text{opt}}}{L}$ [−]	η_{perf} [%]	$\sigma_{\text{eq,max}}$ [MPa]	$\frac{\eta_{\text{opt}}}{L}$ [−]	η_{perf} [%]	$\sigma_{\text{eq,max}}$ [MPa]
0.10	0.5	0.001	1.2	8.0	0.02	-3.6	7.7	0.00	0.0	8.0
0.10	1.0	0.001	1.2	19.2	0.02	-17.9	15.8	0.02	-3.3	18.6
0.10	1.5	0.001	1.2	32.1	0.02	-21.0	25.3	0.02	-14.3	27.5
0.10	2.0	0.001	1.2	45.1	0.02	-22.1	35.1	0.02	-19.6	36.2
0.10	2.5	0.001	1.2	58.0	0.04	-24.8	43.6	0.02	-22.8	44.8
0.10	3.0	0.001	1.2	71.1	0.04	-28.0	51.2	0.02	-25.0	53.3
0.10	3.5	0.001	1.2	84.5	0.04	-29.9	59.3	0.02	-26.6	62.0
0.10	4.0	0.001	1.2	98.4	0.04	-30.6	68.3	0.02	-28.1	70.7
0.10	4.5	0.001	1.2	112.7	0.04	-31.5	77.3	0.02	-29.3	79.6
0.10	5.0	0.001	1.2	127.4	0.04	-32.4	86.1	0.02	-30.4	88.7
0.20	0.5	0.001	1.2	10.2	0.04	-16.6	8.5	0.02	-8.9	9.3
0.20	1.0	0.001	1.2	25.6	0.06	-28.7	18.2	0.02	-22.0	19.9
0.20	1.5	0.001	1.2	42.5	0.08	-32.7	28.6	0.04	-25.4	31.7
0.20	2.0	0.001	1.2	61.1	0.08	-35.6	39.4	0.04	-32.2	41.5
0.20	2.5	0.001	1.2	81.1	0.08	-37.9	50.4	0.04	-34.4	53.2
0.20	3.0	0.001	1.2	102.0	0.10	-40.7	60.5	0.04	-36.0	65.3
0.20	3.5	0.001	1.2	123.8	0.10	-43.4	70.1	0.04	-37.2	77.8
0.20	4.0	0.001	1.2	146.3	0.10	-45.6	79.6	0.04	-38.2	90.4
0.20	4.5	0.001	1.2	169.2	0.10	-47.3	89.2	0.04	-38.9	103.3
0.20	5.0	0.001	1.2	192.7	0.10	-48.0	100.1	0.04	-39.6	116.4
0.30	0.5	0.001	1.2	12.5	0.08	-23.0	9.7	0.02	-15.6	10.6
0.30	1.0	0.001	1.2	31.9	0.08	-27.9	23.0	0.06	-26.6	23.4
0.30	1.5	0.001	1.2	54.8	0.14	-35.2	35.5	0.06	-34.3	36.0
0.30	2.0	0.001	1.2	79.8	0.12	-40.8	47.2	0.06	-37.3	50.0
0.30	2.5	0.001	1.2	106.5	0.14	-42.7	61.0	0.08	-40.8	63.1
0.30	3.0	0.001	1.2	134.5	0.14	-44.9	74.1	0.08	-44.5	74.6
0.30	3.5	0.001	1.2	163.5	0.16	-46.7	87.2	0.08	-46.3	87.7
0.30	4.0	0.001	1.2	193.3	0.16	-48.4	99.7	0.08	-47.7	101.1
0.30	4.5	0.001	1.2	223.7	0.16	-49.8	112.2	0.08	-48.8	114.6
0.30	5.0	0.001	1.2	254.7	0.16	-50.4	126.2	0.08	-49.7	128.2
0.40	0.5	0.001	1.2	15.0	0.10	-23.0	11.6	0.06	-22.6	11.6
0.40	1.0	0.001	1.2	39.4	0.12	-31.4	27.0	0.08	-33.7	26.1
0.40	1.5	0.001	1.2	68.2	0.16	-37.1	42.9	0.10	-39.1	41.6
0.40	2.0	0.001	1.2	99.8	0.16	-42.3	57.6	0.10	-45.3	54.6
0.40	2.5	0.001	1.2	133.3	0.16	-45.7	72.4	0.10	-48.0	69.3
0.40	3.0	0.001	1.2	168.4	0.16	-48.0	87.6	0.10	-49.8	84.5
0.40	3.5	0.001	1.2	204.5	0.16	-48.8	104.8	0.10	-51.1	100.1
0.40	4.0	0.001	1.2	241.6	0.16	-49.3	122.6	0.10	-51.9	116.1
0.40	4.5	0.001	1.2	279.4	0.16	-49.6	140.8	0.10	-52.6	132.4
0.40	5.0	0.001	1.2	317.7	0.16	-49.8	159.4	0.10	-53.1	149.0
0.50	0.5	0.001	1.2	17.6	0.16	-26.1	13.0	0.08	-24.9	13.2
0.50	1.0	0.001	1.2	46.8	0.18	-36.5	29.7	0.10	-36.8	29.5
0.50	1.5	0.001	1.2	81.4	0.18	-41.3	47.7	0.12	-45.3	44.5
0.50	2.0	0.001	1.2	119.1	0.18	-44.0	66.7	0.12	-49.2	60.6
0.50	2.5	0.001	1.2	159.0	0.18	-45.6	86.5	0.12	-51.4	77.2
0.50	3.0	0.001	1.2	200.5	0.18	-46.6	107.2	0.12	-52.9	94.5
0.50	3.5	0.001	1.2	243.2	0.18	-47.1	128.6	0.12	-53.8	112.4
0.50	4.0	0.001	1.2	286.8	0.18	-47.4	150.7	0.12	-54.4	130.7
0.50	4.5	0.001	1.2	331.0	0.18	-47.6	173.5	0.12	-54.8	149.6
0.50	5.0	0.001	1.2	375.8	0.18	-47.6	196.8	0.12	-55.1	168.8
0.60	0.5	0.001	1.2	20.2	0.16	-23.3	15.5	0.10	-26.8	14.8
0.60	1.0	0.001	1.2	54.4	0.20	-34.0	35.9	0.14	-39.9	32.7
0.60	1.5	0.001	1.2	94.9	0.20	-40.2	56.7	0.14	-48.6	48.8
0.60	2.0	0.001	1.2	139.0	0.20	-42.8	79.5	0.14	-52.2	66.5
0.60	2.5	0.001	1.2	185.5	0.20	-44.3	103.3	0.14	-54.2	84.9
0.60	3.0	0.001	1.2	233.5	0.20	-45.1	128.1	0.14	-55.5	103.9
0.60	3.5	0.001	1.2	282.7	0.20	-45.6	153.8	0.14	-56.3	123.6
0.60	4.0	0.001	1.2	332.7	0.22	-45.8	180.2	0.14	-56.7	143.9
0.60	4.5	0.001	1.2	383.3	0.22	-45.9	207.5	0.14	-57.0	164.8
0.60	5.0	0.001	1.2	434.4	0.20	-45.8	235.4	0.14	-57.1	186.2
0.70	0.5	0.001	1.2	22.8	0.16	-21.6	17.9	0.12	-28.4	16.3
0.70	1.0	0.001	1.2	62.2	0.20	-32.2	42.1	0.16	-43.0	35.4
0.70	1.5	0.001	1.2	108.8	0.20	-36.2	69.3	0.16	-50.2	54.2
0.70	2.0	0.001	1.2	159.3	0.20	-38.3	98.2	0.16	-53.8	73.6
0.70	2.5	0.001	1.2	212.3	0.20	-39.5	128.5	0.16	-56.0	93.4
0.70	3.0	0.001	1.2	266.8	0.20	-40.0	160.1	0.16	-57.4	113.6
0.70	3.5	0.001	1.2	322.5	0.20	-39.8	194.1	0.16	-58.1	135.1
0.70	4.0	0.001	1.2	378.8	0.20	-38.8	231.8	0.16	-58.5	157.2
0.70	4.5	0.001	1.2	435.8	0.20	-37.9	270.7	0.16	-58.7	179.9
0.70	5.0	0.001	1.2	493.2	0.20	-37.0	310.7	0.16	-58.7	203.9
0.80	0.5	0.001	1.2	25.4	0.20	-21.5	19.9	0.14	-29.9	17.8
0.80	1.0	0.001	1.2	69.8	0.20	-29.3	49.3	0.18	-44.3	38.8
0.80	1.5	0.001	1.2	122.4	0.22	-34.7	80.0	0.18	-53.3	57.1
0.80	2.0	0.001	1.2	179.5	0.22	-36.8	113.5	0.18	-56.7	77.8
0.80	2.5	0.001	1.2	239.2	0.24	-38.9	146.3	0.18	-58.6	99.0
0.80	3.0	0.001	1.2	300.6	0.24	-40.3	179.6	0.18	-59.8	120.8
0.80	3.5	0.001	1.2	363.1	0.24	-41.1	213.9	0.18	-60.0	145.1
0.80	4.0	0.001	1.2	426.2	0.24	-41.5	249.5	0.18	-60.1	169.9
0.80	4.5	0.001	1.2	489.6	0.24	-40.6	290.6	0.18	-60.1	195.3
0.80	5.0	0.001	1.2	553.3	0.24	-39.8	332.9	0.18	-60.0	221.3

$\frac{W}{L}$ [−]	θ [deg]	$\frac{t}{L}$ [−]	$\frac{R}{L}$ [−]	$\sigma_{\mathrm{eq,max}}$ [MPa]	$\frac{\eta_{\mathrm{opt}}}{L}$ [−]	η_{perf} [%]	$\sigma_{\mathrm{eq,max}}$ [MPa]	$\frac{\eta_{\mathrm{opt}}}{L}$ [−]	η_{perf} [%]	$\sigma_{\mathrm{eq,max}}$ [MPa]
0.90	0.5	0.001	1.2	27.9	0.16	-17.9	22.9	0.16	-31.1	19.3
0.90	1.0	0.001	1.2	77.1	0.22	-27.6	55.8	0.18	-45.6	42.0
0.90	1.5	0.001	1.2	135.3	0.22	-31.1	93.2	0.20	-54.4	61.7
0.90	2.0	0.001	1.2	198.4	0.24	-34.6	129.8	0.20	-57.8	83.6
0.90	2.5	0.001	1.2	264.3	0.24	-35.6	170.1	0.20	-58.7	109.1
0.90	3.0	0.001	1.2	331.8	0.24	-35.1	215.4	0.20	-59.3	135.0
0.90	3.5	0.001	1.2	400.3	0.24	-34.1	263.6	0.20	-59.7	161.5
0.90	4.0	0.001	1.2	469.4	0.26	-34.2	308.8	0.20	-59.9	188.4
0.90	4.5	0.001	1.2	538.7	0.26	-34.9	350.8	0.20	-59.9	215.9
0.90	5.0	0.001	1.2	608.0	0.26	-35.2	393.7	0.20	-59.9	244.0
1.00	0.5	0.001	1.2	30.5	0.18	-16.8	25.4	0.18	-32.3	20.7
1.00	1.0	0.001	1.2	84.5	0.20	-24.3	63.9	0.20	-47.2	44.6
1.00	1.5	0.001	1.2	148.5	0.22	-28.2	106.7	0.20	-52.6	70.4
1.00	2.0	0.001	1.2	217.9	0.24	-30.9	150.5	0.22	-58.0	91.5
1.00	2.5	0.001	1.2	290.2	0.24	-29.9	203.3	0.22	-59.2	118.4
1.00	3.0	0.001	1.2	364.3	0.24	-28.9	259.1	0.22	-59.4	148.0
1.00	3.5	0.001	1.2	439.2	0.26	-29.7	308.9	0.22	-59.4	178.1
1.00	4.0	0.001	1.2	514.6	0.26	-30.0	360.4	0.22	-59.5	208.6
1.00	4.5	0.001	1.2	590.0	0.26	-28.5	422.0	0.22	-59.4	239.4
1.00	5.0	0.001	1.2	665.3	0.26	-27.1	485.0	0.22	-59.3	270.5
1.25	0.5	0.001	1.2	37.1	0.18	-14.2	31.8	0.22	-34.6	24.3
1.25	1.0	0.001	1.2	102.6	0.20	-18.6	83.5	0.24	-49.5	51.8
1.25	1.5	0.001	1.2	180.8	0.24	-21.5	142.0	0.24	-55.1	81.2
1.25	2.0	0.001	1.2	265.7	0.26	-21.6	208.4	0.24	-58.2	111.1
1.25	2.5	0.001	1.2	354.2	0.26	-19.4	285.3	0.24	-60.0	141.5
1.25	3.0	0.001	1.2	444.7	0.28	-18.8	361.2	0.26	-60.7	174.8
1.25	3.5	0.001	1.2	536.0	0.28	-18.1	439.2	0.24	-60.8	210.1
1.25	4.0	0.001	1.2	627.7	0.28	-16.2	525.7	0.24	-60.9	245.4
1.25	4.5	0.001	1.2	719.1	0.28	-14.5	614.5	0.24	-60.9	281.1
1.25	5.0	0.001	1.2	810.2	0.28	-13.0	705.0	0.24	-60.9	317.0
1.50	0.5	0.001	1.2	43.1	0.18	-10.0	38.8	0.24	-33.5	28.7
1.50	1.0	0.001	1.2	119.5	0.24	-14.6	102.1	0.26	-47.1	63.2
1.50	1.5	0.001	1.2	211.8	0.24	-13.1	184.0	0.28	-53.9	97.7
1.50	2.0	0.001	1.2	312.8	0.24	-11.3	277.4	0.28	-57.9	131.8
1.50	2.5	0.001	1.2	418.8	0.28	-11.7	369.8	0.28	-60.3	166.3
1.50	3.0	0.001	1.2	527.8	0.28	-9.8	475.9	0.28	-60.5	208.2
1.50	3.5	0.001	1.2	638.5	0.28	-8.1	586.9	0.28	-60.3	253.4
1.50	4.0	0.001	1.2	750.1	0.28	-6.4	701.8	0.26	-60.5	295.9
1.50	4.5	0.001	1.2	861.8	0.28	-4.9	819.4	0.26	-60.8	337.6
1.50	5.0	0.001	1.2	973.4	0.28	-3.5	938.9	0.26	-61.0	379.7
0.10	0.5	0.002	1.2	14.4	0.00	0.0	14.4	0.00	0.0	14.4
0.10	1.0	0.002	1.2	31.7	0.02	-2.8	30.8	0.00	0.0	31.7
0.10	1.5	0.002	1.2	52.4	0.02	-10.5	46.9	0.00	0.0	52.4
0.10	2.0	0.002	1.2	76.0	0.02	-17.3	62.9	0.02	-2.4	74.2
0.10	2.5	0.002	1.2	100.9	0.02	-19.0	81.7	0.02	-8.6	92.2
0.10	3.0	0.002	1.2	126.4	0.02	-20.2	100.8	0.02	-13.1	109.9
0.10	3.5	0.002	1.2	152.1	0.02	-21.0	120.2	0.02	-16.3	127.3
0.10	4.0	0.002	1.2	177.6	0.02	-21.5	139.4	0.02	-18.5	144.8
0.10	4.5	0.002	1.2	203.1	0.02	-21.7	159.0	0.02	-20.2	162.1
0.10	5.0	0.002	1.2	228.7	0.04	-23.4	175.2	0.02	-21.6	179.3
0.20	0.5	0.002	1.2	16.4	0.02	-8.5	15.0	0.00	0.0	16.4
0.20	1.0	0.002	1.2	40.1	0.04	-18.9	32.6	0.02	-7.8	37.0
0.20	1.5	0.002	1.2	69.4	0.06	-24.0	52.7	0.02	-19.1	56.2
0.20	2.0	0.002	1.2	100.5	0.06	-27.6	72.7	0.02	-21.0	79.3
0.20	2.5	0.002	1.2	132.4	0.08	-30.5	92.0	0.02	-21.9	103.5
0.20	3.0	0.002	1.2	166.6	0.08	-33.2	111.3	0.04	-24.0	126.6
0.20	3.5	0.002	1.2	202.4	0.08	-34.5	132.5	0.04	-27.9	146.0
0.20	4.0	0.002	1.2	239.7	0.08	-35.6	154.3	0.04	-30.9	165.6
0.20	4.5	0.002	1.2	278.3	0.08	-36.6	176.4	0.04	-32.2	188.7
0.20	5.0	0.002	1.2	318.1	0.08	-37.5	198.9	0.04	-33.2	212.4
0.30	0.5	0.002	1.2	18.8	0.06	-12.7	16.4	0.02	-4.7	17.9
0.30	1.0	0.002	1.2	49.5	0.08	-22.4	38.4	0.02	-14.8	42.2
0.30	1.5	0.002	1.2	86.1	0.10	-26.9	62.9	0.04	-23.3	66.0
0.30	2.0	0.002	1.2	125.7	0.12	-31.0	86.7	0.06	-25.7	93.4
0.30	2.5	0.002	1.2	168.9	0.14	-35.7	108.7	0.06	-31.0	116.5
0.30	3.0	0.002	1.2	215.2	0.14	-39.0	131.2	0.06	-33.3	143.5
0.30	3.5	0.002	1.2	263.6	0.14	-41.6	153.9	0.06	-35.1	171.1
0.30	4.0	0.002	1.2	313.8	0.14	-43.6	177.0	0.06	-36.5	199.4
0.30	4.5	0.002	1.2	365.7	0.14	-44.9	201.5	0.06	-37.6	228.2
0.30	5.0	0.002	1.2	419.0	0.14	-46.0	226.4	0.08	-39.8	252.3
0.40	0.5	0.002	1.2	21.7	0.06	-13.5	18.8	0.02	-9.6	19.6
0.40	1.0	0.002	1.2	59.5	0.12	-24.3	45.0	0.06	-22.0	46.4
0.40	1.5	0.002	1.2	104.4	0.14	-29.8	73.3	0.08	-27.0	76.2
0.40	2.0	0.002	1.2	154.5	0.14	-33.1	103.3	0.08	-32.6	104.2
0.40	2.5	0.002	1.2	209.4	0.16	-37.4	131.1	0.08	-35.7	134.7
0.40	3.0	0.002	1.2	267.7	0.16	-41.0	157.8	0.10	-38.1	165.6
0.40	3.5	0.002	1.2	328.6	0.16	-42.8	188.0	0.10	-42.4	189.2
0.40	4.0	0.002	1.2	391.8	0.16	-44.1	218.9	0.10	-44.5	217.3
0.40	4.5	0.002	1.2	456.9	0.16	-45.2	250.4	0.10	-46.1	246.4
0.40	5.0	0.002	1.2	523.7	0.18	-46.1	282.4	0.10	-47.3	275.8
0.50	0.5	0.002	1.2	25.0	0.12	-17.0	20.8	0.04	-12.5	21.9
0.50	1.0	0.002	1.2	69.6	0.16	-25.5	51.9	0.08	-24.3	52.7
0.50	1.5	0.002	1.2	123.3	0.18	-31.9	84.0	0.10	-31.5	84.5
0.50	2.0	0.002	1.2	183.9	0.18	-35.5	118.5	0.10	-35.9	117.9
0.50	2.5	0.002	1.2	250.0	0.18	-38.4	154.0	0.12	-40.7	148.3
0.50	3.0	0.002	1.2	320.0	0.18	-40.5	190.4	0.12	-44.6	177.4
0.50	3.5	0.002	1.2	393.1	0.20	-42.7	225.1	0.12	-46.8	209.1
0.50	4.0	0.002	1.2	468.8	0.20	-44.2	261.4	0.12	-48.5	241.3
0.50	4.5	0.002	1.2	546.6	0.20	-45.0	300.4	0.12	-49.9	274.1
0.50	5.0	0.002	1.2	626.3	0.20	-45.7	340.1	0.12	-50.9	307.3
0.60	0.5	0.002	1.2	28.5	0.16	-17.5	23.5	0.06	-14.9	24.2
0.60	1.0	0.002	1.2	80.2	0.18	-24.9	60.2	0.10	-26.4	59.0
0.60	1.5	0.002	1.2	142.9	0.20	-30.1	99.8	0.12	-34.2	94.0
0.60	2.0	0.002	1.2	214.0	0.20	-34.6	139.9	0.14	-38.9	130.8
0.60	2.5	0.002	1.2	291.7	0.20	-37.4	182.6	0.14	-45.0	160.3
0.60	3.0	0.002	1.2	373.8	0.20	-39.4	226.3	0.14	-47.9	194.7
0.60	3.5	0.002	1.2	459.3	0.20	-41.0	271.1	0.14	-50.0	229.7
0.60	4.0	0.002	1.2	547.7	0.20	-42.2	316.8	0.14	-51.6	265.3
0.60	4.5	0.002	1.2	638.4	0.20	-43.1	363.4	0.14	-52.8	301.4
0.60	5.0	0.002	1.2	730.9	0.20	-43.8	410.9	0.14	-53.8	338.0
0.70	0.5	0.002	1.2	32.0	0.18	-17.1	26.6	0.08	-16.4	26.8
0.70	1.0	0.002	1.2	90.9	0.20	-23.1	69.9	0.12	-28.4	65.1
0.70	1.5	0.002	1.2	162.7	0.20	-28.0	117.1	0.14	-36.6	103.2
0.70	2.0	0.002	1.2	244.6	0.20	-31.3	168.1	0.16	-42.1	141.5
0.70	2.5	0.002	1.2	333.8	0.20	-33.7	221.4	0.16	-47.7	174.8
0.70	3.0	0.002	1.2	428.1	0.22	-36.7	271.1	0.16	-50.4	212.4
0.70	3.5	0.002	1.2	526.2	0.22	-38.9	321.7	0.16	-52.4	250.6
0.70	4.0	0.002	1.2	627.3	0.22	-40.2	375.3	0.16	-53.9	289.3
0.70	4.5	0.002	1.2	730.9	0.22	-41.2	429.7	0.16	-55.1	328.5
0.70	5.0	0.002	1.2	836.4	0.22	-42.0	484.9	0.16	-56.0	368.1
0.80	0.5	0.002	1.2	35.6	0.20	-17.0	29.6	0.10	-17.4	29.4
0.80	1.0	0.002	1.2	101.5	0.20	-21.7	79.5	0.14	-30.0	71.0
0.80	1.5	0.002	1.2	182.2	0.20	-25.3	136.0	0.16	-38.5	112.0
0.80	2.0	0.002	1.2	274.7	0.22	-29.7	193.0	0.18	-43.5	155.2
0.80	2.5	0.002	1.2	375.4	0.22	-32.1	254.8	0.18	-49.8	188.5
0.80	3.0	0.002	1.2	481.9	0.22	-33.9	318.7	0.18	-52.7	227.9
0.80	3.5	0.002	1.2	592.6	0.22	-35.1	384.3	0.18	-54.7	268.5
0.80	4.0	0.002	1.2	706.6	0.22	-36.1	451.5	0.18	-56.2	309.4
0.80	4.5	0.002	1.2	823.3	0.22	-36.8	520.1	0.18	-57.4	350.8
0.80	5.0	0.002	1.2	942.0	0.24	-37.7	586.5	0.18	-58.3	392.5
0.90	0.5	0.002	1.2	39.2	0.20	-15.6	33.1	0.12	-18.3	32.1
0.90	1.0	0.002	1.2	111.9	0.18	-18.8	90.9	0.16	-31.3	76.9
0.90	1.5	0.002	1.2	201.1	0.22	-23.2	154.4	0.18	-40.1	120.5
0.90	2.0	0.002	1.2	303.9	0.22	-26.7	222.7	0.18	-44.9	167.5
0.90	2.5	0.002	1.2	415.7	0.22	-28.8	295.8	0.20	-49.3	210.6
0.90	3.0	0.002	1.2	533.8	0.24	-30.4	371.7	0.20	-53.5	248.1
0.90	3.5	0.002	1.2	656.6	0.24	-32.4	443.6	0.20	-56.5	285.5
0.90	4.0	0.002	1.2	783.0	0.24	-34.0	516.5	0.20	-57.4	333.2
0.90	4.5	0.002	1.2	912.2	0.24	-34.8	595.2	0.20	-57.9	383.6
0.90	5.0	0.002	1.2	1043.5	0.24	-35.3	675.1	0.20	-58.4	434.6
1.00	0.5	0.002	1.2	42.9	0.22	-14.7	36.6	0.14	-19.1	34.7
1.00	1.0	0.002	1.2	122.4	0.18	-17.3	101.2	0.18	-32.5	82.5
1.00	1.5	0.002	1.2	220.1	0.20	-20.8	174.3	0.20	-41.6	128.5
1.00	2.0	0.002	1.2	333.2	0.22	-24.2	252.6	0.20	-46.6	177.9
1.00	2.5	0.002	1.2	456.1	0.22	-26.1	337.1	0.20	-49.8	228.8
1.00	3.0	0.002	1.2	586.0	0.24	-28.4	419.6	0.20	-52.1	280.8
1.00	3.5	0.002	1.2	721.0	0.24	-29.6	507.4	0.22	-54.6	327.5
1.00	4.0	0.002	1.2	860.0	0.24	-30.4	598.4	0.22	-56.9	370.8
1.00	4.5	0.002	1.2	1002.0	0.24	-30.5	696.0	0.22	-58.5	415.4
1.00	5.0	0.002	1.2	1146.2	0.24	-30.2	800.5	0.22	-58.7	473.3

$\frac{W}{L}$ [−]	θ [deg]	$\frac{t}{L}$ [−]	$\frac{R}{L}$ [−]	$\sigma_{\text{eq,max}}$ [MPa]	$\frac{\eta_{\text{opt}}}{L}$ [−]	η_{perf} [%]	$\sigma_{\text{eq,max}}$ [MPa]	$\frac{\eta_{\text{opt}}}{L}$ [−]	η_{perf} [%]	$\sigma_{\text{eq,max}}$ [MPa]
1.25	0.5	0.002	1.2	52.4	0.18	-11.1	46.5	0.18	-21.0	41.4
1.25	1.0	0.002	1.2	148.3	0.18	-14.3	127.1	0.22	-34.7	96.9
1.25	1.5	0.002	1.2	266.8	0.20	-16.9	221.6	0.24	-43.6	150.3
1.25	2.0	0.002	1.2	404.6	0.22	-19.4	326.0	0.24	-48.9	206.8
1.25	2.5	0.002	1.2	554.5	0.24	-21.3	436.2	0.24	-52.2	265.1
1.25	3.0	0.002	1.2	713.2	0.24	-21.1	562.5	0.24	-54.6	323.7
1.25	3.5	0.002	1.2	878.3	0.24	-20.6	697.7	0.24	-56.5	382.5
1.25	4.0	0.002	1.2	1048.3	0.26	-21.8	820.1	0.24	-57.9	441.4
1.25	4.5	0.002	1.2	1222.0	0.26	-20.8	967.2	0.24	-59.1	500.3
1.25	5.0	0.002	1.2	1398.4	0.26	-19.9	1119.5	0.24	-60.0	559.5
1.50	0.5	0.002	1.2	62.2	0.16	-9.4	56.3	0.20	-22.3	48.3
1.50	1.0	0.002	1.2	173.6	0.18	-11.4	153.9	0.24	-34.0	114.5
1.50	1.5	0.002	1.2	312.1	0.22	-13.3	270.7	0.26	-42.5	179.4
1.50	2.0	0.002	1.2	473.3	0.24	-14.6	404.0	0.26	-46.8	251.9
1.50	2.5	0.002	1.2	648.9	0.24	-14.0	558.2	0.28	-50.4	321.8
1.50	3.0	0.002	1.2	834.9	0.24	-13.0	726.3	0.28	-54.8	377.5
1.50	3.5	0.002	1.2	1028.6	0.24	-12.0	905.4	0.28	-57.7	434.8
1.50	4.0	0.002	1.2	1228.2	0.28	-12.5	1074.7	0.28	-58.6	508.0
1.50	4.5	0.002	1.2	1432.2	0.28	-12.3	1256.6	0.28	-59.2	583.9
1.50	5.0	0.002	1.2	1639.6	0.28	-11.3	1454.3	0.28	-59.4	666.1
0.10	0.5	0.005	1.2	33.7	0.00	0.0	33.7	0.00	0.0	33.7
0.10	1.0	0.005	1.2	69.7	0.00	0.0	69.7	0.00	0.0	69.7
0.10	1.5	0.005	1.2	108.4	0.02	-0.8	107.6	0.00	0.0	108.4
0.10	2.0	0.005	1.2	150.1	0.02	-3.3	145.1	0.00	0.0	150.1
0.10	2.5	0.005	1.2	194.9	0.02	-6.0	183.1	0.00	0.0	194.9
0.10	3.0	0.005	1.2	243.1	0.02	-8.9	221.5	0.00	0.0	243.1
0.10	3.5	0.005	1.2	294.1	0.02	-11.6	260.0	0.00	0.0	294.1
0.10	4.0	0.005	1.2	348.1	0.02	-13.8	300.1	0.00	0.0	348.1
0.10	4.5	0.005	1.2	404.2	0.02	-14.8	344.4	0.00	0.0	404.2
0.10	5.0	0.005	1.2	464.4	0.02	-16.1	389.7	0.02	-0.0	464.3
0.20	0.5	0.005	1.2	35.6	0.02	-4.0	34.2	0.00	0.0	35.6
0.20	1.0	0.005	1.2	77.1	0.02	-7.3	71.5	0.00	0.0	77.1
0.20	1.5	0.005	1.2	126.0	0.04	-9.2	114.4	0.00	0.0	126.0
0.20	2.0	0.005	1.2	182.7	0.04	-15.7	154.1	0.00	0.0	182.7
0.20	2.5	0.005	1.2	246.6	0.04	-17.6	203.1	0.02	-6.6	230.4
0.20	3.0	0.005	1.2	315.6	0.06	-19.1	255.2	0.02	-13.8	271.9
0.20	3.5	0.005	1.2	387.3	0.06	-23.4	296.5	0.02	-16.6	323.2
0.20	4.0	0.005	1.2	462.0	0.06	-24.6	348.5	0.02	-18.0	379.0
0.20	4.5	0.005	1.2	538.8	0.06	-25.5	401.2	0.02	-19.1	436.0
0.20	5.0	0.005	1.2	616.4	0.08	-27.0	450.0	0.02	-19.9	493.8
0.30	0.5	0.005	1.2	37.8	0.04	-5.0	35.9	0.00	0.0	37.8
0.30	1.0	0.005	1.2	86.4	0.04	-9.7	78.0	0.00	0.0	86.4
0.30	1.5	0.005	1.2	148.7	0.06	-15.0	126.3	0.02	-9.8	134.2
0.30	2.0	0.005	1.2	223.0	0.08	-19.6	179.3	0.02	-12.2	195.9
0.30	2.5	0.005	1.2	305.4	0.10	-22.2	237.5	0.02	-13.8	263.3
0.30	3.0	0.005	1.2	391.7	0.10	-24.6	295.4	0.04	-19.8	314.2
0.30	3.5	0.005	1.2	483.1	0.12	-27.4	350.8	0.04	-21.6	378.8
0.30	4.0	0.005	1.2	578.3	0.12	-29.6	407.0	0.04	-23.0	445.5
0.30	4.5	0.005	1.2	676.5	0.12	-30.9	467.4	0.04	-24.0	514.0
0.30	5.0	0.005	1.2	777.9	0.12	-32.0	528.7	0.04	-24.9	584.2
0.40	0.5	0.005	1.2	40.4	0.06	-5.9	38.0	0.00	0.0	40.4
0.40	1.0	0.005	1.2	97.6	0.08	-12.1	85.8	0.02	-7.1	90.7
0.40	1.5	0.005	1.2	175.0	0.10	-17.4	144.6	0.04	-10.9	155.9
0.40	2.0	0.005	1.2	266.9	0.12	-21.6	209.2	0.04	-16.3	223.3
0.40	2.5	0.005	1.2	366.3	0.14	-25.0	274.8	0.06	-20.9	289.7
0.40	3.0	0.005	1.2	473.9	0.14	-27.0	345.8	0.06	-23.4	362.9
0.40	3.5	0.005	1.2	587.7	0.16	-30.8	406.9	0.06	-25.3	438.8
0.40	4.0	0.005	1.2	706.5	0.16	-32.5	476.7	0.08	-28.7	503.4
0.40	4.5	0.005	1.2	829.7	0.16	-34.0	547.2	0.08	-30.5	576.5
0.40	5.0	0.005	1.2	956.9	0.18	-35.5	617.1	0.08	-32.0	650.8
0.50	0.5	0.005	1.2	43.3	0.08	-6.2	40.6	0.02	-3.6	41.7
0.50	1.0	0.005	1.2	110.4	0.12	-13.2	95.8	0.04	-8.2	101.3
0.50	1.5	0.005	1.2	203.2	0.14	-18.7	165.2	0.06	-14.5	173.7
0.50	2.0	0.005	1.2	311.2	0.16	-22.5	241.1	0.06	-18.9	252.5
0.50	2.5	0.005	1.2	430.7	0.18	-25.0	323.2	0.08	-23.6	329.0
0.50	3.0	0.005	1.2	559.8	0.18	-28.8	398.7	0.08	-26.3	412.5
0.50	3.5	0.005	1.2	696.1	0.18	-30.8	481.9	0.10	-30.0	487.2
0.50	4.0	0.005	1.2	838.7	0.18	-32.5	566.4	0.10	-32.2	568.6
0.50	4.5	0.005	1.2	986.8	0.20	-34.5	646.5	0.10	-34.0	651.5
0.50	5.0	0.005	1.2	1139.8	0.20	-36.6	722.5	0.10	-35.5	735.7
0.60	0.5	0.005	1.2	46.6	0.10	-6.3	43.6	0.02	-3.5	44.9
0.60	1.0	0.005	1.2	124.2	0.14	-13.5	107.5	0.04	-9.5	112.4
0.60	1.5	0.005	1.2	232.3	0.16	-18.4	189.5	0.08	-17.1	192.6
0.60	2.0	0.005	1.2	356.9	0.18	-21.9	278.8	0.10	-21.9	278.7
0.60	2.5	0.005	1.2	496.9	0.18	-24.4	375.8	0.10	-26.0	368.0
0.60	3.0	0.005	1.2	647.2	0.20	-27.6	468.5	0.12	-30.0	453.2
0.60	3.5	0.005	1.2	806.3	0.20	-30.0	564.5	0.12	-32.8	541.7
0.60	4.0	0.005	1.2	973.0	0.20	-31.6	665.3	0.12	-35.0	632.2
0.60	4.5	0.005	1.2	1146.5	0.20	-33.0	767.6	0.12	-36.8	724.3
0.60	5.0	0.005	1.2	1325.8	0.22	-34.5	867.8	0.12	-38.3	817.9
0.70	0.5	0.005	1.2	50.1	0.12	-6.3	46.9	0.04	-5.0	47.6
0.70	1.0	0.005	1.2	138.7	0.16	-13.5	120.0	0.06	-11.2	123.1
0.70	1.5	0.005	1.2	261.2	0.18	-17.7	215.0	0.10	-18.3	213.4
0.70	2.0	0.005	1.2	404.3	0.20	-20.4	321.9	0.12	-23.8	308.1
0.70	2.5	0.005	1.2	563.5	0.20	-23.4	431.4	0.12	-27.9	406.2
0.70	3.0	0.005	1.2	735.0	0.20	-25.4	548.1	0.14	-32.3	497.8
0.70	3.5	0.005	1.2	917.0	0.20	-27.1	668.5	0.14	-35.1	594.7
0.70	4.0	0.005	1.2	1108.1	0.22	-29.8	777.7	0.14	-37.4	693.8
0.70	4.5	0.005	1.2	1307.0	0.22	-31.6	894.4	0.14	-39.2	794.7
0.70	5.0	0.005	1.2	1512.8	0.22	-32.8	1016.9	0.16	-41.0	892.4
0.80	0.5	0.005	1.2	53.8	0.14	-6.2	50.5	0.04	-4.8	51.2
0.80	1.0	0.005	1.2	153.6	0.18	-13.3	133.1	0.08	-12.4	134.6
0.80	1.5	0.005	1.2	290.5	0.20	-16.8	241.8	0.12	-19.2	234.6
0.80	2.0	0.005	1.2	451.4	0.20	-19.1	365.2	0.14	-25.3	337.0
0.80	2.5	0.005	1.2	629.5	0.20	-21.2	496.1	0.14	-29.6	443.3
0.80	3.0	0.005	1.2	822.0	0.20	-23.0	633.1	0.16	-34.2	540.9
0.80	3.5	0.005	1.2	1026.6	0.22	-25.6	763.5	0.16	-37.1	645.6
0.80	4.0	0.005	1.2	1241.8	0.22	-27.0	906.0	0.16	-39.4	752.6
0.80	4.5	0.005	1.2	1465.9	0.22	-28.3	1051.7	0.16	-41.2	861.6
0.80	5.0	0.005	1.2	1697.7	0.22	-29.3	1200.0	0.16	-42.7	972.2
0.90	0.5	0.005	1.2	57.6	0.14	-6.0	54.1	0.06	-5.6	54.4
0.90	1.0	0.005	1.2	169.1	0.20	-13.1	146.9	0.10	-13.3	146.5
0.90	1.5	0.005	1.2	320.8	0.20	-15.2	272.1	0.14	-20.5	254.9
0.90	2.0	0.005	1.2	498.4	0.18	-16.6	415.6	0.16	-26.6	365.6
0.90	2.5	0.005	1.2	695.0	0.18	-18.5	566.7	0.16	-31.0	479.5
0.90	3.0	0.005	1.2	907.9	0.20	-20.8	719.1	0.18	-35.8	582.9
0.90	3.5	0.005	1.2	1134.6	0.22	-23.0	873.7	0.18	-38.8	694.6
0.90	4.0	0.005	1.2	1373.1	0.22	-24.3	1039.8	0.18	-41.1	808.7
0.90	4.5	0.005	1.2	1621.7	0.22	-25.4	1210.6	0.18	-43.0	924.8
0.90	5.0	0.005	1.2	1879.1	0.22	-26.3	1385.1	0.18	-44.5	1042.5
1.00	0.5	0.005	1.2	61.6	0.16	-5.9	58.0	0.08	-5.8	58.1
1.00	1.0	0.005	1.2	184.9	0.22	-12.7	161.4	0.12	-14.1	158.8
1.00	1.5	0.005	1.2	351.6	0.20	-13.8	303.0	0.16	-21.6	275.6
1.00	2.0	0.005	1.2	545.1	0.16	-14.7	464.9	0.18	-27.8	393.8
1.00	2.5	0.005	1.2	760.1	0.18	-17.0	631.2	0.18	-32.3	514.7
1.00	3.0	0.005	1.2	993.1	0.20	-19.0	804.9	0.20	-35.6	639.2
1.00	3.5	0.005	1.2	1241.6	0.20	-20.2	990.5	0.20	-40.3	741.1
1.00	4.0	0.005	1.2	1503.2	0.22	-21.9	1173.5	0.20	-42.7	861.3
1.00	4.5	0.005	1.2	1776.0	0.22	-22.9	1369.2	0.20	-44.6	983.4
1.00	5.0	0.005	1.2	2058.5	0.22	-23.7	1570.1	0.20	-46.2	1106.8
1.25	0.5	0.005	1.2	72.5	0.20	-5.7	68.4	0.10	-6.4	67.8
1.25	1.0	0.005	1.2	226.0	0.26	-11.0	201.2	0.16	-15.8	190.2
1.25	1.5	0.005	1.2	429.2	0.16	-10.8	383.0	0.18	-23.4	328.9
1.25	2.0	0.005	1.2	662.0	0.16	-12.4	580.1	0.20	-29.0	469.9
1.25	2.5	0.005	1.2	921.1	0.18	-14.0	792.3	0.22	-34.4	604.5
1.25	3.0	0.005	1.2	1202.7	0.20	-15.4	1017.9	0.22	-37.4	752.7
1.25	3.5	0.005	1.2	1503.5	0.20	-16.4	1256.4	0.24	-40.2	899.8
1.25	4.0	0.005	1.2	1820.7	0.22	-17.5	1502.9	0.24	-45.0	1001.3
1.25	4.5	0.005	1.2	2151.9	0.22	-18.2	1759.4	0.24	-46.9	1142.4
1.25	5.0	0.005	1.2	2495.4	0.22	-18.9	2024.1	0.24	-48.5	1284.2
1.50	0.5	0.005	1.2	84.3	0.20	-5.5	79.7	0.12	-7.2	78.2
1.50	1.0	0.005	1.2	271.0	0.28	-9.2	246.0	0.18	-17.9	222.4
1.50	1.5	0.005	1.2	507.6	0.22	-10.5	454.1	0.22	-25.1	380.3
1.50	2.0	0.005	1.2	778.1	0.16	-10.4	696.9	0.24	-30.7	539.6
1.50	2.5	0.005	1.2	1079.5	0.18	-11.8	952.4	0.24	-33.9	713.8
1.50	3.0	0.005	1.2	1407.4	0.20	-12.7	1228.1	0.26	-39.2	855.4
1.50	3.5	0.005	1.2	1758.2	0.20	-13.7	1517.1	0.26	-41.5	1028.3
1.50	4.0	0.005	1.2	2128.4	0.22	-14.3	1823.2	0.26	-43.4	1204.4
1.50	4.5	0.005	1.2	2515.4	0.22	-14.7	2144.8	0.26	-45.0	1382.5
1.50	5.0	0.005	1.2	2916.9	0.24	-15.4	2469.0	0.26	-46.5	1561.4

$\frac{W}{L}$ [−]	θ [deg]	$\frac{t}{L}$ [−]	$\frac{R}{L}$ [−]	$\sigma_{\mathrm{eq,max}}$ [MPa]	$\frac{\eta_{\mathrm{opt}}}{L}$ [−]	η_{perf} [%]	$\sigma_{\mathrm{eq,max}}$ [MPa]	$\frac{\eta_{\mathrm{opt}}}{L}$ [−]	η_{perf} [%]	$\sigma_{\mathrm{eq,max}}$ [MPa]
0.10	0.5	0.008	1.2	52.8	0.00	0.0	52.8	0.00	0.0	52.8
0.10	1.0	0.008	1.2	107.7	0.00	0.0	107.7	0.00	0.0	107.7
0.10	1.5	0.008	1.2	164.9	0.00	0.0	164.9	0.00	0.0	164.9
0.10	2.0	0.008	1.2	224.8	0.02	-0.6	223.5	0.00	0.0	224.8
0.10	2.5	0.008	1.2	287.5	0.02	-1.9	282.1	0.00	0.0	287.5
0.10	3.0	0.008	1.2	353.3	0.02	-3.4	341.3	0.00	0.0	353.3
0.10	3.5	0.008	1.2	421.9	0.02	-5.0	400.8	0.00	0.0	421.9
0.10	4.0	0.008	1.2	494.0	0.02	-6.7	460.9	0.00	0.0	494.0
0.10	4.5	0.008	1.2	569.2	0.02	-8.5	520.9	0.00	0.0	569.2
0.10	5.0	0.008	1.2	647.7	0.02	-10.3	581.3	0.00	0.0	647.7
0.20	0.5	0.008	1.2	55.5	0.02	-2.2	54.3	0.00	0.0	55.5
0.20	1.0	0.008	1.2	114.9	0.02	-4.0	110.3	0.00	0.0	114.9
0.20	1.5	0.008	1.2	181.2	0.02	-6.3	169.8	0.00	0.0	181.2
0.20	2.0	0.008	1.2	254.7	0.02	-7.5	235.7	0.00	0.0	254.7
0.20	2.5	0.008	1.2	335.9	0.04	-10.4	300.9	0.00	0.0	335.9
0.20	3.0	0.008	1.2	424.9	0.04	-14.1	365.1	0.00	0.0	424.9
0.20	3.5	0.008	1.2	521.0	0.04	-15.5	440.2	0.02	-0.5	518.5
0.20	4.0	0.008	1.2	623.6	0.04	-16.6	519.9	0.02	-5.7	588.0
0.20	4.5	0.008	1.2	732.0	0.04	-17.6	603.2	0.02	-10.4	655.7
0.20	5.0	0.008	1.2	846.5	0.06	-20.8	670.8	0.02	-14.5	723.9
0.30	0.5	0.008	1.2	58.1	0.02	-2.7	56.5	0.00	0.0	58.1
0.30	1.0	0.008	1.2	123.5	0.04	-5.5	116.8	0.00	0.0	123.5
0.30	1.5	0.008	1.2	201.6	0.04	-8.3	184.8	0.00	0.0	201.6
0.30	2.0	0.008	1.2	293.0	0.06	-12.3	257.1	0.02	-2.6	285.5
0.30	2.5	0.008	1.2	398.0	0.06	-14.4	340.7	0.02	-9.1	361.9
0.30	3.0	0.008	1.2	514.7	0.08	-18.0	422.3	0.02	-10.6	459.9
0.30	3.5	0.008	1.2	640.4	0.08	-19.5	515.4	0.02	-11.9	564.2
0.30	4.0	0.008	1.2	773.9	0.10	-22.4	600.2	0.02	-13.1	672.8
0.30	4.5	0.008	1.2	915.8	0.10	-24.0	695.9	0.04	-18.1	749.8
0.30	5.0	0.008	1.2	1060.7	0.10	-25.2	793.6	0.04	-20.3	845.3
0.40	0.5	0.008	1.2	60.9	0.04	-3.7	58.6	0.00	0.0	60.9
0.40	1.0	0.008	1.2	134.0	0.06	-6.7	125.1	0.00	0.0	134.0
0.40	1.5	0.008	1.2	226.2	0.08	-10.5	202.4	0.02	-5.6	213.4
0.40	2.0	0.008	1.2	338.8	0.10	-14.3	290.4	0.02	-7.4	313.8
0.40	2.5	0.008	1.2	469.8	0.10	-16.8	390.8	0.04	-12.2	412.4
0.40	3.0	0.008	1.2	614.2	0.12	-20.0	491.2	0.04	-14.6	524.3
0.40	3.5	0.008	1.2	771.0	0.14	-22.3	599.2	0.04	-16.6	643.0
0.40	4.0	0.008	1.2	937.1	0.14	-25.0	702.7	0.06	-20.9	741.5
0.40	4.5	0.008	1.2	1108.8	0.14	-26.5	815.5	0.06	-22.7	857.6
0.40	5.0	0.008	1.2	1286.0	0.16	-28.6	918.2	0.06	-24.1	976.7
0.50	0.5	0.008	1.2	64.1	0.06	-4.2	61.4	0.00	0.0	64.1
0.50	1.0	0.008	1.2	146.2	0.10	-7.4	135.5	0.02	-4.0	140.4
0.50	1.5	0.008	1.2	254.2	0.10	-10.9	226.3	0.02	-5.3	240.6
0.50	2.0	0.008	1.2	389.5	0.12	-14.8	332.0	0.04	-10.4	348.9
0.50	2.5	0.008	1.2	546.3	0.14	-18.2	447.1	0.06	-14.9	465.0
0.50	3.0	0.008	1.2	720.5	0.16	-21.5	565.5	0.06	-17.7	592.9
0.50	3.5	0.008	1.2	908.1	0.16	-23.5	694.5	0.08	-21.5	712.7
0.50	4.0	0.008	1.2	1104.3	0.18	-25.6	821.9	0.08	-23.8	841.7
0.50	4.5	0.008	1.2	1308.5	0.18	-28.2	940.0	0.08	-25.5	974.3
0.50	5.0	0.008	1.2	1520.2	0.18	-29.5	1071.5	0.08	-27.0	1109.9
0.60	0.5	0.008	1.2	67.6	0.08	-4.3	64.7	0.02	-2.7	65.8
0.60	1.0	0.008	1.2	159.5	0.12	-7.7	147.3	0.02	-3.8	153.4
0.60	1.5	0.008	1.2	284.5	0.14	-11.6	251.4	0.04	-7.9	262.1
0.60	2.0	0.008	1.2	443.1	0.16	-15.6	374.0	0.06	-12.5	387.6
0.60	2.5	0.008	1.2	626.4	0.18	-18.8	508.8	0.08	-16.9	520.4
0.60	3.0	0.008	1.2	830.3	0.18	-21.4	652.7	0.08	-20.2	662.7
0.60	3.5	0.008	1.2	1046.5	0.18	-23.1	804.4	0.10	-23.8	797.2
0.60	4.0	0.008	1.2	1273.8	0.18	-24.6	960.2	0.10	-26.1	941.2
0.60	4.5	0.008	1.2	1511.2	0.20	-26.6	1109.8	0.10	-27.9	1088.8
0.60	5.0	0.008	1.2	1757.7	0.20	-28.8	1251.7	0.12	-30.8	1215.5
0.70	0.5	0.008	1.2	71.3	0.08	-4.2	68.3	0.02	-2.6	69.5
0.70	1.0	0.008	1.2	173.5	0.14	-7.6	160.3	0.04	-5.7	163.7
0.70	1.5	0.008	1.2	316.7	0.16	-11.7	279.6	0.06	-9.4	286.8
0.70	2.0	0.008	1.2	498.1	0.18	-15.4	421.6	0.08	-14.0	428.2
0.70	2.5	0.008	1.2	710.0	0.20	-17.9	582.9	0.10	-18.9	576.1
0.70	3.0	0.008	1.2	940.3	0.20	-20.1	751.4	0.10	-22.1	732.2
0.70	3.5	0.008	1.2	1185.4	0.20	-22.3	921.1	0.12	-25.7	880.6
0.70	4.0	0.008	1.2	1443.8	0.20	-23.7	1101.7	0.12	-28.1	1038.6
0.70	4.5	0.008	1.2	1714.3	0.20	-25.0	1286.4	0.14	-31.1	1181.8
0.70	5.0	0.008	1.2	1995.7	0.20	-26.1	1474.6	0.14	-33.1	1334.4

$\frac{W}{L}$ [−]	θ [deg]	$\frac{t}{L}$ [−]	$\frac{R}{L}$ [−]	$\sigma_{\mathrm{eq,max}}$ [MPa]	$\frac{\eta_{\mathrm{opt}}}{L}$ [−]	η_{perf} [%]	$\sigma_{\mathrm{eq,max}}$ [MPa]	$\frac{\eta_{\mathrm{opt}}}{L}$ [−]	η_{perf} [%]	$\sigma_{\mathrm{eq,max}}$ [MPa]
0.80	0.5	0.008	1.2	75.2	0.10	-4.1	72.1	0.04	-3.6	72.5
0.80	1.0	0.008	1.2	188.2	0.16	-7.5	174.0	0.06	-6.5	176.0
0.80	1.5	0.008	1.2	350.0	0.18	-11.6	309.4	0.08	-10.4	313.5
0.80	2.0	0.008	1.2	556.2	0.20	-15.2	471.9	0.10	-15.5	469.8
0.80	2.5	0.008	1.2	793.4	0.20	-17.3	656.1	0.12	-20.3	632.4
0.80	3.0	0.008	1.2	1049.9	0.20	-18.8	852.2	0.14	-24.1	796.5
0.80	3.5	0.008	1.2	1323.5	0.20	-20.2	1056.2	0.14	-27.3	962.3
0.80	4.0	0.008	1.2	1612.7	0.20	-21.5	1266.8	0.14	-29.7	1133.3
0.80	4.5	0.008	1.2	1916.0	0.20	-22.6	1483.0	0.16	-32.9	1284.9
0.80	5.0	0.008	1.2	2231.9	0.22	-24.0	1697.3	0.16	-35.1	1449.5
0.90	0.5	0.008	1.2	79.3	0.10	-3.9	76.2	0.04	-3.5	76.5
0.90	1.0	0.008	1.2	203.4	0.18	-7.3	188.5	0.08	-6.6	190.0
0.90	1.5	0.008	1.2	384.6	0.20	-11.4	340.7	0.10	-11.2	341.4
0.90	2.0	0.008	1.2	616.3	0.22	-14.3	528.1	0.12	-17.0	511.8
0.90	2.5	0.008	1.2	877.0	0.20	-15.8	738.7	0.14	-21.6	687.4
0.90	3.0	0.008	1.2	1159.1	0.20	-17.1	961.4	0.14	-25.0	869.4
0.90	3.5	0.008	1.2	1460.9	0.18	-17.6	1203.0	0.16	-28.7	1042.3
0.90	4.0	0.008	1.2	1780.3	0.20	-18.9	1443.0	0.16	-31.2	1225.6
0.90	4.5	0.008	1.2	2115.6	0.20	-20.5	1681.8	0.18	-33.6	1405.2
0.90	5.0	0.008	1.2	2465.4	0.20	-21.5	1936.4	0.18	-36.7	1560.6
1.00	0.5	0.008	1.2	83.5	0.12	-3.8	80.3	0.06	-3.7	80.4
1.00	1.0	0.008	1.2	219.0	0.18	-7.0	203.6	0.08	-6.8	204.1
1.00	1.5	0.008	1.2	420.4	0.22	-11.2	373.6	0.12	-12.0	370.2
1.00	2.0	0.008	1.2	676.8	0.22	-13.7	583.9	0.14	-18.1	554.1
1.00	2.5	0.008	1.2	960.6	0.18	-13.9	827.1	0.16	-22.7	742.5
1.00	3.0	0.008	1.2	1268.1	0.16	-14.6	1083.1	0.16	-26.1	936.5
1.00	3.5	0.008	1.2	1597.5	0.18	-16.2	1338.4	0.18	-29.9	1120.4
1.00	4.0	0.008	1.2	1946.7	0.18	-17.3	1610.5	0.18	-32.4	1315.3
1.00	4.5	0.008	1.2	2313.6	0.18	-18.2	1892.6	0.18	-34.5	1514.9
1.00	5.0	0.008	1.2	2696.5	0.20	-19.6	2167.8	0.20	-36.9	1700.3
1.25	0.5	0.008	1.2	94.5	0.14	-3.4	91.3	0.08	-3.7	91.0
1.25	1.0	0.008	1.2	261.6	0.22	-6.6	244.4	0.12	-7.6	241.8
1.25	1.5	0.008	1.2	520.4	0.26	-11.0	463.3	0.16	-14.7	443.8
1.25	2.0	0.008	1.2	830.5	0.18	-10.7	742.0	0.18	-20.5	660.2
1.25	2.5	0.008	1.2	1171.0	0.16	-11.3	1038.3	0.20	-24.9	879.4
1.25	3.0	0.008	1.2	1540.5	0.16	-12.3	1350.4	0.20	-28.1	1107.0
1.25	3.5	0.008	1.2	1936.9	0.18	-13.4	1676.8	0.22	-32.1	1315.7
1.25	4.0	0.008	1.2	2357.6	0.18	-14.3	2019.4	0.22	-34.5	1544.0
1.25	4.5	0.008	1.2	2800.4	0.18	-15.2	2376.0	0.22	-36.5	1778.1
1.25	5.0	0.008	1.2	3263.1	0.20	-16.0	2740.5	0.22	-38.2	2016.8
1.50	0.5	0.008	1.2	106.2	0.16	-2.8	103.2	0.08	-3.6	102.3
1.50	1.0	0.008	1.2	308.7	0.24	-6.3	289.4	0.14	-8.8	281.6
1.50	1.5	0.008	1.2	625.8	0.28	-9.8	564.3	0.18	-17.1	518.6
1.50	2.0	0.008	1.2	987.4	0.14	-10.0	888.7	0.20	-22.0	770.3
1.50	2.5	0.008	1.2	1383.0	0.16	-9.8	1247.3	0.22	-25.9	1024.7
1.50	3.0	0.008	1.2	1812.3	0.16	-10.7	1618.5	0.24	-29.9	1271.3
1.50	3.5	0.008	1.2	2272.9	0.16	-11.5	2011.3	0.24	-32.2	1541.5
1.50	4.0	0.008	1.2	2762.2	0.18	-12.2	2424.8	0.24	-34.1	1821.4
1.50	4.5	0.008	1.2	3277.5	0.18	-12.9	2855.7	0.26	-37.5	2049.6
1.50	5.0	0.008	1.2	3816.4	0.20	-13.4	3303.4	0.26	-40.1	2287.5
0.10	0.5	0.001	1.6	10.4	0.02	-2.0	10.2	0.00	0.0	10.4
0.10	1.0	0.001	1.6	24.4	0.02	-17.7	20.1	0.02	-0.5	24.3
0.10	1.5	0.001	1.6	39.6	0.02	-20.4	31.5	0.02	-9.3	35.9
0.10	2.0	0.001	1.6	55.1	0.02	-21.7	43.1	0.02	-14.0	47.4
0.10	2.5	0.001	1.6	70.9	0.02	-22.5	55.0	0.02	-17.1	58.8
0.10	3.0	0.001	1.6	87.3	0.04	-24.0	66.4	0.02	-19.3	70.5
0.10	3.5	0.001	1.6	104.3	0.04	-25.4	77.8	0.02	-21.0	82.4
0.10	4.0	0.001	1.6	121.9	0.04	-26.8	89.2	0.02	-22.6	94.4
0.10	4.5	0.001	1.6	140.0	0.04	-28.2	100.5	0.02	-24.0	106.4
0.10	5.0	0.001	1.6	158.6	0.04	-29.6	111.7	0.02	-25.4	118.3
0.20	0.5	0.001	1.6	13.1	0.04	-15.6	11.0	0.02	-7.0	12.1
0.20	1.0	0.001	1.6	31.5	0.06	-29.1	22.3	0.02	-22.1	24.6
0.20	1.5	0.001	1.6	52.2	0.06	-32.8	35.1	0.02	-24.6	39.4
0.20	2.0	0.001	1.6	75.0	0.06	-35.3	48.5	0.04	-26.3	55.3
0.20	2.5	0.001	1.6	99.3	0.06	-37.1	62.4	0.04	-31.7	67.8
0.20	3.0	0.001	1.6	124.5	0.06	-38.5	76.6	0.04	-35.8	80.0
0.20	3.5	0.001	1.6	150.6	0.08	-40.1	90.3	0.04	-38.9	92.1
0.20	4.0	0.001	1.6	177.4	0.08	-41.7	103.4	0.04	-40.8	105.1
0.20	4.5	0.001	1.6	204.8	0.08	-43.2	116.4	0.04	-42.1	118.7
0.20	5.0	0.001	1.6	232.6	0.08	-44.4	129.4	0.04	-43.1	132.3

$\frac{W}{L}$ [−]	θ [deg]	$\frac{t}{L}$ [−]	$\frac{R}{L}$ [−]	$\sigma_{\mathrm{eq,max}}$ [MPa]	$\frac{\eta_{\mathrm{opt}}}{L}$ [−]	η_{perf} [%]	$\sigma_{\mathrm{eq,max}}$ [MPa]	$\frac{\eta_{\mathrm{opt}}}{L}$ [−]	η_{perf} [%]	$\sigma_{\mathrm{eq,max}}$ [MPa]
0.30	0.5	0.001	1.6	15.8	0.08	-24.5	11.9	0.02	-15.7	13.3
0.30	1.0	0.001	1.6	39.1	0.08	-30.7	27.1	0.04	-27.6	28.3
0.30	1.5	0.001	1.6	66.5	0.10	-36.2	42.4	0.04	-32.1	45.1
0.30	2.0	0.001	1.6	96.2	0.10	-40.5	57.3	0.06	-38.9	58.7
0.30	2.5	0.001	1.6	127.8	0.12	-42.5	73.4	0.06	-43.4	72.3
0.30	3.0	0.001	1.6	160.7	0.12	-44.9	88.5	0.06	-45.7	87.2
0.30	3.5	0.001	1.6	194.7	0.12	-46.7	103.8	0.06	-47.4	102.3
0.30	4.0	0.001	1.6	229.7	0.12	-48.1	119.2	0.06	-48.8	117.6
0.30	4.5	0.001	1.6	265.4	0.12	-49.2	134.7	0.06	-49.9	133.0
0.30	5.0	0.001	1.6	301.7	0.12	-50.2	150.3	0.06	-50.8	148.4
0.40	0.5	0.001	1.6	18.7	0.10	-25.6	13.9	0.04	-20.5	14.9
0.40	1.0	0.001	1.6	47.6	0.12	-36.4	30.3	0.06	-33.4	31.7
0.40	1.5	0.001	1.6	81.5	0.12	-41.0	48.1	0.08	-40.0	48.9
0.40	2.0	0.001	1.6	118.4	0.16	-44.4	65.8	0.08	-45.9	64.1
0.40	2.5	0.001	1.6	157.5	0.16	-47.1	83.4	0.08	-49.7	79.2
0.40	3.0	0.001	1.6	198.3	0.16	-48.9	101.4	0.08	-52.2	94.8
0.40	3.5	0.001	1.6	240.5	0.16	-50.2	119.9	0.08	-53.6	111.7
0.40	4.0	0.001	1.6	283.7	0.16	-51.1	138.7	0.08	-54.6	128.7
0.40	4.5	0.001	1.6	327.8	0.16	-51.9	157.8	0.08	-55.5	146.0
0.40	5.0	0.001	1.6	372.7	0.16	-52.4	177.3	0.08	-56.2	163.3
0.50	0.5	0.001	1.6	21.7	0.14	-27.3	15.8	0.06	-24.5	16.4
0.50	1.0	0.001	1.6	56.0	0.16	-40.4	33.4	0.08	-38.0	34.8
0.50	1.5	0.001	1.6	96.2	0.16	-46.4	51.6	0.10	-44.0	53.9
0.50	2.0	0.001	1.6	139.9	0.16	-49.3	71.0	0.10	-49.1	71.3
0.50	2.5	0.001	1.6	186.0	0.18	-51.1	90.9	0.10	-52.5	88.4
0.50	3.0	0.001	1.6	234.0	0.18	-52.5	111.2	0.10	-55.0	105.3
0.50	3.5	0.001	1.6	283.5	0.18	-53.3	132.4	0.10	-57.0	122.0
0.50	4.0	0.001	1.6	334.2	0.18	-53.6	154.9	0.10	-58.6	138.5
0.50	4.5	0.001	1.6	385.8	0.18	-53.8	178.1	0.10	-59.0	158.0
0.50	5.0	0.001	1.6	438.1	0.16	-54.0	201.7	0.10	-58.8	180.5
0.60	0.5	0.001	1.6	24.7	0.16	-26.6	18.2	0.08	-27.5	17.9
0.60	1.0	0.001	1.6	64.7	0.20	-39.6	39.0	0.10	-41.9	37.6
0.60	1.5	0.001	1.6	111.3	0.20	-44.0	62.3	0.10	-47.3	58.7
0.60	2.0	0.001	1.6	161.8	0.20	-46.6	86.5	0.12	-50.7	79.8
0.60	2.5	0.001	1.6	215.0	0.20	-48.2	111.4	0.12	-53.9	99.2
0.60	3.0	0.001	1.6	270.2	0.18	-49.5	136.4	0.12	-56.2	118.3
0.60	3.5	0.001	1.6	326.9	0.18	-50.7	161.1	0.12	-58.1	137.0
0.60	4.0	0.001	1.6	384.9	0.18	-51.6	186.2	0.12	-59.6	155.4
0.60	4.5	0.001	1.6	443.8	0.18	-52.3	211.5	0.12	-59.9	178.1
0.60	5.0	0.001	1.6	503.5	0.18	-52.9	237.1	0.12	-59.5	203.9
0.70	0.5	0.001	1.6	27.8	0.16	-26.6	20.4	0.10	-30.5	19.3
0.70	1.0	0.001	1.6	73.5	0.20	-40.2	44.0	0.12	-45.4	40.2
0.70	1.5	0.001	1.6	126.8	0.20	-45.3	69.4	0.12	-50.8	62.4
0.70	2.0	0.001	1.6	184.3	0.20	-47.6	96.6	0.12	-53.7	85.2
0.70	2.5	0.001	1.6	244.6	0.20	-49.0	124.7	0.12	-55.5	108.9
0.70	3.0	0.001	1.6	306.8	0.20	-49.9	153.9	0.12	-56.6	133.3
0.70	3.5	0.001	1.6	370.5	0.20	-50.3	184.0	0.14	-58.2	154.9
0.70	4.0	0.001	1.6	435.4	0.20	-50.6	215.1	0.14	-59.6	176.1
0.70	4.5	0.001	1.6	501.3	0.20	-50.7	247.3	0.14	-60.0	200.3
0.70	5.0	0.001	1.6	567.9	0.20	-50.6	280.5	0.14	-59.6	229.5
0.80	0.5	0.001	1.6	30.8	0.18	-26.1	22.7	0.12	-32.6	20.7
0.80	1.0	0.001	1.6	82.3	0.20	-37.3	51.5	0.14	-48.5	42.4
0.80	1.5	0.001	1.6	142.3	0.20	-42.1	82.4	0.14	-54.1	65.3
0.80	2.0	0.001	1.6	206.9	0.20	-44.8	114.2	0.14	-57.2	88.7
0.80	2.5	0.001	1.6	274.6	0.20	-46.5	146.9	0.14	-59.0	112.6
0.80	3.0	0.001	1.6	344.2	0.20	-47.1	182.1	0.14	-60.1	137.3
0.80	3.5	0.001	1.6	415.3	0.20	-47.0	220.0	0.14	-60.8	162.6
0.80	4.0	0.001	1.6	487.4	0.22	-46.9	258.6	0.14	-61.3	188.6
0.80	4.5	0.001	1.6	560.2	0.22	-47.2	295.9	0.14	-61.6	215.3
0.80	5.0	0.001	1.6	633.6	0.22	-47.2	334.5	0.14	-61.3	245.1
0.90	0.5	0.001	1.6	33.7	0.20	-24.9	25.3	0.14	-34.7	22.0
0.90	1.0	0.001	1.6	90.5	0.22	-36.0	58.0	0.16	-50.4	44.8
0.90	1.5	0.001	1.6	156.6	0.22	-40.7	92.8	0.16	-56.8	67.6
0.90	2.0	0.001	1.6	227.7	0.22	-43.6	128.4	0.16	-60.0	91.1
0.90	2.5	0.001	1.6	301.9	0.22	-45.3	165.0	0.16	-61.7	115.7
0.90	3.0	0.001	1.6	378.1	0.22	-45.8	205.0	0.16	-62.3	142.5
0.90	3.5	0.001	1.6	455.6	0.22	-45.5	248.1	0.16	-62.6	170.4
0.90	4.0	0.001	1.6	533.9	0.22	-45.2	292.5	0.16	-62.7	199.3
0.90	4.5	0.001	1.6	612.9	0.22	-44.9	337.9	0.16	-62.6	229.5
0.90	5.0	0.001	1.6	692.2	0.22	-44.5	384.2	0.16	-62.3	260.8

$\frac{W}{L}$ [−]	θ [deg]	$\frac{t}{L}$ [−]	$\frac{R}{L}$ [−]	$\sigma_{\mathrm{eq,max}}$ [MPa]	$\frac{\eta_{\mathrm{opt}}}{L}$ [−]	η_{perf} [%]	$\sigma_{\mathrm{eq,max}}$ [MPa]	$\frac{\eta_{\mathrm{opt}}}{L}$ [−]	η_{perf} [%]	$\sigma_{\mathrm{eq,max}}$ [MPa]
1.00	0.5	0.001	1.6	36.7	0.20	-22.5	28.4	0.16	-37.0	23.1
1.00	1.0	0.001	1.6	98.9	0.22	-31.6	67.6	0.16	-48.8	50.6
1.00	1.5	0.001	1.6	171.4	0.22	-36.6	108.7	0.18	-55.9	75.7
1.00	2.0	0.001	1.6	249.5	0.22	-39.2	151.7	0.18	-60.1	99.4
1.00	2.5	0.001	1.6	330.6	0.24	-40.4	197.1	0.18	-61.7	126.6
1.00	3.0	0.001	1.6	413.8	0.24	-42.1	239.7	0.18	-62.4	155.6
1.00	3.5	0.001	1.6	498.1	0.24	-43.1	283.2	0.18	-62.8	185.2
1.00	4.0	0.001	1.6	583.2	0.24	-43.7	328.3	0.18	-63.1	215.3
1.00	4.5	0.001	1.6	668.6	0.24	-43.7	376.2	0.18	-63.2	246.0
1.00	5.0	0.001	1.6	754.2	0.24	-43.5	426.2	0.18	-63.2	277.3
1.25	0.5	0.001	1.6	44.1	0.20	-17.8	36.3	0.18	-37.5	27.6
1.25	1.0	0.001	1.6	119.5	0.24	-26.6	87.6	0.20	-52.7	56.5
1.25	1.5	0.001	1.6	207.7	0.26	-30.2	145.1	0.20	-57.9	87.4
1.25	2.0	0.001	1.6	302.7	0.26	-33.0	202.8	0.20	-60.9	118.3
1.25	2.5	0.001	1.6	401.5	0.26	-33.3	267.9	0.20	-62.7	149.6
1.25	3.0	0.001	1.6	502.3	0.26	-32.7	338.0	0.20	-63.8	181.9
1.25	3.5	0.001	1.6	604.1	0.26	-32.0	410.5	0.20	-64.2	216.4
1.25	4.0	0.001	1.6	706.4	0.26	-31.4	484.6	0.20	-64.4	251.2
1.25	4.5	0.001	1.6	808.7	0.26	-30.8	559.7	0.20	-64.6	286.2
1.25	5.0	0.001	1.6	910.6	0.26	-30.2	635.3	0.20	-64.7	321.6
1.50	0.5	0.001	1.6	51.2	0.22	-14.5	43.8	0.22	-38.9	31.3
1.50	1.0	0.001	1.6	138.7	0.24	-20.1	110.8	0.22	-50.9	68.1
1.50	1.5	0.001	1.6	241.6	0.24	-19.9	193.4	0.24	-57.7	102.2
1.50	2.0	0.001	1.6	352.4	0.26	-19.6	283.4	0.24	-62.5	132.3
1.50	2.5	0.001	1.6	467.7	0.26	-19.7	375.5	0.24	-64.5	165.9
1.50	3.0	0.001	1.6	585.3	0.28	-20.2	467.3	0.24	-64.7	206.5
1.50	3.5	0.001	1.6	703.9	0.28	-20.7	558.2	0.24	-64.8	247.5
1.50	4.0	0.001	1.6	822.7	0.28	-19.9	659.2	0.24	-64.9	288.8
1.50	4.5	0.001	1.6	941.3	0.28	-19.2	761.0	0.24	-64.9	330.7
1.50	5.0	0.001	1.6	1059.2	0.28	-18.5	862.9	0.24	-64.4	376.6
0.10	0.5	0.002	1.6	18.7	0.00	0.0	18.7	0.00	0.0	18.7
0.10	1.0	0.002	1.6	41.3	0.02	-1.1	40.8	0.00	0.0	41.3
0.10	1.5	0.002	1.6	67.7	0.02	-10.0	60.9	0.00	0.0	67.7
0.10	2.0	0.002	1.6	96.6	0.02	-16.8	80.4	0.00	0.0	96.6
0.10	2.5	0.002	1.6	126.3	0.02	-18.8	102.6	0.02	-4.6	120.6
0.10	3.0	0.002	1.6	156.0	0.02	-19.6	125.4	0.02	-8.0	143.6
0.10	3.5	0.002	1.6	186.5	0.02	-20.4	148.5	0.02	-10.5	166.8
0.10	4.0	0.002	1.6	217.3	0.02	-20.9	171.8	0.02	-12.6	190.0
0.10	4.5	0.002	1.6	248.6	0.02	-21.3	195.6	0.02	-14.2	213.2
0.10	5.0	0.002	1.6	280.4	0.02	-21.7	219.5	0.02	-15.7	236.5
0.20	0.5	0.002	1.6	21.2	0.02	-8.6	19.4	0.00	0.0	21.2
0.20	1.0	0.002	1.6	51.4	0.04	-19.0	41.7	0.02	-5.9	48.4
0.20	1.5	0.002	1.6	86.4	0.06	-22.8	66.8	0.02	-18.2	70.7
0.20	2.0	0.002	1.6	124.0	0.06	-28.4	88.7	0.02	-20.9	98.1
0.20	2.5	0.002	1.6	163.2	0.06	-30.1	114.1	0.02	-22.4	126.7
0.20	3.0	0.002	1.6	204.4	0.06	-31.4	140.2	0.02	-23.4	156.6
0.20	3.5	0.002	1.6	248.5	0.06	-32.8	166.9	0.02	-24.3	188.1
0.20	4.0	0.002	1.6	294.2	0.08	-34.6	192.5	0.02	-25.1	220.3
0.20	4.5	0.002	1.6	341.3	0.08	-36.7	216.1	0.04	-27.6	247.1
0.20	5.0	0.002	1.6	389.6	0.08	-38.5	239.7	0.04	-30.1	272.4
0.30	0.5	0.002	1.6	24.4	0.04	-12.3	21.4	0.02	-3.0	23.7
0.30	1.0	0.002	1.6	62.2	0.08	-23.7	47.5	0.02	-14.7	53.1
0.30	1.5	0.002	1.6	106.2	0.10	-29.7	74.7	0.04	-23.6	81.1
0.30	2.0	0.002	1.6	154.3	0.10	-32.8	103.7	0.04	-26.7	113.0
0.30	2.5	0.002	1.6	205.7	0.12	-35.5	132.6	0.04	-29.0	146.1
0.30	3.0	0.002	1.6	260.9	0.12	-39.0	159.1	0.04	-31.0	180.0
0.30	3.5	0.002	1.6	318.5	0.12	-41.7	185.8	0.06	-34.7	208.0
0.30	4.0	0.002	1.6	378.1	0.12	-43.8	212.6	0.06	-37.7	235.5
0.30	4.5	0.002	1.6	439.5	0.12	-45.5	239.5	0.06	-40.1	263.2
0.30	5.0	0.002	1.6	502.6	0.12	-47.0	266.6	0.06	-42.1	291.2
0.40	0.5	0.002	1.6	28.1	0.08	-16.4	23.5	0.02	-9.4	25.5
0.40	1.0	0.002	1.6	73.9	0.12	-26.8	54.1	0.04	-19.8	59.3
0.40	1.5	0.002	1.6	127.7	0.12	-32.3	86.5	0.06	-28.6	91.3
0.40	2.0	0.002	1.6	186.8	0.14	-36.1	119.4	0.06	-32.2	126.6
0.40	2.5	0.002	1.6	251.5	0.14	-40.4	149.9	0.06	-35.2	162.9
0.40	3.0	0.002	1.6	319.8	0.14	-43.6	180.5	0.08	-38.8	195.8
0.40	3.5	0.002	1.6	391.1	0.14	-46.0	211.3	0.08	-42.0	226.7
0.40	4.0	0.002	1.6	464.9	0.14	-47.9	242.3	0.08	-44.5	257.9
0.40	4.5	0.002	1.6	541.0	0.14	-49.1	275.3	0.08	-46.5	289.3
0.40	5.0	0.002	1.6	619.0	0.14	-50.1	309.2	0.08	-48.2	320.9

$\frac{W}{L}$ [−]	θ [deg]	$\frac{t}{L}$ [−]	$\frac{R}{L}$ [−]	$\sigma_{\mathrm{eq,max}}$ [MPa]	$\frac{\eta_{\mathrm{opt}}}{L}$ [−]	η_{perf} [%]	$\sigma_{\mathrm{eq,max}}$ [MPa]	$\frac{\eta_{\mathrm{opt}}}{L}$ [−]	η_{perf} [%]	$\sigma_{\mathrm{eq,max}}$ [MPa]
0.50	0.5	0.002	1.6	32.2	0.12	-19.2	26.0	0.04	-12.6	28.1
0.50	1.0	0.002	1.6	85.8	0.16	-30.9	59.2	0.06	-23.7	65.5
0.50	1.5	0.002	1.6	149.1	0.16	-36.5	94.7	0.08	-32.6	100.6
0.50	2.0	0.002	1.6	220.2	0.18	-42.0	127.8	0.08	-37.0	138.7
0.50	2.5	0.002	1.6	297.2	0.18	-44.7	164.2	0.08	-40.1	177.9
0.50	3.0	0.002	1.6	378.3	0.18	-46.7	201.5	0.10	-42.8	216.4
0.50	3.5	0.002	1.6	462.9	0.18	-48.3	239.5	0.10	-45.6	251.6
0.50	4.0	0.002	1.6	550.4	0.18	-49.5	278.1	0.10	-47.8	287.2
0.50	4.5	0.002	1.6	640.3	0.18	-50.4	317.6	0.10	-49.6	323.0
0.50	5.0	0.002	1.6	732.5	0.18	-51.0	358.6	0.10	-51.0	358.9
0.60	0.5	0.002	1.6	36.4	0.12	-18.0	29.8	0.06	-15.7	30.7
0.60	1.0	0.002	1.6	97.8	0.16	-28.4	70.0	0.08	-26.8	71.5
0.60	1.5	0.002	1.6	171.3	0.20	-36.4	109.0	0.10	-36.3	109.1
0.60	2.0	0.002	1.6	254.4	0.20	-42.0	147.5	0.10	-41.1	149.9
0.60	2.5	0.002	1.6	343.9	0.20	-44.1	192.1	0.10	-44.3	191.5
0.60	3.0	0.002	1.6	438.1	0.18	-46.0	236.6	0.10	-46.6	233.9
0.60	3.5	0.002	1.6	536.2	0.18	-47.7	280.4	0.10	-48.3	277.1
0.60	4.0	0.002	1.6	637.4	0.18	-49.0	324.9	0.10	-49.7	320.9
0.60	4.5	0.002	1.6	741.3	0.18	-50.1	370.0	0.12	-51.1	362.7
0.60	5.0	0.002	1.6	847.5	0.18	-50.9	415.9	0.12	-52.4	403.5
0.70	0.5	0.002	1.6	40.5	0.14	-18.2	33.2	0.08	-17.6	33.4
0.70	1.0	0.002	1.6	110.3	0.20	-29.4	77.9	0.10	-30.0	77.2
0.70	1.5	0.002	1.6	194.0	0.20	-36.3	123.6	0.12	-39.6	117.1
0.70	2.0	0.002	1.6	289.1	0.20	-40.4	172.4	0.12	-44.6	160.2
0.70	2.5	0.002	1.6	391.4	0.20	-43.4	221.5	0.12	-47.9	204.0
0.70	3.0	0.002	1.6	498.9	0.20	-45.7	271.0	0.12	-50.2	248.3
0.70	3.5	0.002	1.6	610.5	0.20	-47.5	320.8	0.12	-52.0	293.1
0.70	4.0	0.002	1.6	725.5	0.20	-48.5	373.3	0.12	-53.3	338.5
0.70	4.5	0.002	1.6	843.4	0.20	-49.3	427.4	0.12	-54.4	384.4
0.70	5.0	0.002	1.6	963.6	0.20	-49.9	482.5	0.12	-55.3	430.9
0.80	0.5	0.002	1.6	44.7	0.16	-18.3	36.5	0.10	-19.1	36.1
0.80	1.0	0.002	1.6	122.5	0.20	-28.0	88.2	0.12	-32.5	82.7
0.80	1.5	0.002	1.6	216.4	0.20	-32.6	145.9	0.14	-42.6	124.2
0.80	2.0	0.002	1.6	323.5	0.22	-36.6	205.0	0.14	-47.7	169.1
0.80	2.5	0.002	1.6	438.5	0.22	-40.6	260.3	0.14	-51.1	214.5
0.80	3.0	0.002	1.6	559.4	0.22	-42.8	319.8	0.14	-53.5	260.1
0.80	3.5	0.002	1.6	684.8	0.22	-44.4	380.6	0.14	-55.3	305.9
0.80	4.0	0.002	1.6	813.9	0.22	-45.7	442.3	0.14	-56.8	352.0
0.80	4.5	0.002	1.6	945.9	0.22	-46.6	504.8	0.14	-57.9	398.4
0.80	5.0	0.002	1.6	1080.4	0.22	-47.3	568.9	0.14	-58.8	445.1
0.90	0.5	0.002	1.6	48.9	0.18	-17.9	40.1	0.10	-19.5	39.3
0.90	1.0	0.002	1.6	134.5	0.20	-24.9	100.9	0.14	-34.8	87.7
0.90	1.5	0.002	1.6	238.2	0.22	-31.3	163.6	0.16	-41.9	138.3
0.90	2.0	0.002	1.6	356.6	0.22	-35.1	231.3	0.16	-49.6	179.7
0.90	2.5	0.002	1.6	483.8	0.22	-38.0	300.1	0.16	-53.9	223.1
0.90	3.0	0.002	1.6	617.5	0.22	-40.2	369.6	0.16	-56.4	269.2
0.90	3.5	0.002	1.6	756.1	0.22	-41.9	439.5	0.16	-58.3	315.2
0.90	4.0	0.002	1.6	898.5	0.22	-43.2	510.0	0.16	-59.8	361.2
0.90	4.5	0.002	1.6	1043.9	0.22	-44.4	580.9	0.16	-61.0	407.6
0.90	5.0	0.002	1.6	1191.9	0.22	-45.3	652.3	0.16	-61.4	459.6
1.00	0.5	0.002	1.6	53.0	0.18	-15.8	44.7	0.12	-21.0	41.9
1.00	1.0	0.002	1.6	146.4	0.22	-22.8	113.0	0.16	-36.9	92.4
1.00	1.5	0.002	1.6	260.1	0.22	-27.9	187.4	0.16	-43.8	146.2
1.00	2.0	0.002	1.6	389.9	0.22	-31.5	267.2	0.16	-48.2	201.8
1.00	2.5	0.002	1.6	529.5	0.22	-34.1	349.1	0.18	-51.7	256.0
1.00	3.0	0.002	1.6	676.2	0.22	-36.0	432.4	0.18	-54.8	305.4
1.00	3.5	0.002	1.6	828.2	0.22	-37.6	516.8	0.18	-57.1	355.2
1.00	4.0	0.002	1.6	984.3	0.24	-39.5	595.9	0.18	-58.8	405.3
1.00	4.5	0.002	1.6	1143.6	0.24	-40.9	675.7	0.18	-60.1	456.4
1.00	5.0	0.002	1.6	1305.5	0.24	-42.1	756.5	0.18	-61.1	508.3
1.25	0.5	0.002	1.6	63.6	0.20	-13.5	55.0	0.16	-23.8	48.5
1.25	1.0	0.002	1.6	175.8	0.24	-17.6	144.8	0.18	-37.3	110.2
1.25	1.5	0.002	1.6	313.4	0.24	-22.1	244.2	0.20	-47.5	164.4
1.25	2.0	0.002	1.6	470.8	0.24	-25.7	349.8	0.20	-52.1	225.5
1.25	2.5	0.002	1.6	640.5	0.24	-28.0	461.1	0.20	-55.2	286.7
1.25	3.0	0.002	1.6	819.1	0.24	-29.7	576.1	0.20	-57.6	347.5
1.25	3.5	0.002	1.6	1004.2	0.26	-31.6	686.4	0.20	-59.4	407.9
1.25	4.0	0.002	1.6	1194.3	0.26	-33.3	796.9	0.20	-60.8	468.0
1.25	4.5	0.002	1.6	1388.1	0.26	-33.6	921.4	0.20	-62.0	527.7
1.25	5.0	0.002	1.6	1584.9	0.26	-33.9	1047.0	0.20	-63.0	586.9

$\frac{W}{L}$ [−]	θ [deg]	$\frac{t}{L}$ [−]	$\frac{R}{L}$ [−]	$\sigma_{\mathrm{eq,max}}$ [MPa]	$\frac{\eta_{\mathrm{opt}}}{L}$ [−]	η_{perf} [%]	$\sigma_{\mathrm{eq,max}}$ [MPa]	$\frac{\eta_{\mathrm{opt}}}{L}$ [−]	η_{perf} [%]	$\sigma_{\mathrm{eq,max}}$ [MPa]
1.50	0.5	0.002	1.6	74.4	0.20	-10.6	66.5	0.18	-25.2	55.7
1.50	1.0	0.002	1.6	204.0	0.22	-14.2	175.1	0.22	-39.4	123.6
1.50	1.5	0.002	1.6	364.2	0.24	-17.5	300.4	0.22	-46.3	195.5
1.50	2.0	0.002	1.6	547.5	0.24	-19.9	438.7	0.22	-50.5	271.1
1.50	2.5	0.002	1.6	745.4	0.24	-20.4	593.1	0.22	-53.5	346.9
1.50	3.0	0.002	1.6	954.1	0.24	-20.2	761.8	0.24	-56.5	415.0
1.50	3.5	0.002	1.6	1170.6	0.24	-19.8	939.0	0.24	-58.9	480.9
1.50	4.0	0.002	1.6	1393.1	0.28	-20.9	1102.3	0.24	-60.7	547.0
1.50	4.5	0.002	1.6	1620.2	0.28	-23.4	1241.1	0.24	-62.1	614.3
1.50	5.0	0.002	1.6	1850.7	0.28	-23.7	1412.6	0.24	-63.1	683.1
0.10	0.5	0.005	1.6	43.8	0.00	0.0	43.8	0.00	0.0	43.8
0.10	1.0	0.005	1.6	90.7	0.00	0.0	90.7	0.00	0.0	90.7
0.10	1.5	0.005	1.6	141.1	0.00	0.0	141.1	0.00	0.0	141.1
0.10	2.0	0.005	1.6	195.5	0.02	-1.0	193.6	0.00	0.0	195.5
0.10	2.5	0.005	1.6	254.1	0.02	-4.6	242.3	0.00	0.0	254.1
0.10	3.0	0.005	1.6	316.2	0.02	-7.9	291.2	0.00	0.0	316.2
0.10	3.5	0.005	1.6	381.3	0.02	-11.0	339.5	0.00	0.0	381.3
0.10	4.0	0.005	1.6	449.0	0.02	-13.7	387.4	0.00	0.0	449.0
0.10	4.5	0.005	1.6	518.6	0.02	-14.8	441.8	0.00	0.0	518.6
0.10	5.0	0.005	1.6	589.5	0.02	-15.6	497.3	0.00	0.0	589.5
0.20	0.5	0.005	1.6	46.0	0.02	-2.5	44.8	0.00	0.0	46.0
0.20	1.0	0.005	1.6	100.1	0.02	-7.2	92.9	0.00	0.0	100.1
0.20	1.5	0.005	1.6	163.8	0.02	-8.7	149.5	0.00	0.0	163.8
0.20	2.0	0.005	1.6	236.4	0.04	-15.6	199.6	0.00	0.0	236.4
0.20	2.5	0.005	1.6	315.7	0.04	-17.6	260.2	0.02	-4.3	302.2
0.20	3.0	0.005	1.6	399.4	0.04	-18.9	323.8	0.02	-10.5	357.6
0.20	3.5	0.005	1.6	484.6	0.06	-23.0	373.3	0.02	-15.0	411.9
0.20	4.0	0.005	1.6	572.8	0.06	-24.7	431.5	0.02	-16.8	476.4
0.20	4.5	0.005	1.6	663.6	0.06	-25.7	493.2	0.02	-17.9	544.8
0.20	5.0	0.005	1.6	757.7	0.06	-26.6	555.9	0.02	-18.9	614.6
0.30	0.5	0.005	1.6	48.6	0.02	-3.3	47.0	0.00	0.0	48.6
0.30	1.0	0.005	1.6	112.1	0.04	-9.5	101.5	0.00	0.0	112.1
0.30	1.5	0.005	1.6	192.4	0.06	-15.5	162.5	0.02	-8.9	175.2
0.30	2.0	0.005	1.6	284.4	0.08	-20.6	225.8	0.02	-11.9	250.5
0.30	2.5	0.005	1.6	383.6	0.08	-22.8	296.1	0.02	-13.6	331.5
0.30	3.0	0.005	1.6	486.6	0.10	-26.6	356.9	0.04	-15.8	409.8
0.30	3.5	0.005	1.6	595.0	0.10	-28.3	426.5	0.04	-21.2	468.9
0.30	4.0	0.005	1.6	710.0	0.10	-30.0	497.1	0.04	-23.1	546.2
0.30	4.5	0.005	1.6	829.0	0.10	-31.4	568.6	0.04	-24.5	625.8
0.30	5.0	0.005	1.6	951.4	0.12	-34.3	625.3	0.04	-25.7	706.9
0.40	0.5	0.005	1.6	51.9	0.06	-4.9	49.3	0.00	0.0	51.9
0.40	1.0	0.005	1.6	126.8	0.08	-12.8	110.6	0.02	-6.7	118.3
0.40	1.5	0.005	1.6	224.6	0.10	-19.1	181.7	0.02	-9.5	203.2
0.40	2.0	0.005	1.6	335.9	0.12	-24.3	254.2	0.04	-16.6	280.1
0.40	2.5	0.005	1.6	454.7	0.12	-26.7	333.4	0.04	-18.7	369.7
0.40	3.0	0.005	1.6	582.2	0.14	-31.3	399.7	0.06	-24.2	441.3
0.40	3.5	0.005	1.6	718.2	0.14	-34.0	474.1	0.06	-26.6	526.8
0.40	4.0	0.005	1.6	859.6	0.14	-35.9	550.9	0.06	-28.6	613.8
0.40	4.5	0.005	1.6	1005.7	0.14	-37.6	628.0	0.06	-30.2	701.9
0.40	5.0	0.005	1.6	1156.2	0.14	-39.0	705.4	0.06	-31.6	791.1
0.50	0.5	0.005	1.6	55.8	0.08	-6.1	52.4	0.02	-1.6	54.9
0.50	1.0	0.005	1.6	143.1	0.10	-14.0	123.1	0.04	-7.1	133.0
0.50	1.5	0.005	1.6	258.2	0.14	-21.1	203.7	0.04	-13.6	223.2
0.50	2.0	0.005	1.6	387.9	0.14	-25.1	290.5	0.06	-19.9	310.6
0.50	2.5	0.005	1.6	529.0	0.16	-30.4	368.3	0.06	-22.8	408.6
0.50	3.0	0.005	1.6	682.3	0.16	-33.1	456.5	0.08	-28.5	488.1
0.50	3.5	0.005	1.6	843.1	0.16	-35.3	545.5	0.08	-31.1	581.0
0.50	4.0	0.005	1.6	1010.7	0.18	-38.2	624.3	0.08	-33.2	675.1
0.50	4.5	0.005	1.6	1184.0	0.18	-40.9	699.4	0.08	-35.0	770.1
0.50	5.0	0.005	1.6	1362.7	0.18	-42.9	778.6	0.08	-36.4	866.1
0.60	0.5	0.005	1.6	60.1	0.10	-6.8	56.0	0.02	-3.4	58.0
0.60	1.0	0.005	1.6	160.3	0.14	-15.9	134.8	0.04	-9.7	144.8
0.60	1.5	0.005	1.6	292.4	0.16	-22.3	227.1	0.06	-16.7	243.4
0.60	2.0	0.005	1.6	440.9	0.18	-26.7	323.2	0.08	-22.8	340.5
0.60	2.5	0.005	1.6	606.1	0.18	-30.9	418.7	0.08	-26.4	446.2
0.60	3.0	0.005	1.6	783.1	0.18	-33.5	520.8	0.10	-32.1	531.4
0.60	3.5	0.005	1.6	969.5	0.20	-36.7	613.6	0.10	-34.9	630.8
0.60	4.0	0.005	1.6	1163.8	0.20	-39.7	701.4	0.10	-37.2	731.2
0.60	4.5	0.005	1.6	1365.1	0.20	-41.7	796.5	0.10	-39.0	832.4
0.60	5.0	0.005	1.6	1572.5	0.20	-42.5	903.8	0.10	-40.6	934.4

$\frac{W}{L}$ [−]	θ [deg]	$\frac{t}{L}$ [−]	$\frac{R}{L}$ [−]	$\sigma_{\mathrm{eq,max}}$ [MPa]	$\frac{\eta_{\mathrm{opt}}}{L}$ [−]	η_{perf} [%]	$\sigma_{\mathrm{eq,max}}$ [MPa]	$\frac{\eta_{\mathrm{opt}}}{L}$ [−]	η_{perf} [%]	$\sigma_{\mathrm{eq,max}}$ [MPa]
0.70	0.5	0.005	1.6	64.6	0.12	-7.2	59.9	0.02	-3.2	62.5
0.70	1.0	0.005	1.6	178.1	0.16	-16.5	148.7	0.06	-11.8	157.0
0.70	1.5	0.005	1.6	326.2	0.18	-22.3	253.5	0.08	-19.0	264.2
0.70	2.0	0.005	1.6	495.3	0.20	-25.9	367.3	0.10	-25.5	369.1
0.70	2.5	0.005	1.6	683.3	0.20	-30.7	473.3	0.10	-29.5	481.8
0.70	3.0	0.005	1.6	884.4	0.20	-33.2	590.8	0.12	-35.3	572.1
0.70	3.5	0.005	1.6	1096.5	0.20	-35.3	709.7	0.12	-38.2	677.1
0.70	4.0	0.005	1.6	1317.9	0.20	-37.1	829.4	0.12	-40.6	783.1
0.70	4.5	0.005	1.6	1547.3	0.22	-38.9	944.8	0.12	-42.5	889.8
0.70	5.0	0.005	1.6	1783.7	0.22	-40.6	1059.2	0.12	-44.1	996.9
0.80	0.5	0.005	1.6	69.3	0.14	-7.4	64.1	0.04	-4.9	65.9
0.80	1.0	0.005	1.6	195.9	0.18	-16.7	163.2	0.08	-13.4	169.6
0.80	1.5	0.005	1.6	359.9	0.20	-20.4	286.5	0.10	-20.9	284.7
0.80	2.0	0.005	1.6	550.0	0.20	-24.9	412.9	0.12	-27.8	397.0
0.80	2.5	0.005	1.6	759.7	0.20	-27.6	550.3	0.12	-32.1	515.6
0.80	3.0	0.005	1.6	984.7	0.22	-30.5	684.6	0.14	-35.5	635.3
0.80	3.5	0.005	1.6	1222.3	0.22	-34.0	806.9	0.14	-40.5	726.8
0.80	4.0	0.005	1.6	1470.5	0.22	-36.1	939.8	0.14	-43.6	830.0
0.80	4.5	0.005	1.6	1727.9	0.22	-37.7	1077.1	0.14	-45.5	941.0
0.80	5.0	0.005	1.6	1993.2	0.22	-39.1	1214.3	0.14	-47.2	1052.0
0.90	0.5	0.005	1.6	74.1	0.14	-7.5	68.6	0.06	-5.7	69.9
0.90	1.0	0.005	1.6	214.1	0.20	-15.7	180.5	0.10	-14.8	182.4
0.90	1.5	0.005	1.6	394.1	0.20	-19.5	317.4	0.12	-22.7	304.8
0.90	2.0	0.005	1.6	604.1	0.20	-22.3	469.3	0.14	-30.0	422.8
0.90	2.5	0.005	1.6	835.0	0.22	-26.6	613.2	0.14	-34.5	547.3
0.90	3.0	0.005	1.6	1083.1	0.22	-28.7	772.7	0.14	-37.7	675.1
0.90	3.5	0.005	1.6	1345.6	0.22	-30.5	935.5	0.14	-40.1	805.6
0.90	4.0	0.005	1.6	1620.1	0.22	-32.1	1100.4	0.16	-42.7	927.6
0.90	4.5	0.005	1.6	1904.8	0.22	-33.5	1266.6	0.16	-45.5	1037.6
0.90	5.0	0.005	1.6	2198.3	0.22	-34.8	1433.4	0.16	-47.7	1149.9
1.00	0.5	0.005	1.6	79.1	0.16	-7.6	73.1	0.06	-5.6	74.6
1.00	1.0	0.005	1.6	232.4	0.20	-15.3	196.9	0.12	-15.5	196.3
1.00	1.5	0.005	1.6	429.2	0.20	-17.5	354.1	0.14	-24.5	324.3
1.00	2.0	0.005	1.6	657.7	0.22	-20.4	523.9	0.14	-30.0	460.3
1.00	2.5	0.005	1.6	909.6	0.22	-23.6	694.9	0.16	-36.6	576.5
1.00	3.0	0.005	1.6	1180.6	0.22	-25.5	879.6	0.16	-40.0	708.7
1.00	3.5	0.005	1.6	1467.6	0.22	-27.2	1069.1	0.16	-42.6	843.1
1.00	4.0	0.005	1.6	1768.0	0.22	-28.6	1262.2	0.16	-44.6	979.1
1.00	4.5	0.005	1.6	2079.8	0.22	-29.9	1457.8	0.16	-46.3	1115.8
1.00	5.0	0.005	1.6	2401.3	0.22	-31.1	1654.9	0.16	-47.8	1253.0
1.25	0.5	0.005	1.6	92.2	0.20	-7.6	85.2	0.10	-6.7	86.0
1.25	1.0	0.005	1.6	278.7	0.20	-11.8	245.7	0.14	-17.9	228.9
1.25	1.5	0.005	1.6	516.8	0.20	-13.6	446.7	0.16	-26.3	381.1
1.25	2.0	0.005	1.6	790.1	0.20	-15.5	667.3	0.18	-33.4	526.4
1.25	2.5	0.005	1.6	1092.2	0.22	-17.5	901.0	0.18	-37.1	687.4
1.25	3.0	0.005	1.6	1418.2	0.24	-20.0	1135.1	0.20	-42.4	816.4
1.25	3.5	0.005	1.6	1764.2	0.24	-21.4	1386.3	0.20	-46.3	948.0
1.25	4.0	0.005	1.6	2127.0	0.24	-23.0	1638.5	0.20	-48.4	1097.7
1.25	4.5	0.005	1.6	2504.1	0.24	-24.1	1900.7	0.20	-50.2	1247.1
1.25	5.0	0.005	1.6	2893.4	0.24	-25.1	2166.5	0.20	-51.8	1395.7
1.50	0.5	0.005	1.6	106.7	0.24	-7.9	98.3	0.12	-8.0	98.2
1.50	1.0	0.005	1.6	328.2	0.22	-10.1	295.2	0.18	-20.8	259.8
1.50	1.5	0.005	1.6	603.7	0.18	-10.6	540.0	0.20	-29.2	427.6
1.50	2.0	0.005	1.6	919.4	0.20	-12.4	805.8	0.20	-33.5	610.9
1.50	2.5	0.005	1.6	1269.1	0.22	-14.1	1090.5	0.22	-40.2	758.8
1.50	3.0	0.005	1.6	1647.1	0.22	-15.4	1392.9	0.22	-43.0	938.8
1.50	3.5	0.005	1.6	2048.8	0.24	-16.8	1705.4	0.22	-45.3	1121.7
1.50	4.0	0.005	1.6	2470.5	0.24	-17.8	2030.6	0.22	-47.1	1305.8
1.50	4.5	0.005	1.6	2909.3	0.24	-18.7	2364.3	0.22	-48.8	1489.8
1.50	5.0	0.005	1.6	3362.9	0.24	-19.6	2705.0	0.22	-50.3	1672.7
0.10	0.5	0.008	1.6	68.6	0.00	0.0	68.6	0.00	0.0	68.6
0.10	1.0	0.008	1.6	139.9	0.00	0.0	139.9	0.00	0.0	139.9
0.10	1.5	0.008	1.6	214.6	0.00	0.0	214.6	0.00	0.0	214.6
0.10	2.0	0.008	1.6	292.9	0.00	0.0	292.9	0.00	0.0	292.9
0.10	2.5	0.008	1.6	375.0	0.00	0.0	375.0	0.00	0.0	375.0
0.10	3.0	0.008	1.6	460.9	0.02	-1.0	456.2	0.00	0.0	460.9
0.10	3.5	0.008	1.6	550.8	0.02	-3.1	533.9	0.00	0.0	550.8
0.10	4.0	0.008	1.6	644.3	0.02	-5.2	611.1	0.00	0.0	644.3
0.10	4.5	0.008	1.6	742.1	0.02	-7.3	688.1	0.00	0.0	742.1
0.10	5.0	0.008	1.6	842.6	0.02	-9.3	764.5	0.00	0.0	842.6
0.20	0.5	0.008	1.6	72.0	0.02	-0.5	71.6	0.00	0.0	72.0
0.20	1.0	0.008	1.6	148.6	0.02	-2.8	144.4	0.00	0.0	148.6
0.20	1.5	0.008	1.6	235.1	0.02	-5.7	221.7	0.00	0.0	235.1
0.20	2.0	0.008	1.6	331.1	0.02	-7.5	306.3	0.00	0.0	331.1
0.20	2.5	0.008	1.6	436.7	0.04	-9.2	396.6	0.00	0.0	436.7
0.20	3.0	0.008	1.6	550.9	0.04	-13.9	474.3	0.00	0.0	550.9
0.20	3.5	0.008	1.6	672.2	0.04	-15.4	568.5	0.00	0.0	672.2
0.20	4.0	0.008	1.6	799.3	0.04	-16.6	666.8	0.02	-3.1	774.6
0.20	4.5	0.008	1.6	931.0	0.04	-17.5	768.1	0.02	-7.2	864.4
0.20	5.0	0.008	1.6	1065.4	0.06	-19.5	858.1	0.02	-10.4	954.1
0.30	0.5	0.008	1.6	74.7	0.02	-2.1	73.2	0.00	0.0	74.7
0.30	1.0	0.008	1.6	159.7	0.04	-4.8	152.1	0.00	0.0	159.7
0.30	1.5	0.008	1.6	261.5	0.04	-8.1	240.4	0.00	0.0	261.5
0.30	2.0	0.008	1.6	380.5	0.06	-12.5	332.9	0.02	-0.8	377.5
0.30	2.5	0.008	1.6	514.4	0.06	-14.9	437.7	0.02	-8.7	469.5
0.30	3.0	0.008	1.6	659.2	0.08	-18.9	534.5	0.02	-10.4	590.8
0.30	3.5	0.008	1.6	811.7	0.08	-20.6	644.6	0.02	-11.6	717.5
0.30	4.0	0.008	1.6	970.3	0.08	-21.9	758.1	0.02	-12.6	848.0
0.30	4.5	0.008	1.6	1138.4	0.10	-25.3	850.9	0.02	-13.8	981.7
0.30	5.0	0.008	1.6	1312.7	0.10	-27.1	956.7	0.04	-16.8	1092.0
0.40	0.5	0.008	1.6	78.0	0.04	-2.9	75.7	0.00	0.0	78.0
0.40	1.0	0.008	1.6	173.7	0.06	-6.6	162.2	0.00	0.0	173.7
0.40	1.5	0.008	1.6	293.6	0.08	-11.0	261.3	0.02	-5.2	278.4
0.40	2.0	0.008	1.6	438.5	0.08	-14.3	375.9	0.02	-7.2	407.0
0.40	2.5	0.008	1.6	601.4	0.10	-18.6	489.7	0.04	-10.6	537.9
0.40	3.0	0.008	1.6	776.3	0.12	-22.5	601.9	0.04	-14.8	661.1
0.40	3.5	0.008	1.6	961.6	0.12	-24.6	725.5	0.04	-16.7	801.5
0.40	4.0	0.008	1.6	1160.6	0.12	-26.5	852.9	0.04	-18.5	946.0
0.40	4.5	0.008	1.6	1366.7	0.14	-29.6	961.7	0.06	-21.5	1072.7
0.40	5.0	0.008	1.6	1579.2	0.14	-32.5	1066.6	0.06	-24.9	1185.4
0.50	0.5	0.008	1.6	81.8	0.06	-3.5	79.0	0.00	0.0	81.8
0.50	1.0	0.008	1.6	189.7	0.08	-7.9	174.8	0.02	-3.8	182.4
0.50	1.5	0.008	1.6	330.6	0.10	-12.4	289.5	0.02	-5.3	313.2
0.50	2.0	0.008	1.6	500.9	0.12	-17.0	415.7	0.04	-10.7	447.5
0.50	2.5	0.008	1.6	692.0	0.14	-21.4	543.8	0.06	-13.5	598.3
0.50	3.0	0.008	1.6	898.9	0.14	-23.8	685.2	0.06	-18.4	733.7
0.50	3.5	0.008	1.6	1123.0	0.16	-27.7	811.8	0.06	-21.0	887.6
0.50	4.0	0.008	1.6	1357.1	0.16	-30.6	941.8	0.06	-23.0	1045.6
0.50	4.5	0.008	1.6	1600.0	0.16	-32.4	1082.1	0.08	-27.4	1161.7
0.50	5.0	0.008	1.6	1851.0	0.16	-33.9	1223.3	0.08	-29.3	1309.2
0.60	0.5	0.008	1.6	86.1	0.06	-3.7	82.9	0.02	-1.6	84.7
0.60	1.0	0.008	1.6	207.0	0.10	-8.6	189.2	0.02	-3.9	199.0
0.60	1.5	0.008	1.6	369.2	0.12	-13.2	320.4	0.04	-8.2	338.8
0.60	2.0	0.008	1.6	565.1	0.14	-17.6	465.5	0.06	-13.3	490.1
0.60	2.5	0.008	1.6	784.3	0.16	-21.9	612.4	0.06	-16.2	656.9
0.60	3.0	0.008	1.6	1027.7	0.18	-25.0	770.5	0.08	-21.7	805.1
0.60	3.5	0.008	1.6	1285.0	0.18	-29.2	909.3	0.08	-24.4	971.4
0.60	4.0	0.008	1.6	1554.4	0.18	-31.2	1069.8	0.08	-26.6	1141.4
0.60	4.5	0.008	1.6	1834.6	0.18	-32.9	1231.8	0.10	-30.9	1267.3
0.60	5.0	0.008	1.6	2124.5	0.18	-34.3	1394.9	0.10	-33.0	1423.7
0.70	0.5	0.008	1.6	90.6	0.08	-4.0	87.0	0.02	-2.3	88.5
0.70	1.0	0.008	1.6	225.2	0.12	-9.1	204.6	0.04	-5.8	212.0
0.70	1.5	0.008	1.6	408.3	0.16	-14.7	348.2	0.06	-10.0	367.4
0.70	2.0	0.008	1.6	630.0	0.18	-18.1	516.2	0.08	-15.3	533.8
0.70	2.5	0.008	1.6	882.0	0.18	-22.4	684.4	0.08	-19.2	712.3
0.70	3.0	0.008	1.6	1156.1	0.18	-24.8	869.6	0.10	-24.4	873.9
0.70	3.5	0.008	1.6	1446.6	0.20	-28.7	1031.7	0.10	-27.3	1051.2
0.70	4.0	0.008	1.6	1751.5	0.20	-31.0	1208.3	0.10	-29.6	1232.2
0.70	4.5	0.008	1.6	2069.2	0.20	-32.6	1394.4	0.12	-32.6	1394.7
0.70	5.0	0.008	1.6	2398.5	0.20	-34.1	1581.7	0.12	-36.2	1530.6
0.80	0.5	0.008	1.6	95.4	0.10	-4.1	91.5	0.02	-2.3	93.3
0.80	1.0	0.008	1.6	243.9	0.14	-9.5	220.7	0.06	-6.8	227.2
0.80	1.5	0.008	1.6	448.3	0.18	-14.9	381.3	0.08	-11.4	397.2
0.80	2.0	0.008	1.6	696.5	0.18	-17.9	571.5	0.10	-17.1	577.3
0.80	2.5	0.008	1.6	979.0	0.20	-22.0	763.5	0.10	-21.7	766.9
0.80	3.0	0.008	1.6	1283.2	0.20	-24.5	969.2	0.12	-26.7	940.6
0.80	3.5	0.008	1.6	1606.6	0.20	-26.3	1184.5	0.12	-29.8	1127.6
0.80	4.0	0.008	1.6	1946.7	0.20	-27.9	1404.4	0.12	-32.3	1318.4
0.80	4.5	0.008	1.6	2301.8	0.22	-30.5	1600.3	0.12	-34.3	1512.5
0.80	5.0	0.008	1.6	2670.1	0.22	-32.9	1792.0	0.14	-36.3	1702.0

$\frac{W}{L}$ [−]	θ [deg]	$\frac{t}{L}$ [−]	$\frac{R}{L}$ [−]	$\sigma_{\mathrm{eq,max}}$ [MPa]	$\frac{\eta_{\mathrm{opt}}}{L}$ [−]	η_{perf} [%]	$\sigma_{\mathrm{eq,max}}$ [MPa]	$\frac{\eta_{\mathrm{opt}}}{L}$ [−]	η_{perf} [%]	$\sigma_{\mathrm{eq,max}}$ [MPa]
0.90	0.5	0.008	1.6	100.4	0.10	-4.1	96.3	0.04	-3.2	97.1
0.90	1.0	0.008	1.6	263.0	0.16	-9.7	237.5	0.06	-6.9	244.8
0.90	1.5	0.008	1.6	489.2	0.18	-13.8	421.4	0.10	-12.6	427.6
0.90	2.0	0.008	1.6	765.8	0.20	-18.0	627.9	0.10	-18.0	627.8
0.90	2.5	0.008	1.6	1075.2	0.20	-20.2	858.2	0.12	-23.7	820.2
0.90	3.0	0.008	1.6	1409.1	0.20	-22.0	1099.5	0.14	-27.8	1016.7
0.90	3.5	0.008	1.6	1764.8	0.22	-24.7	1328.2	0.14	-32.0	1199.4
0.90	4.0	0.008	1.6	2139.5	0.22	-26.9	1563.8	0.14	-34.6	1399.1
0.90	4.5	0.008	1.6	2531.0	0.22	-28.3	1815.4	0.14	-36.7	1601.9
0.90	5.0	0.008	1.6	2937.6	0.22	-29.5	2070.1	0.14	-38.5	1807.2
1.00	0.5	0.008	1.6	105.5	0.12	-4.1	101.2	0.04	-3.1	102.2
1.00	1.0	0.008	1.6	282.5	0.18	-9.8	254.9	0.08	-7.6	261.0
1.00	1.5	0.008	1.6	531.3	0.20	-13.9	457.6	0.10	-13.2	461.0
1.00	2.0	0.008	1.6	834.9	0.20	-16.4	697.9	0.12	-19.9	668.9
1.00	2.5	0.008	1.6	1170.8	0.20	-18.2	957.9	0.14	-25.5	871.8
1.00	3.0	0.008	1.6	1534.0	0.22	-20.1	1225.5	0.14	-29.0	1088.4
1.00	3.5	0.008	1.6	1921.4	0.22	-22.6	1487.0	0.16	-33.0	1286.7
1.00	4.0	0.008	1.6	2330.0	0.22	-24.0	1771.7	0.16	-36.8	1473.6
1.00	4.5	0.008	1.6	2757.4	0.22	-25.2	2062.4	0.16	-39.0	1683.1
1.00	5.0	0.008	1.6	3201.4	0.22	-26.4	2357.7	0.16	-40.8	1894.8
1.25	0.5	0.008	1.6	118.8	0.14	-4.0	114.1	0.06	-3.6	114.6
1.25	1.0	0.008	1.6	333.4	0.22	-9.4	302.0	0.12	-8.5	304.9
1.25	1.5	0.008	1.6	645.1	0.22	-12.5	564.7	0.14	-16.8	536.5
1.25	2.0	0.008	1.6	1008.0	0.20	-13.0	877.1	0.16	-23.3	773.4
1.25	2.5	0.008	1.6	1408.3	0.20	-14.2	1208.5	0.18	-27.7	1017.9
1.25	3.0	0.008	1.6	1842.2	0.20	-15.4	1558.0	0.18	-32.4	1245.3
1.25	3.5	0.008	1.6	2305.9	0.22	-17.2	1908.7	0.18	-35.1	1497.1
1.25	4.0	0.008	1.6	2795.9	0.22	-18.3	2283.0	0.18	-37.2	1754.9
1.25	4.5	0.008	1.6	3309.3	0.24	-20.0	2647.7	0.20	-39.3	2008.1
1.25	5.0	0.008	1.6	3843.5	0.24	-20.7	3047.1	0.20	-42.6	2207.3
1.50	0.5	0.008	1.6	132.8	0.20	-3.7	128.0	0.08	-3.8	127.8
1.50	1.0	0.008	1.6	390.3	0.24	-8.9	355.4	0.14	-10.4	349.6
1.50	1.5	0.008	1.6	762.0	0.24	-11.0	678.6	0.16	-19.1	616.5
1.50	2.0	0.008	1.6	1181.3	0.20	-10.5	1057.8	0.18	-24.8	888.4
1.50	2.5	0.008	1.6	1643.4	0.18	-11.2	1459.8	0.20	-30.1	1149.5
1.50	3.0	0.008	1.6	2144.6	0.20	-12.4	1879.1	0.20	-32.8	1440.5
1.50	3.5	0.008	1.6	2680.6	0.22	-13.5	2319.0	0.22	-36.4	1704.3
1.50	4.0	0.008	1.6	3247.8	0.22	-14.5	2777.9	0.22	-40.4	1934.6
1.50	4.5	0.008	1.6	3842.6	0.22	-15.4	3250.3	0.22	-42.3	2217.6
1.50	5.0	0.008	1.6	4462.2	0.22	-16.2	3737.5	0.22	-43.9	2502.9
0.10	0.5	0.001	2.0	12.8	0.02	-1.4	12.6	0.00	0.0	12.8
0.10	1.0	0.001	2.0	29.3	0.02	-16.8	24.4	0.00	0.0	29.3
0.10	1.5	0.001	2.0	46.6	0.02	-19.8	37.4	0.02	-4.3	44.6
0.10	2.0	0.001	2.0	64.6	0.02	-21.1	51.0	0.02	-8.6	59.1
0.10	2.5	0.001	2.0	83.5	0.02	-22.1	65.0	0.02	-11.3	74.0
0.10	3.0	0.001	2.0	103.1	0.02	-22.8	79.6	0.02	-13.7	89.0
0.10	3.5	0.001	2.0	123.5	0.02	-23.5	94.5	0.02	-15.8	104.0
0.10	4.0	0.001	2.0	144.5	0.02	-23.9	110.0	0.02	-17.8	118.9
0.10	4.5	0.001	2.0	166.2	0.02	-24.3	125.8	0.02	-19.5	133.7
0.10	5.0	0.001	2.0	188.3	0.04	-24.9	141.5	0.02	-21.1	148.5
0.20	0.5	0.001	2.0	15.8	0.04	-15.1	13.4	0.02	-4.4	15.1
0.20	1.0	0.001	2.0	37.3	0.06	-27.5	27.0	0.02	-21.7	29.1
0.20	1.5	0.001	2.0	61.3	0.06	-33.7	40.6	0.02	-25.2	45.8
0.20	2.0	0.001	2.0	87.7	0.06	-37.5	54.9	0.02	-27.2	63.8
0.20	2.5	0.001	2.0	115.5	0.06	-39.6	69.8	0.02	-28.5	82.5
0.20	3.0	0.001	2.0	144.3	0.06	-41.2	84.9	0.02	-29.4	101.9
0.20	3.5	0.001	2.0	174.0	0.06	-42.3	100.4	0.02	-30.1	121.5
0.20	4.0	0.001	2.0	204.3	0.06	-43.0	116.5	0.04	-31.1	140.7
0.20	4.5	0.001	2.0	235.2	0.06	-43.5	133.0	0.04	-32.4	158.9
0.20	5.0	0.001	2.0	266.6	0.06	-43.9	149.5	0.04	-33.4	177.5
0.30	0.5	0.001	2.0	18.8	0.08	-26.0	13.9	0.02	-15.7	15.9
0.30	1.0	0.001	2.0	45.8	0.08	-33.5	30.5	0.04	-28.7	32.7
0.30	1.5	0.001	2.0	76.8	0.08	-37.9	47.7	0.04	-34.0	50.6
0.30	2.0	0.001	2.0	110.4	0.08	-40.8	65.4	0.04	-37.6	68.9
0.30	2.5	0.001	2.0	145.8	0.10	-43.1	83.0	0.04	-40.0	87.5
0.30	3.0	0.001	2.0	182.7	0.10	-45.0	100.6	0.04	-41.8	106.3
0.30	3.5	0.001	2.0	220.6	0.10	-46.3	118.5	0.04	-43.2	125.3
0.30	4.0	0.001	2.0	259.5	0.10	-47.3	136.7	0.04	-43.8	145.7
0.30	4.5	0.001	2.0	299.1	0.10	-48.1	155.3	0.04	-44.4	166.4
0.30	5.0	0.001	2.0	339.3	0.10	-48.7	174.1	0.04	-44.7	187.5
0.40	0.5	0.001	2.0	22.1	0.10	-28.4	15.8	0.04	-21.3	17.4
0.40	1.0	0.001	2.0	54.9	0.12	-37.2	34.5	0.06	-35.0	35.7
0.40	1.5	0.001	2.0	93.0	0.12	-43.3	52.8	0.06	-42.0	53.9
0.40	2.0	0.001	2.0	134.1	0.12	-47.0	71.1	0.06	-45.8	72.7
0.40	2.5	0.001	2.0	177.7	0.12	-49.6	89.6	0.06	-48.3	91.9
0.40	3.0	0.001	2.0	223.0	0.12	-51.5	108.1	0.06	-50.0	111.4
0.40	3.5	0.001	2.0	269.7	0.12	-53.1	126.5	0.06	-51.4	131.2
0.40	4.0	0.001	2.0	317.6	0.12	-54.0	146.2	0.06	-52.4	151.1
0.40	4.5	0.001	2.0	366.5	0.12	-54.7	166.1	0.06	-53.3	171.3
0.40	5.0	0.001	2.0	416.1	0.12	-55.1	186.7	0.06	-53.8	192.4
0.50	0.5	0.001	2.0	25.5	0.12	-30.4	17.7	0.06	-26.2	18.8
0.50	1.0	0.001	2.0	64.1	0.14	-41.8	37.4	0.08	-36.8	40.6
0.50	1.5	0.001	2.0	108.9	0.14	-47.8	56.8	0.08	-44.5	60.4
0.50	2.0	0.001	2.0	157.3	0.14	-51.1	76.9	0.08	-48.9	80.4
0.50	2.5	0.001	2.0	208.3	0.14	-52.9	98.2	0.08	-51.9	100.2
0.50	3.0	0.001	2.0	261.5	0.14	-54.1	120.1	0.08	-54.2	119.7
0.50	3.5	0.001	2.0	316.3	0.14	-54.9	142.7	0.08	-56.0	139.2
0.50	4.0	0.001	2.0	372.4	0.14	-55.3	166.3	0.08	-57.4	158.6
0.50	4.5	0.001	2.0	429.5	0.16	-55.6	190.9	0.08	-58.5	178.3
0.50	5.0	0.001	2.0	487.5	0.16	-56.3	213.1	0.08	-59.4	198.2
0.60	0.5	0.001	2.0	28.9	0.16	-29.6	20.3	0.06	-26.3	21.3
0.60	1.0	0.001	2.0	73.5	0.16	-41.9	42.7	0.10	-37.3	46.0
0.60	1.5	0.001	2.0	125.0	0.16	-47.6	65.5	0.10	-44.6	69.3
0.60	2.0	0.001	2.0	180.7	0.16	-50.9	88.7	0.10	-48.7	92.6
0.60	2.5	0.001	2.0	239.3	0.16	-53.1	112.3	0.10	-51.6	115.7
0.60	3.0	0.001	2.0	300.2	0.16	-54.7	136.2	0.10	-53.9	138.5
0.60	3.5	0.001	2.0	362.9	0.16	-55.4	161.7	0.10	-55.6	161.3
0.60	4.0	0.001	2.0	427.1	0.16	-55.6	189.8	0.10	-56.9	184.0
0.60	4.5	0.001	2.0	492.4	0.16	-55.6	218.6	0.10	-58.0	206.8
0.60	5.0	0.001	2.0	558.7	0.16	-55.5	248.6	0.10	-58.9	229.9
0.70	0.5	0.001	2.0	32.3	0.16	-31.6	22.1	0.10	-33.4	21.5
0.70	1.0	0.001	2.0	83.2	0.20	-42.7	47.7	0.10	-46.3	44.7
0.70	1.5	0.001	2.0	141.8	0.20	-48.1	73.6	0.10	-51.8	68.4
0.70	2.0	0.001	2.0	204.7	0.20	-50.8	100.7	0.10	-54.7	92.7
0.70	2.5	0.001	2.0	270.8	0.20	-52.1	129.8	0.10	-56.6	117.6
0.70	3.0	0.001	2.0	339.1	0.20	-52.9	159.8	0.10	-57.8	143.2
0.70	3.5	0.001	2.0	409.2	0.20	-53.4	190.9	0.10	-58.5	169.6
0.70	4.0	0.001	2.0	480.8	0.20	-53.6	222.9	0.10	-59.1	196.6
0.70	4.5	0.001	2.0	553.7	0.20	-53.8	255.9	0.10	-59.3	225.6
0.70	5.0	0.001	2.0	627.6	0.20	-53.8	290.0	0.10	-59.3	255.6
0.80	0.5	0.001	2.0	35.7	0.18	-31.3	24.5	0.10	-33.9	23.6
0.80	1.0	0.001	2.0	92.9	0.20	-42.4	53.5	0.12	-49.9	46.6
0.80	1.5	0.001	2.0	158.7	0.20	-47.2	83.8	0.12	-56.2	69.5
0.80	2.0	0.001	2.0	229.3	0.18	-49.9	114.9	0.12	-59.4	93.2
0.80	2.5	0.001	2.0	303.1	0.18	-51.5	147.1	0.12	-61.2	117.6
0.80	3.0	0.001	2.0	379.3	0.18	-51.8	182.8	0.12	-61.6	145.6
0.80	3.5	0.001	2.0	457.3	0.18	-52.0	219.7	0.12	-61.7	175.0
0.80	4.0	0.001	2.0	536.6	0.20	-52.1	257.0	0.12	-61.7	205.7
0.80	4.5	0.001	2.0	617.0	0.20	-52.2	295.2	0.12	-61.5	237.5
0.80	5.0	0.001	2.0	698.3	0.20	-52.1	334.6	0.12	-61.3	270.4
0.90	0.5	0.001	2.0	38.9	0.20	-30.4	27.1	0.12	-36.7	24.6
0.90	1.0	0.001	2.0	101.9	0.20	-41.4	59.7	0.12	-48.0	53.0
0.90	1.5	0.001	2.0	174.2	0.20	-46.6	92.9	0.14	-54.0	80.1
0.90	2.0	0.001	2.0	251.5	0.20	-49.8	126.3	0.14	-57.5	106.8
0.90	2.5	0.001	2.0	332.2	0.20	-51.5	161.3	0.14	-59.8	133.5
0.90	3.0	0.001	2.0	415.2	0.20	-52.0	199.5	0.14	-61.4	160.1
0.90	3.5	0.001	2.0	499.8	0.20	-52.2	238.7	0.14	-62.7	186.6
0.90	4.0	0.001	2.0	585.6	0.20	-52.3	279.6	0.14	-63.1	215.8
0.90	4.5	0.001	2.0	672.4	0.20	-52.1	322.2	0.14	-62.9	249.4
0.90	5.0	0.001	2.0	760.0	0.20	-51.9	365.7	0.14	-62.6	284.5
1.00	0.5	0.001	2.0	42.3	0.20	-27.4	30.7	0.14	-39.6	25.5
1.00	1.0	0.001	2.0	111.3	0.20	-37.7	69.3	0.14	-51.6	53.8
1.00	1.5	0.001	2.0	190.4	0.22	-43.3	107.9	0.14	-56.9	82.2
1.00	2.0	0.001	2.0	275.1	0.22	-46.4	147.5	0.14	-59.9	110.3
1.00	2.5	0.001	2.0	363.1	0.22	-48.2	188.1	0.14	-61.7	139.0
1.00	3.0	0.001	2.0	453.4	0.22	-49.3	229.6	0.14	-62.9	168.3
1.00	3.5	0.001	2.0	545.2	0.22	-50.1	272.0	0.14	-63.7	198.2
1.00	4.0	0.001	2.0	638.0	0.22	-50.6	315.2	0.14	-64.0	229.9
1.00	4.5	0.001	2.0	731.6	0.22	-50.9	359.4	0.14	-64.0	263.1
1.00	5.0	0.001	2.0	825.8	0.22	-51.0	404.6	0.14	-64.0	297.4

$\frac{W}{L}$ [−]	θ [deg]	$\frac{t}{L}$ [−]	$\frac{R}{L}$ [−]	$\sigma_{\text{eq,max}}$ [MPa]	$\frac{\eta_{\text{opt}}}{L}$ [−]	η_{perf} [%]	$\sigma_{\text{eq,max}}$ [MPa]	$\frac{\eta_{\text{opt}}}{L}$ [−]	η_{perf} [%]	$\sigma_{\text{eq,max}}$ [MPa]
1.25	0.5	0.001	2.0	50.6	0.20	-21.9	39.6	0.16	-40.5	30.1
1.25	1.0	0.001	2.0	134.1	0.24	-34.2	88.2	0.18	-53.5	62.3
1.25	1.5	0.001	2.0	230.4	0.24	-39.3	139.9	0.18	-60.2	91.7
1.25	2.0	0.001	2.0	333.3	0.24	-41.5	195.0	0.18	-63.4	121.9
1.25	2.5	0.001	2.0	440.0	0.24	-42.5	252.8	0.18	-64.6	155.6
1.25	3.0	0.001	2.0	548.9	0.26	-43.5	309.9	0.18	-65.4	189.8
1.25	3.5	0.001	2.0	659.0	0.26	-44.3	367.3	0.18	-65.9	224.7
1.25	4.0	0.001	2.0	769.7	0.26	-44.5	427.2	0.18	-66.2	260.4
1.25	4.5	0.001	2.0	880.6	0.26	-44.5	488.5	0.18	-66.3	297.1
1.25	5.0	0.001	2.0	991.6	0.26	-44.4	551.1	0.18	-66.2	335.0
1.50	0.5	0.001	2.0	58.5	0.24	-18.6	47.6	0.20	-41.1	34.5
1.50	1.0	0.001	2.0	155.3	0.24	-26.5	114.2	0.20	-56.2	68.0
1.50	1.5	0.001	2.0	267.4	0.24	-28.4	191.4	0.20	-61.5	102.9
1.50	2.0	0.001	2.0	387.4	0.24	-29.0	275.3	0.20	-64.7	136.9
1.50	2.5	0.001	2.0	511.8	0.24	-29.0	363.3	0.20	-66.0	173.9
1.50	3.0	0.001	2.0	638.6	0.26	-31.1	439.9	0.20	-66.4	214.5
1.50	3.5	0.001	2.0	766.4	0.26	-32.5	517.0	0.20	-66.7	255.4
1.50	4.0	0.001	2.0	894.5	0.26	-33.1	598.6	0.20	-66.9	296.3
1.50	4.5	0.001	2.0	1022.6	0.26	-33.1	683.9	0.20	-67.0	337.2
1.50	5.0	0.001	2.0	1150.2	0.26	-32.9	772.0	0.20	-67.1	378.1
0.10	0.5	0.002	2.0	23.0	0.00	0.0	23.0	0.00	0.0	23.0
0.10	1.0	0.002	2.0	50.8	0.02	-0.5	50.5	0.00	0.0	50.8
0.10	1.5	0.002	2.0	82.4	0.02	-9.6	74.5	0.00	0.0	82.4
0.10	2.0	0.002	2.0	115.9	0.02	-15.9	97.4	0.00	0.0	115.9
0.10	2.5	0.002	2.0	150.2	0.02	-18.3	122.7	0.02	-0.4	149.6
0.10	3.0	0.002	2.0	184.8	0.02	-19.2	149.4	0.02	-3.3	178.8
0.10	3.5	0.002	2.0	219.8	0.02	-19.7	176.4	0.02	-5.4	208.0
0.10	4.0	0.002	2.0	255.5	0.02	-20.2	204.0	0.02	-6.9	237.8
0.10	4.5	0.002	2.0	292.7	0.02	-20.7	232.0	0.02	-8.3	268.3
0.10	5.0	0.002	2.0	330.8	0.02	-21.2	260.5	0.02	-9.6	299.2
0.20	0.5	0.002	2.0	26.2	0.02	-8.8	23.8	0.00	0.0	26.2
0.20	1.0	0.002	2.0	62.1	0.04	-19.1	50.3	0.02	-3.1	60.2
0.20	1.5	0.002	2.0	102.7	0.04	-22.2	80.0	0.02	-14.6	87.8
0.20	2.0	0.002	2.0	146.4	0.06	-27.4	106.2	0.02	-20.4	116.5
0.20	2.5	0.002	2.0	192.5	0.06	-30.7	133.4	0.02	-22.4	149.3
0.20	3.0	0.002	2.0	240.6	0.06	-33.3	160.6	0.02	-23.9	183.1
0.20	3.5	0.002	2.0	291.2	0.06	-34.8	189.9	0.02	-25.2	217.9
0.20	4.0	0.002	2.0	344.1	0.06	-36.2	219.5	0.02	-26.1	254.3
0.20	4.5	0.002	2.0	398.5	0.06	-37.4	249.3	0.02	-26.9	291.3
0.20	5.0	0.002	2.0	454.1	0.06	-38.5	279.5	0.02	-27.6	328.7
0.30	0.5	0.002	2.0	30.0	0.04	-12.5	26.2	0.02	-1.9	29.4
0.30	1.0	0.002	2.0	74.2	0.08	-25.3	55.4	0.02	-14.7	63.3
0.30	1.5	0.002	2.0	125.1	0.08	-29.7	87.9	0.04	-20.2	99.8
0.30	2.0	0.002	2.0	180.6	0.08	-32.8	121.4	0.04	-27.8	130.4
0.30	2.5	0.002	2.0	238.9	0.10	-36.1	152.6	0.04	-30.5	166.1
0.30	3.0	0.002	2.0	301.5	0.10	-39.2	183.3	0.04	-32.9	202.2
0.30	3.5	0.002	2.0	366.7	0.10	-41.6	214.1	0.04	-34.9	238.6
0.30	4.0	0.002	2.0	434.0	0.10	-43.5	245.1	0.04	-36.6	275.3
0.30	4.5	0.002	2.0	503.2	0.10	-45.1	276.3	0.04	-37.9	312.3
0.30	5.0	0.002	2.0	574.1	0.10	-46.4	307.6	0.04	-39.1	349.5
0.40	0.5	0.002	2.0	34.3	0.08	-17.7	28.3	0.02	-9.5	31.1
0.40	1.0	0.002	2.0	87.3	0.12	-28.0	62.8	0.04	-20.5	69.4
0.40	1.5	0.002	2.0	149.0	0.12	-36.8	94.2	0.06	-26.3	109.8
0.40	2.0	0.002	2.0	215.7	0.12	-40.3	128.7	0.06	-33.8	142.8
0.40	2.5	0.002	2.0	288.3	0.12	-43.3	163.6	0.06	-38.3	177.9
0.40	3.0	0.002	2.0	364.9	0.12	-45.5	198.9	0.06	-41.0	215.1
0.40	3.5	0.002	2.0	444.6	0.12	-47.2	234.7	0.06	-43.2	252.6
0.40	4.0	0.002	2.0	527.1	0.12	-48.6	270.9	0.06	-44.9	290.3
0.40	4.5	0.002	2.0	611.9	0.12	-49.7	307.6	0.06	-46.3	328.3
0.40	5.0	0.002	2.0	698.9	0.12	-50.7	344.7	0.06	-47.5	366.6
0.50	0.5	0.002	2.0	39.0	0.10	-19.3	31.5	0.04	-13.0	33.9
0.50	1.0	0.002	2.0	100.6	0.14	-33.3	67.1	0.06	-25.4	75.1
0.50	1.5	0.002	2.0	172.6	0.14	-38.7	105.7	0.06	-31.1	118.8
0.50	2.0	0.002	2.0	251.8	0.14	-42.5	144.7	0.08	-35.6	162.1
0.50	2.5	0.002	2.0	337.6	0.14	-45.5	184.1	0.08	-40.2	202.0
0.50	3.0	0.002	2.0	427.8	0.14	-47.7	224.0	0.08	-43.3	242.5
0.50	3.5	0.002	2.0	521.7	0.14	-49.3	264.4	0.08	-45.7	283.4
0.50	4.0	0.002	2.0	618.6	0.14	-50.6	305.4	0.08	-47.5	324.8
0.50	4.5	0.002	2.0	718.4	0.14	-51.7	347.1	0.08	-49.0	366.5
0.50	5.0	0.002	2.0	820.5	0.14	-52.5	389.4	0.08	-50.2	408.7
0.60	0.5	0.002	2.0	43.7	0.12	-20.6	34.7	0.06	-16.5	36.5
0.60	1.0	0.002	2.0	113.9	0.16	-34.2	74.9	0.08	-29.4	80.4
0.60	1.5	0.002	2.0	196.4	0.16	-39.6	118.6	0.08	-35.9	125.8
0.60	2.0	0.002	2.0	289.0	0.16	-43.8	162.5	0.08	-40.5	172.0
0.60	2.5	0.002	2.0	388.1	0.16	-46.8	206.6	0.08	-43.6	218.8
0.60	3.0	0.002	2.0	492.1	0.16	-49.0	251.2	0.08	-45.9	266.2
0.60	3.5	0.002	2.0	600.1	0.16	-50.6	296.2	0.08	-47.6	314.4
0.60	4.0	0.002	2.0	711.6	0.16	-52.0	341.9	0.08	-49.0	363.2
0.60	4.5	0.002	2.0	826.1	0.16	-53.0	388.3	0.08	-50.0	412.7
0.60	5.0	0.002	2.0	943.4	0.16	-53.8	435.4	0.08	-50.9	462.8
0.70	0.5	0.002	2.0	48.5	0.14	-21.4	38.2	0.08	-17.4	40.1
0.70	1.0	0.002	2.0	127.7	0.20	-32.8	85.7	0.10	-32.7	86.0
0.70	1.5	0.002	2.0	221.6	0.20	-41.6	129.3	0.10	-40.6	131.6
0.70	2.0	0.002	2.0	327.1	0.20	-45.2	179.3	0.10	-45.5	178.4
0.70	2.5	0.002	2.0	439.7	0.18	-47.8	229.5	0.10	-48.7	225.4
0.70	3.0	0.002	2.0	557.6	0.18	-49.9	279.3	0.10	-51.1	272.5
0.70	3.5	0.002	2.0	679.9	0.18	-51.5	329.9	0.10	-52.9	319.9
0.70	4.0	0.002	2.0	805.9	0.18	-52.7	381.1	0.10	-54.3	367.9
0.70	4.5	0.002	2.0	935.0	0.18	-53.6	434.2	0.10	-55.5	416.4
0.70	5.0	0.002	2.0	1067.0	0.18	-54.1	490.0	0.10	-56.4	465.1
0.80	0.5	0.002	2.0	53.1	0.16	-21.9	41.5	0.08	-19.4	42.9
0.80	1.0	0.002	2.0	141.5	0.20	-32.6	95.3	0.10	-33.3	94.3
0.80	1.5	0.002	2.0	246.7	0.20	-40.5	146.7	0.12	-42.8	141.2
0.80	2.0	0.002	2.0	365.1	0.20	-44.1	204.0	0.12	-48.9	186.4
0.80	2.5	0.002	2.0	491.3	0.20	-46.4	263.4	0.12	-52.6	232.7
0.80	3.0	0.002	2.0	623.5	0.20	-48.0	324.0	0.12	-55.2	279.4
0.80	3.5	0.002	2.0	760.4	0.20	-49.3	385.8	0.12	-57.0	326.8
0.80	4.0	0.002	2.0	901.1	0.20	-50.2	448.7	0.12	-58.4	374.8
0.80	4.5	0.002	2.0	1045.2	0.20	-50.9	512.8	0.12	-59.5	423.4
0.80	5.0	0.002	2.0	1192.0	0.18	-51.5	578.6	0.12	-60.3	472.8
0.90	0.5	0.002	2.0	57.8	0.18	-20.9	45.7	0.10	-21.6	45.3
0.90	1.0	0.002	2.0	154.8	0.20	-31.6	105.8	0.12	-36.4	98.4
0.90	1.5	0.002	2.0	271.0	0.22	-37.3	170.0	0.12	-43.0	154.5
0.90	2.0	0.002	2.0	401.5	0.24	-41.4	235.4	0.12	-47.4	211.4
0.90	2.5	0.002	2.0	540.8	0.20	-43.9	303.5	0.12	-50.4	268.5
0.90	3.0	0.002	2.0	686.6	0.20	-46.3	368.9	0.14	-52.9	323.6
0.90	3.5	0.002	2.0	837.3	0.20	-48.1	434.2	0.14	-54.7	379.4
0.90	4.0	0.002	2.0	992.1	0.20	-49.7	499.4	0.14	-56.0	436.3
0.90	4.5	0.002	2.0	1150.2	0.20	-50.9	564.7	0.14	-57.0	494.3
0.90	5.0	0.002	2.0	1311.1	0.20	-51.9	630.0	0.14	-57.8	553.6
1.00	0.5	0.002	2.0	62.5	0.18	-18.5	50.9	0.12	-23.6	47.7
1.00	1.0	0.002	2.0	168.2	0.22	-29.3	118.9	0.14	-39.4	101.9
1.00	1.5	0.002	2.0	295.4	0.22	-36.1	188.6	0.14	-46.4	158.3
1.00	2.0	0.002	2.0	438.4	0.22	-40.3	261.8	0.14	-51.0	214.8
1.00	2.5	0.002	2.0	591.1	0.22	-43.4	334.3	0.14	-54.2	270.8
1.00	3.0	0.002	2.0	750.8	0.22	-46.0	405.8	0.14	-56.5	326.5
1.00	3.5	0.002	2.0	915.8	0.22	-48.0	476.6	0.14	-58.3	381.7
1.00	4.0	0.002	2.0	1085.1	0.22	-49.1	552.7	0.14	-59.8	436.5
1.00	4.5	0.002	2.0	1257.8	0.22	-49.9	629.8	0.14	-60.9	491.2
1.00	5.0	0.002	2.0	1433.3	0.22	-50.6	708.7	0.14	-61.9	545.8
1.25	0.5	0.002	2.0	74.2	0.18	-15.5	62.7	0.14	-25.6	55.2
1.25	1.0	0.002	2.0	201.0	0.24	-24.7	151.4	0.16	-40.2	120.2
1.25	1.5	0.002	2.0	354.9	0.24	-29.6	249.7	0.18	-46.5	190.0
1.25	2.0	0.002	2.0	528.2	0.24	-33.4	351.8	0.18	-52.6	250.6
1.25	2.5	0.002	2.0	713.7	0.24	-36.4	454.2	0.18	-56.3	311.6
1.25	3.0	0.002	2.0	908.0	0.24	-38.8	555.8	0.18	-58.9	372.9
1.25	3.5	0.002	2.0	1108.6	0.24	-40.8	656.3	0.18	-60.7	435.2
1.25	4.0	0.002	2.0	1314.2	0.24	-42.0	762.4	0.18	-62.0	498.9
1.25	4.5	0.002	2.0	1523.7	0.24	-42.8	871.0	0.18	-62.9	564.6
1.25	5.0	0.002	2.0	1736.1	0.24	-43.6	978.9	0.18	-63.5	633.0
1.50	0.5	0.002	2.0	85.9	0.22	-13.9	74.0	0.16	-27.0	62.7
1.50	1.0	0.002	2.0	232.2	0.24	-18.7	188.8	0.20	-40.7	137.7
1.50	1.5	0.002	2.0	411.1	0.24	-22.5	318.5	0.20	-51.4	199.7
1.50	2.0	0.002	2.0	612.8	0.24	-25.8	455.0	0.20	-55.8	270.8
1.50	2.5	0.002	2.0	829.1	0.24	-27.5	600.9	0.20	-59.0	340.1
1.50	3.0	0.002	2.0	1055.9	0.24	-28.5	754.7	0.20	-61.4	407.4
1.50	3.5	0.002	2.0	1290.6	0.26	-30.2	901.0	0.20	-63.3	473.1
1.50	4.0	0.002	2.0	1531.1	0.26	-32.6	1031.5	0.20	-64.5	543.3
1.50	4.5	0.002	2.0	1776.1	0.26	-33.9	1174.7	0.20	-65.1	620.1
1.50	5.0	0.002	2.0	2024.6	0.26	-34.5	1326.2	0.20	-65.3	701.9

$\frac{W}{L}$ [−]	θ [deg]	$\frac{t}{L}$ [−]	$\frac{R}{L}$ [−]	$\sigma_{\mathrm{eq,max}}$ [MPa]	$\frac{\eta_{\mathrm{opt}}}{L}$ [−]	η_{perf} [%]	$\sigma_{\mathrm{eq,max}}$ [MPa]	$\frac{\eta_{\mathrm{opt}}}{L}$ [−]	η_{perf} [%]	$\sigma_{\mathrm{eq,max}}$ [MPa]
0.10	0.5	0.005	2.0	53.9	0.00	0.0	53.9	0.00	0.0	53.9
0.10	1.0	0.005	2.0	111.8	0.00	0.0	111.8	0.00	0.0	111.8
0.10	1.5	0.005	2.0	174.3	0.00	0.0	174.3	0.00	0.0	174.3
0.10	2.0	0.005	2.0	241.3	0.00	0.0	241.3	0.00	0.0	241.3
0.10	2.5	0.005	2.0	312.9	0.02	-4.1	300.2	0.00	0.0	312.9
0.10	3.0	0.005	2.0	388.1	0.02	-7.5	358.9	0.00	0.0	388.1
0.10	3.5	0.005	2.0	466.2	0.02	-10.6	416.7	0.00	0.0	466.2
0.10	4.0	0.005	2.0	546.0	0.02	-13.3	473.7	0.00	0.0	546.0
0.10	4.5	0.005	2.0	627.9	0.02	-14.6	536.2	0.00	0.0	627.9
0.10	5.0	0.005	2.0	710.3	0.02	-15.3	601.8	0.00	0.0	710.3
0.20	0.5	0.005	2.0	56.5	0.02	-0.7	56.1	0.00	0.0	56.5
0.20	1.0	0.005	2.0	123.3	0.02	-6.9	114.8	0.00	0.0	123.3
0.20	1.5	0.005	2.0	201.3	0.02	-9.0	183.3	0.00	0.0	201.3
0.20	2.0	0.005	2.0	288.4	0.04	-15.6	243.5	0.00	0.0	288.4
0.20	2.5	0.005	2.0	381.4	0.04	-17.6	314.1	0.02	-1.2	376.8
0.20	3.0	0.005	2.0	478.4	0.04	-19.0	387.4	0.02	-6.5	447.1
0.20	3.5	0.005	2.0	577.6	0.06	-21.0	456.5	0.02	-10.5	517.0
0.20	4.0	0.005	2.0	679.2	0.06	-24.5	512.5	0.02	-13.7	586.2
0.20	4.5	0.005	2.0	784.7	0.06	-26.3	578.5	0.02	-16.6	654.8
0.20	5.0	0.005	2.0	893.2	0.06	-27.3	649.1	0.02	-18.1	732.0
0.30	0.5	0.005	2.0	59.7	0.02	-3.0	57.9	0.00	0.0	59.7
0.30	1.0	0.005	2.0	138.0	0.04	-9.7	124.7	0.00	0.0	138.0
0.30	1.5	0.005	2.0	234.6	0.06	-16.2	196.7	0.02	-7.4	217.3
0.30	2.0	0.005	2.0	342.3	0.08	-20.7	271.5	0.02	-11.8	302.0
0.30	2.5	0.005	2.0	457.2	0.08	-24.3	346.0	0.02	-13.5	395.5
0.30	3.0	0.005	2.0	576.6	0.08	-26.1	426.3	0.02	-14.6	492.3
0.30	3.5	0.005	2.0	702.0	0.10	-27.6	508.1	0.04	-16.0	589.3
0.30	4.0	0.005	2.0	832.9	0.10	-31.1	573.8	0.04	-20.2	664.6
0.30	4.5	0.005	2.0	970.2	0.10	-33.3	647.3	0.04	-23.8	738.9
0.30	5.0	0.005	2.0	1111.2	0.10	-35.1	721.5	0.04	-26.4	817.6
0.40	0.5	0.005	2.0	63.8	0.04	-4.8	60.7	0.00	0.0	63.8
0.40	1.0	0.005	2.0	155.7	0.08	-13.8	134.2	0.02	-6.5	145.5
0.40	1.5	0.005	2.0	271.6	0.10	-21.0	214.5	0.02	-9.5	245.7
0.40	2.0	0.005	2.0	400.4	0.10	-24.4	302.5	0.04	-17.0	332.2
0.40	2.5	0.005	2.0	537.2	0.12	-30.1	375.6	0.04	-19.4	433.0
0.40	3.0	0.005	2.0	682.6	0.12	-32.7	459.4	0.04	-21.4	536.4
0.40	3.5	0.005	2.0	836.8	0.12	-34.9	544.7	0.04	-23.3	641.8
0.40	4.0	0.005	2.0	997.6	0.12	-36.8	630.3	0.06	-26.5	733.5
0.40	4.5	0.005	2.0	1163.4	0.12	-38.4	716.2	0.06	-29.6	819.5
0.40	5.0	0.005	2.0	1333.7	0.12	-39.8	802.4	0.06	-32.0	907.1
0.50	0.5	0.005	2.0	68.6	0.06	-6.3	64.3	0.02	-0.3	68.4
0.50	1.0	0.005	2.0	175.1	0.10	-15.7	147.7	0.02	-6.4	163.8
0.50	1.5	0.005	2.0	309.6	0.12	-22.9	238.7	0.04	-14.1	266.0
0.50	2.0	0.005	2.0	459.1	0.14	-29.5	323.9	0.06	-21.1	362.2
0.50	2.5	0.005	2.0	619.7	0.14	-32.4	418.7	0.06	-24.4	468.8
0.50	3.0	0.005	2.0	792.6	0.14	-35.1	514.4	0.06	-27.2	577.2
0.50	3.5	0.005	2.0	974.4	0.14	-37.3	610.6	0.06	-29.5	686.9
0.50	4.0	0.005	2.0	1163.0	0.16	-39.9	698.7	0.06	-31.4	797.9
0.50	4.5	0.005	2.0	1357.6	0.16	-41.4	794.9	0.06	-33.0	909.9
0.50	5.0	0.005	2.0	1557.6	0.16	-42.7	893.0	0.06	-34.3	1022.7
0.60	0.5	0.005	2.0	73.9	0.08	-7.3	68.5	0.02	-3.4	71.4
0.60	1.0	0.005	2.0	195.1	0.12	-17.0	162.0	0.04	-10.0	175.5
0.60	1.5	0.005	2.0	348.3	0.14	-24.2	264.2	0.06	-17.9	286.0
0.60	2.0	0.005	2.0	518.3	0.16	-30.7	359.3	0.08	-23.2	397.9
0.60	2.5	0.005	2.0	704.7	0.16	-33.9	466.0	0.08	-28.8	501.6
0.60	3.0	0.005	2.0	904.5	0.18	-37.0	570.0	0.08	-32.1	614.1
0.60	3.5	0.005	2.0	1113.6	0.18	-40.7	660.5	0.08	-34.7	727.5
0.60	4.0	0.005	2.0	1330.8	0.18	-42.5	765.7	0.08	-36.8	841.6
0.60	4.5	0.005	2.0	1555.0	0.18	-43.7	874.9	0.08	-38.5	956.2
0.60	5.0	0.005	2.0	1785.4	0.18	-44.8	986.1	0.08	-40.0	1071.0
0.70	0.5	0.005	2.0	79.5	0.10	-8.1	73.0	0.02	-3.3	76.8
0.70	1.0	0.005	2.0	215.5	0.14	-18.0	176.8	0.06	-12.7	188.3
0.70	1.5	0.005	2.0	386.6	0.16	-24.9	290.5	0.08	-20.8	306.2
0.70	2.0	0.005	2.0	578.3	0.18	-31.5	396.1	0.08	-25.3	431.9
0.70	2.5	0.005	2.0	791.2	0.18	-34.8	515.6	0.10	-31.9	538.8
0.70	3.0	0.005	2.0	1017.2	0.20	-38.3	627.8	0.10	-36.4	647.0
0.70	3.5	0.005	2.0	1254.2	0.20	-41.3	735.6	0.10	-39.2	763.0
0.70	4.0	0.005	2.0	1500.4	0.20	-42.8	858.0	0.10	-41.4	879.1
0.70	4.5	0.005	2.0	1754.6	0.20	-44.0	982.6	0.10	-43.3	995.0
0.70	5.0	0.005	2.0	2015.5	0.20	-44.9	1109.8	0.10	-44.9	1110.5

$\frac{W}{L}$ [−]	θ [deg]	$\frac{t}{L}$ [−]	$\frac{R}{L}$ [−]	$\sigma_{\mathrm{eq,max}}$ [MPa]	$\frac{\eta_{\mathrm{opt}}}{L}$ [−]	η_{perf} [%]	$\sigma_{\mathrm{eq,max}}$ [MPa]	$\frac{\eta_{\mathrm{opt}}}{L}$ [−]	η_{perf} [%]	$\sigma_{\mathrm{eq,max}}$ [MPa]
0.80	0.5	0.005	2.0	85.2	0.12	-8.8	77.7	0.04	-5.1	80.8
0.80	1.0	0.005	2.0	235.8	0.16	-18.7	191.8	0.08	-14.7	201.2
0.80	1.5	0.005	2.0	424.3	0.18	-25.1	317.7	0.10	-23.3	325.6
0.80	2.0	0.005	2.0	640.0	0.20	-31.9	435.7	0.10	-28.8	455.7
0.80	2.5	0.005	2.0	876.9	0.20	-35.1	568.7	0.10	-32.8	589.3
0.80	3.0	0.005	2.0	1129.1	0.20	-37.7	703.1	0.12	-36.2	719.9
0.80	3.5	0.005	2.0	1393.9	0.22	-40.1	834.5	0.12	-40.1	834.4
0.80	4.0	0.005	2.0	1669.1	0.20	-41.8	970.9	0.12	-43.0	952.0
0.80	4.5	0.005	2.0	1953.3	0.20	-43.5	1103.1	0.12	-45.1	1072.8
0.80	5.0	0.005	2.0	2245.1	0.20	-45.1	1233.6	0.12	-46.7	1197.4
0.90	0.5	0.005	2.0	91.0	0.14	-9.4	82.5	0.04	-5.1	86.4
0.90	1.0	0.005	2.0	256.4	0.18	-19.1	207.3	0.08	-15.1	217.7
0.90	1.5	0.005	2.0	462.5	0.20	-25.2	346.1	0.10	-23.5	353.9
0.90	2.0	0.005	2.0	700.7	0.22	-29.0	497.8	0.12	-31.8	477.7
0.90	2.5	0.005	2.0	961.2	0.22	-33.8	636.1	0.12	-36.1	614.3
0.90	3.0	0.005	2.0	1239.0	0.22	-37.3	776.3	0.12	-39.2	753.0
0.90	3.5	0.005	2.0	1530.9	0.22	-38.9	935.3	0.12	-41.7	892.7
0.90	4.0	0.005	2.0	1834.6	0.22	-40.3	1095.4	0.12	-43.7	1032.8
0.90	4.5	0.005	2.0	2148.3	0.22	-41.5	1256.9	0.12	-45.4	1172.6
0.90	5.0	0.005	2.0	2470.4	0.22	-42.5	1419.7	0.12	-46.9	1311.8
1.00	0.5	0.005	2.0	97.0	0.16	-9.9	87.4	0.06	-6.2	91.0
1.00	1.0	0.005	2.0	276.8	0.18	-17.4	228.6	0.10	-17.0	229.6
1.00	1.5	0.005	2.0	501.3	0.20	-22.5	388.6	0.12	-26.0	370.9
1.00	2.0	0.005	2.0	760.9	0.22	-28.3	545.6	0.14	-31.5	521.5
1.00	2.5	0.005	2.0	1044.7	0.22	-31.0	721.3	0.14	-39.1	635.9
1.00	3.0	0.005	2.0	1347.8	0.22	-33.2	899.9	0.14	-42.5	775.6
1.00	3.5	0.005	2.0	1666.7	0.22	-35.2	1079.5	0.14	-45.1	915.6
1.00	4.0	0.005	2.0	1998.7	0.24	-37.2	1255.7	0.14	-47.2	1055.2
1.00	4.5	0.005	2.0	2341.7	0.22	-38.7	1436.6	0.14	-49.0	1193.6
1.00	5.0	0.005	2.0	2694.2	0.22	-40.2	1612.3	0.14	-50.6	1330.5
1.25	0.5	0.005	2.0	112.4	0.18	-9.6	101.5	0.08	-7.2	104.3
1.25	1.0	0.005	2.0	328.0	0.20	-14.8	279.5	0.14	-20.4	261.2
1.25	1.5	0.005	2.0	598.9	0.20	-17.2	496.0	0.16	-28.8	426.4
1.25	2.0	0.005	2.0	908.7	0.24	-22.0	708.4	0.16	-36.2	579.5
1.25	2.5	0.005	2.0	1248.5	0.24	-25.0	936.0	0.16	-40.0	749.2
1.25	3.0	0.005	2.0	1612.6	0.24	-26.9	1178.2	0.16	-42.8	921.8
1.25	3.5	0.005	2.0	1996.6	0.24	-28.7	1424.2	0.16	-45.1	1095.6
1.25	4.0	0.005	2.0	2397.1	0.24	-30.3	1672.0	0.16	-47.0	1269.5
1.25	4.5	0.005	2.0	2811.6	0.24	-31.7	1919.5	0.16	-48.7	1442.5
1.25	5.0	0.005	2.0	3238.0	0.24	-33.1	2165.4	0.16	-50.2	1613.7
1.50	0.5	0.005	2.0	129.2	0.22	-10.3	115.9	0.12	-9.1	117.4
1.50	1.0	0.005	2.0	381.7	0.22	-12.5	333.8	0.16	-22.7	294.9
1.50	1.5	0.005	2.0	694.5	0.22	-14.1	596.3	0.18	-32.2	471.0
1.50	2.0	0.005	2.0	1051.5	0.24	-16.6	877.3	0.18	-36.8	664.4
1.50	2.5	0.005	2.0	1444.2	0.24	-18.6	1175.0	0.18	-40.1	865.4
1.50	3.0	0.005	2.0	1865.7	0.24	-20.2	1488.2	0.20	-45.0	1026.0
1.50	3.5	0.005	2.0	2311.0	0.24	-21.7	1810.5	0.20	-48.6	1188.8
1.50	4.0	0.005	2.0	2776.2	0.24	-23.0	2138.5	0.20	-51.1	1357.5
1.50	4.5	0.005	2.0	3258.1	0.24	-24.2	2470.0	0.20	-52.9	1533.1
1.50	5.0	0.005	2.0	3754.5	0.24	-25.3	2802.9	0.20	-54.3	1716.2
0.10	0.5	0.008	2.0	84.9	0.00	0.0	84.9	0.00	0.0	84.9
0.10	1.0	0.008	2.0	172.5	0.00	0.0	172.5	0.00	0.0	172.5
0.10	1.5	0.008	2.0	264.8	0.00	0.0	264.8	0.00	0.0	264.8
0.10	2.0	0.008	2.0	361.6	0.00	0.0	361.6	0.00	0.0	361.6
0.10	2.5	0.008	2.0	463.3	0.00	0.0	463.3	0.00	0.0	463.3
0.10	3.0	0.008	2.0	569.2	0.00	0.0	569.2	0.00	0.0	569.2
0.10	3.5	0.008	2.0	680.1	0.02	-2.3	664.6	0.00	0.0	680.1
0.10	4.0	0.008	2.0	794.6	0.02	-4.5	758.5	0.00	0.0	794.6
0.10	4.5	0.008	2.0	913.7	0.02	-6.8	851.8	0.00	0.0	913.7
0.10	5.0	0.008	2.0	1035.6	0.02	-8.8	944.0	0.00	0.0	1035.6
0.20	0.5	0.008	2.0	88.6	0.00	0.0	88.6	0.00	0.0	88.6
0.20	1.0	0.008	2.0	182.9	0.02	-1.7	179.8	0.00	0.0	182.9
0.20	1.5	0.008	2.0	289.6	0.02	-5.4	274.1	0.00	0.0	289.6
0.20	2.0	0.008	2.0	407.8	0.02	-7.5	377.3	0.00	0.0	407.8
0.20	2.5	0.008	2.0	536.6	0.04	-8.8	489.1	0.00	0.0	536.6
0.20	3.0	0.008	2.0	673.9	0.04	-13.8	580.7	0.00	0.0	673.9
0.20	3.5	0.008	2.0	817.5	0.04	-15.4	691.6	0.00	0.0	817.5
0.20	4.0	0.008	2.0	966.7	0.04	-16.6	806.2	0.00	0.0	966.7
0.20	4.5	0.008	2.0	1119.4	0.04	-17.5	923.5	0.02	-3.2	1083.1
0.20	5.0	0.008	2.0	1276.3	0.04	-18.3	1043.0	0.02	-6.1	1198.1

$\frac{W}{L}$ [−]	θ [deg]	$\frac{t}{L}$ [−]	$\frac{R}{L}$ [−]	$\sigma_{\mathrm{eq,max}}$ [MPa]	$\frac{\eta_{\mathrm{opt}}}{L}$ [−]	η_{perf} [%]	$\sigma_{\mathrm{eq,max}}$ [MPa]	$\frac{\eta_{\mathrm{opt}}}{L}$ [−]	η_{perf} [%]	$\sigma_{\mathrm{eq,max}}$ [MPa]
0.30	0.5	0.008	2.0	91.7	0.02	-1.6	90.2	0.00	0.0	91.7
0.30	1.0	0.008	2.0	196.7	0.04	-3.8	189.4	0.00	0.0	196.7
0.30	1.5	0.008	2.0	321.9	0.04	-8.1	295.7	0.00	0.0	321.9
0.30	2.0	0.008	2.0	466.8	0.06	-13.0	406.1	0.00	0.0	466.8
0.30	2.5	0.008	2.0	626.5	0.06	-15.6	528.9	0.02	-7.9	577.1
0.30	3.0	0.008	2.0	796.1	0.08	-18.2	651.4	0.02	-10.2	715.1
0.30	3.5	0.008	2.0	972.9	0.08	-21.8	760.7	0.02	-11.4	862.1
0.30	4.0	0.008	2.0	1157.4	0.08	-23.4	887.1	0.02	-12.5	1013.0
0.30	4.5	0.008	2.0	1347.6	0.08	-24.6	1015.7	0.02	-13.4	1167.3
0.30	5.0	0.008	2.0	1550.3	0.08	-26.1	1146.2	0.02	-14.5	1324.8
0.40	0.5	0.008	2.0	95.4	0.04	-2.4	93.1	0.00	0.0	95.4
0.40	1.0	0.008	2.0	214.2	0.06	-7.0	199.1	0.00	0.0	214.2
0.40	1.5	0.008	2.0	362.4	0.08	-11.8	319.5	0.02	-5.4	342.9
0.40	2.0	0.008	2.0	534.9	0.08	-15.6	451.6	0.02	-7.1	496.6
0.40	2.5	0.008	2.0	725.6	0.10	-20.5	576.6	0.02	-8.7	662.2
0.40	3.0	0.008	2.0	928.2	0.10	-22.7	717.1	0.04	-15.1	787.7
0.40	3.5	0.008	2.0	1140.7	0.12	-25.3	852.3	0.04	-17.0	946.7
0.40	4.0	0.008	2.0	1368.2	0.12	-29.9	959.7	0.04	-18.9	1109.2
0.40	4.5	0.008	2.0	1605.2	0.12	-31.8	1095.2	0.04	-20.6	1274.4
0.40	5.0	0.008	2.0	1849.2	0.12	-33.4	1231.5	0.04	-22.0	1442.0
0.50	0.5	0.008	2.0	100.0	0.04	-3.1	96.8	0.00	0.0	100.0
0.50	1.0	0.008	2.0	234.1	0.08	-8.8	213.5	0.02	-3.9	225.0
0.50	1.5	0.008	2.0	407.0	0.10	-14.4	348.3	0.02	-5.6	384.2
0.50	2.0	0.008	2.0	606.6	0.12	-19.5	488.0	0.04	-11.1	539.5
0.50	2.5	0.008	2.0	828.1	0.12	-22.4	642.4	0.04	-13.5	716.0
0.50	3.0	0.008	2.0	1064.1	0.14	-27.1	775.3	0.06	-18.4	868.6
0.50	3.5	0.008	2.0	1320.7	0.14	-30.4	919.3	0.06	-22.1	1029.2
0.50	4.0	0.008	2.0	1588.1	0.14	-32.6	1071.2	0.06	-24.4	1200.7
0.50	4.5	0.008	2.0	1864.7	0.14	-34.4	1223.8	0.06	-26.3	1374.0
0.50	5.0	0.008	2.0	2149.6	0.14	-35.9	1376.9	0.06	-27.9	1548.8
0.60	0.5	0.008	2.0	105.1	0.06	-3.8	101.1	0.00	0.0	105.1
0.60	1.0	0.008	2.0	255.5	0.10	-10.1	229.7	0.02	-4.0	245.2
0.60	1.5	0.008	2.0	452.6	0.12	-15.8	381.0	0.04	-9.0	412.0
0.60	2.0	0.008	2.0	679.7	0.14	-20.9	537.4	0.06	-14.1	583.6
0.60	2.5	0.008	2.0	932.1	0.16	-24.2	706.1	0.06	-17.4	769.9
0.60	3.0	0.008	2.0	1209.1	0.16	-29.6	850.8	0.06	-20.4	962.3
0.60	3.5	0.008	2.0	1502.5	0.16	-32.1	1019.8	0.08	-26.4	1105.8
0.60	4.0	0.008	2.0	1808.4	0.16	-34.2	1190.3	0.08	-29.0	1284.4
0.60	4.5	0.008	2.0	2125.3	0.16	-36.0	1361.2	0.08	-31.1	1464.1
0.60	5.0	0.008	2.0	2452.3	0.18	-37.8	1524.4	0.08	-32.9	1644.7
0.70	0.5	0.008	2.0	110.5	0.08	-4.2	105.9	0.02	-2.2	108.1
0.70	1.0	0.008	2.0	277.6	0.12	-11.1	246.7	0.04	-6.2	260.3
0.70	1.5	0.008	2.0	498.2	0.14	-16.7	415.0	0.06	-11.2	442.4
0.70	2.0	0.008	2.0	753.3	0.16	-21.9	588.5	0.08	-15.0	640.1
0.70	2.5	0.008	2.0	1040.8	0.18	-25.8	772.5	0.08	-20.9	823.2
0.70	3.0	0.008	2.0	1353.8	0.18	-30.8	936.8	0.08	-24.4	1023.7
0.70	3.5	0.008	2.0	1683.9	0.18	-33.2	1125.6	0.08	-27.0	1228.4
0.70	4.0	0.008	2.0	2028.9	0.18	-35.1	1315.9	0.10	-31.5	1389.1
0.70	4.5	0.008	2.0	2386.9	0.18	-36.9	1506.6	0.10	-35.2	1547.8
0.70	5.0	0.008	2.0	2756.6	0.20	-39.1	1679.9	0.10	-37.2	1730.1
0.80	0.5	0.008	2.0	116.2	0.10	-4.5	111.0	0.02	-2.2	113.6
0.80	1.0	0.008	2.0	300.1	0.14	-11.9	264.4	0.04	-6.2	281.5
0.80	1.5	0.008	2.0	543.5	0.16	-17.3	449.5	0.08	-12.2	477.3
0.80	2.0	0.008	2.0	826.5	0.18	-22.4	641.3	0.08	-17.2	684.1
0.80	2.5	0.008	2.0	1150.2	0.18	-25.6	855.7	0.10	-24.0	874.3
0.80	3.0	0.008	2.0	1497.1	0.20	-30.7	1038.0	0.10	-27.7	1081.8
0.80	3.5	0.008	2.0	1863.8	0.20	-33.6	1238.2	0.10	-30.6	1293.0
0.80	4.0	0.008	2.0	2247.8	0.20	-35.5	1450.1	0.10	-32.9	1507.2
0.80	4.5	0.008	2.0	2646.8	0.20	-37.2	1662.2	0.10	-34.9	1723.5
0.80	5.0	0.008	2.0	3059.0	0.20	-38.7	1873.7	0.10	-36.5	1941.5
0.90	0.5	0.008	2.0	122.1	0.12	-4.7	116.4	0.04	-3.2	118.3
0.90	1.0	0.008	2.0	323.0	0.16	-12.5	282.5	0.06	-7.7	298.1
0.90	1.5	0.008	2.0	588.4	0.18	-17.5	485.2	0.08	-13.1	511.3
0.90	2.0	0.008	2.0	904.6	0.20	-21.6	708.8	0.10	-20.0	723.6
0.90	2.5	0.008	2.0	1258.4	0.20	-25.9	932.6	0.10	-24.4	951.6
0.90	3.0	0.008	2.0	1638.6	0.20	-28.2	1177.3	0.12	-30.7	1136.0
0.90	3.5	0.008	2.0	2041.4	0.22	-32.1	1386.5	0.12	-33.8	1352.2
0.90	4.0	0.008	2.0	2463.7	0.22	-35.2	1596.3	0.12	-36.2	1570.8
0.90	4.5	0.008	2.0	2902.9	0.22	-37.0	1828.1	0.12	-38.3	1790.9
0.90	5.0	0.008	2.0	3357.0	0.22	-38.5	2065.2	0.12	-40.1	2011.8
1.00	0.5	0.008	2.0	128.2	0.12	-4.9	122.0	0.04	-3.1	124.2
1.00	1.0	0.008	2.0	346.0	0.16	-11.9	304.9	0.08	-8.7	315.8
1.00	1.5	0.008	2.0	635.0	0.20	-16.3	531.6	0.10	-14.9	540.3
1.00	2.0	0.008	2.0	982.0	0.20	-20.9	776.6	0.12	-22.4	762.1
1.00	2.5	0.008	2.0	1365.7	0.22	-23.8	1040.7	0.12	-27.1	996.2
1.00	3.0	0.008	2.0	1778.8	0.22	-27.9	1281.9	0.12	-30.4	1237.3
1.00	3.5	0.008	2.0	2217.0	0.22	-29.8	1557.2	0.14	-34.5	1452.0
1.00	4.0	0.008	2.0	2677.0	0.22	-31.4	1836.0	0.14	-38.8	1637.3
1.00	4.5	0.008	2.0	3155.8	0.24	-33.2	2109.4	0.14	-41.5	1847.2
1.00	5.0	0.008	2.0	3651.3	0.24	-35.3	2360.9	0.14	-43.3	2068.6
1.25	0.5	0.008	2.0	144.0	0.16	-5.2	136.4	0.06	-3.8	138.5
1.25	1.0	0.008	2.0	404.8	0.20	-12.0	356.3	0.10	-9.9	364.6
1.25	1.5	0.008	2.0	760.4	0.20	-14.5	650.4	0.12	-17.8	625.1
1.25	2.0	0.008	2.0	1174.5	0.20	-16.3	983.4	0.14	-25.0	880.3
1.25	2.5	0.008	2.0	1630.4	0.20	-17.9	1339.0	0.16	-30.7	1129.7
1.25	3.0	0.008	2.0	2122.7	0.22	-20.9	1678.9	0.16	-35.2	1374.6
1.25	3.5	0.008	2.0	2646.2	0.24	-24.2	2006.4	0.16	-38.0	1641.5
1.25	4.0	0.008	2.0	3196.8	0.24	-25.5	2380.1	0.16	-40.2	1911.9
1.25	4.5	0.008	2.0	3771.1	0.24	-26.8	2758.8	0.16	-42.1	2184.3
1.25	5.0	0.008	2.0	4366.2	0.24	-28.1	3140.3	0.16	-43.7	2457.2
1.50	0.5	0.008	2.0	160.4	0.18	-5.1	152.3	0.08	-4.2	153.7
1.50	1.0	0.008	2.0	467.7	0.22	-10.9	416.6	0.12	-11.5	413.8
1.50	1.5	0.008	2.0	888.6	0.22	-12.8	775.0	0.16	-21.8	694.5
1.50	2.0	0.008	2.0	1364.7	0.22	-13.6	1178.5	0.16	-26.7	1000.1
1.50	2.5	0.008	2.0	1889.4	0.22	-14.8	1609.8	0.18	-33.1	1264.1
1.50	3.0	0.008	2.0	2456.5	0.22	-16.0	2062.8	0.18	-36.0	1571.3
1.50	3.5	0.008	2.0	3060.5	0.24	-18.1	2507.5	0.18	-38.4	1886.0
1.50	4.0	0.008	2.0	3696.7	0.24	-19.2	2986.4	0.18	-40.3	2205.8
1.50	4.5	0.008	2.0	4361.2	0.24	-20.3	3475.8	0.18	-42.0	2528.3
1.50	5.0	0.008	2.0	5050.7	0.24	-21.3	3972.6	0.20	-44.0	2830.0

Appendix H - Evaluation of various polynomial regression models

Appendix H provides an evaluation of polynomial regression models by comparing their Root Mean Squared Error (RMSE) and the R-squared values. Additionally, an example illustrates the risk of overfitting for a polynomial degree that is too large.

The RMSE measures the average magnitude of prediction errors, providing an indication of how close the predicted values are to the actual simulated values [17]. The R-squared value quantifies the proportion of variance in the output that is explained by the model, serving as a measure of its overall fit with a value between 0 and 1 [17]. As observed in Tables 17, 18, 19, 20 and 21, increasing the polynomial degree results in a lower RMSE and an R-squared value closer to 1. This indicates an improved fit as the polynomial degree increases.

Table 17: Tapered flexure: $\frac{\eta_{\text{optimal}}}{L}$

Model	RMSE [−]	R-squared [−]	Coefficients
poly1111	0.0333	0.794	5
poly1112	0.0324	0.805	12
poly1121	0.0324	0.805	12
poly1211	0.0317	0.813	12
poly2111	0.0185	0.936	12
poly2211	0.0172	0.944	13
poly3211	0.0153	0.956	24
poly4322	0.0123	0.971	59
poly4444	0.0121	0.972	70
poly6544	0.0091	0.984	199

Table 18: Tapered flexure: $\eta_{\text{performance}}$

Model	RMSE [%]	R-squared [−]	Coefficients
poly1111	8.7306	0.623	5
poly1112	8.1613	0.670	12
poly1121	8.0373	0.680	12
poly1211	7.8546	0.695	12
poly2111	5.1666	0.868	12
poly2211	4.6640	0.892	13
poly3211	2.9008	0.958	24
poly4322	1.5914	0.987	59
poly4444	1.4406	0.990	70
poly6544	0.9887	0.995	199

Table 19: Bow-tie flexure: $\frac{\eta_{\text{optimal}}}{L}$

Model	RMSE [−]	R-squared [−]	Coefficients
poly1111	0.0197	0.923	5
poly1112	0.0152	0.954	12
poly1121	0.0151	0.955	12
poly1211	0.0132	0.965	12
poly2111	0.0143	0.959	12
poly2211	0.0122	0.971	13
poly3211	0.0093	0.983	24
poly4322	0.0064	0.992	59
poly4444	0.0063	0.992	70
poly6544	0.0055	0.994	199

Table 20: Bow-tie flexure: $\eta_{\text{performance}}$

Model	RMSE [%]	R-squared [−]	Coefficients
poly1111	7.9454	0.839	5
poly1112	7.6418	0.851	12
poly1121	7.1918	0.868	12
poly1211	7.1115	0.871	12
poly2111	5.8551	0.913	12
poly2211	5.1388	0.933	13
poly3211	3.9650	0.960	24
poly4322	2.0070	0.990	59
poly4444	1.7897	0.992	70
poly6544	1.2976	0.996	199

Table 21: Sheet flexure: $\sigma_{\text{eq,max}}$

Model	RMSE [MPa]	R-squared [−]	Coefficients
poly1111	359.5664	0.748	5
poly1112	129.9433	0.967	12
poly1121	125.1707	0.969	12
poly1211	124.2685	0.970	12
poly2111	129.9656	0.967	12
poly2211	124.2656	0.970	13
poly3211	54.3012	0.994	24
poly4322	14.3781	1.000	59
poly4444	7.0404	1.000	70
poly6544	1.6064	1.000	199

Example plots of four different prediction models $\frac{\eta_{optimal}}{L}$ tapered flexure

Figure H.1 illustrates how different polynomial orders influence the fit of a prediction model. In these graphs the solid and open dots represent the simulation output data, while the solid and dashed lines represent the prediction models. In Figure H.1a (poly1111), where all degrees are set to 1, the model results in a linear approximation. By introducing higher polynomial degrees, as seen in Figures H.1b (poly2211) and H.1c (poly4322), the prediction model aligns more closely with the simulation output. However, as shown in Figure H.1d (poly6544), a very high polynomial order can lead to overfitting, where the model follows the training data too closely rather than generalizing the data. The simulation output is limited by the resolution of $\frac{\eta}{L}$, and while the poly4322 model smooths out this behavior, the poly6544 model attempts to fit these discrete data points too precisely.

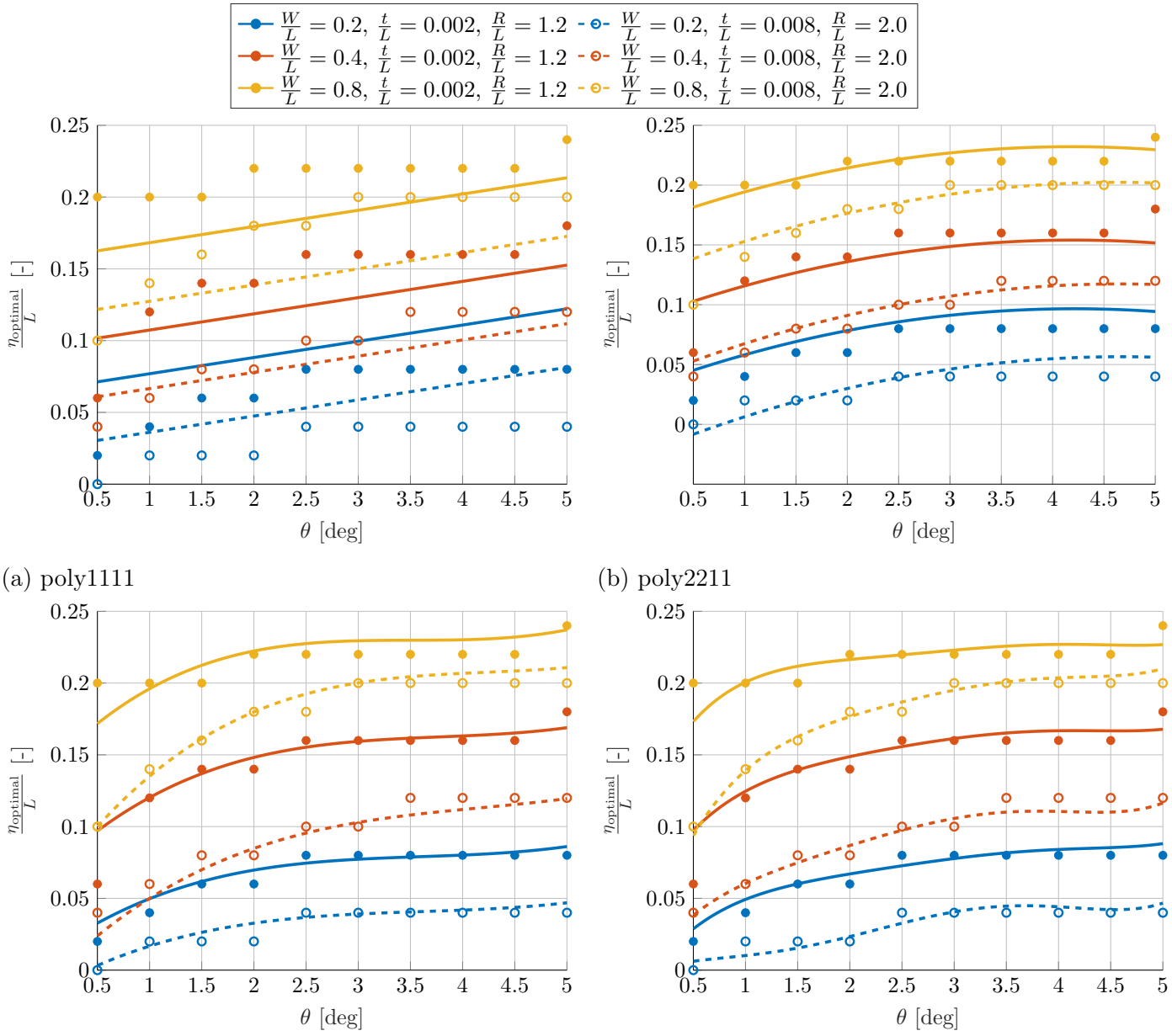

(a) poly1111

(b) poly2211

(c) poly4322

(d) poly6544

Figure H.1: Comparison of different poly models for the prediction of $\frac{\eta_{optimal}}{L}$ of the tapered flexure

Appendix I - MATLAB code for all prediction models

Appendix I provides the MATLAB code for all of the prediction models.

Prediction model: Tapered flexure $\eta_{optimal}$

```
%% ================================================================================================
% Function that predicts eta_optimal/L based on input parameters {W/L,t/L,theta,R/L}
% using a polynomial regression model that is fitted to ANSYS FEA data
%
% Input              Unit    Dataset range       Description
%   x1 = W/L         [-]     [0.1 - 1.5]         Width/Length of the flexure
%   x2 = theta       [deg]   [0.5 - 5]           Prescribed rotation of the flexure
%   x3 = t/L         [-]     [0.001 - 0.008]     Thickness/Length of the flexure
%   x4 = R/L         [-]     [1.2 - 2.0]         Radius/Length of the flexure
%
% Output:
%   y =  eta_opt/L   [-]                         Optimal eta/Length of the flexure
%
% See for additional information:
% Chapter 3, Chapter 4, Chapter 5, Appendix G, Appendix H and Appendix J of:
%   T. Bomer, "Flange design for stress reduction in radially arranged sheet flexures with one
    rotational degree of freedom",
%   MSc Thesis, University of Twente, 2025
%================================================================================================

function y = predict_optimal_shape_tapered_flexure(x1, x2, x3, x4)
    % Coefficients
    C = [-0.105586, 0.664928, 0.060997, -5.184208, 0.070382, -0.672907, 0.124221, -0.013263,
    -8.767283, -5.014556, 2487.455286, -0.156726, -0.034158, -17.231680, -0.005579, 0.132027,
    -0.106346, -0.017603, 0.001174, 24.480351, -2.056795, -0.015586, -2496.547148, -321.813628,
    0.341349, 0.002860, 0.004488, 6.283105, 10.881290, -979.825399, -0.029526, -0.002422, 5.275085,
    0.042743, 0.027195, 0.010115, 0.000916, -10.047132, -7.117723, 0.267457, 0.108895, 1728.596025,
    320.018606, 14.539333, -0.133754, 0.002757, -0.003721, -0.000442, 0.946344, 4.546755, -0.853325,
     -536.844108, -75.374962, 0.007803, -0.000303, 0.001460, -3.604134, -1.992845, 307.765152];

    % Poly4322 model
    y = C(1) + C(2)*x1 + C(3)*x2 + C(4)*x3 + C(5)*x4 + C(6)*x1^2 + C(7)*x1*x2 + C(8)*x2^2 + C(9)*x1*
    x3 + C(10)*x2*x3 + C(11)*x3^2 + C(12)*x1*x4 + C(13)*x2*x4 + C(14)*x3*x4 + C(15)*x4^2 + C(16)*x1
    ^3 + C(17)*x1^2*x2 + C(18)*x1*x2^2 + C(19)*x2^3 + C(20)*x1^2*x3 + C(21)*x1*x2*x3 + C(22)*x2^2*x3
     + C(23)*x1*x3^2 + C(24)*x2*x3^2 + C(25)*x1^2*x4 + C(26)*x1*x2*x4 + C(27)*x2^2*x4 + C(28)*x1*x3*
    x4 + C(29)*x2*x3*x4 + C(30)*x3^2*x4 + C(31)*x1*x4^2 + C(32)*x2*x4^2 + C(33)*x3*x4^2 + C(34)*x1^4
     + C(35)*x1^3*x2 + C(36)*x1^2*x2^2 + C(37)*x1*x2^3 + C(38)*x1^3*x3 + C(39)*x1^2*x2*x3 + C(40)*x1
    *x2^2*x3 + C(41)*x2^3*x3 + C(42)*x1^2*x3^2 + C(43)*x1*x2*x3^2 + C(44)*x2^2*x3^2 + C(45)*x1^3*x4
    + C(46)*x1^2*x2*x4 + C(47)*x1*x2^2*x4 + C(48)*x2^3*x4 + C(49)*x1^2*x3*x4 + C(50)*x1*x2*x3*x4 + C
    (51)*x2^2*x3*x4 + C(52)*x1*x3^2*x4 + C(53)*x2*x3^2*x4 + C(54)*x1^2*x4^2 + C(55)*x1*x2*x4^2 + C
    (56)*x2^2*x4^2 + C(57)*x1*x3*x4^2 + C(58)*x2*x3*x4^2 + C(59)*x3^2*x4^2;
end
```

Prediction model: Tapered flexure $\eta_{\text{performance}}$

```
%% ============================================================================================
% predict_optimal_stress_reduction_tapered_flexure
% ----------------------------------------
% Function that predicts eta_performance based on input parameters {W/L,t/L,theta,R/L}
% using a polynomial regression model that is fitted to ANSYS FEA data
%
% Input             Unit    Dataset range       Description
%   x1 = W/L        [-]     [0.1 - 1.5]         Width/Length of the flexure
%   x2 = theta      [deg]   [0.5 - 5]           Prescribed rotation of the flexure
%   x3 = t/L        [-]     [0.001 - 0.008]     Thickness/Length of the flexure
%   x4 = R/L        [-]     [1.2 - 2.0]         Radius/Length of the flexure
%
% Output:
%   y =  eta_perf   [%]                         Stress reduction of tapered eta_optimal in
    comparison with sheet flexure that has same input parameters (negative value = stress reduction,
     positive = stress increase)
%
% See for additional information:
% Chapter 3, Chapter 4, Chapter 5, Appendix G, Appendix H and Appendix J of:
%   T. Bomer, "Flange design for stress reduction in radially arranged sheet flexures with one
    rotational degree of freedom",
%   MSc Thesis, University of Twente, 2025
% ============================================================================================

function y = predict_optimal_stress_reduction_tapered_flexure(x1, x2, x3, x4)
    % Coefficients
    C = [-11.970809, -65.709084, -20.943292, 5537.207616, 28.250229, 231.612093, -4.823861,
    4.420300, 2175.972431, 3407.319995, -779962.585598, -110.311992, -1.924943, -378.682493,
    -8.143109, -176.326499, 23.795367, 2.260860, -0.323724, -12694.494215, -3130.691379,
    -931.902740, 697114.237639, 29169.143262, 37.077234, -11.596376, 0.814823, 7618.893785,
    -241.539830, -7692.867685, 33.408944, 0.377148, -91.062602, 36.846461, -6.239076, -1.905464,
    -0.054853, 2481.270227, 734.956382, 131.523912, 74.805533, 129627.841835, 18305.897640,
    6083.714742, 14.761796, 2.139170, 0.288745, -0.158108, 759.245354, 501.415533, 4.923750,
    -447472.317689, 20892.909363, -19.717898, 0.339378, 0.238525, -1287.870374, -142.391743,
    63833.026096];

    % Poly4322 model
    y = C(1) + C(2)*x1 + C(3)*x2 + C(4)*x3 + C(5)*x4 + C(6)*x1^2 + C(7)*x1*x2 + C(8)*x2^2 + C(9)*x1*
    x3 + C(10)*x2*x3 + C(11)*x3^2 + C(12)*x1*x4 + C(13)*x2*x4 + C(14)*x3*x4 + C(15)*x4^2 + C(16)*x1
    ^3 + C(17)*x1^2*x2 + C(18)*x1*x2^2 + C(19)*x2^3 + C(20)*x1^2*x3 + C(21)*x1*x2*x3 + C(22)*x2^2*x3
     + C(23)*x1*x3^2 + C(24)*x2*x3^2 + C(25)*x1^2*x4 + C(26)*x1*x2*x4 + C(27)*x2^2*x4 + C(28)*x1*x3*
    x4 + C(29)*x2*x3*x4 + C(30)*x3^2*x4 + C(31)*x1*x4^2 + C(32)*x2*x4^2 + C(33)*x3*x4^2 + C(34)*x1^4
     + C(35)*x1^3*x2 + C(36)*x1^2*x2^2 + C(37)*x1*x2^3 + C(38)*x1^3*x3 + C(39)*x1^2*x2*x3 + C(40)*x1
    *x2^2*x3 + C(41)*x2^3*x3 + C(42)*x1^2*x3^2 + C(43)*x1*x2*x3^2 + C(44)*x2^2*x3^2 + C(45)*x1^3*x4
    + C(46)*x1^2*x2*x4 + C(47)*x1*x2^2*x4 + C(48)*x2^3*x4 + C(49)*x1^2*x3*x4 + C(50)*x1*x2*x3*x4 + C
    (51)*x2^2*x3*x4 + C(52)*x1*x3^2*x4 + C(53)*x2*x3^2*x4 + C(54)*x1^2*x4^2 + C(55)*x1*x2*x4^2 + C
    (56)*x2^2*x4^2 + C(57)*x1*x3*x4^2 + C(58)*x2*x3*x4^2 + C(59)*x3^2*x4^2;
end
```

Prediction model: Bow-tie flexure η_{optimal}

```
%% ============================================================================================================
% predict_optimal_shape_bowtie_flexure
% ------------------------------------
% Function that predicts eta_optimal/L based on input parameters {W/L,t/L,theta,R/L}
% using a polynomial regression model that is fitted to ANSYS FEA data
%
% Input              Unit    Dataset range       Description
%   x1 = W/L         [-]     [0.1 - 1.5]         Width/Length of the flexure
%   x2 = theta       [deg]   [0.5 - 5]           Prescribed rotation of the flexure
%   x3 = t/L         [-]     [0.001 - 0.008]     Thickness/Length of the flexure
%   x4 = R/L         [-]     [1.2 - 2.0]         Radius/Length of the flexure
%
% Output:
%   y =  eta_opt/L   [-]                         Optimal eta/Length of the flexure
%
% See for additional information:
% Chapter 3, Chapter 4, Chapter 5, Appendix G, Appendix H and Appendix J of:
%   T. Bomer, "Flange design for stress reduction in radially arranged sheet flexures with one
    rotational degree of freedom",
%   MSc Thesis, University of Twente, 2025
% ============================================================================================================

function y = predict_optimal_shape_bowtie_flexure(x1, x2, x3, x4)
    % Coefficients
    C = [-0.025685, 0.334928, 0.044114, -23.821523, 0.025101, 0.221493, 0.142960, -0.016296,
    -78.716537, 5.074499, 3419.178573, -0.288321, -0.033228, 8.291185, -0.003938, -0.284376,
    -0.072093, -0.025959, 0.000968, 43.637581, 17.399603, 0.410226, -435.654409, -1655.972134,
    0.097725, -0.041836, 0.012501, 22.912897, -1.521063, -276.500946, 0.066456, 0.004759, -0.393929,
     0.068274, 0.014288, 0.003980, 0.001841, -9.115268, -2.429106, -1.220748, -0.068837, 35.377057,
    -116.547233, 181.103969, 0.018911, 0.009475, 0.003039, -0.000410, -7.000724, -1.788561,
    -0.541877, 212.406641, 296.525865, -0.032321, 0.003305, -0.002131, -2.161172, 0.757576,
    -323.547980];

    % Poly4322 model
    y = C(1) + C(2)*x1 + C(3)*x2 + C(4)*x3 + C(5)*x4 + C(6)*x1^2 + C(7)*x1*x2 + C(8)*x2^2 + C(9)*x1*
    x3 + C(10)*x2*x3 + C(11)*x3^2 + C(12)*x1*x4 + C(13)*x2*x4 + C(14)*x3*x4 + C(15)*x4^2 + C(16)*x1
    ^3 + C(17)*x1^2*x2 + C(18)*x1*x2^2 + C(19)*x2^3 + C(20)*x1^2*x3 + C(21)*x1*x2*x3 + C(22)*x2^2*x3
     + C(23)*x1*x3^2 + C(24)*x2*x3^2 + C(25)*x1^2*x4 + C(26)*x1*x2*x4 + C(27)*x2^2*x4 + C(28)*x1*x3*
    x4 + C(29)*x2*x3*x4 + C(30)*x3^2*x4 + C(31)*x1*x4^2 + C(32)*x2*x4^2 + C(33)*x3*x4^2 + C(34)*x1^4
     + C(35)*x1^3*x2 + C(36)*x1^2*x2^2 + C(37)*x1*x2^3 + C(38)*x1^3*x3 + C(39)*x1^2*x2*x3 + C(40)*x1
    *x2^2*x3 + C(41)*x2^3*x3 + C(42)*x1^2*x3^2 + C(43)*x1*x2*x3^2 + C(44)*x2^2*x3^2 + C(45)*x1^3*x4
    + C(46)*x1^2*x2*x4 + C(47)*x1*x2^2*x4 + C(48)*x2^3*x4 + C(49)*x1^2*x3*x4 + C(50)*x1*x2*x3*x4 + C
    (51)*x2^2*x3*x4 + C(52)*x1*x3^2*x4 + C(53)*x2*x3^2*x4 + C(54)*x1^2*x4^2 + C(55)*x1*x2*x4^2 + C
    (56)*x2^2*x4^2 + C(57)*x1*x3*x4^2 + C(58)*x2*x3*x4^2 + C(59)*x3^2*x4^2;
end
```

Prediction model: Bow-tie flexure $\eta_{\text{performance}}$

```
%% ================================================================================================
% predict_optimal_stress_reduction_bowtie_flexure
% ---------------------------------------
% Function that predicts eta_performance based on input parameters {W/L,t/L,theta,R/L}
% using a polynomial regression model that is fitted to ANSYS FEA data
%
% Input             Unit    Dataset range       Description
%   x1 = W/L        [-]     [0.1 - 1.5]         Width/Length of the flexure
%   x2 = theta      [deg]   [0.5 - 5]           Prescribed rotation of the flexure
%   x3 = t/L        [-]     [0.001 - 0.008]     Thickness/Length of the flexure
%   x4 = R/L        [-]     [1.2 - 2.0]         Radius/Length of the flexure
%
% Output:
%   y =  eta_perf   [%]                         Stress reduction of bowt-tie eta_optimal in
    comparison with sheet flexure that has same input parameters (negative value = stress reduction,
     positive = stress increase)
%
% See for additional information:
% Chapter 3, Chapter 4, Chapter 5, Appendix G, Appendix H and Appendix J of:
%   T. Bomer, "Flange design for stress reduction in radially arranged sheet flexures with one
    rotational degree of freedom",
%   MSc Thesis, University of Twente, 2025
% ================================================================================================

function y = predict_optimal_stress_reduction_bowtie_flexure(x1, x2, x3, x4)
    % Coefficients
    C = [13.976244, -99.431152, -25.670343, -565.389901, 4.668544, 141.705617, -25.532453, 5.853098,
     20013.307557, 5904.562256, -602789.740769, -36.252288, -0.052983, 3474.520989, -0.401944,
    -92.108721, 23.876730, 5.832684, -0.387741, -16485.329642, -4736.497822, -1471.543397,
    -163078.385763, 24229.105605, 18.454610, -4.590890, -0.300934, 1653.495180, -487.961395,
    -189359.486885, 6.745600, 1.275427, -1435.662419, 22.762366, -7.639793, -1.524599, -0.411299,
    5099.503926, 1090.949754, 122.625086, 124.547975, -9572.151573, 185215.266753, -6813.571700,
    -2.846825, 2.003651, 0.482312, -0.101144, -807.538509, -151.404696, 108.988385, -114887.628949,
    7802.926997, -3.323408, -0.534175, 0.140394, 535.978888, -75.707265, 91308.482187];

    % Poly4322 model
    y = C(1) + C(2)*x1 + C(3)*x2 + C(4)*x3 + C(5)*x4 + C(6)*x1^2 + C(7)*x1*x2 + C(8)*x2^2 + C(9)*x1*
    x3 + C(10)*x2*x3 + C(11)*x3^2 + C(12)*x1*x4 + C(13)*x2*x4 + C(14)*x3*x4 + C(15)*x4^2 + C(16)*x1
    ^3 + C(17)*x1^2*x2 + C(18)*x1*x2^2 + C(19)*x2^3 + C(20)*x1^2*x3 + C(21)*x1*x2*x3 + C(22)*x2^2*x3
     + C(23)*x1*x3^2 + C(24)*x2*x3^2 + C(25)*x1^2*x4 + C(26)*x1*x2*x4 + C(27)*x2^2*x4 + C(28)*x1*x3*
    x4 + C(29)*x2*x3*x4 + C(30)*x3^2*x4 + C(31)*x1*x4^2 + C(32)*x2*x4^2 + C(33)*x3*x4^2 + C(34)*x1^4
     + C(35)*x1^3*x2 + C(36)*x1^2*x2^2 + C(37)*x1*x2^3 + C(38)*x1^3*x3 + C(39)*x1^2*x2*x3 + C(40)*x1
    *x2^2*x3 + C(41)*x2^3*x3 + C(42)*x1^2*x3^2 + C(43)*x1*x2*x3^2 + C(44)*x2^2*x3^2 + C(45)*x1^3*x4
    + C(46)*x1^2*x2*x4 + C(47)*x1*x2^2*x4 + C(48)*x2^3*x4 + C(49)*x1^2*x3*x4 + C(50)*x1*x2*x3*x4 + C
    (51)*x2^2*x3*x4 + C(52)*x1*x3^2*x4 + C(53)*x2*x3^2*x4 + C(54)*x1^2*x4^2 + C(55)*x1*x2*x4^2 + C
    (56)*x2^2*x4^2 + C(57)*x1*x3*x4^2 + C(58)*x2*x3*x4^2 + C(59)*x3^2*x4^2;
end
```

Prediction model: Sheet flexure $\sigma_{\mathbf{eq,max}}$

```
%% ================================================================================================
% predict_sigma_max_sheet_flexure
% ---------------------------------------
% Function that predicts sigma_max of the sheet flexure based on input parameters {W/L,t/L,theta,R/L
    }
% using a polynomial regression model that is fitted to ANSYS FEA data
%
% Input             Unit    Dataset range       Description
%   x1 = W/L        [-]     [0.1 - 1.5]         Width/Length of the flexure
%   x2 = theta      [deg]   [0.5 - 5]           Prescribed rotation of the flexure
%   x3 = t/L        [-]     [0.001 - 0.008]     Thickness/Length of the flexure
%   x4 = R/L        [-]     [1.2 - 2.0]         Radius/Length of the flexure
%
% Output:
%   y =  sigma_max  [MPa]                       maximum von Mises stress of the sheet flexure
%
% See for additional information:
% Chapter 3, Chapter 4, Chapter 5, Appendix G, Appendix H and Appendix J of:
%   T. Bomer, "Flange design for stress reduction in radially arranged sheet flexures with one
    rotational degree of freedom",
%   MSc Thesis, University of Twente, 2025
% ================================================================================================
function y = predict_sigma_max_sheet_flexure(x1, x2, x3, x4)
    % Coefficients
    C = [-84.308271, 129.815603, 102.614591, 30811.671581, 27.385359, 25.252928, -140.485222,
    -28.707924, -100917.189919, -26849.073753, -99927.620591, 32.708276, -44.547683, -6180.759652,
    -5.922639, -131.293387, 97.948254, 34.087171, 3.118464, 52524.890165, 32987.514623, 5651.786553,
     4826964.868005, 1084343.607309, -57.398709, 57.548837, 7.408151, 28262.101824, 15614.866655,
    -1441324.431593, -25.445113, 15.591040, -201.964993, 80.999587, -27.750323, -4.610381,
    -4.142724, -19716.974819, -1258.480498, 6828.317903, -645.209641, 878425.118443,
    -4433441.229235, -121506.600249, -24.464283, -6.970698, 3.698379, -0.514976, -2443.745359,
    20893.360953, 900.559071, -2309795.191204, -362674.257315, 39.688573, -18.778354, -1.943609,
    -5577.074229, -2514.050982, 825031.553562];

    % Poly4322 model
    y = C(1) + C(2)*x1 + C(3)*x2 + C(4)*x3 + C(5)*x4 + C(6)*x1^2 + C(7)*x1*x2 + C(8)*x2^2 + C(9)*x1*
    x3 + C(10)*x2*x3 + C(11)*x3^2 + C(12)*x1*x4 + C(13)*x2*x4 + C(14)*x3*x4 + C(15)*x4^2 + C(16)*x1
    ^3 + C(17)*x1^2*x2 + C(18)*x1*x2^2 + C(19)*x2^3 + C(20)*x1^2*x3 + C(21)*x1*x2*x3 + C(22)*x2^2*x3
     + C(23)*x1*x3^2 + C(24)*x2*x3^2 + C(25)*x1^2*x4 + C(26)*x1*x2*x4 + C(27)*x2^2*x4 + C(28)*x1*x3*
    x4 + C(29)*x2*x3*x4 + C(30)*x3^2*x4 + C(31)*x1*x4^2 + C(32)*x2*x4^2 + C(33)*x3*x4^2 + C(34)*x1^4
     + C(35)*x1^3*x2 + C(36)*x1^2*x2^2 + C(37)*x1*x2^3 + C(38)*x1^3*x3 + C(39)*x1^2*x2*x3 + C(40)*x1
    *x2^2*x3 + C(41)*x2^3*x3 + C(42)*x1^2*x3^2 + C(43)*x1*x2*x3^2 + C(44)*x2^2*x3^2 + C(45)*x1^3*x4
    + C(46)*x1^2*x2*x4 + C(47)*x1*x2^2*x4 + C(48)*x2^3*x4 + C(49)*x1^2*x3*x4 + C(50)*x1*x2*x3*x4 + C
    (51)*x2^2*x3*x4 + C(52)*x1*x3^2*x4 + C(53)*x2*x3^2*x4 + C(54)*x1^2*x4^2 + C(55)*x1*x2*x4^2 + C
    (56)*x2^2*x4^2 + C(57)*x1*x3*x4^2 + C(58)*x2*x3*x4^2 + C(59)*x3^2*x4^2;
end
```

Appendix J - Error heat maps for all prediction models

Appendix J provides detailed error heat maps for all prediction models. The heat maps present the maximum relative error between the poly4322 model and the ANSYS output across different $\frac{W}{L}$ and θ configurations. All configurations that share the same $\frac{W}{L}$ and θ values are grouped within a single cell, the maximum absolute error among these configurations is then used to generate the color gradient of the heat map. Additionally, each cell now includes the minimum and maximum error that occurs within the set of configurations that associated with that cell.

Prediction model: Tapered flexure η_{optimal}

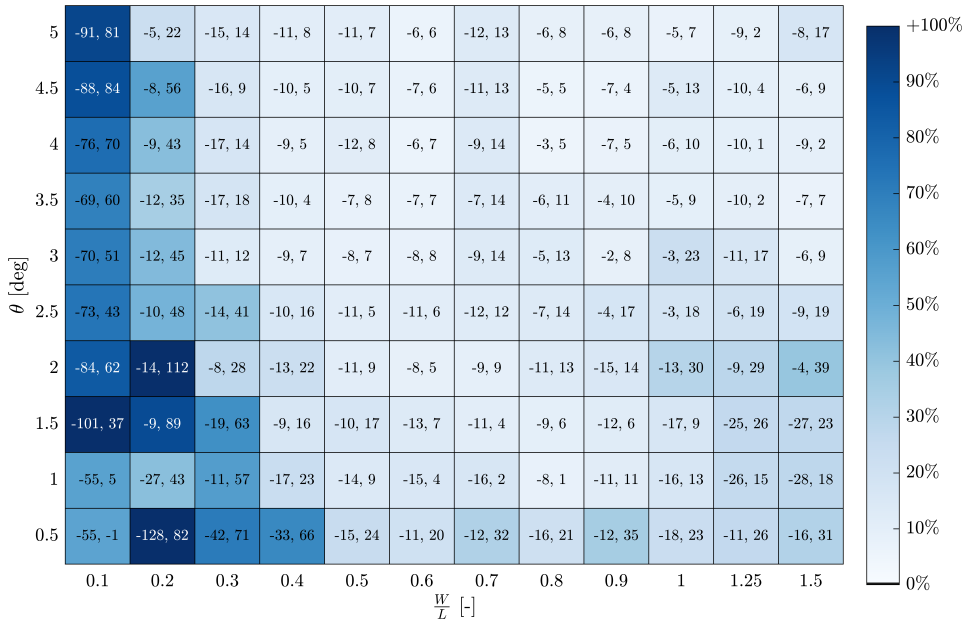

Figure J.1: [minimum, maximum] relative error [%] for predicted $\frac{\eta_{\text{optimal}}}{L}$ of the tapered flexure with maximum relative |error| used for color

Prediction model: Tapered flexure $\eta_{\text{performance}}$

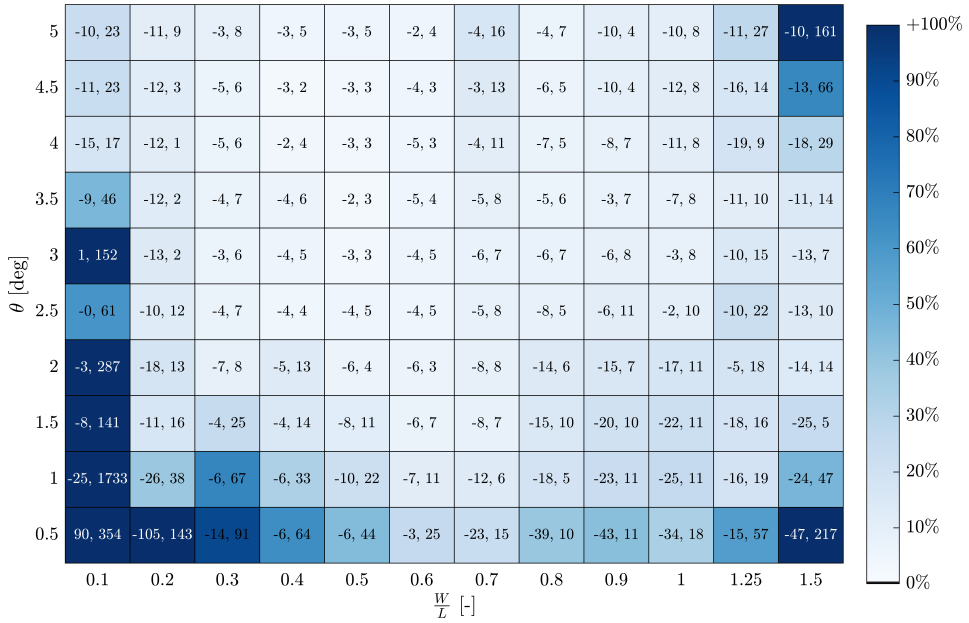

Figure J.2: [minimum, maximum] relative error [%] for predicted $\eta_{\text{performance}}$ of the tapered flexure with maximum relative |error| used for color

Prediction model: Bow-tie flexure η_{optimal}

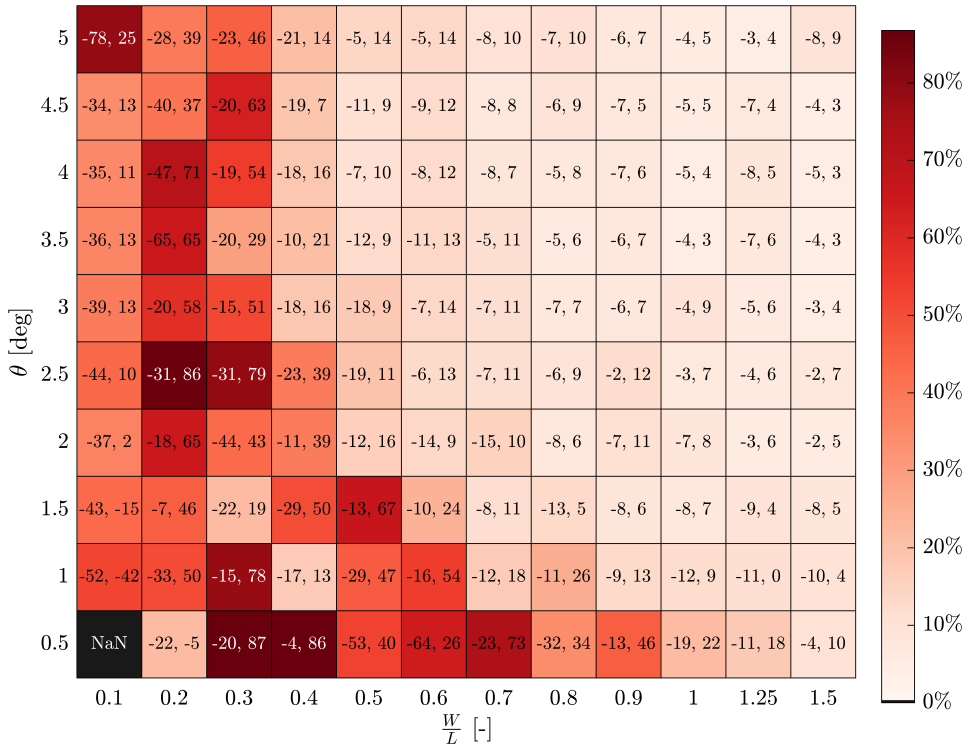

Figure J.3: [minimum, maximum] relative error [%] for predicted $\frac{\eta_{\text{optimal}}}{L}$ of the bow-tie flexure with maximum relative |error| used for color

Prediction model: Bow-tie flexure $\eta_{\text{performance}}$

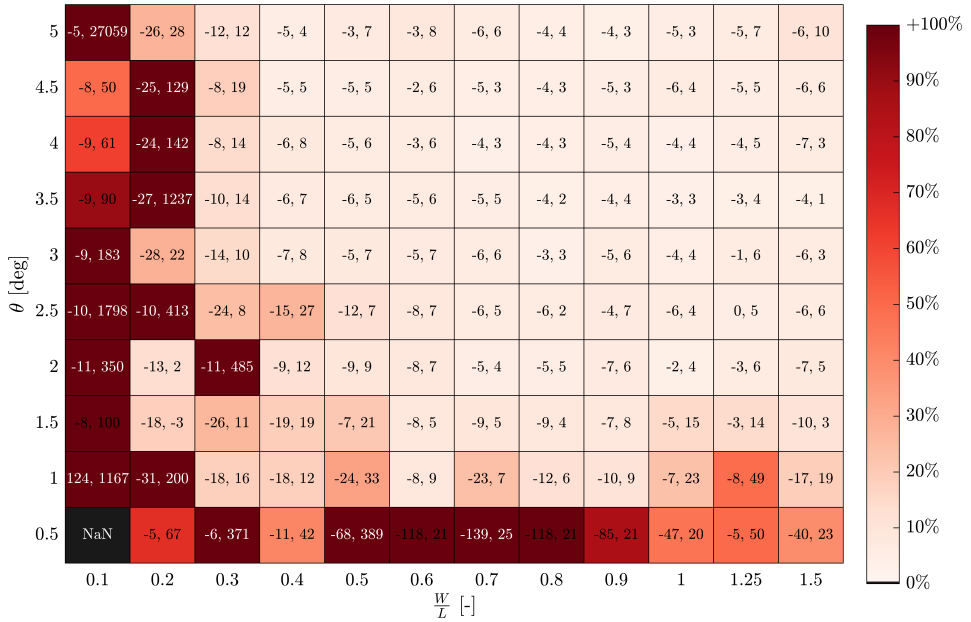

Figure J.4: [minimum, maximum] relative error [%] for predicted $\eta_{\text{performance}}$ of the bow-tie flexure with maximum relative |error| used for color

Prediction model: Sheet flexure $\sigma_{\mathbf{eq,max}}$

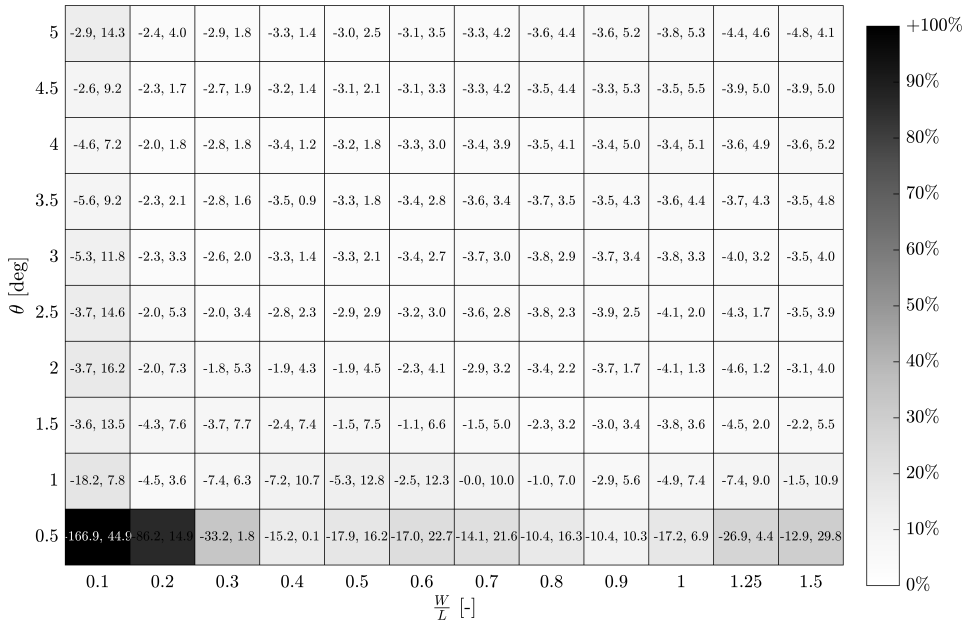

Figure J.5: [minimum, maximum] relative error [%] $\sigma_{\mathrm{eq,max}}$ the sheet flexure with maximum relative |error| used for color

Appendix K - Modifying the inner edge and comparing support stiffness

Appendix K examines whether altering the inner vertical edge of the tapered flexure can reduce the stress even further. To ensure a fair comparison between this flexure, the sheet flexure and the tapered flexure, the support stiffness is included as a performance metric. Additionally, two figures illustrate how η affects the supports stiffness of the tapered and bow-tie flexure.

The inner edge flexure is illustrated in Figure K.1. It is a modified version of the tapered flexure that replaces the inner vertical edge with an arc that passes through the points C and D. The inner edge flexure is derived within the geometry of the sheet flexure and is fully defined by distance η, γ and specific geometric constraints that are applied to the points. The arc's center P is constrained to move along the flexures symmetry line. Increasing the distance γ, progressively removes material from the inner side of the flexure.

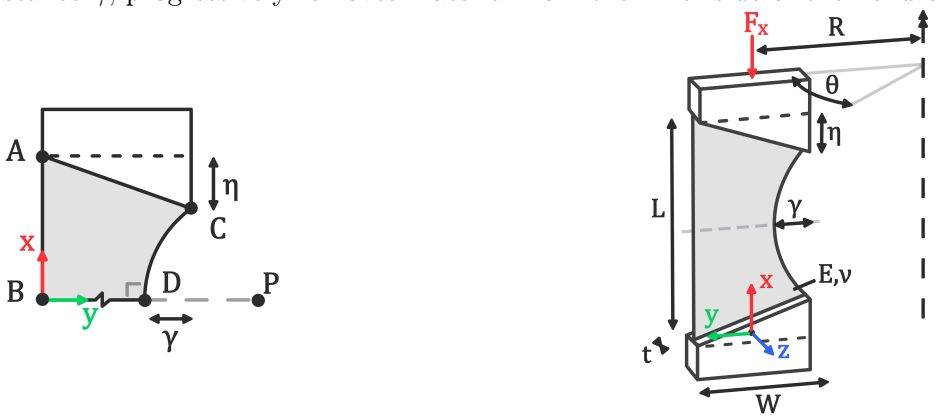

(a) 2D schematic of η and γ input parameters (b) 3D schematic of all input parameters

Figure K.1: Inner edge flexure

The maximum von Mises stress is compared between four flexure designs: the sheet flexure (black), the tapered flexure (orange), the inner edge flexure (grey), and a tapered flexure with minimal W (blue). This flexure has is similar to the tapered flexure but with a width equal to the smallest width of the inner edge flexure. All flexure shapes are illustrated in Figure K.2. The flexures are modeled with $L = 100$ mm, $t = 0.5$ mm, $R = 75$ mm, $E = 193$ GPa, $G = 74$ GPa and a prescribed rotation of $\theta = [0.5 - 5]°$. The sheet flexure, tapered flexure and inner edge flexure are modeled with $W = 50$ mm. The γ of the inner edge flexure is set to 25 mm and therefore the tapered flexure with minimal W is modeled with $W = 25$ mm. The tapered flexure and inner flexure have $\eta = 16$ mm and thus the tapered flexure with minimal W has an η of 8 mm.

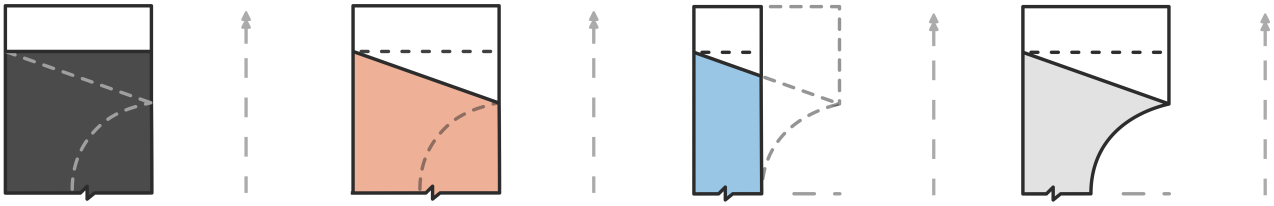

(a) Sheet flexure (b) Tapered flexure (c) Tapered flexure minimal W (d) Vertical edge flexure

Figure K.2: Four flexure designs

Comparing these designs solely by stress is insufficient, as more slender flexures inherently experience less stress. To provide a fair comparison, the support stiffness of each design is also evaluated. The support stiffness is determined by applying a constant axial force F_x of 10 N, along the prescribed boundary conditions of Chapter 2.1, and measuring the displacement difference along the global $x-$axis of the top flange with and without the applied force. The maximum von Mises stress and the support stiffness are illustrated in Figure K.3. The stress comparison shows that the inner edge flexure experiences lower stress compared to the sheet flexure and the tapered flexure. The tapered flexure with minimal W has a maximum stress that

is similar to that of the inner edge flexure. The support stiffness comparison illustrates a rapid decrease in stiffness as the prescribed rotation increases for all flexures. It also illustrates that the inner edge flexure and the tapered flexure with minimal W have a similar support stiffness. The support stiffness of these flexures is significantly lower than the sheet and tapered flexure. The inner edge flexure is deemed obsolete, as it has similar stress and support stiffness compared to that of the tapered flexure with minimal W. In other words, one can simply design a tapered flexure with minimal W, achieving the same performance without the need for the inner edge modification.

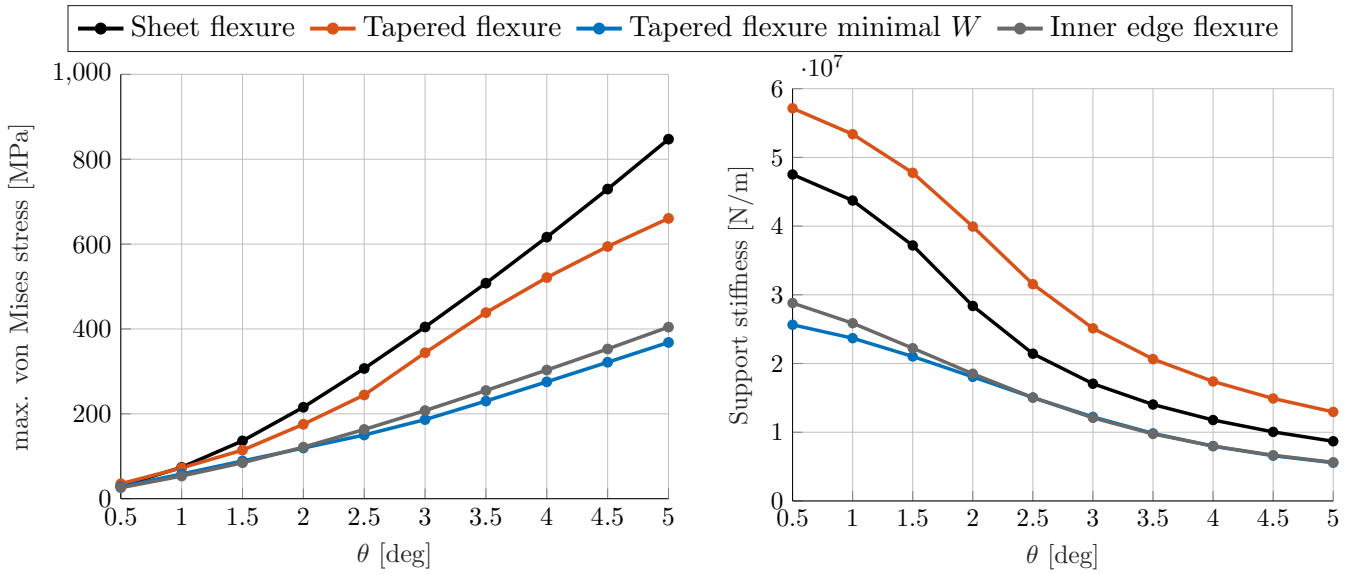

(a) maximum Von Mises stress (b) Support stiffness

Figure K.3: Comparison of the four flexure types over prescribed rotation

The effect of η on the support stiffness of a tapered flexure with $W = 50$ mm and a bow-tie flexure with $W = 100$ mm is illustrated in Figure K.4. Other parameters: $L = 100$ mm, $t = 0.5$ mm, $R = 75$ mm, $E = 193$ GPa, $G = 74$ GPa, and a prescribed rotation of $\theta = [0.5 - 5]°$. It is observed that wider sheet flexures have a higher support stiffness along the global $x-$axis. Furthermore, the figure illustrates that both the tapered flexure and bow-tie flexure have a larger support stiffness than their original sheet flexure. This indicates that η does not only reduce stress but also increases the support stiffness. This could be attributed to wider flexures exhibiting higher support stiffness, and increasing η removes material from the top and bottom flanges, which in a way decreases the slenderness of the flexure. Further study could provide a more detailed understanding of how η influences the overall stiffness behavior of the flexures.

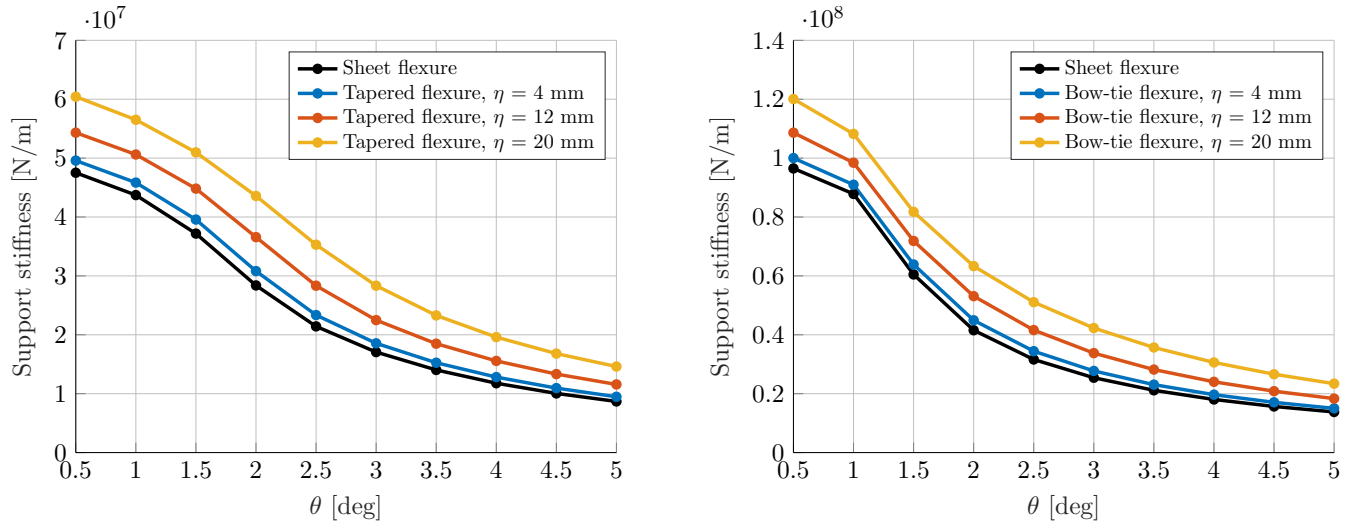

(a) Tapered flexure $W = 50$ mm (b) Bow-tie flexure $W = 100$ mm

Figure K.4: Support stiffness in global $x-$direction evaluated for various values of η